Response of dosimetric devices to proton beams

UNIVERSIDAD
DE GRANADA

Juan Alejandro de la Torre González

Programa de doctorado en Física y Ciencias del Espacio
Universidad de Granada

This dissertation is submitted for the degree of
Doctor en Ciencias Físicas

Supervisors: Dra. Marta Anguiano Millán
Dr. Miguel Ángel Carvajal Rodríguez

Editor: Universidad de Granada. Tesis Doctorales
Autor: Juan Alejandro de la Torre González
ISBN: 978-84-1195-870-7
URI: https://hdl.handle.net/10481/107605

A mi familia,
por todo su apoyo durante todos estos años.

Agradecimientos

Resumir en un par de páginas todo lo que he vivido a lo largo de estos años no es tarea sencilla. Aunque parezca mentira, la célebre frase de Ortega y Gasset, *"Yo soy yo y mis circunstancias"*, refleja con precisión el mensaje que deseo transmitir con estas palabras. Todo esto no tendría sentido sin las personas que han estado a mi lado y que han hecho posible la realización de esta tesis. Durante estos cuatro años, he compartido innumerables momentos que han moldeado tanto este trabajo como a mí mismo. Un sinfín de anécdotas e historias inundan mi mente, y sin ellas, nada de todo esto tendría el mismo sentido.

En primer lugar, quiero expresar mi más profundo agradecimiento a Marta Anguiano, directora de esta tesis, por su inestimable ayuda a lo largo de estos años. Durante todo este tiempo, me has guiado y ayudado a crecer tanto personal como profesionalmente. No ha habido un solo día en el que no me hayas recibido con una sonrisa ni intentado resolver mis dudas. Gracias por estar siempre ahí. También quiero reconocer las enseñanzas de Miguel Ángel Carvajal (Migue), codirector de esta tesis. Aunque nuestro trato no ha sido tan cercano como el que he tenido con Marta, siempre he podido contar contigo cuando lo he necesitado. Gracias por tu apoyo y orientación.

Este recorrido no estaría completo sin mencionar a Antonio M. Lallena, cuya pasión por la física me inspiró desde aquellas clases de interacción radiación-materia durante el máster. Gracias por estar siempre dispuesto a compartir tus conocimientos y por fomentar en mí el entusiasmo por esta disciplina. En ese mismo contexto, tuve el honor de conocer a uno de mis referentes en este campo, el profesor Francesc Salvat, a quien agradezco profundamente por su ayuda inestimable cada vez que surgían dudas sobre PENELOPE.

También quiero expresar mi gratitud a los integrantes del grupo de investigación ECsens con los que he tenido el placer de trabajar: Alberto J. Palma, Juan Antonio, Isidoro y Antonio. Gracias por ayudarme, junto a Migue, a comprender mejor el funcionamiento de los dosímetros y por brindarme la oportunidad de participar en campañas experimentales. En este ámbito, también quiero agradecer a Damián Guirado por su dedicación y por sacrificar

parte de su tiempo libre para llevar a cabo dichas mediciones experimentales.

Recordando mi estancia en Prévessin, quiero dar las gracias a todas las personas que hicieron de aquellos tres meses una experiencia inolvidable. En especial, a Francesc Salvat-Pujol y Alexandra Şerban, por su acogida y por los buenos momentos compartidos mientras explorábamos los entresijos de FLUKA. Junto a vosotros descubrí un nuevo enfoque de la física. Gracias por todo lo que me enseñasteis.

A mis compañeros del grupo de investigación que han compartido conmigo esta etapa: Dani, Álvaro, Ana María, Garví, Irene, Laura y Lidia, gracias por los buenos momentos y por los innumerables cafés que levantaron mi ánimo cuando más lo necesitaba. No puedo olvidar a Joaquín, Fran, Jesús, David, Emilio, Víctor, Alex, Antònia, David, Elena, Juan, Matilde, Nishal, Pablo, Pablo, Pedro, Victor, David y Reza. Gracias por demostrarme que hay vida más allá del trabajo; animándome a recitar encima de un escenario o hacer deporte tres veces a la semana. Y como olvidar aquella costumbre de las cervezas de los viernes o aquellas noches de karaoke. Gracias por hacer estos cuatro años un poco más amenos.

Tampoco me puedo olvidar de mis amigos del pueblo: Miguel, Raúl, Paco, Juan Carlos, Vero y Rubén. Gracias por todo. Parece increíble pensar en aquel día en que dejamos nuestro hogar para mudarnos a la gran ciudad. Son muchas las historias que hemos compartido y, aunque este trabajo marque el cierre de una etapa, sé que seguiréis ahí. A pesar de que la vida nos haya llevado por caminos distintos, sé que siempre podré contar con vosotros. Espero que sigamos en contacto como hasta ahora.

Por último, pero no menos importante, quiero agradecer a mi familia por su apoyo incondicional. Raúl y Alberto, gracias por seguir preocupándoos por vuestro hermano pequeño, por las comidas de los sábados en el pueblo y por hacerme rabiar como cuando éramos niños. A mis sobrinos Daniel y Martín, gracias por llenar mi vida de alegría con vuestra energía y sonrisas; el futuro es vuestro, nunca dejéis de soñar. Y, por supuesto, a mis padres: gracias por estar siempre ahí, por intentar comprenderme a pesar de que a veces os costara y por brindarme todo vuestro apoyo. Sin vosotros, nada de esto habría sido posible.

Abstract

In this thesis, the physical models implemented in the general-purpose Monte Carlo codes PENH, FLUKA, and TOPAS are validated. To achieve this, a concise review of the theoretical framework describing proton interactions with matter is presented. This is followed by a detailed comparison with experimental available data. The validation process includes two main aspects: firstly, the multiple Coulomb scattering algorithms is checked. Secondly, both nuclear reactions and nuclear elastic scattering are reviewed.

Following the validation of the Monte Carlo codes used in this thesis, the optimal tracking parameters for PENH are determined, while those proposed in the scientific literature for FLUKA and TOPAS are reviewed. To identify the optimal set of parameters, the Fano test is implemented. Additionally, a novel approach to estimate the effects of nuclear reactions using the Fano test is applied to the considered Monte Carlo codes. After establishing the optimal tracking parameters, the calibration factor k_{Q,Q_0} and the perturbation factors p_Q are determined for the CRGR10/C5B/UG2 ionization chamber, which was selected due to its availability for future experimental measurements.

Finally, a Monte Carlo model is developed to estimate the response of an *in vivo* dosimeter for proton therapy. The BPW34S photodiode is chosen for this purpose because of its favourable response to photon radiation. The Monte Carlo model is subsequently tested using experimental data from a clinical photon source. Once validated, this Monte Carlo model is used to investigate the feasibility of *in vivo* dosimeters in proton therapy, including the characterization of the BPW34S photodiode with respect to energy and angular dependence.

Resumen

En esta tesis se validan algunos de los modelos físicos implementados en los códigos Monte Carlo de propósito general PENH, FLUKA y TOPAS. Para ello, se presenta una revisión concisa del marco teórico que describe las interacciones de los protones con la materia. A continuación, se realiza una comparación detallada con los datos experimentales disponibles. El proceso de validación incluye dos aspectos principales: en primer lugar, la comprobación de los algoritmos de dispersión múltiple de Coulomb. En segundo lugar, se revisan tanto la implementacion de las reacciones nucleares como de la dispersión elástica nuclear.

Tras la validación de los códigos Monte Carlo utilizados en esta tesis, se determinan los parámetros óptimos de *tracking* para PENH, mientras que se revisan los propuestos en la literatura científica para FLUKA y TOPAS. Para identificar el conjunto óptimo de parámetros, se implementa el test de Fano. Además, se aplica a los códigos Monte Carlo considerados un enfoque novedoso para estimar los efectos de las reacciones nucleares utilizando la prueba de Fano. Tras establecer los parámetros óptimos de seguimiento, se determinan el factor de calibración k_{Q,Q_0} y los factores de perturbación p_Q para la cámara de ionización CRGR10-C5B-UG2, seleccionada por su disponibilidad para futuras medidas experimentales.

Finalmente, se desarrolla un modelo Monte Carlo para estimar la respuesta de un dosímetro *in vivo* para terapia de protones. Para ello se elige el fotodiodo BPW34S por su favorable respuesta en el caso de fotones. Posteriormente, el modelo Monte Carlo se compara con datos experimentales que han sido obtenidos con una fuente de fotones de 6 MV de un acelerador lineal de uso clínico. Una vez realizado este estudio preliminar, este modelo Monte Carlo se utiliza para investigar la viabilidad de los dosímetros *in vivo* en la terapia de protones, incluyendo la caracterización de la respuesta del fotodiodo BPW34S con respecto a la energía del haz de protones, así como la dependencia angular.

Table of contents

Nomenclature

Acronyms / Abbreviations

BP Bragg Peak

CoP Code of Practice

CSDA Continuous Slowing Down Approximation

EPID Electronic portal imaging device

HCL Harvard Cyclotron Laboratory

HEE Hard Elastic Event

IAEA International Atomic Energy Agency

IC Ionization Chamber

ICRU International Committee for Radiological Units

IMRT Intensity-modulated radiation therapy

LBL Lawrence Berkeley Laboratory

LDR Light-dependent resistor

LET Linear Energy Transfer

LHC Large Hadron Collider

MC Monte Carlo

MCS Multiple Coulomb Scattering

MFP Mean Free Path

MGH Massachusetts General Hospital

MLFC Multilayer Faraday Cup

MOSFET Metal oxide field effect transistor

NIST National Institute of Standards and Technology

PEANUT Pre-Equilibrium Approach to NUclear Thermalization

SLAC Stanford Linear Accelerator Center

SOBP Spread-Out Bragg Peak

TLD Thermoluminiscence detector

TPS Treatment Planning System

VMAT Volumetric modulated arc therapy

Introduction

Particle therapy is one of the most consolidated techniques in the field of radiation therapy [1]. This kind of therapy uses ion beams to treat patients with cancer. If protons are used as source particles, this type of therapy is known as proton therapy. The proton therapy is the most developed method among the wide range of techniques that make up the particle therapy.

The idea of using protons as particle source was suggested by Robert R. Wilson in 1946 at the Harvard Cyclotron Laboratory (HCL) [2]. In the paper where Wilson suggested this idea, he introduced the concept of particle therapy for deep-seated tumours treatment. He noted the important role of protons due to their low energy range for clinical practice. In that time, compact accelerators were only a dream and the most feasible ion was the proton one.

On the one hand, in that paper, the advantages of using protons instead of photons are discussed. These advantages, which are clearly evident in the depth dose curve, and which are a consequence of the way in which protons interact with matter and the finite range of these kind of particles, are remarked. These advantages, characteristics of the depth-dose curve helps to reduce the absorbed dose in the healthy tissue without changing the deposited dose in the tumour. Besides, the absorbed dose is almost zero beyond the region where the maximum dose is deposited. This special feature is known as Bragg peak (BP). This allows the medical physicist to shape very well the irradiated zone, avoiding critical organs like, for example, lungs, optical nerve or rectum, depending on the body area irradiated.

On the the other hand, Wilson pointed out two problems related to this kind of therapy: the energy straggling and the large scattering for protons, which produce a significant broadening in the proton beam. However, these two features can be useful for clinical practice. On the one hand, energy straggling can help with the implementation of a spread-out Bragg peak (SOBP). A SOBP is a superposition of monoenergetic proton beams [3, 4], correctly weighted to deliver a constant dose along the extended tumour volume of the patient. On the other hand, broadening of the proton beam due to scattering allows to irradiate a tumoural

region without using complex techniques. A proof of this is the use of passive scatters during proton irradiation [3].

After Wilson suggested the proton therapy, the first experiment using this technique was carried out with a synchrocyclotron at the Lawrence Berkeley Laboratory (LBL) in the early 1950s [5]. In that experiment, the possible biological effects that protons could produce in mice was studied. Nowadays, it has been shown that the biological effects of high energy protons are similar to photon effects. However, a large biological impact has been found for low energy protons [3, 6]. This would increase the effectiveness of the proton therapy comparing to traditional techniques. Nevertheless, it is important to note that the precision in proton therapy is vital if a large dose amount is to be avoided from being delivered to the healthy tissue next to the cancerous zone. Due to the high gradient of dose deposition in the Bragg peak, an important damage in the healthy tissue can be produced, if the tumoural area is not properly delimited. The resolution of this problem has motivated the development of different techniques (prompt gamma cameras [7], *in vivo* PET [8] or nuclear magnetic resonance imaging [9]) to track the proton beam and assure that the tumour is properly irradiated.

In 1954, the first patient was treated with protons at LBL [10]. This patient had a metastatic breast cancer, which had spread to her brain. Her pituitary gland was then irradiated with a proton beam to suppress its activity. This was a simple case because the doctors used a bony landmarks of the skull (sella turcica) as reference point for the proton irradiation. Despite Wilson's idea, the doctors did not use the BP for irradiation. Instead, they used a crossfire technique, using the depth-dose plateau. This treatment was successful and proved the viability of this type of treatment. Between 1954 and 1957, 30 patients were treated in this laboratory [3].

After the first attempt in the LBL, the clinical practice started in HCL in 1959. The clinical program in this center was developed by a collaboration between the HCL and the Massachusetts General Hospital (MGH). This collaboration was very fruitful and the HCL became a reference center until its closure in 2002. In this center, 9116 patients were treated, generating a valuable amount of data that have been used in the analysis and improvement of proton therapy [3].

During the late twentieth century, the technology related to this therapy kept improving and a large quantity of proton therapy centers were opened around the world. Some of those new centers were built in Uppsala, Dubna, St. Petersburg, Orsay or Chiba. Nowadays, there

are 109 proton therapy centers around the world and 60 centers will be built in the following years. 350336 people have been treated during 70 years, but a high increase in the number of patients treated with this technique is expected [11]. In Spain, there are two working private centers in Madrid. Additionally, ten centers will be built in this country during the 2020's decade. This fact will position Spain as one of the countries with more proton therapy centers in Europe.

Despite of the fact that proton therapy is a well-established technique, it must face up to some challenges, such as *in vivo* range verification [7, 8, 12] or the reduction of uncertainties for the absorbed doses in patients [13, 14]. In proton therapy, as well as in other forms of radiotherapy (e.g. with photon or electron) the main objective is to deliver the desired dose to the tumour region. To achieve this goal, the maximum uncertainty allowed by the International Committee for Radiological Units (ICRU) is 5% [15].

Treatment Planning Systems (TPS) are used in the clinical practice in order to design the treatment for patients. To do that, the TPS uses a wide range of algorithms to simulate the interaction between protons and matter. The main objetive of TPS is getting a 3% for the relative uncertainties obtained in the dose calculation. To achieve this goal, these algorithms are calibrated with measured dose profiles in water and air for different kinds of beams [16].

In order to measure these dose profiles, the most used devices are ionization chambers. However, the output of these detectors must be corrected by using the correction factors k_{Q,Q_0} [17]. Although these factors can be measured [18–20], it is difficult to characterize these devices for every proton beam employed in the clinical practice due to, among other problems, the scarce time that the proton accelerator is available [21, 22]. For all the reasons mentioned above, Monte Carlo (MC) simulations can be used to determinate the k_{Q,Q_0} factor, being the gold standard for this type of calculations [23–27]. The MC codes PENELOPE/PENH [28, 29], TOPAS [30, 31] and FLUKA-CERN [32, 33] are usually considered. Other way to apply MC simulations to improve the clinical practice could be the characterization of *in vivo* detector. *In vivo* dosimetry consists in the measuring of the dose delivered to the patient during the treatment. Its implementation could be key to detect any problem during an irradiation session [34]. There is a wide range of detectors used in this field, e.g. thermoluminiscence detectors (TLD), metal oxide field effect transistors (MOSFET), diodes, photodiodes, light-dependent resistors (LDR) or radiochromic films [34–37].

The amazing development of MC techniques has made it possible to perform *in silico* experiments that would have required a big deal of effort to perform experimentally. In addition, this type of simulations has allowed to save a large amount of beam time. This is a very valuable situation for the clinical practice. For all these reasons, as it has been noted above, MC simulations have become the gold standard for the calculation of several magnitudes in medical physics.

Despite the widespread use of MC simulation, it is important to note that the results obtained from this type of simulation will never replace the experimental data. This is due to the way that MC results are obtained. MC results are strongly conditioned by physical models implemented in these kind of codes (that usually have several approximations) and how these models are implemented in tracking algorithms used to transport particles through matter. For this reason, some discrepancies can be found between experimental and MC data. In the scientific literature can be found a wide range of studies whose aim is to check the validity of these models. For example, Vilches *et al.* [38] did a study of the implementation of the scattering algorithm for electron in PENELOPE (v2003 and v2005), Geant3, Geant4, EGSnrc and MCNPX. In this study, discrepancies between the experimental data obtained by Kulchitsky and Latyshev [39] and the results calculated with PENELOPE (v2003), Geant3, Geant4 and MCNPX were found. This example highlights the importance of the validation of the physical models used in MC simulations.

With this in mind, it is important to check the validity of the physical models used in the general purpose MC codes to describe the interaction between protons and matter, in particular, to achieve this goal, experimental data can be used to validate the results obtained with the MC models. This information could help to identify the limits of the use of these techniques. In addition, knowledge of the limitations of the MC codes provides a strong robustness to the results obtained with this type of simulations.

To sum up, the main objective of this thesis is to use the MC codes PENH, TOPAS and FLUKA-CERN (via FLAIR [40]) to characterize the dosimetric devices used in proton therapy. To achieve this goal is essential to check the validity of the physical models implemented in these MC codes, in order to describe correctly the interaction mechanisms of protons with matter. This will be followed by an analysis of the tracking parameters that are going to be employed in our MC simulations. With all these validations, we can guarantee that we will obtain robust results in the subsequent analysis that we will carry out.

In the first chapter, proton interaction with matter is reviewed. The physical mechanism of interactions is described in a detailed way.

In the second chapter, a brief description of the MC methods is done. Furthermore, a detailed description of the physical models implemented in the MC code used in this thesis is given.

In the third chapter, an analysis of the multiple Coulomb scattering (MCS) algorithms is given. The perform of these algorithms are studied for the different MC codes considered. These types of algorithms have an important role to simulate properly the energy deposition in MC simulation. On top of that, the physical models used to describe elastic nuclear interactions and nuclear reactions are checked. These interactions are fundamental to calculate the off-axis dose in proton therapy treatment [41] and it is essential to check their performance to validate the results of the MC codes when an analysis of the deposited dose in healthy tissue is done.

In the fourth chapter, the characterization of ionization chambers, using MC simulation, is implemented. To reach that goal, a study of the tracking parameters is done. To optimise the tracking parameters used in the simulations, the Fano test has been employed in order to analyze the performance of the MC codes considered. After that, the calibration method is reviewed and applied to a toy model. The results with this toy model will help us to understand how the different parts of the ionization chamber affect to the correction factor. Finally, an ionization chamber are going to be characterized using the MC simulations for proton therapy.

The fifth chapter gives a brief introduction to *in vivo* dosimetry, focusing on the study of photodiodes. A simulation, using photons as primary particles, is implemented as a proof of concept for the characterization of these type of devices. This is due to the fact that, in the scientific bibliography, there are experimental data that can be compared with the results obtained in the MC simulations carried out in this thesis. Afterwards, a study of the viability of this kind of dosimetry is done for proton therapy. Finally, the energy and angular dependence of devices under study are analyzed. This information allow us to characterize this type of devices for the clinical practice in proton therapy.

In the last chapter, conclusions and future work of this thesis are discussed.

Chapter 1

Interaction of protons with matter

If I have seen further than others, it is by standing upon the shoulders of giants

Isaac Newton

The particular way in which protons interact with matter helps to spare the healthy tissue without reducing the deposited dose in the tumour site. The depth dose curve related to a proton beam, that is called the Bragg curve (Figure 1.1), has a flat plateau at the beginning and a characteristic peak at the end of the curve [42].

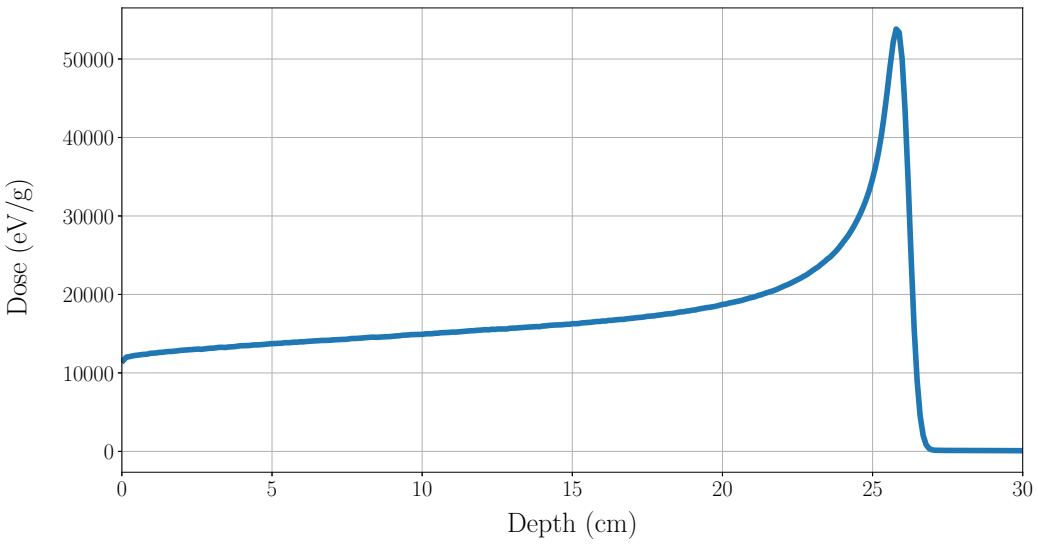

Fig. 1.1 Bragg curve for a 200 MeV proton pencil beam in water.

Protons basically interact by two mechanisms: they lose energy and are deflected by myriad electromagnetic interactions with the atoms of the material in which they move, and they can also collide head-on with an atomic nucleus and undergo a nuclear interaction. On the one hand, as noted above, the first kind of process is the electromagnetic interaction of protons with matter (elastic collisions with the whole atom, radiation emission, atomic excitations and ionizations), and there is currently a solid theoretical framework for describing this type of interaction. On the other hand, the other process mentioned has a more empirical description. Nevertheless, the description available is sufficient to simulate the nuclear processes associated with the transport of protons at energies used in proton therapy (50-250 MeV). In the following subsections, the theoretical description of the interactions of protons with matter is reviewed.

1.1 Stopping processes

Stopping processes can be defined as all events where protons lose a fraction of their energy. Mainly, protons are going to lose their energy via electromagnetic processes: elastic collisions with the whole atom, and inelastic collisions with atomic electrons, which results in atomic excitations and ionizations. In this subsection, a brief summary will be given to explain how all these processes influence the interaction of protons with matter and how they can be described mathematically.

1.1.1 Electronic Mass Stopping Power

In the first place, the effect of inelastic collisions with atomic electrons are described. On the one hand, if the proton interacts with distant atomic electrons, this interaction is known as *soft* collision. In the *soft* collisions, protons lose a small amount of energy and they suffer a small deflection. This kind of interaction is related to atomic excitation of the medium atom. On top of that, *soft* collisions are the most frequent interactions for protons. On the other hand, if the proton interacts with close electrons, this interaction is called *hard* collision. The *hard* collisions are related with atomic ionization, then secondary particles are generated in these kind of processes. *Hard* interactions are characterized by large energy losses and deflection angles.

To quantify the energy losses related to these kind of processes, the electronic mass stopping power is defined as the energy loss per unit length due to inelastic electromagnetic interactions. For fast charged particles (around 10 MeV to 1 GeV for protons), the mass electronic stopping power is described by the Bethe formula [43–47]:

$$\frac{1}{\rho}S_{\mathrm{el}} = 4\pi r_{\mathrm{e}}^2 m_{\mathrm{e}} c^2 N_{\mathrm{A}} \frac{Z}{A}\frac{z^2}{\beta^2}\left[\log\left(\frac{2m_{\mathrm{e}}c^2\beta^2}{I(1-\beta^2)}\right) - \beta^2\right] , \tag{1.1}$$

where r_{e} is the classical radius of the electron, m_{e} is the mass of the electron, c is the speed of light in vacuum, z is the atomic number of the projectile, Z is the atomic number of the target, N_{A} is the Avogadro number, A is the molar mass of the target atom, β is the projectile's speed normalised to the speed of light and I is the mean excitation energy of the medium. This expression has been deduced using the first Born approximation [44, 48].

The main parameter that characterized the medium where the proton moves, apart from Z and A, is the mean excitation energy (I). This parameter can be defined as a geometric average of the ionization and excitation energies of the atomic shell of the target material, weighted by the corresponding oscillator strengths [43, 44]. The standard values of I are collected in the ICRU report 37 [49] for a wide range of elements and materials. Besides, there is an experimental fit [43] that can reproduce the tendency of the data collected in the ICRU report 37 for elements with atomic number $Z \geq 4$:

$$I = Z\,(9.6 + 6.25\exp[-0.075Z])\ \ [\mathrm{eV}] . \tag{1.2}$$

To estimate the mean excitation energy for compounds, the following expression is used [49–52]:

$$\log(I) = \frac{\sum_j \omega_j (Z_j/A_j)\log(I_j)}{\omega_j (Z_j/A_j)} , \tag{1.3}$$

where ω_j is the weight fraction, Z_j is the atomic number, A_j is the atomic weight and I_j is the mean excitation energy of the j-th element.

As has been commented above, the Bethe formula only offers a good description when the incident particle moves fast. In addition, the Bethe formula does not take into account other important relativistic effects as the polarization of the medium. To improve the results given by the Bethe formula, several correction factors must be used [47]:

- **Shell corrections**. In the deduction of the Bethe formula, the movement of the atomic electron is not considered. This simplification has a significant implication when the

incident particle has low energy. This term tries to correct the Bethe formula at low energies, considering the movement of the atomic electron in the material [51].

- **Barkas correction**. The Bethe formula predicts the same energy loss for a particle and its antiparticle, because it is proportional to the the projectile charge squared. However, it turns out that this is wrong, because there are differences between the stopping power of a particle and its antiparticle [53]. These differences are related to a term in the electronic stopping power that is proportional to z^3 and it is not considered when it is used the first Born approximation to derivate the Bethe formula [48]. The Barkas term is only significant for low energy. In the range of energies used in this thesis (50-250 MeV), this term does not play a relevant role in the electronic stopping power.

- **Lindhard-Sørensen correction**. The Lindhard-Sørensen correction corresponds to a term in the electronic stopping power that is proportional to z^4 [48] and is only significant for low energies. As in the case of the Barkas correction, the Lindhard-Sørensen correction does not affect the electronic stopping power of protons for the energy range considered.

- **Density correction**. This correction term is related to the effect of the density of the medium in which the protons are moving. For a low-density medium (e.g. air), protons can be expected to interact with a single distant atom due to the relatively small number of atoms in this material compared to a high-density material. However, in the latter medium, the protons will interact with several atoms at once. This creates a screen effect that reduces the energy losses associated with inelastic electromagnetic interactions, more important at high energies for protons ($\sim$ 1 GeV) due to a relativistic effect [43]. In this work, the contribution of this term is negligible due to the energy range considered.

All these corrections help to improve the results obtained with the Bethe formula. The low energy limit of the corrected expression, including all the terms described above, is found around 0.75 MeV for protons [47].

1.1.2 Nuclear Mass Stopping Power

Other mechanisms by which protons can lose energy are elastic collisions with atoms. These interactions are scarce. When an elastic collision is produced, the impinging proton loses a small amount of energy. This energy loss creates a recoil atom. The transferred energy to this recoil atom is proportional to the mass ratio of the particles involved in this event. This means that energy loss due to these kind of collisions is insignificant for heavy

targets, but could be significant for light ones ($\sim 1\%$ of the total energy loss) [43].

To quantify the effect of elastic collisions in the proton energy losses, ICRU defines the nuclear mass stopping power. This magnitude is defined in terms of the cross section for elastic collision between protons and the target atom [50], and for a proton of energy E is given by:

$$\frac{1}{\rho}S_{\text{nucl}}(E) = 2\pi\,\frac{N_{\text{A}}}{A}\int_0^{W_{\max}} Q(\theta,E)\frac{d\sigma_{\text{elast}}}{d\Omega}\sin(\theta)d\theta\ , \tag{1.4}$$

where N_{A} is the Avogadro number, A is the molar mass of the target atom, $W_{\max}$ is the maximum energy transferred in the collision, θ is the deflection angle in the center-of-mass system and $Q(E,\theta)$ is the recoil energy of the target atom, which is given by [54, 50]:

$$Q(E,\theta) = \left(\frac{2m_{\text{t}}c^2E\left(E+2mc^2\right)}{(m_{\text{t}}c^2+mc^2)^2+2m_{\text{t}}c^2E}\right)\sin^2(\theta/2)\ , \tag{1.5}$$

m and m_{t} are the mass of the proton and the target atom, respectively. The quantity in the parenthesis is $W_{\max}$. The nuclear mass stopping power is only relevant for low energies ($E \sim$ keV) and its contribution can be neglected in the clinical energy range [55]. The nuclear stopping power could only be important in the region around the Bragg peak, where the energy of the protons is low. It is important to highlight the exceptional case of hydrogen. This nucleus has the same mass as a proton. For this reason, large energy losses can be related to the elastic interactions of protons with hydrogen atoms.

1.1.3 Radiative Mass Stopping Power

When protons travel through matter, they are continuously interacting with electromagnetic fields generated by atoms in the medium where they are moving. As a result of this interaction, protons can change their directions, emitting braking radiation (*bremsstrahlung*). To quantify the energy losses related to proton *bremsstrahlung*, the radiative mass stopping power is defined as [43]:

$$\frac{1}{\rho}S_{\text{rad}}(E) = \frac{N_{\text{A}}}{A}\int_0^{E} k\frac{d\sigma}{dk}dk\ , \tag{1.6}$$

where E is the energy of the proton, k is the energy of the emitted photon and $\dfrac{d\sigma}{dk}$ is the differential *bremsstrahlung* cross section. The following relation between the mass radiation

stopping power and the power emitted by accelerated proton, P, [56] can be obtained:

$$\frac{1}{\rho}S_{\text{rad}} = \frac{P}{\rho v} \propto \frac{Z^2}{\rho v m^2} \,, \tag{1.7}$$

where v is the speed of the proton. It is clear that the mass radiation stopping power is proportional to the square of the atomic mass of the medium and inversely proportional to the square of the proton mass. Due to the large mass of protons, this quantity can be neglected for the clinical energy ranges (50-250 MeV), but it plays a significant role at higher energies ($\sim$ 1 GeV) [55].

1.1.4 Range

Electronic and nuclear mass proton stopping power have been defined to quantify the proton energy losses due to electromagnetic processes. A more general magnitude can be used to quantify these effects, without caring the kind of electromagnetic interaction (elastic or inelastic processes). This magnitude is called total mass stopping power and can be defined in the following way :

$$\frac{1}{\rho}S_{\text{total}} = \frac{1}{\rho}S_{\text{nucl}} + \frac{1}{\rho}S_{\text{el}} \,. \tag{1.8}$$

For energies used in clinical practice, the total stopping power is approximately the electronic mass stopping power due to the small losses associated with the elastic interactions.

Total mass stopping power is only defined for elements, but it can be extended to compounds using the Bragg additivity rule [43, 57]. This rule considers that each atom in the mixture contributes independently to the total mass stopping power of the compound. Using this approximation, the effects of chemical bounds of the compound are neglected. The Bragg additivity rule can be expressed as:

$$\left(\frac{1}{\rho}S_{\text{total}}\right)_{\text{compound}} = \sum_{i=1}^{N} \omega_i \left(\frac{1}{\rho}S_{\text{total}}\right)_i \,, \tag{1.9}$$

where $\left(\frac{1}{\rho}S_{\text{total}}\right)_{\text{compound}}$ is the total stopping power of the compound, N is the number of elements in the compounds, ω_i is the weight fraction of the i-th element and $\left(\frac{1}{\rho}S_{\text{total}}\right)_i$ is the total stopping power of the i-th element.

As charged particles interact continuously with matter, they can only travel a finite distance inside the medium where they are moving. In order to quantify the mean distance that a proton with an initial energy E_0 travels in a material, a new magnitude is proposed. This magnitude is the range, and in order to calculate it, it will be considered that protons are going to lose their energy continuously along the path that it follows. Under this hypothesis, the range of a particle with initial energy E_0 can be calculated as follows

$$R = \int_0^{E_0} S_{\text{total}}^{-1}(E) dE \ . \tag{1.10}$$

This analytical approximation to calculate the range is known as Continuous Slowing Down Approximation (CSDA). It is widely used in clinical practice, for example, in TPS or in condensed MC codes. This analytical formalism allows to calculate the range in a simple way, being a good magnitude to characterize a proton beam in clinical practice [17]. On top of that, a database with the range information for a wide range of materials have been calculated using CSDA by the National Institute of Standards and Technology (NIST) [58].

Furthermore, there are another alternative ways to estimate the range of a proton beam. One of these uses an experimental relation between the range and the initial energy of the proton. This relation is known as the Bragg-Kleeman rule:

$$R = \alpha E_0^p \ , \tag{1.11}$$

where α and p are fit parameters. For water $\alpha = 2.2 \cdot 10^{-3}$ cm $\cdot$ MeV^{-p} and $p = 1.77$ [59]. This theoretical framework has been used to make analytical calculations related to proton depth-dose curve [4, 59]. In addition, the Bragg-Kleeman rule gives a simple description of the Bragg curve that allow to build Spread-Out Bragg Peak in an undemanding way, as it is done in this thesis [4] (Appendix B).

Alternatively, an experimental definition for the range, which is called mean projected range, is given in [57]. The mean projected range of a proton with initial energy E_0 is defined as the distance which the initial proton beam fluence has been halved. From this definition, it can be shown the following relation for the mean projected range (R_{mp}):

$$R_{\text{mp}} = d_{80} \ , \tag{1.12}$$

where d_{80} is the depth at which the dose beyond the Bragg peak has a value equal to 80% of the maximum point of the Bragg peak.

1.1.5 Energy Straggling

As have been discussed in the introduction of this section, an accurate description of the mean energy loss due to electromagnetic interactions in a finite path can be done for protons. However, these kind of processes have a stochastic nature; in other words, protons do not loss the same amount of energy in each interaction with the atoms of the medium. This phenomenon is known as energy straggling.

When a proton travels through a material medium, it interacts with a large number of atoms along its track. The most probable energy losses in these interactions are of the order of 20 eV. For compound media by light elements (e.g. air), around the 80% of all losses are smaller than 100 eV [50].

The total energy losses (ε) in a track with a length x is given by the straggling distribution function $f(\varepsilon,x)d\varepsilon$. This function is not symmetrical to the mean energy loss (quantity related to the stopping power), so the most probable energy loss is not equal to the mean energy loss. The asymmetry in the straggling function results from the fact that interactions with a large energy transfers are rare [43, 50], because *soft* interactions are more probable than *hard* interactions.

The first attempt to calculate the straggling distribution function was done by Evan J. Williams [60]. Using an earlier Bohr calculation [61, 62], Williams found that the straggling distribution could be described by a Gaussian function for a thick slab of material. In order to obtain this result, Williams followed a classical approach. In his calculation, he considered a large number of interactions of the protons in the material with small energy losses. Under this considerations, the straggling function is [45]:

$$f(\varepsilon,x)d\varepsilon = \frac{1}{\sqrt{2\pi}\sigma(x)} \exp\left(\frac{-(\varepsilon-\mu_\varepsilon)^2}{2\sigma^2(x)}\right) , \tag{1.13}$$

where μ_ε is the mean energy loss in a path whose length is x and $\sigma^2(x)$ is the variance of the distribution. The variance is given by the following expression:

$$\sigma^2(x) = 2\pi r_e^2 m_e c^2 z^2 \frac{N_A Z}{A\beta^2} W_{max}\rho x = \xi(x) W_{max} , \tag{1.14}$$

where W_{max} is the maximum energy loss in an interaction and $\xi(x)$ is the straggling parameter, whose value is given by:

$$\xi(x) = 2\pi r_e^2 m_e c^2 z^2 \frac{N_A Z}{A\beta^2}\rho x . \tag{1.15}$$

After Williams' attempt, Lev D. Landau developed a theory to calculate the straggling distribution function for a thin slab of material [63]. To calculate the straggling function, Landau described the straggling phenomenon using the following transport equation [46, 63]:

$$\frac{\partial f(\varepsilon,x)}{\partial x} = \int_0^\infty f(\varepsilon-\varepsilon',x)\omega(\varepsilon',E)d\varepsilon' - f(\varepsilon,x)\sigma(E)\,, \tag{1.16}$$

with E the proton energy, $\sigma(E)$ the total interaction cross section and $\omega(\varepsilon,E)$ the proton interaction probability. This probability is calculated as:

$$\omega(\varepsilon,E) = \rho\frac{N_\mathrm{A}}{A}\frac{d\sigma}{d\varepsilon}\,, \tag{1.17}$$

where $\dfrac{d\sigma}{d\varepsilon}$ is the total differential cross section with an energy loss ε. Solving the integro-differential equation (1.16) through a Laplace transform, the following expression is found

$$f(\varepsilon,x)d\varepsilon = \frac{1}{\xi(x)}\varphi_\mathrm{L}(\lambda_\mathrm{L})\,, \tag{1.18}$$

where the function $\varphi_\mathrm{L}(\lambda_\mathrm{L})$ corresponds to the deviation from the mean energy loss and it is defined as

$$\varphi_\mathrm{L}(\lambda_\mathrm{L}) = \frac{1}{\pi}\int_0^\infty \exp\left[-y\left(\log(y)-\lambda_\mathrm{L}\right)\right]\sin(\pi y)\,dy\,, \tag{1.19}$$

and λ_L is a universal parameter given by

$$\lambda_\mathrm{L} = \frac{\varepsilon-\xi(x)\left(\log\left[\dfrac{\xi(\mathrm{x})}{\bar{\varepsilon}}\right]+1-\gamma\right)}{\xi(x)}, \tag{1.20}$$

with $\bar{\varepsilon}$ the mean energy loss and γ the Euler's constant. The $\varphi_\mathrm{L}(\lambda_\mathrm{L})$ function has been tabulated in [64].

Later, P.V. Vavilov deduced a general expression to describe the energy straggling in a material medium [65]. As Landau did, Vavilov described the straggling phenomenon using the following transport equation, but he took into account the physical constrains due to the maximum energy transfer related to inelastic electromagnetic interaction [46, 65]:

$$\frac{\partial f(\varepsilon,x)}{\partial x} = \int_0^{u(\varepsilon)} f(\varepsilon-\varepsilon',x)\omega(\varepsilon',E)_\mathrm{V}d\varepsilon' - f(\varepsilon,x)\int_0^{W_\mathrm{max}}\omega(\varepsilon',E)_\mathrm{V}d\varepsilon'\,, \tag{1.21}$$

where

$$u(\varepsilon) = \begin{cases} \varepsilon & \text{if} \quad \varepsilon' < W_{\max} \\ \\ W_{\max} & \text{if} \quad \varepsilon' \geq W_{\max} \end{cases} \tag{1.22}$$

and

$$\omega(\varepsilon', E)_{\mathrm{V}} = \begin{cases} \omega(\varepsilon', E) & \text{if} \quad \varepsilon' < W_{\max} \\ \\ 0 & \text{if} \quad \varepsilon' \geq W_{\max}\,. \end{cases} \tag{1.23}$$

In an analogue way to the methods followed by Landau, Vavilov solved the equation (1.21) using the Laplace transform. From this procedure, he obtained the following expression for energy straggling [45, 65]:

$$f(\varepsilon, x)d\varepsilon = \frac{1}{\xi(x)}\varphi_{\mathrm{V}}(\lambda_{\mathrm{V}}, x, \beta^2)d\lambda_{\mathrm{V}}\,, \tag{1.24}$$

with $\varphi_{\mathrm{V}}(\lambda_{\mathrm{V}}, x, \beta^2)$ the Vavilov function, given by:

$$\varphi(\lambda_{\mathrm{V}}, x, \beta^2) = \frac{x}{\pi}\exp\left[x(1+\beta^2\gamma)\right]\int_0^{\infty}\exp\left(xf_1(y)\right)\cos\left(\lambda_{\mathrm{V}}y + xf_2(y)\right)dy\,, \tag{1.25}$$

where λ_{V}, f_1 and f_2 are defined by:

$$\lambda_{\mathrm{V}} = \frac{\varepsilon - \mu_{\varepsilon}}{W_{\max}} - x(1+\beta^2-\gamma)\,, \tag{1.26}$$

$$f_1(y) = \beta^2\left(\log\, y - Ci(y)\right) - \cos(y) - ySi(y)\,, \tag{1.27}$$

$$f_2(y) = y\left(\log\, y - Ci(y)\right) + \sin(y) + \beta^2 Si(y)\,, \tag{1.28}$$

where $Si(y)$ and $Ci(y)$ are the sine and cosine integral functions, respectively [66].

The values of the Vavilov's function have been tabulated by Seltzer and Berger [67]. If a thin thickness is considered, the Vavilov's function tends to the Landau's function [43, 65]. Apart from that, if a thick material slab is considered, the Vavilov's function tends to a Gaussian distribution [43, 46]. In short, the Vavilov's formalism gives the more completed description of the energy straggling. However, its mathematical formulation is very demanding in a computational level. For this reason, A. Crispin and G. N. Fowler [68] established a criterion to determinate which straggling description should be used. The criterion established by Crispin and Fowler is based in the parameter k:

$$k = \frac{\xi(x)}{W_{\max}}\,, \tag{1.29}$$

where $\xi(x)$ is the straggling parameter. According to k, three cases can be distinguished:

- $k \geq 1$. In this cases, protons suffer a lot of inelastic interactions. Under this circumstances, the energy fluctuations can be described by a Gaussian distribution (Williams' formalism).
- $k \leq 0.01$. This is the opposite case, there is a small number of interactions in the material. This case is well-described by the Landau's expression.
- $0.01 < k < 1$. This is the intermediate case. For these cases, neither Williams' nor Landau's theoretical framework can describe the energy straggling for protons. To describe the straggling is necessary to use the Vavilov's expression.

1.2 Scattering processes

Another significant effect of proton collisions with atoms in the material medium is scattering. Scattering produces angular deflection of the protons. This type of effect is important for the precise determination of off-axis dose features. Depending on the thickness of the material, three regimes can be distinguished [43]:

1. **Single scattering**. When proton travels through a foil whose length is smaller than or equal to the mean free path (MFP) of the proton in the material. For this thickness regime, protons may only interact once, producing a single scattering event.
2. **Plural scattering**. This regime can be applied when the length of the foil is slightly bigger than a MFP. In this case, a few scattering events could be produced in the material slab.
3. **Multiple scattering**. When the length of the foil is such that 20 or more scattering event are produced, the multiple scattering theory can be used. Under these circumstances, a statistical model can be applied to describe this physical process.

In the simulations performed in this thesis, the theoretical framework of the multiple scattering is enough to make a good description of the scattering for protons. For this reason, a brief description of the most commonly used multiple scattering theories will be made in the following sections.

1.2.1 Molière Theory

The Molière theory gives a theoretical framework to describe the angular distribution of a proton beam after traveling through a foil. To build this theoretical framework, Molière considered that the angular deflections of protons in a material are small. Under this hypothesis, the change with depth (t) of the proton angular distribution ($f(\theta,t)$) can be described by the following integro-differential equation [69, 70]:

$$\frac{\partial f(\theta,t)}{\partial t} = N\int f(\theta-\theta',t)\frac{d\sigma(\theta')}{d\theta'}d\theta' - Nf(\theta,t)\int \theta'\frac{d\sigma(\theta')}{d\theta'}d\theta' \,, \tag{1.30}$$

where N is the number of scattering atoms per volume units, $\dfrac{d\sigma(\theta')}{d\theta'}$ is the differential scattering cross section. The expression (1.30) is very similar to those used by Landau and Vavilov to describe the energy straggling (eqs. (1.16) and (1.21)). In an analog way to the methods used to solve equations (1.16) and (1.21), Molière used the Hankel transform [71] to obtain the following solution to equation (1.30):

$$f(\theta,t) = \int_0^\infty \eta d\eta J_0(\eta\theta)\exp\left[-Nt\int_0^\infty \frac{d\sigma(\theta')}{d\theta'}\theta' d\theta'\left(1-J_0(\eta\theta')\right)\right] \,, \tag{1.31}$$

where $J_0(x)$ is the Bessel function of the first kind. In its deduction, Molière considered that $\dfrac{d\sigma(\theta')}{d\theta'}$ was the screened Rutherford scattering cross section [69, 70]. Under this hypothesis, the following magnitudes can be defined:

$$\chi_c(t) = \sqrt{\frac{4\pi N_a t\, Z(Z+1)}{A}}\frac{ze}{pv} \,, \tag{1.32}$$

$$\chi_0 = \frac{1}{0.885pc}\left(\frac{e^2}{\hbar c}\right) m_e c^2 Z^{1/3} \,, \tag{1.33}$$

$$\chi_a^2 = \chi_0^2\left(1.13+3.76\left(\frac{zZe^2}{\hbar v}\right)^2\right) \,, \tag{1.34}$$

$$B(t) - \log\, B(t) = \log\left(\frac{\chi_c^2(t)}{1.167\chi_a^2}\right) \,, \tag{1.35}$$

$$\vartheta(t) = \frac{\theta}{\chi_c(t)\,B(t)^{1/2}} \,, \tag{1.36}$$

where $\chi_c(t)$ is the characteristic single scattering angle, e is the electron charge, p is the lineal momentum of the charged particle, v is the velocity of the charged particle, χ_a is the screening angle, $\hbar$ is the reduced Planck constant and $B(t)$ is the reduced target thickness. $B(t)$ has been obtained solving the trancendental equation (1.35). Furthermore, the reduced angle defined by eq. (1.36) has been introduced to simplify the deduction of the angular distribution. Making the algebraic calculation indicated in [69, 70], the following expression can be deduced from equation (1.31) [45, 69, 70]:

$$f(\theta,t)\theta d\theta = \vartheta d\vartheta \sum_{n=0}^{\infty} \frac{g^{(n)}(\vartheta)}{B^n(t)} , \tag{1.37}$$

where terms $g^{(n)}(\vartheta)$ are defined as

$$g^{(n)}(\vartheta) = \frac{1}{n!}\int_0^{\infty} u du J_0(\vartheta u)\exp\left(-\frac{1}{4}u^2\right)\left[\frac{1}{4}u^2\log\left(\frac{1}{4}u^2\right)\right]^n . \tag{1.38}$$

Taking into account in the above expansion only the first term, $n = 0$, we have

$$f(\theta,t)\theta d\theta \approx \frac{2\theta}{\chi_c(t)B^{1/2}(t)}\exp\left(-\frac{\theta^2}{\chi_c^2(t)B(t)}\right)d\theta . \tag{1.39}$$

Expression (1.39) is known as the Gaussian approximation of the Molière distribution. It can describe in an accurate way the 90% of the small angles contribution to scattering [70]. For large angles, it is necessary to add the contribution of $g^{(1)}(\vartheta)$. This function describes the non-gaussian tails due to large scattering angles. Terms with $n > 1$ only offer small corrections to the non-gaussian tails.

1.2.2 Fermi-Eyges theory

An alternative formalism used to describe the scattering profile is the Fermi-Eyges theory [72, 73]. The use of this theoretical framework is very common in medical physics. It is employed to characterize the proton beam used in the clinical practice [74–78]. This theory was first introduced by Fermi in a lecture about cosmic rays. B. Rossi and K. Greisen [72], who were in this lecture, found interesting the subject explained by Fermi and they decided to publish these results with Fermi's permission [74]. In its analysis, Fermi assumed that he had a proton point source emitting in the positive direction of the z axis in an infinite medium (Figure 1.2). Due to scattering, the proton beam will open up, increasing the size of the proton field (blue cone in Figure 1.2). The aim of this formalism is to determine the distribution of lateral displacements with respect to the z axis, $\vec{r}$, and the direction of the protons, $\vec{\Omega}$, reaching a plane at z_0 after a total displacement s. The proton directions will be

expressed using the projected angles, whose definition is:

$$\theta_x = \arctan\left(\frac{dx}{dz}\right), \qquad \theta_y = \arctan\left(\frac{dy}{dz}\right). \tag{1.40}$$

Later, L. Eyges [73] extended the Fermi's formalism to include energy losses, ΔE, within CSDA [74, 79]; in other words, the energy losses are calculated considering that

$$\Delta E = S_{\text{total}} \cdot s. \tag{1.41}$$

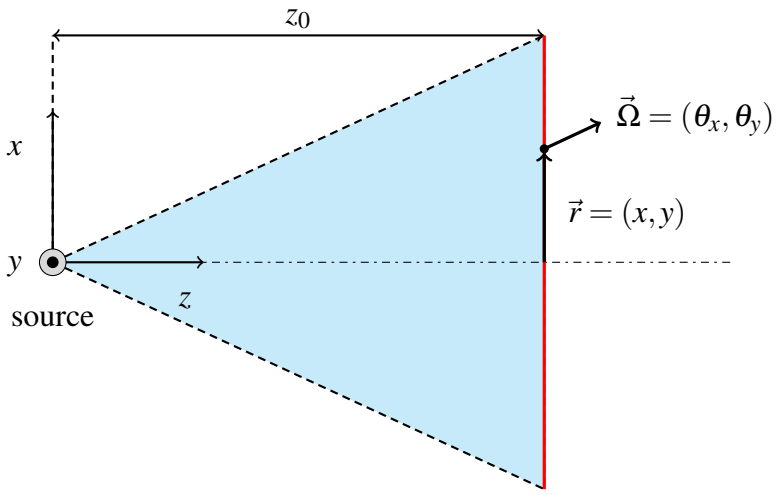

Fig. 1.2 Basic sketch of the scattering process. A proton pencil beam interacts with a material medium, opening the beam spatial distribution. The beam particles in a plane at z_0 will be characterised by the lateral displacement ($\vec{r}$) and its direction ($\vec{\Omega}$).

Let define $\Phi(s;\vec{r},\vec{\Omega})$ as the probability of finding a proton with $(\vec{r},\vec{\Omega})$ after a path s. For the energies used in the clinical practice, it can be assumed that the differential cross section for elastic scattering of protons are dominated by small angle processes, i.e., it is assumed that protons follow straight paths in the z axis. Due to that, total displacement can be approximated by the displacement in the z axis

$$s = z_0\sqrt{1+\left(\frac{x}{z_0}\right)^2+\left(\frac{y}{z_0}\right)^2} \approx z_0\,. \tag{1.42}$$

With this approximation, $\Phi(s;\vec{r},\vec{\Omega})$ can be rewritten as $\Phi(z_0;\vec{r},\vec{\Omega})$.

After this explanation, let introduce $F(z_0;x,\theta_x)$. This function is the probability density for a proton at a depth z_0 to have a lateral displacement x and its direction of motion making a projected angle θ_x with z axis. This function is a narrow bell shape centered in $x=0$ and $\theta_x=0$. Besides, this distribution is symmetrical under inversion:

$$F(z;x,\theta_x) = F(z;-x,\theta_x) = F(z;x,-\theta_x)\ . \tag{1.43}$$

On top of that, due to the symmetry that have the scattering processes for the transversal plane of motion, $\Phi(z_0;\vec{r},\vec{\Omega})$ can be expressed as:

$$\Phi(z_0;\vec{r},\vec{\Omega}) = F(z_0;x,\theta_x)F(z_0;y,\theta_y)\ . \tag{1.44}$$

Following the deduction in the appendix of [74], the analytical expression for $F(z_0;x,\theta_x)$ is:

$$F(z_0;x,\theta_x) = \frac{1}{4\pi\sqrt{B(z_0)}}\exp\left(-\frac{A_0(z_0)x^2 - 2A_1(z_0)x\theta_x + A_2(z_0)\theta_x^2}{4B(z_0)}\right)\ , \tag{1.45}$$

with $B(z_0) = A_0(z_0)A_2(z_0) - A_1(z_0)^2$ being the emittance of the proton beam. $2A_2(z_0)$ is the variance of the spatial distribution in z_0, $2A_0(z_0)$ is the variance of the angular distribution in z_0 and $2A_1(z_0)$ is the covariance. The expressions for the variance of the spatial distribution, the variance of the angular distribution and the covariance are given by [79]:

$$A_0(z_0) = \int_0^{z_0} T(\mu)d\mu\ , \tag{1.46}$$

$$A_1(z_0) = \int_0^{z_0} (z_0-\mu)T(\mu)d\mu\ , \tag{1.47}$$

$$A_2(z_0) = \int_0^{z_0} (z_0-\mu)^2T(\mu)d\mu\ , \tag{1.48}$$

where $T(\mu)$ is the scattering power. Scattering power is a measure of the effectiveness of a material in deflecting a beam of charged particles by multiple scattering. This magnitude is defined as [43, 74, 79]:

$$T(\mu) = \frac{d\bar{\theta^2}}{d\mu}\ , \tag{1.49}$$

where μ is the material thickness and $\bar{\theta^2}$ is the mean square scattering angle.

1.3 Nuclear interactions

Finally, it is time to discuss nuclear interactions. As have been commented above, protons mainly interact with matter though electromagnetic processes. In spite of the fact that hadronic interactions are nowhere near as frequent as the electromagnetic interactions, it is important to have a good description of these kinds of processes. For example, a good description of nuclear interactions is essential to determine, in an accurate way, dose deposited beyond the BP. Due to their complexity, a full theoretical description of these types of interactions is not available. For proton therapy applications an approximated description is done, which will be discussed below.

According to the ICRU [80], nuclear interactions can be classified in three categories. The first category is known as elastic interactions. In this type of interactions, the incident projectile scatters off the target nucleus, the kinetic energy of the system does not change and the internal state of the projectile and the target nucleus keep being the same. A typical case of this sort of reaction is:

$$^{27}Al\ (p,p)\ ^{27}Al.$$

It is important to highlight the case of the hydrogen. This element is part a wide range of compounds used in the clinical practice, e.g., water or Polymethyl methacrylate (PMMA). From the point of view of nuclear reactions, the case of hydrogen is unique, as it interacts only by elastic collisions. It is important to note that the proton interacting with the hydrogen nucleus loses a large amount of kinetic energy due to its similar mass.

The second kind of nuclear interactions are the non-elastic ones. In these types of nuclear interactions, the kinetic energy is not conserved. In this category, interactions where the target nucleus may undergo break-up are found. An example of a non-elastic interaction is

$$^{16}O\ (p,\alpha)\ ^{13}N.$$

Finally, the last category is known as inelastic interactions. In this kind of processes, the target nucleus is excited by the projectile. As the kinetic energy is not conserved due to the excitation of the target nucleus, the inelastic interactions are a subset of non-elastic interactions. Moreover, in this sort of interactions, the final and the initial nucleus are the same. For instance, an inelastic process is

$$^{40}Ca\ (p,p)\ ^{40}Ca^{*}.$$

Both inelastic and non-elastic interactions, where kinetic energy is not conserved, will be labelled as *nuclear reactions* along this thesis.

Despite their low frequency, if they are compared with electromagnetic interactions, nuclear reactions have a profound effect on how protons deposit their energy in the medium. The most obvious effect of nuclear reactions is related to proton fluence. When a proton undergoes a nuclear reaction, that proton is lost, producing secondary particles with a smaller range than the original one [81, 82]. These losses cause a slowly decrease in the proton fluence (Figure 1.3). If this decreasing is taken into account, the fluence of a proton beam of range R_0 can be described according to the model proposed by Bortfeld [59] as:

$$\Phi(z) = \Phi_0 \frac{1 + \lambda_\Phi (R_0 - z)}{1 + \lambda_\Phi R_0} \,, \tag{1.50}$$

where z is the distance that the proton travels inside the medium, Φ_0 is the proton fluence at the initial point considered and λ_Φ is an experimental parameter that takes into account the proton losses due to nuclear reactions. For water, the value of λ_Φ is 0.0012 cm^{-1} [59]. This value was calculated by M. Lee *et al.* [83] using a fit to the available experimental data [84].

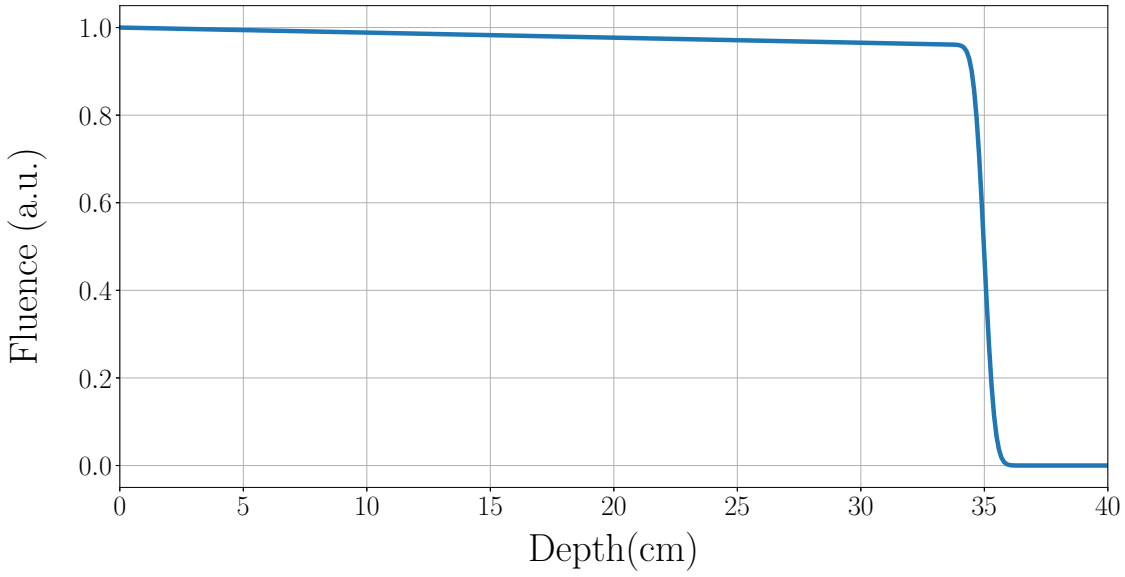

Fig. 1.3 Fluence profile for a 200 MeV proton pencil beam in water, using eq.(1.50).

An important contribution to the depth-dose curve associated with nuclear interactions is that a proton can drastically changes its direction, when it undergoes a nuclear interaction. This leads to an increase in the scattering contribution at large angles that produces an increas-

ing of the off-axis dose. To describe the contribution of nuclear interactions to the deposited dose, in addition to scattering processes due to nuclear interactions, it is also important to analyse the effect of the nuclear secondary particles. The heavy charged secondary particles deliver their energy close to the point where the nuclear reaction occurs. This increases the energy deposition in the plateau region of the depth-dose curve and, therefore, reduces it in the BP's region. Instead, the uncharged particles deposit their energy far from where they are produced, increasing off-axis dose. This could be related to the appearance of the radiation-induced second primary tumours in organs that are far from the irradiated area [78, 85].

1.3.1 Physics models for nuclear reactions

As commented above, there is no a solid theoretical framework that can describe nuclear reactions. Instead of a unified theory that explains all these type of reactions, there is a wide range of models that provides a good description of individual processes. Below is a brief explanation of the models used to describe nuclear reactions:

- **Intranuclear cascade model**. It is a dynamic model, based in Monte Carlo simulation, that describes the nuclear reactions for $E > 100$ MeV (being E the kinetic energy of the incident proton) [86]. In this energy range, the wavelength of the proton is smaller than the distance between the nucleons that compound the nuclear medium. Under these conditions, the nuclear reactions can be described as a set of nucleon-nucleon interactions. To determinate the products produced in the nuclear reaction, the proton is transported through the nuclear medium, simulating the possible interactions between the projectile and nucleons of the target [86, 87]. Despite the classical treatment, some quantum effects can be taken into account such as the Pauli blocking effect. Several models are based on this philosophy. These include the Bertini model, the Liège model or the binary model [88].

- **Equilibrium model**. This theoretical model is used to describe the nuclear reactions for low energies ($E < 20$ MeV) [88]. This model suggests that the impinging proton does not have the necessary energy to escape from the target nucleus. This event gives rise to what is known as a compound nucleus. The absorbed proton loses its energy through scattering nuclear interactions with the target nucleons. This increase in the energy of the nuclear medium can produce a spontaneous emission of a nucleon similar to the way a molecule evaporates from a hot liquid. For this reason, this model is also

known as evaporation model. The nucleons that escapes from the compound nucleus are the products of the nuclear reaction [86].

- **Preequilibrium model**. For $20 < E < 100$ MeV, neither the intranuclear cascade nor equilibrium model can describe the nuclear reactions [89]. In this energy range, the nuclear reactions have got characteristics between direct reactions and decays through the states of compounds nucleus. To reproduce these processes, a exciton model is used. This type of model describes the evolution of an excited nucleus, due to a proton interaction, in terms of a system of excitons, where an exciton is defined as a particle-hole pair in the nuclear Fermi sea used to model the target nucleus. The model tracks how the nuclear system evolves from an initial configuration (usually with few excitons) toward statistical equilibrium through successive interactions between nucleons. This model can reproduce the shape of the angle-integrated energy spectra of secondary particles in a proper way [89, 90].

Chapter 2

Monte Carlo simulation

> In order to understand the world, one has to turn away from it on occasion.
>
> *Albert Camus*

MC technique is a numerical method employed to solve numerical problems using pseudo-random number sampling. This technique was first used by Georges-Louis Leclerc, Comte de Buffon, to solve Buffon's needle problem in the 18^{th} century. This problem involves calculating the probability that a needle will land on a line, given a floor of equally spaced parallel lines. To solve this problem, Compte de Buffon used random mechanisms to obtain mathematical results. It is important to note that this is the first documented case of the use of the MC method [91]. Alternatively, MC methods were proposed by S. Ulam and J. von Neumann in 1947 [92, 93] to study the interaction between high energy neutrons and nuclei, but were firstly employed by M.L. Goldberger [94]. The first MC code developed to describe the interaction of photons and electrons with matter was ETRAN (Electron TRANsport) [95, 96]. At the same time, an independent group in the Stanford Lineal Accelerator Center (SLAC) started to develop a MC code (EGS3) that simulates the transport of electrons, positrons and photons in matter. It was the first MC code used in medical physics [97]. After this first attempt, the MC codes have improved their physical models and new types of particles have been included in the simulations (e.g. protons, neutrons or alpha particles). Currently, there are a large number of general purpose MC codes available, e.g. EGSnrc[98], PHITS [99], MCNPX [100], FLUKA [32, 33], Geant4 [101–103] or PENELOPE/PENH/PENHAN [28, 29, 54].

MC simulations are widely used in medical physics. For example, it can be used to determine the concentration of radioisotopes produced by a particle beam, particle scattering

in radioactive facilities, accurate dose maps used for radiation protection, dosimetric calculations in the clinical practice, among other important quantities in this field. In this thesis, MC simulation will be used to characterise dosimetric devices used in clinical practice for proton therapy. All the commented topic that used MC simulation as a tool have a feature in common: they are problems of radiation-matter interaction. Any problem related to the transport of charged particles in matter is well determined by the solution of the Boltzmann transport equation. Finding an analytical solution to this equation is only possible for cases with infinite or semi-infinite geometries. This fact considerably limits the field of application of the Boltzmann transport equation. This means that obtaining an analytical solution for geometries with finite elements is practically impossible. Therefore, using this equation to calculate the quantities used in medical physics is unfeasible due to the types of geometries considered for these kind of problems [104–106].

In order to calculate the quantities needed for clinical practice, MC simulations are used. It is important to note that the results obtained are equivalent to solve the Boltzmann transport equation [104, 106]. To implement an algorithm based on MC techniques to solve the problem of radiation transport, probability distributions that describe proton interactions with matter are needed. Therefore, the cross section of the different kind of processes are used to simulate the proton transport in matter. Using the cross section as probability distributions, the different features of proton interactions are described: mean free path, energy losses and scattering related to proton interactions. Furthermore, other important quantities as production of secondary particles is taking into account in the simulations thanks to the cross sections [105, 107].

In this chapter, a brief description of the features and the implementation of the physics models in the MC codes used in this thesis (PENH, FLUKA and TOPAS) is given.

2.1 Implementation of the physics models in Monte Carlo codes

In this section, a review of the implementation of proton interactions with matter in MC codes is given. Firstly, it is important to note that detail interaction models has been implemented for particles with a low number of interactions, such as photons or neutrons. However, this approach is not feasible for simulating the transport of charged particles, as

they undergo a large number of interactions. To overcome the problem related to the transport of charged particles, the use of MCS theory has been proposed as solution. Using MCS theory, a group of several interactions can be merged in a unique "pseudo-interaction" with the physical features of all the individual interactions of the charged particle in that group. Depending on the implementation of this idea, two classes of MC codes can be distinguished [108, 109]:

- *Class-I:* all the possible interactions of the charged particles in a pathlength s are grouped in a unique "pseudo-interaction". The energy loss and deflection of these particles are determined by using CSDA and MCS theories. This simulation scheme allows reducing the computing time of the simulation, but increase the uncertainty due to the analytical models used.

- *Class-II:* in this scheme, interactions of charged particles are divided in two categories: *soft* and *hard* interactions. On the one hand, *soft* interactions are characterised by small energy losses and deflections. On the other hand, *hard* interactions have energy losses or deflections larger than a determinate threshold that depends on the MC code. In order to perform the simulation, *soft* interactions are grouped together in a unique "pseudo-interaction". Instead, *hard* interaction are simulated in detail.

All MC codes can be classified in one of theses classes. Having commented on the basic scheme of a MC code, a brief review of the physics models implemented in the different MC codes used in this thesis is made in the following subsections.

2.1.1 PENH

One of the Monte Carlo codes used in our study is the last version of PENH [29], an extension of the electron, positron, and photon transport code PENELOPE [28], which simulates the transport of protons and also accounts for neutron generation and transport in an approximate way [29]. PENH operates in conjunction with PENELOPE, which describes the interactions of photons (Rayleigh scattering, Compton scattering, photoelectric absorption, and electron-positron pair production), and of electrons and positrons (elastic collisions, inelastic collisions, impact ionization of inner shells, *bremsstrahlung* emission, and positron annihilation).

PENH describes electromagnetic interactions of protons (elastic and inelastic collisions, impact ionization of inner shells), and proton induced nuclear reactions. PENH also accounts for atomic relaxation with the emission of either characteristic x-rays or Auger electrons.

PENH can be cataloged as a class-II simulation code. PENH simulates *hard* interactions in detail (from the corresponding differential cross sections), while the aggregate effect of *soft* interactions is simulated in a condensed manner, by using approximate multiple scattering theory. *Hard* and *soft* interactions refer to events in which the energy loss and/or the angular deflection of the transported particle are, respectively, above or below certain cutoff values. The angular deflection and the lateral displacement due to the multiple *soft* interactions that occur in a path length between consecutive *hard* events are simulated by using the random-hinge method, which consists in dividing each step in two segments of random length. The artificial hinge event occurs at the end of the first segment where the particle changes its energy and direction of movement according to adequate energy-loss and angular distributions [110]. The energy cutoff, W_{CCH}, are chosen by the user, who must also set the absorption energies, E_{abs}, of the various particles in each material. The energy cutoff plays a key role in the simulation of inelastic interactions, as it is the threshold that separates the *soft* interactions from the *hard* ones. The deflection cutoff is determined by the program in terms of the user-defined tracking parameters C_1 and C_2 (which are dimensionless and may take values between 0 and 0.2) through an energy-dependent relation. The larger the values of C_1 and C_2, the larger the deflection cutoff; in the limit $C_1 = C_2 = 0$ the simulation of collisions becomes purely detailed (i.e., nominally exact). For the different particles simulated by PENH, the values of the above parameters could be independent.

Proton nuclear reactions are simulated in PENH as *hard* interactions. To simulate these processes, PENH uses nuclear databases in ENDF-6 format (ENDF/B and TENDL-2019). The code also accounts for the production of neutrons in proton-induced nuclear reactions, and approximately describes the contribution of these particles to the dose distribution from proton beams. Neutrons are assumed to undergo elastic collisions and induce nuclear reactions. The latter are considered as purely absorptive processes that end the trajectory of the neutron and deposit locally a fraction (defined by the parameter FNABS) of its kinetic energy (see [29] for details).

In PENH, elastic nuclear processes are described using an optical potential in the calculation of the differential elastic cross section. The differential cross section for collisions with a bare nucleus is obtained from partial-wave calculations [111] with the optical-model potentials proposed by Koning and Delaroche [112] for protons and neutrons [29].

Recently, a new extension of PENH was released. This new extension is called PENHAN [54] and it allows to simulate the transport of alpha particles in matter. In this code, alpha

particles are simulated taking into account the electromagnetic interactions and the elastic nuclear processes. Nuclear reactions for alpha particles are considered as purely absorptive processes as in the case of neutrons. To model the effects of the nuclear elastic interactions for alpha particles, the optical potentials considered by Su and Han [113] are employed. On top of that, an update in the models used to simulate the elastic nuclear interactions have been carried out for protons and neutrons. The following optical potentials have been used to simulate this interaction: the proposed by B. A. Watson et al. (1969) [114] for low-energy ($E < 35$ MeV) protons and neutrons colliding with light nuclei having mass number A less than 24 anf higher than $A = 6$; for $E >= 35$ and $A > 6$ or for $A >= 24$ for any energy, that of Koning and Delaroche mentioned above [112]. In the case of collisions of protons with light nuclei ($A \leq 6$), for which optical-model potentials are not expected to yield realistic results, PENHAN uses the empirical parametrization of the nuclear elastic differential cross section described by Galyuzov and Kosov [115]. This new feature related to the nuclear elastic scattering model has been introduced in PENHAN due to the results presented in section 3.3.5.

2.1.2 FLUKA

Other Monte Carlo code used in this thesis to perform the simulations is the CERN code FLUKA [32, 33]. This code was originally designed for transporting particles in the Large Hadron Collider (LHC) energy regime. However, the most recent developments in this code has allowed to implement the physics model for the energies used in particle therapy.

This MC code implements a condensed (class-I) tracking algorithm for charged particles, i.e. each particle trajectory is simulated as a succession of steps and the effect of elastic collisions along each step is described by an original implementation of multiple scattering, based on the Molière theory of MCS [116]. In this algorithm, two parts can be distinguished, the path length correction algorithm and the angular correlation algorithm. The fist algorithm determinate the position of the particle after a jump in the simulation, taking into account the energy straggling. The second algorithm estimates the change in the direction due to the interaction that the particle has in the path length.

The description of electronic energy losses is based on a statistical approach developed by Fassò *et al.* [117], which describes the mean energy loss along each step and its fluctuations around the mean. To determinate the mean energy loss, CSDA model is used. To apply the CSDA model, modified Bethe formula is considered for energies larger that 0.1 MeV. For lower energies, a fit to experimental data collected by the ICRU is used [118]. Regarding to

compound stopping power, a experimental fit is used when the data are available. If there are no experimental data, the Bragg' sum rule is used. The algorithm that control the energy losses also manages the production of secondary particles. If the deposited energy is larger than a determinate threshold, a secondary electron will be produce.

Hadron-nucleus interactions are simulated by two different models, depending on the energy range of the tracked particle [32, 119]. If the particle's momentum is in the range $[5\ \mathrm{GeV/c}, 20\ \mathrm{TeV/c}]$, Glauber-Gribov multiple scattering followed by Generalized Intranuclear Cascade will be used to simulate the nuclear interactions. For $|\vec{p}| < 5$ GeV/c, PEANUT (Pre-Equilibrium Approach to NUclear Thermalization) model will be employed. This model includes a Generalized IntraNuclear Cascade with smooth transition to a preequilibrium stage performed with standard assumptions on excitation energy. The PEANUT implementation of the cascade model uses MC simulation to calculate the interactions between hadrons and nuclei until the impinging hadron and the secondary particles produced in the nucleus reach 50 MeV. Afterwards, all the secondary particles will be added to the secondary stack and the target nucleus will remain in an excited state. In that moment, the evaporation and compound models are employed to calculate the final state of the nucleus and estimate the secondary particles emitted during the deexcitation process [120].

Although FLUKA is a MC code with a fixed physical model, some tracking parameters can be modified. It is important to highlight the maximum step length (`STEPSIZE`) or the absorption energy of the transported particles (`EMFCUT` and `PART-THRes`). A correct choice of these parameters is essential to avoid artefacts in the FLUKA simulation [24].

2.1.3 TOPAS

The last Monte Carlo code used to perform simulations is TOPAS, which wraps and extends the GEANT4 Simulation Toolkit [30, 31]. As a toolkit, TOPAS does not has fixed physical models that are used in its simulations. This makes it difficult to classify it according to tracking algorithms, as depending on the physics model used it can be a class-I or class-II code. In this work, the following physics modules are going to be used:

- *G4EmStandardPhysics_option4*: this physics module has been chosen because it introduces significant improvements over older models in other physics module that implements the electromagnetic interactions [121, 122]. The multiple scattering of protons are described by using the *Wentzel VI* model (a class-II algorithm) [88].

Ionisation is handle by the *Bragg* model for energies below 2 MeV. For energies larger than 2 MeV, ionization processes are simulated using the Bethe formalism [123].

- *G4HadronPhysicsQGSP_BIC_HP*: this package implements the inelastic nuclear interaction in TOPAS/Geant4. In this module, inelastic nuclear processes are implemented by the Quark-Gluon String model, the Fritiof parton model, Binary and Precompound models [123].

  To simulate the inelastic interaction of protons in the energy range used in proton therapy, the Binary Cascade (BIC) model is used to simulate the nuclear reactions. When these models are used, the Precompound model is also called to simulate the de-excitation of the remaining nuclei after inelastic interactions. After that, evaporation model is used to determinate the final state of the interaction [123].

- *G4HadronElasticPhysicsHP*: this physics library implements the nuclear elastic interactions for hadronic particles. For the proton case, this module uses the CHIPS model for low energy. This model uses the Kosov's parameterised cross sections [124]. For medium and high energy, the Baranshenkov-Glauber-Gribov cross sections are used to simulate the nuclear elastic interaction. For high energy neutrons ($E \geq 20$ MeV), this physics module uses the CHIPS model to simulate the elastic nuclear interactions. For neutron with a smaller energy, the *NeutronHPElastic* model is used [125].

- *G4StoppingPhysics*: this module provides the nuclear capture at rest of negatively charged particle, using a Bertini cascade model (for π^-, K^-, Σ^-, Ξ^- and Ω^- particles) and a precompound model (for antiprotons and muons) [126].

- *G4DecayPhysics*: this package manages the decay of particles in flight and at rest. It calculates the mean free path for decay of the particle for each step, converting the decay time in the rest frame to a decay length. Once a particle disintegrates, it selects a decay mode for the particle according to its branching ratios. For a given decay channel, the daughter particle momenta are calculated in the rest frame of the parent [88].

- *G4IonBinaryCascadePhysics*: this model describes the inelastic nuclear interactions for ions, using a binary cascade model. For this purpose, the initial state of the cascade is prepared in the form of two nuclei. The lighter nucleus is chosen as the projectile. The nucleons in the projectile are brought into the initial state of the cascade. To simulate the nuclear interaction, the Fermi momentum and the local field of the target nuclei are taken into account in the calculation of the binary collisions [88].

As far as the parameters of the tracking are concerned, it is important to comment on the following parameters:

- `dRoverRange`: this is an internal parameter of the electromagnetic physics module used in this work. It controls the maximum reduction of fraction of energy of the transported particle [88, 127].
- `finalRange`: this is an internal parameter of the electromagnetic physics module used in this work. It controls the absorption energy of the transported particle [88, 127].
- `MaxStepSize`: this is a TOPAS tracking parameter that controls the maximum step size in a given geometric volume of the simulation [128].
- `CutForAllParticles`: this is a TOPAS tracking parameter to control the absorption energy of the simulated particle. There are analogue commands to control the absorption energy of a particular particle type, e.g. `CutForProton` [128].

Chapter 3

Validation of physics models used in Monte Carlo codes

All human things are subject to decay,
and when fate summons, Monarchs
must obey

Mac Flecknoe
John Dryden

MC simulations are currently considered one of the most useful tools used in medical physics. They have a wide range of application in this field. For example, this type of simulation can be used to accurately determine important parameters for a radiotherapy treatment. In addition, they can be used for the characterisation of the response of radiation detectors, such as ionization chambers. On top of that, MC simulations can help to the design of these devices. For all these applications, MC simulations play a key role in medical physics and they are considered, due to their accuracy, the gold standard for many important calculations in the clinical practice.

However, MC simulations are not perfect tools and they may have some imperfections related to the implementation of the physics models used to simulate the transport of particle through a material medium. A clear example of this idea is given by Vilches *et al.* [38]. They found that using different MC codes to simulate the interaction of electrons with thin foils to calculate the angular distribution of these particles can produce significant changes due to the implemented physics models in the different MC codes used. This may leads to a systematic error which is superimposed on the statistical uncertainties associated with the random sampling used in these codes. To improve the results obtained with MC codes, it is

essential to determinate and quantify these systematic uncertainties and correct them.

In this chapter, a review of the physics models implemented in the MC codes is given. In order to determinate the systematic uncertainties associated with these models, an exhaustive comparison between experimental and MC data is used. The final objective of this comparison is to validate the electromagnetic and nuclear interaction models used in the transport of the protons to do the MC results obtained in this thesis more reliable and highly robust. Part of the results presented in this chapter have been published in [129].

3.1 Multiple Coulomb scattering algorithms

One of the most important components of a MC simulation is the MCS algorithm. This algorithm plays a key role in the simulation, as its correct implementation is essential for the calculation of dose maps, angular distributions and other quantities that are of great interest in clinical practice. Furthermore, for protons, most of the interactions that produce scattering events are *soft* interactions. This fact allows to simulate this type of interaction using a condensed algorithm. So, a properly optimised MC algorithm can dramatically speed up a simulation.

Due to the importance of the MCS algorithms, their implementation in the MC codes used in this thesis will be verified in this section. To check the performance of these algorithms, the available experimental data will be used (Gottschalk *et al.* [130] and Verbeek *et al.* [131]). The aim of these two experiments is to determine the angular distribution of a proton beam after impacting a thin slab of the material under investigation. With this information, the accuracy of the MCS algorithm can be checked quickly and easily. The review, based in this kind of experiments, allows the performance of the MCS algorithms to be evaluated over a wide range of elements and compounds used in clinical practice.

3.1.1 Experimental data

Table 3.1 lists the cases used to validate the MCS models implemented in the MC codes obtained from a study by Gottschalk *et al.* [130] and another one by Verbeek *et al.* [131]. In the study of Gottschalk *et al.*, they measured the angular distributions of 158.6 MeV proton beams impinging on slabs of various materials and thicknesses. For cases where multiple measurements were available for the same thickness, the average value was used.

Table 3.1 Summary of experimental information considered in the present section. Data for 158.6 MeV protons are from the experiment of Gottschalk *et al.* [130], while those for 100, 160 and 220 MeV protons are from the experiment of Verbeek *et al.* [131]. For each slab material, it is listed the energy E_p of incident protons, the corresponding CSDA range R (extracted from [130, 131]), the intervals of thicknesses t, those of characteristic angles θ_0 of the angular distributions of transmitted protons and the number of available data.

target	E_p (MeV)	R (g cm^{-2})	t (g cm^{-2})	θ_0 (mrad)	# data
Be	158.6	21.11	0.06 – 20.31	1.0 – 42.5	15
C	158.6	19.27	0.32 – 1.62	3.2 – 7.7	5
Al	100.0	10.01	1.89 – 8.10	19.9 – 57.7	4
	158.6	22.16	0.22 – 21.25	3.5 – 87.0	9
	160.0	22.72	1.89 – 16.20	12.4 – 49.0	5
	220.0	39.16	4.05 – 29.70	13.8 – 52.2	5
Cu	158.6	25.92	0.05 – 24.25	2.2 – 118.6	13
Zn	158.6	25.99	0.19 – 0.38	4.9 – 7.1	2
Sn	158.6	30.16	0.09 – 0.35	4.1 – 8.1	3
Pb	158.6	35.21	0.03 – 31.57	2.3 – 175.4	16
U	158.6	36.78	3.63 – 17.43	36.9 – 95.3	5
Lexan	158.6	17.58	0.09 – 1.46	1.7 – 7.4	5
Nylon	158.6	17.20	0.09 – 3.01	1.7 – 10.7	6
Polystyrene	158.6	17.50	0.35 – 15.75	3.3 – 42.0	8
Lucite	100.0	7.93	1.79 – 5.95	14.3 – 34.1	5
	158.6	17.59	0.37 – 1.45	3.6 – 7.6	3
	160.0	18.14	2.57 – 14.28	10.9 – 35.6	8
	220.0	31.39	3.57 – 23.80	9.4 – 33.7	5
Teflon	158.6	21.01	0.06 – 19.91	1.6 – 64.0	9
Brass	100.0	11.92	4.24 – 8.47	43.0 – 75.0	3
	158.6	26.35	1.34 – 24.40	14.1 – 115.9	7
	160.0	26.81	4.24 – 21.18	26.0 – 86.0	5
	220.0	45.87	5.93 – 33.88	23.6 – 78.6	5

In total, the experimental dataset used as reference includes 106 targets made of 14 different materials (8 elements and 6 compounds). Slabs with thicknesses greater than 97% of the CSDA range for 158.6 MeV protons were excluded, as the transmitted protons had lost a large fraction of their initial energy. This implies not only that simulations would be slow but also that the resulting distribution are not completely attributable to elastic collisions, which are the kind of processes that we want to describe through MCS formalism.

For slabs with small and moderate thicknesses, the angular distributions of transmitted protons are nearly Gaussian, with deviations from that shape visible only at very large angles [57, 130], where the effects of the finite size and structure of the atomic nucleus may be appreciable. As the experiment carried out by Gottschalk *et al.* was performed by using a dosimeter, only those angles for which the dose is larger than 1% of the central peak value were actually measured and this excludes the non-Gaussian tails of the distribution, which contains a very small fraction of the emerging protons. The characteristic angle of the angular distribution, θ_0, was determined by fitting the Gaussian distribution

$$f(\theta) = A \exp\left(-\frac{\theta^2}{2\,\theta_0^2}\right), \tag{3.1}$$

with $A \equiv f(\theta = 0)$, to the experimental data.

The other set of measurements were performed by Verbeek *et al.* [131], where proton beams with energies of 100, 160 and 220 MeV were impinged on targets of Al, lucite, and brass with various thicknesses. A total of 45 cases were included in this analysis (see Table 3.1). These measurements were made using an IBA Proteus Plus treatment system, which consists of an isochronous cyclotron that accelerates protons to 228 MeV. Lower energies were achieved by using an energy degrader. The measurements were made with a Lynx PT detector with a 30×30 cm^2 active area and 0.5 mm spatial resolution. To remove the scattering contribution of the measurement system, a series of off-target measurements were made and deconvolved from the total signal. To do that, the total signal was model as a convolution between the effect of air scattering and the contribution of the material slab to the scattering:

$$\phi_{\text{total}}(\theta) = \phi_{\text{air}}(\theta) * \phi_{\text{slab}}(\theta), \tag{3.2}$$

where $\phi_i(\theta)$ can be written as

$$\phi_i(\theta) = A_i \exp\left(-\frac{\theta^2}{2\sigma_i^2}\right), \tag{3.3}$$

where *i* denotes the case under consideration. Expanding eq.(3.2) using the Fourier transform, it is obtained that:

$$\mathscr{F}(\phi_{\text{slab}}) = \frac{\mathscr{F}(\phi_{\text{total}})}{\mathscr{F}(\phi_{\text{air}})} \,. \tag{3.4}$$

The anti-Fourier transform of two dividing Gaussian distributions is a Gaussian distribution whose variance is the difference of the individual variances:

$$\sigma^2_{\text{slab}} = \sigma^2_{\text{total}} - \sigma^2_{\text{air}} \,. \tag{3.5}$$

Therefore, if it is known the total and air signal, the effect of the signal due to the material slab can easily be determined.

3.1.2 Monte Carlo simulation

The simulations conducted to evaluate the MCS algorithms involved a pencil beam of protons directed perpendicularly onto a material slab with a given initial energy. The experimental datasets mentioned in the previous section were exclusively influenced by the effects of the target slab on the proton beams. These values were obtained after correcting the experimental measurements for the effects of the beam and the detector sizes, the scattering in the air between the source and the slab and between the latter and the measuring plane, and the beam aperture due to the collimator and anti-scatter slits used to delimit the proton beams. For this reason, the simulations only considered the transport of protons through the slab in vacuum, a methodology also employed by other authors [131, 132]. The energies of the proton beams and the materials and thicknesses of the slabs are those indicated in the corresponding experiments, which are summarized in Table 3.1. The material compositions adopted in the simulations are also taken from [130], and they are given in Table 3.2.

In PENH and TOPAS, all protons that crossed the slab were scored using a phase space file to determine their angular distributions, $f_{\text{MC}}(\theta)$, where θ is the angle of the exit direction relative to the outgoing normal to the back surface of the slab. For FLUKA, the USRYIELD card was activated to score a double-differential particle yield around an extended target. From the particle yield, the angular distributions needed to extract the characteristic angles is derived.

The distribution that has been obtained from the simulation was normalized so that the integral of $f_{\text{MC}}(\theta)$ over θ (from 0 to $\pi/2$) equals the probability that an incident proton crosses the slab and emerges through its posterior surface. In each simulation run, $1 \cdot 10^6$

Table 3.2 Composition of the slab materials considered in the present simulation. For each material, it is expressed the elements present, their atomic numbers, weight fractions, the material density, ρ, and the corresponding mean excitation energy, I. In agreement with the data quoted by Verbeek *et al.* [131], in the case of the proton energies 100, 160 and 220 MeV, the brass composition considered was 58% Cu, 39% Zn and 3% Pb, with $\rho = 8.47\,\mathrm{g\,cm^{-3}}$ and $I = 333.2$ eV, values slightly different from those indicated in this table.

material	Z	weight fraction	ρ ($\mathrm{g\,cm^{-3}}$)	I (eV)
Be	4	1.000	1.853	63.7
C	6	1.000	2.220	81.0
Al	13	1.000	2.700	166.0
Cu	29	1.000	8.960	322.0
Zn	30	1.000	8.900	330.0
Sn	50	1.000	7.298	488.0
Pb	82	1.000	11.350	823.0
U	92	1.000	18.700	890.0
Lexan			1.200	73.1
H	1	0.074		
C	6	0.741		
O	8	0.185		
Nylon			1.130	64.8
H	1	0.100		
C	6	0.549		
N	7	0.107		
O	8	0.244		
Polystyrene			1.032	68.7
H	1	0.077		
C	6	0.923		
Lucite			1.200	74.0
H	1	0.081		
C	6	0.600		
O	8	0.320		
Teflon			2.200	99.1
C	6	0.240		
F	9	0.760		
Brass			8.489	333.0
Cu	29	0.615		
Zn	30	0.352		
Pb	82	0.033		

histories were considered. The corresponding characteristic angles were obtained in the same way as the experimental values, i.e., by fitting the function $f(\theta)$, defined in equation (3.1), to the simulated distributions, $f_{\mathrm{MC}}(\theta)$. The fits were performed by means of the Levenberg-Marquardt method [133].

Regarding the tracking parameters used in these simulations, for the case of PENH, those used in the simulation are listed in Table 3.3. They were chosen taking into account the previous results obtained by Plaza [121]. Besides, following the recommendation to use this code for thin geometries, the DSMAX parameter has been set to one tenth of the smaller length for each body. For the simulations performed with TOPAS, the default parameters are chosen. Finally, for the simulations carried out with FLUKA, the `DEFAULTS` card, which activates the `PRECISIOn` mode was used. This mode establishes an absorption energy of 100 keV for photons, electron, positrons, protons, and other particles except for neutrons, for which $1 \cdot 10^{-5}$ eV has been used. The maximum fraction of kinetic energy lost in a step was set to 0.05 and the threshold for delta ray production was 100 keV.

Table 3.3 Tracking parameters used in PENH to implement the simulation to validate the MCS models.

	γ	$e^{\mp}$	p	n
E_{abs} (keV)	50	50	2000	2000
C_1		0.1	0.01	0.0
C_2		0.1	0.01	0.0
W_{cc} (keV)		50	20	
W_{cr} (keV)		50		
`FNABS`				1.0

3.1.3 Comparison with the experimental results

For each experimental situation (proton beam energy, target material and slab thickness), the characteristic angles $(\theta_0^{\mathrm{MC}})_i$ obtained from the MC simulations was compared to the corresponding experimental value, $(\theta_0^{\mathrm{exp}})_i$. The degree of agreement was quantified by means of the weighted difference:

$$\zeta_i = \frac{(\theta_0^{\mathrm{MC}})_i - (\theta_0^{\mathrm{exp}})_i}{(\sigma_{\theta_0}^{\mathrm{exp}})_i}, \tag{3.6}$$

where $(\sigma_{\theta_0}^{\mathrm{exp}})_i$ is the uncertainty of the experimental value. It is important to highlight that when the MC result exceeds the experimental value ($\zeta_i > 0$) the simulation will give off-axis absorbed doses higher than the experimental measurements. Conversely, when $\zeta_i < 0$ the simulated absorbed doses will be concentrated close to the beam axis, giving an underestimation of the out-of-axis dose.

Assuming that the experimental data follow the normal distribution with mean $(\theta_0^{\mathrm{exp}})_i$ and standard deviation $(\sigma_{\theta_0}^{\mathrm{exp}})_i$, characteristic angles θ_0 such that $|\theta_0 - (\theta_0^{\mathrm{exp}})_i| > 5(\sigma_{\theta_0}^{\mathrm{exp}})_i$ are expected to be very unlikely. Therefore, simulated characteristic angles that give $\zeta_i > 5$ are considered to differ significantly from the measurement.

To assess the overall agreement between the MC results and experimental data, reduced χ^2 values were evaluated for different groups of data, such as those with the same proton beam energy, slab material or experiment. The reduced χ^2 statistic is defined as:

$$\chi^2 = \frac{1}{N}\sum_{i=1}^{N}(\zeta_i)^2\,, \tag{3.7}$$

where the index i runs over the N data included in the comparison group. Evidently, the smaller the value of χ^2, the better the overall agreement between MC and experimental characteristic angles.

The uncertainty of each χ^2 value was estimated from the statistical uncertainties of the MC results by considering a set of 1000 pseudo-data that were generated by sampling the normal distributions $\mathrm{N}[(\theta_0^{\mathrm{MC}})_k, (\sigma_{\theta_0}^{\mathrm{MC}})_k]$ for each MC run and calculating the corresponding χ^2 using equation (3.7). The uncertainty of χ^2 was obtained from the distribution of the χ^2 values calculated from the pseudo-data set.

To compare with the experimental results, we calculated the relative differences

$$\delta_i = \frac{(\theta_0^{\mathrm{MC}})_i}{(\theta_0^{\mathrm{exp}})_i} - 1\,, \tag{3.8}$$

between MC and experimental characteristic angles, as well as the ranges of these relative differences, their averages

$$\overline{\delta} = \frac{1}{N}\sum_{i=1}^{N}\delta_i\,, \tag{3.9}$$

and the average of the absolute values of the relative differences

$$\overline{|\delta|} = \frac{1}{N}\sum_{i=1}^{N}|\delta_i|\,, \tag{3.10}$$

by considering the data grouped according to the slab composition or the proton energy. In these equations, N is the number of data included in each comparison group.

3.1.4 Results

Figure 3.1 shows the ζ_i values obtained from equation (3.6) as a function of target slab thickness. The red circles represent results from comparisons with the data of Gottschalk *et al.* [130] for 158.6 MeV protons, while the blue, black and green squares represent results from comparisons with the angles reported by Verbeek *et al.* [131] for protons at energies of 100, 160 and 220 MeV respectively. The grey bands mark the limits $\zeta_i = \pm 3$ and $\zeta_i = \pm 5$.

Most of the characteristic angles derived from the MC simulations fall within $|\zeta_i| < 5$. The average ζ values obtained are 0.5 ± 2.0 for PENH, 1.7 ± 4.0 for FLUKA and 0.8 ± 2.6 for TOPAS. About 60% of the ζ_i values are positive for all three codes, suggesting that in these cases the MC simulations produce angular distributions with a wider spread than those observed experimentally.

Table 3.4 summarises the cases where $|\zeta_i| > 5$, taking into account the uncertainty. Out of the 151 experimental data points analysed, 5 cases were found in PENH, 23 in FLUKA and 11 in TOPAS. In particular, for 100 MeV protons, none of the three codes produced cases with $|\zeta_i| > 5$. Among the FLUKA results for 100 MeV protons, there are only three cases (Al with $t = 8.100\ \mathrm{g\,cm^{-2}}$, brass with $t = 6.776\ \mathrm{g\,cm^{-2}}$ and $t = 8.470\ \mathrm{g\,cm^{-2}}$) gave $|\zeta_i| > 3$. The largest $|\zeta_i|$ values for each code (shown in bold in Table 3.4) occurred for the same target, brass, at $t = 24.398\ \mathrm{g\,cm^{-2}}$ and 158.6 MeV protons. These high positive values indicate potential experimental challenges with this target. Furthermore, for the Cu target with $t = 10.130\ \mathrm{g\,cm^{-2}}$ and 158.6 MeV protons, all three codes produced the most negative ζ_i values: $\zeta_i = -8.5 \pm 0.8$, -3.9 ± 0.6 and -6.4 ± 0.8 for PENH, FLUKA and TOPAS respectively.

Fuchs *et al.* [134] suggested that the agreement between MC simulations and experimental characteristic angles decreases with increasing target thickness. To assess whether this pattern holds for these simulation results, the data in Figure 3.1 were divided into 15 thickness subintervals, each containing 10 data points (except the first, which contains 11).

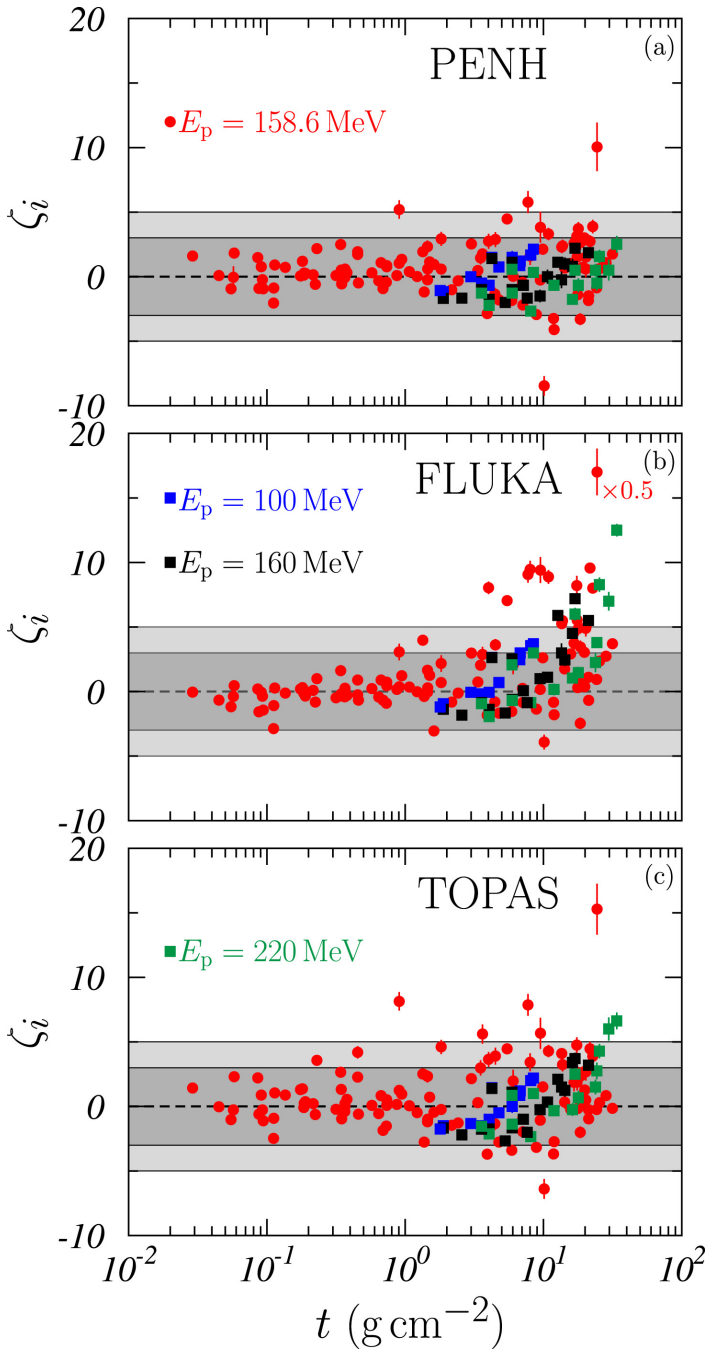

Fig. 3.1 Values of the weighted differences ζ_i, defined in equation (3.6), as functions of the target thickness t. Red circles represent the values obtained for the data of Gottschalk *et al.* [130] for 158.6 MeV protons, and squares are for the data of Verbeek *et al.* [131] for $E_p = 100$ MeV (blue squares), $E_p = 160$ MeV (black squares) and $E_p = 220$ MeV (green squares). Uncertainties (for a coverage factor $k = 1$) are included. The dark and clear gray bands correspond to the values $\zeta_i = \pm 3$ and ± 5, respectively. Results for (a) PENH, (b) FLUKA and (c) TOPAS are shown. The FLUKA value for $t = 24.398$ g cm^{-2} has been divided by 2 to fit on the scale of the figure.

Table 3.4 List of cases with $|\zeta_i| > 5$ within the uncertainty. The proton beam energies, the slab thicknesses and the codes are indicated. The ζ_i values shown in boldface are the largest ones for each code.

			ζ_i		
E_p (MeV)	target	t (g cm^{-2})	PENH	FLUKA	TOPAS
158.6	Be	17.862		4.9 ± 0.5	
		20.313		5.0 ± 0.7	
	Al	13.569		5.3 ± 0.4	
	Cu	10.130	-8.5 ± 0.8		-6.4 ± 0.8
	Pb	0.907	5.2 ± 0.7		8.1 ± 0.7
		1.823			4.6 ± 0.5
		9.517	3.8 ± 1.2	9.4 ± 1.0	5.7 ± 1.2
		17.516		5.5 ± 0.4	
		20.196		4.9 ± 0.6	
		22.756		8.0 ± 0.4	
	U	3.630			5.6 ± 0.8
		7.720	5.8 ± 0.8	9.1 ± 0.6	7.9 ± 0.8
		13.750		5.5 ± 0.5	
		17.430		8.2 ± 0.8	4.7 ± 0.6
	Brass	4.004		8.0 ± 0.5	
		5.466		7.0 ± 0.2	
		8.008		9.5 ± 0.7	
		10.868		8.9 ± 0.5	
		21.714		9.6 ± 0.3	4.5 ± 0.5
		24.398	$\mathbf{10.1 \pm 1.9}$	$\mathbf{34.0 \pm 1.8}$	$\mathbf{15.3 \pm 2.0}$
160.0	Brass	12.710		5.9 ± 0.3	
		16.940		7.2 ± 0.4	
		21.180		5.5 ± 0.3	
220.0	Al	29.700		7.0 ± 0.7	6.0 ± 0.9
	Brass	16.940		6.0 ± 0.5	
		25.410		8.3 ± 0.6	
		33.880		12.5 ± 0.5	6.6 ± 0.7

The average ζ_i value for each subinterval was then calculated, as shown in Figure 3.2.

For FLUKA, the values show an upward trend for $t > 5$ g cm^{-2}, reaching approximately $\overline{\zeta} \sim 8$ in the last subinterval. This increase in $\overline{\zeta}$ is less pronounced for TOPAS and even weaker for PENH, which yielded $|\overline{\zeta}| < 2$ in all intervals. These results confirm the reported decrease in agreement with experiment as target thickness increases, with the threshold thickness for this effect being lower for the class-II code PENH. The thinnest target giving $\overline{\zeta}_i > 5$ in FLUKA is brass at $t = 4.004$ g cm^{-2}, while in PENH and TOPAS it is Pb at

$t = 0.907\ \mathrm{g\,cm^{-2}}$ (see Table 3.4).

Table 3.5 lists the reduced χ^2 values obtained by grouping the data by target composition, proton energy or experiment. Cases where $\chi^2 > 10$, within the uncertainty, are highlighted in bold; these include 4 cases for PENH, 15 for FLUKA and 7 for TOPAS. Considering all data, the total χ^2 for FLUKA is 4.4 and 2.5 times higher than for PENH and TOPAS, respectively. For 158.6 MeV proton beams, uranium and brass are two targets where all three codes give $\chi^2 > 10$. Specifically, for uranium, χ^2_{FLUKA} is about 3.7 times χ^2_{PENH} and 1.5 times χ^2_{TOPAS}. For brass, the χ^2 value of FLUKA is about 10.1 and 4.8 times that of PENH and TOPAS respectively. The χ^2 value for 158.6 MeV protons in brass is the highest observed for any data grouping in all three codes. In particular, the FLUKA results for brass give consistently higher χ^2 values than the other two codes.

The various materials studied were also divided into light and heavy targets. The light target group included Be, C and Al and the compounds Lexan, Nylon, Polystyrene, Lucite and Teflon, all composed of elements with atomic numbers $Z < 29$. The heavy target group included Cu, Zn, Sn, Pb, U (elements with $Z \geq 29$) and brass. Table 3.6 shows the reduced

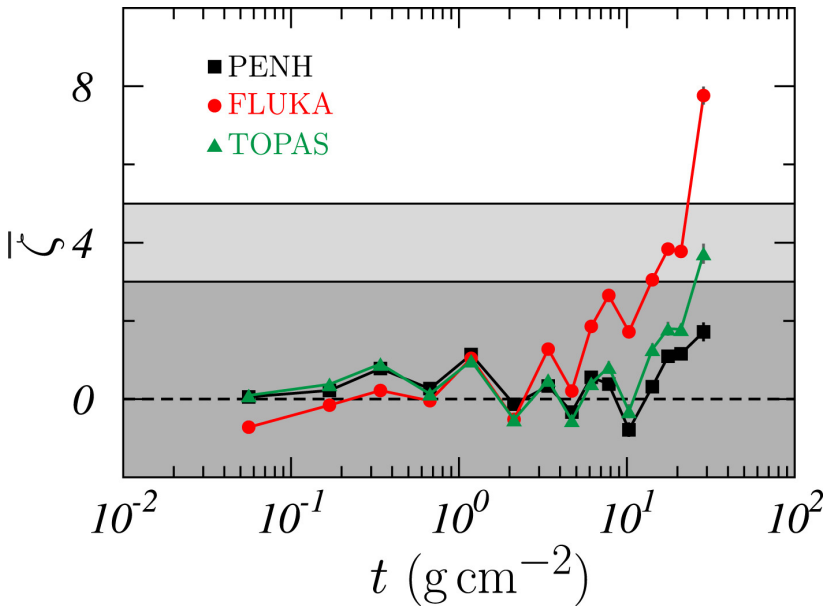

Fig. 3.2 Averages of ζ_i values obtained by classifying the data in 15 subintervals spanning the whole t range analyzed. Results for PENH (black squares), FLUKA (red circles) and TOPAS (green triangles) are shown. Uncertainties are displayed as gray bars. The dark and light gray bands correspond to $\zeta_i = \pm 3$ and $+5$, respectively.

Table 3.5 Reduced χ^2 values, as given by equation (3.7), from the comparison between MC and experimental characteristic angles for the indicated groups of data. Uncertainties were evaluated as described in Section 3.1.3. The values with $\chi^2 > 10$ within the uncertainty are given in boldface.

target	E_p (MeV)	χ^2		
		PENH	FLUKA	TOPAS
all	all	4.2 ± 0.3	$\mathbf{18.6 \pm 0.9}$	7.4 ± 0.5
all	158.6	5.2 ± 0.4	$\mathbf{21.0 \pm 1.2}$	8.4 ± 0.6
Al/Lucite/Brass	100.0/160.0/220.0	1.8 ± 0.2	$\mathbf{13.1 \pm 0.5}$	5.1 ± 0.4
	100.0	1.5 ± 0.2	4.7 ± 0.3	2.0 ± 0.2
	158.6	$\mathbf{9.8 \pm 2.0}$	$\mathbf{83.2 \pm 6.6}$	$\mathbf{18.7 \pm 3.2}$
	160.0	1.9 ± 0.2	$\mathbf{10.0 \pm 0.6}$	4.2 ± 0.4
	220.0	2.0 ± 0.3	$\mathbf{23.5 \pm 1.3}$	8.7 ± 1.0
Be	158.6	3.2 ± 0.4	6.7 ± 0.7	3.1 ± 0.5
C	158.6	0.8 ± 0.1	2.4 ± 0.3	0.4 ± 0.1
Al	all	2.7 ± 0.2	6.8 ± 0.6	4.9 ± 0.6
	100.0/160.0/220.0	2.1 ± 0.3	8.8 ± 0.9	5.8 ± 0.9
	100.0	1.3 ± 0.4	4.9 ± 0.7	2.0 ± 0.5
	158.6	3.6 ± 0.5	3.7 ± 0.5	3.5 ± 0.5
	160.0	1.8 ± 0.4	6.8 ± 1.2	3.9 ± 1.0
	220.0	3.1 ± 0.6	$\mathbf{13.8 \pm 2.0}$	$\mathbf{10.7 \pm 2.2}$
Cu	158.6	7.5 ± 1.0	1.9 ± 0.4	5.1 ± 0.8
Zn	158.6	0.1 ± 0.1	0.1 ± 0.1	0.2 ± 0.1
Sn	158.6	0.4 ± 0.1	0.8 ± 0.1	1.3 ± 0.2
Pb	158.6	6.2 ± 0.9	$\mathbf{16.7 \pm 1.5}$	$\mathbf{12.9 \pm 1.3}$
U	158.6	$\mathbf{10.4 \pm 2.1}$	$\mathbf{38.4 \pm 3.6}$	$\mathbf{26.0 \pm 3.5}$
Lexan	158.6	0.4 ± 0.1	0.6 ± 0.1	0.9 ± 0.2
Nylon	158.6	1.4 ± 0.2	1.9 ± 0.2	0.9 ± 0.2
Polysterene	158.6	4.3 ± 0.5	2.2 ± 0.3	7.6 ± 0.7
Lucite	all	1.1 ± 0.2	1.5 ± 0.2	1.9 ± 0.2
	100.0/160.0/220.0	1.2 ± 0.2	1.7 ± 0.3	2.2 ± 0.2
	100.0	0.8 ± 0.3	1.4 ± 0.4	1.5 ± 0.3
	158.6	0.3 ± 0.2	0.1 ± 0.1	0.5 ± 0.3
	160.0	1.6 ± 0.3	1.9 ± 0.4	3.1 ± 0.4
	220.0	0.9 ± 0.3	1.7 ± 0.7	1.4 ± 0.4
Teflon	158.6	2.0 ± 0.4	1.9 ± 0.3	1.3 ± 0.3
Brass	all	$\mathbf{9.2 \pm 2.0}$	$\mathbf{99.1 \pm 6.6}$	$\mathbf{21.7 \pm 3.3}$
	100.0/160.0/220.0	2.3 ± 0.4	$\mathbf{33.4 \pm 1.5}$	8.5 ± 0.9
	100.0	2.7 ± 0.3	$\mathbf{9.9 \pm 0.6}$	2.8 ± 0.3
	158.6	$\mathbf{21.9 \pm 5.3}$	$\mathbf{221.1 \pm 17.0}$	$\mathbf{46.2 \pm 8.3}$
	160.0	2.5 ± 0.5	$\mathbf{26.0 \pm 1.5}$	6.3 ± 0.8
	220.0	1.9 ± 0.7	$\mathbf{54.8 \pm 3.2}$	$\mathbf{14.0 \pm 2.0}$

Table 3.6 Reduced χ^2 values obtained by comparing the MC and the experimental characteristic angles after grouping the targets into light and heavy materials (see the text), elements and compounds, and for different values of the proton energy. Note that for 100, 160 and 220 MeV the only light elementary target is Al, the only light compound target is lucite and the only heavy compound target is brass. For these energies no elemental heavy targets were available.

		χ^2					
		PENH		FLUKA		TOPAS	
E_p (MeV)	targets	light	heavy	light	heavy	light	heavy
all	all	2.2 ± 0.1	7.3 ± 0.7	3.8 ± 0.2	41.8 ± 2.2	3.1 ± 0.2	14.2 ± 1.1
	elementary	2.7 ± 0.2	6.4 ± 0.5	6.2 ± 0.4	12.5 ± 0.7	3.8 ± 0.3	10.4 ± 0.7
	compound	1.7 ± 0.1	9.2 ± 2.0	1.6 ± 0.1	99.1 ± 6.6	2.5 ± 0.1	21.7 ± 3.3
100.0/160.0/220.0	all	1.6 ± 0.2	—	4.8 ± 0.4	—	3.8 ± 0.4	—
	elementary	2.1 ± 0.3	—	8.8 ± 0.9	—	5.8 ± 0.9	—
	compound	1.2 ± 0.2	2.3 ± 0.4	1.7 ± 0.3	33.4 ± 1.5	2.2 ± 0.2	8.5 ± 0.9
100.0	all	1.1 ± 0.3	—	3.0 ± 0.4	—	1.7 ± 0.3	—
	elementary	1.3 ± 0.4	—	4.9 ± 0.7	—	2.0 ± 0.5	—
	compound	0.8 ± 0.3	2.7 ± 0.3	1.4 ± 0.4	9.9 ± 0.6	1.5 ± 0.3	2.8 ± 0.3
158.6	all	2.5 ± 0.2	8.8 ± 1.0	3.2 ± 0.2	44.2 ± 2.7	2.7 ± 0.2	15.9 ± 1.5
	elementary	2.9 ± 0.3	6.4 ± 0.5	5.0 ± 0.4	12.5 ± 0.7	2.8 ± 0.3	10.4 ± 0.7
	compound	2.1 ± 0.2	21.9 ± 5.3	1.6 ± 0.1	221.1 ± 17.0	2.7 ± 0.2	46.2 ± 8.3
160.0	all	1.7 ± 0.3	—	3.8 ± 0.5	—	3.4 ± 0.5	—
	elementary	1.8 ± 0.4	—	6.8 ± 1.2	—	3.9 ± 1.0	—
	compound	1.6 ± 0.3	2.5 ± 0.5	1.9 ± 0.4	26.0 ± 1.5	3.1 ± 0.4	6.3 ± 0.8
220.0	all	2.0 ± 0.3	—	7.8 ± 1.1	—	6.1 ± 1.2	—
	elementary	3.1 ± 0.6	—	13.8 ± 2.0	—	10.7 ± 2.2	—
	compound	0.9 ± 0.3	1.9 ± 0.7	1.7 ± 0.7	54.8 ± 3.2	1.4 ± 0.4	14.0 ± 2.0

χ^2 values obtained for different proton energies. Since brass was the only heavy material used in the experiment of Verbeek *et al.* [131], the rows labelled "all" and "elementary" for 100, 160 and 220 MeV proton beams are empty.

It is noteworthy that the χ^2 values for light targets are consistently lower than those for heavy targets in all data groups, suggesting that the three codes provide better descriptions of MCS in light materials than in heavy ones. This trend has been reported previously by Gottschalk *et al.* [130] and Fuchs *et al.* [134]. The observed $\chi^2_{\text{heavy}}/\chi^2_{\text{light}}$ ratio ranges are $[0.9; 10.6]$ for PENH, $[2.0; 140.1]$ for FLUKA, and $[1.6; 17.0]$ for TOPAS.

The effect of nuclear reactions was investigated by disabling them and re-running the simulations for the energies and targets used in the experiment carried out by Verbeek *et al.* [131]. Table 3.7 shows the χ^2 values obtained by comparing the characteristic angles of the angular distributions in simulations with and without nuclear reactions. As expected, given the proton energies involved, the effect is small, with maximum χ^2 values of 0.5 for PENH, 1.6 for FLUKA and 1.0 for TOPAS.

Table 3.7 Reduced χ^2 values, as given by equation (3.7), for the various groups of data indicated, from the comparison between MC characteristic angles found in simulations including and excluding nuclear reactions. The cases considered are those of the experiment by Verbeek *et al.* [131]. Uncertainties are given with a coverage factor $k = 1$.

		χ^2		
target	E_p (MeV)	PENH	FLUKA	TOPAS
Al/Lucite/Brass	100/160/220	0.2 ± 0.3	0.6 ± 0.3	0.5 ± 0.3
	100	0.2 ± 0.5	0.7 ± 0.7	0.4 ± 0.5
	160	0.2 ± 0.4	0.3 ± 0.5	0.6 ± 0.5
	220	0.3 ± 0.4	0.9 ± 0.7	0.4 ± 0.4
Al	100/160/220	0.1 ± 0.4	0.7 ± 0.7	0.3 ± 0.4
	100	0.1 ± 0.7	0.3 ± 1.1	0.2 ± 0.7
	160	0.1 ± 0.6	0.2 ± 0.8	0.5 ± 0.8
	220	0.1 ± 0.6	1.6 ± 1.5	0.3 ± 0.6
Lucite	100/160/220	0.3 ± 0.4	0.7 ± 0.5	0.8 ± 0.5
	100	0.3 ± 0.7	1.0 ± 0.9	0.6 ± 0.9
	160	0.2 ± 0.6	0.3 ± 0.6	1.0 ± 0.9
	220	0.4 ± 0.8	1.0 ± 1.2	0.6 ± 0.9
Brass	100/160/220	0.3 ± 0.4	0.4 ± 0.6	0.3 ± 0.5
	100	0.2 ± 0.8	0.6 ± 1.1	0.4 ± 1.0
	160	0.1 ± 0.7	0.5 ± 0.9	0.3 ± 0.7
	220	0.5 ± 0.7	0.1 ± 0.8	0.3 ± 0.7

Table 3.8 Comparison between the average relative differences $\overline{\delta}$ obtained by Fuchs *et al.* [134] with various versions of Geant4 and those found in the present work, for the data of Gottschalk *et al.*) [130]. The last column shows the corresponding ranges of relative differences.

code	$\overline{\delta}$ (%)	range (%)
Geant4.10.1	4.8 ± 5.5	[-22.7; 8.1]
Geant4.10.1 - Wentzel	0.7 ± 4.8	[-17.9;11.2]
Geant4.10.2	0.6 ± 4.9	[-17.8;10.9]
TOPAS	0.9 ± 4.5	[-15.7;11.6]
PENH	0.9 ± 4.0	[-14.5;12.0]
FLUKA	1.2 ± 4.8	[-18.0;15.0]

In recent years, several authors have compared the experimental data used in this study with MC results. Fuchs *et al.* [134] performed a comprehensive analysis using Geant4 versions 10.1 and 10.2, and reported average values and ranges for the relative differences between the MC characteristic angles and the experimental angles obtained by Gottschalk *et al.* [130].

The results of Fuchs *et al.* [134] suggest that data accuracy improved with successive versions of the code. Table 3.8 compares the average relative differences $\overline{\delta}$ obtained with TOPAS with those reported by Fuchs *et al.* [134], along with the variation intervals for the relative differences δ_i. The introduction of the Wentzel model for multiple scattering, which has been the default model in Geant4 since version 10.2, has significantly improved the accuracy of the data. The results obtained in this study are in good agreement with those of version 10.2; this consistency is expected, since the Wentzel model was also used in the current simulations with TOPAS. The results for the other two codes used in this study, which are included in Table 3.8 for completeness, are close to those of TOPAS, although FLUKA shows a slightly wider range of differences.

Makarova *et al.* [132] compared two Geant4 (v.10.2) calculations using the Urban and Wentzel multiple scattering models with results from the Molière-Fano-Hanson theory for $E_\mathrm{p} = 158.6$ MeV and the materials and thicknesses used by Gottschalk *et al.* [130]. They provided characteristic angles for some of the cases analysed. Figure 3.3 shows the relative differences

$$\Delta_i = \frac{(\theta_0^{\mathrm{Geant4}})_i}{(\theta_0^{\mathrm{TOPAS}})_i} - 1\,, \tag{3.11}$$

between the $(\theta_0^{\text{Geant4}})_i$ values from their calculations and those obtained with TOPAS, $(\theta_0^{\text{TOPAS}})_i$. In the simulations performed in this thesis, TOPAS generally yields larger values than Makarova *et al.* [132], resulting in mostly negative Δ_i values. Agreement between TOPAS and Geant4-Wentzel (black triangles) is fairly strong ($|\Delta_i| \leq 5\%$), though it tends to decline with increasing target thickness. Differences between TOPAS and Geant4-Urban results (red squares) are more pronounced, supporting the observations made by Fuchs *et al.* [134].

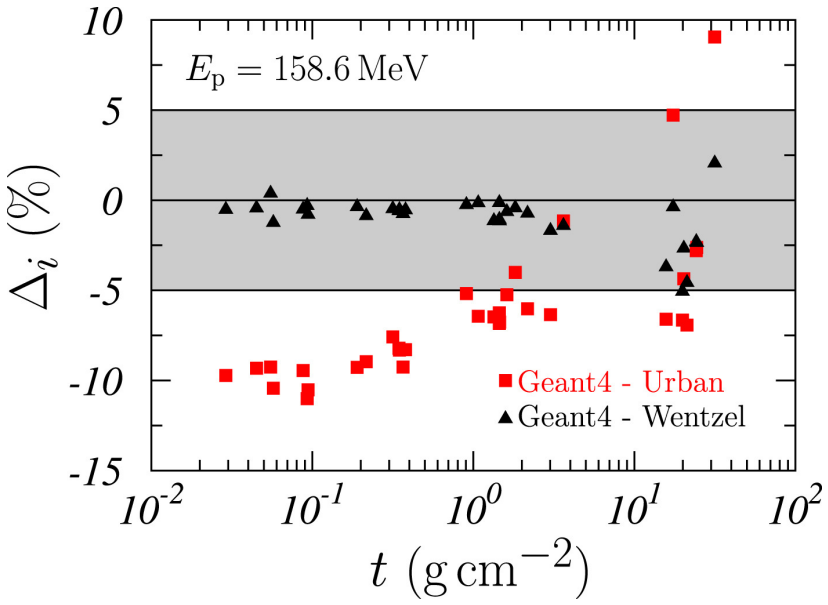

Fig. 3.3 Relative differences, Δ_i, as defined in equation (3.11), between the characteristic angles quoted by Makarova *et al.* [132] for Geant4.10.2 with the Urban (red solid squares) and Wentzel (black solid triangles) MCS models and those obtained with TOPAS in the present work, for some of the data from the experiment by Gottschalk *et al.* [130] with 158.6 MeV protons. The gray band indicates the range $\pm 5\%$.

Verbeek *et al.* [131] compared their measurements with results from simulations with PENH and TOPAS, although they did not mention the versions of the codes used. Their simulation parameters differ from those we choose in the simulations carried out in this thesis, being more stringent than ours. The $\overline{|\delta|}$ values given by Verbeek *et al.* [131], for the three target materials and the three proton energies, are compared with the averages of the absolute values of the relative differences obtained from the present simulations in Table 3.9. The reason of the larger uncertainties found in the results obtained in this thesis is that, while the data of Verbeek *et al.* include only the statistical uncertainties due to the MC procedure, we have also accounted for the variability of the data of each group (by summing

Table 3.9 Comparison of the averages of the absolute values of the relative differences between MC and experimental characteristic angles for the experiment of Verbeek *et al.* [74]. Only the MC uncertainties are included in the data of Verbeek *et al.*.

		$\overline{\lvert\delta\rvert}$ (%)			
		PENH		TOPAS	
target	E_p (MeV)	this work	Verbeek *et al.*	this work	Verbeek *et al.*
Al	100	2.2 ± 1.4	1.9 ± 0.3	2.7 ± 1.7	2.7 ± 0.3
	160	2.4 ± 2.3	3.2 ± 0.3	2.9 ± 2.1	3.0 ± 0.3
	220	2.4 ± 2.1	3.1 ± 0.3	3.1 ± 1.9	2.8 ± 0.3
Lucite	100	1.4 ± 1.3	1.2 ± 0.3	2.1 ± 2.0	2.5 ± 0.3
	160	2.1 ± 1.6	2.7 ± 0.3	3.0 ± 2.0	3.6 ± 0.3
	220	1.9 ± 1.7	2.4 ± 0.3	2.3 ± 2.0	2.8 ± 0.3
Brass	100	6.4 ± 3.3	6.1 ± 0.3	6.5 ± 3.4	7.2 ± 0.3
	160	3.6 ± 1.7	2.3 ± 0.3	5.0 ± 2.0	4.0 ± 0.3
	220	1.5 ± 1.0	1.1 ± 0.3	3.9 ± 2.0	3.0 ± 0.3

up quadratically the MC statistical uncertainty and the standard deviation of the data in the group). Globally, the trends of the results from the two works are similar.

Androulakaki *et al.* [135] performed simulations using the codes FLUKA, PHITS, Geant4 (v.10.5.p01) and MCNP6.1. Although they did not provide the numerical values of the characteristic angles or the relative differences compared to the Gottschalk *et al.* data [130], the values were presented in graphical form. Although this limits the depth of analysis, the values plotted appear to be of a similar order of magnitude to those found in this study and other referenced publications.

Finally, to sum up, in most of the 151 cases analysed, the weighted differences ζ_i between simulation results and experimental measurements remained below 5. Higher values of ζ_i were observed in only 5, 23, and 11 cases for PENH, FLUKA, and TOPAS, respectively. Notably, in FLUKA, ζ_i increases significantly for target thicknesses $t > 5\,g/cm^2$, whereas this trend is much less pronounced in TOPAS and PENH. The relative differences obtained in our calculations are consistent with results from similar simulations using previous versions of these codes. It is worth noting that in Geant4 and TOPAS, the Wentzel multiple scattering model yields results that agree more closely with experimental data compared to the Urban model. The reduced χ^2 statistics further supported and reinforced the findings derived from the weighted and relative differences. In summary, among the three codes analyzed, PENH

provides the most accurate reproduction of the characteristic angles measured by Gottschalk et al. [130] and Verbeek et al. [131]. TOPAS performs slightly worse than PENH, while FLUKA exhibits significantly larger discrepancies.

3.2 Nuclear reactions models

Nuclear reactions play an important role in proton therapy. This kind of interaction is an important mechanism for describing off-axis dose deposition because they can produce secondary uncharged particles that deposit their energy far from where they are produced [41, 74, 136]. These kinds of particles are essential to describe the possible production of radiation-induced second primary tumours [78]. As can be seen from all these examples, nuclear reactions play a key role in correctly describing the interaction of protons with matter. It is therefore necessary to check the correct implementation of this interaction mechanism to ensure that MC codes can correctly calculate the dose deposition due to protons.

To verify the right implementation of nuclear reactions in the MC codes, the study of the charge distribution deposited by a proton beam in a multilayer Faraday cup (MLFC) will be used. This experiment is notable for its simplicity, since there is no need to take into account the type of response that the measuring devices would have, as in the case of dose deposition, and it is also easy to design a MLFC that does not introduce effects on the charge measurement due to its geometry. On top of that, this type of experimental setup also allows to validate the nuclear interaction model of the simulation codes in a simple way. This is because the range of the secondary charged particles generated by the nuclear reactions is much smaller than the range of the electromagnetic interaction associated with the primary beam, so that the growth zone before the peak of the charge distribution deposited in the MLFC can be attributed entirely to nuclear reactions. Otherwise, the charge deposited in the region of the Bragg peak is related to electromagnetic interactions. Due to the fact that it is easy to separate the contribution of electromagnetic interactions and nuclear reactions to the signal of the MLFC, this experiment is an excellent candidate to validate the results of MC simulation codes related to nuclear reactions in a simple way [81, 82].

3.2.1 Experimental data

The experimental results that will be used as a reference to validate the nuclear reaction models implemented in the MC codes have been extracted from the measurements of Gottschalk *et al.* [81] and Paganetti *et al.* [82]. These experiments were performed with the

proton beam of the HCL. In these pair of experimental measurements, a MLFC has been used. This detector is an advanced diagnostic instrument used to measure the deposited charge of a particle beam, in order to quantify the number of particles in the beam. Unlike a traditional Faraday cup, which consists of a single conductive collecting surface, the multilayer design incorporates multiple conductive layers separated by insulating materials (Figure 3.4). This structure allows for a more detailed analysis of particle fluence by capturing and measuring current at different depths within the device, given a spatial distribution of how protons are stopped in the detector. The beam used in the HCL was focused on the MLFC using a special set of magnets consisting of a deflecting magnet and three pairs of quadrupoles. The beam used in this pair of experiments has got a nominal energy of 160 MeV. The characteristics and composition of the MLFCs used in each of the articles are different and they will be detailed in the following paragraphs. The uncertainty associated with the experimental data is only given in Paganetti *et al.* [82] and it is 0.26 pC/10^9 protons. As the experimental setup used in both experimental measurements are similar, the uncertainty value given by Paganetti *et al.* [82] will be used for the data of Gottschalk *et al.* [81] as well.

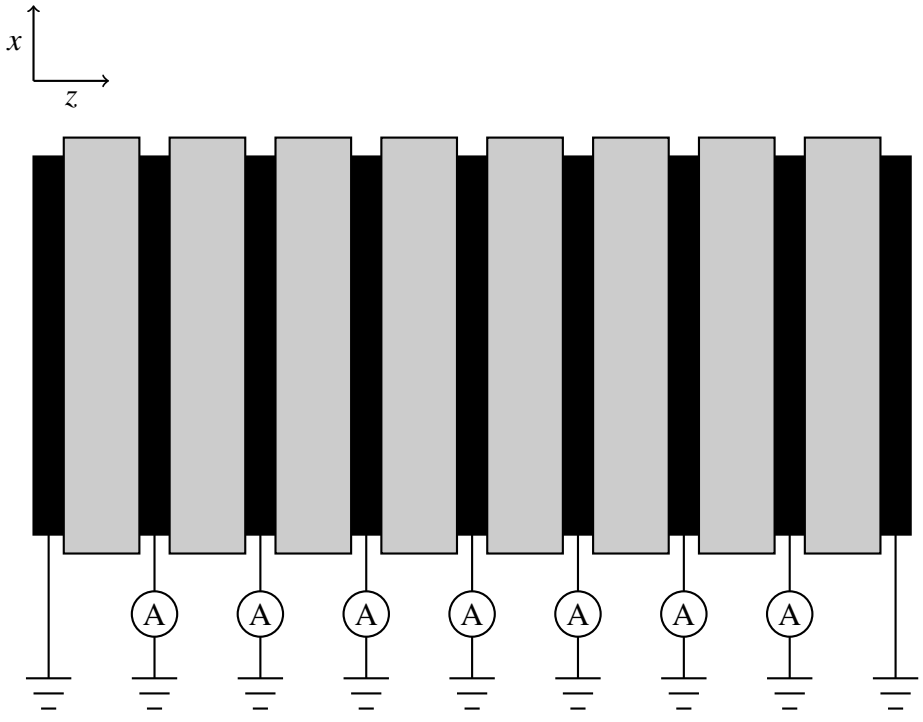

Fig. 3.4 Basic sketch of an MLFC. In the this figure, the grey slabs represent a insulating material, while the black slabs are made of an conducting material. Besides, it has been assumed that the proton beam moves in the positive direction along the z axis.

Regarding to the characteristic of the MLFCs used in the reference article, on the one hand, in Gottschalk *et al.* [81], the used MLFC has a cross section of 7.6×7.6 cm^2 and consists of 66 pairs of conductive and insulating plates (collectors), although there are only 64 active charge collection channels. Each active collector is connected to ground via a low impedance load cell. This setup allows to correctly measure the distribution of particles stopping along the MLFC. As for the collector material, the conductive plate is made of copper ($\rho = 8.96$ g/cm^3) with a thickness of 0.0529 cm, while the insulating plate is made of Kapton ($\rho = 1.42$ g/cm^3) with a thickness of 0.00255 cm.

On the other hand, in Paganetti *et al.* [82], the MLFC has a cross section of 15×15 cm^2 and consists of 66 pairs of conductive and insulating plates, although only 64 of them allow measurement of the deposited charge. The first collector is attached to an aluminium foil enclosure, which allows a connection to ground to be made. The next 64 collectors are connected to a current integrator to measure the charge deposited by the incident protons. The last collector is also connected to ground. The collectors consist of a conductive brass ($\rho = 8.489$ g/cm^3) plate with a thickness of 0.00254 cm and a high-density polyethylene ($\rho = 0.98$ g/cm^3) insulating plate with a thickness of 0.317 cm.

3.2.2 Monte Carlo simulation

In order to implement these experiments in the MC simulation codes considered in this thesis, 10^8 protons was simulated in each case. The proton source used in the simulation was a pencil beam. This simplification is taken into account because the measurements made by these experimental groups have been obtained using a detector that has no spatial resolution to distinguish the spatial and angular structure of the proton beam used in the irradiation. So, these features of the beam do not affect to the result of the simulation. This pencil beam has been considered with an energy spectrum described by a normal distribution $\mathcal{N}(E_0,\, \sigma_E)$. The parameters characterising this source for the different simulation codes are given in Table 3.10. The parameters used to generate the energy spectrum were extracted from [82, 137, 138]. This set of parameters has been chosen to reproduce the experimental width and position of the charge deposited in the region of the Bragg peak.

Furthermore, in order to reproduce the experimental results, a 1.5 m thick air layer between the point source described above and the MLFC has been considered in the simulation. The geometry used to simulate the MLFC implements the description given in section 3.2.1. A summary of the properties of the materials used is given in Table 3.11, in order to eliminate

Table 3.10 Beam parameters used to reproduce the experimental results of Gottschalk *et al.* [81] and Paganetti *et al.* [82].

Study	Code	E_0 (MeV)	σ_E (MeV)
Gottschalk *et al.*	PENH	159.5	0.35
	TOPAS	158.0	0.50
	FLUKA	158.0	0.35
Paganetti *et al.*	PENH	159.7	0.50
	TOPAS	160.0	0.50
	FLUKA	160.8	0.50

possible uncertainties due to the use of the predefined materials.

Table 3.11 Composition of the slab materials considered in the present simulations. For each material, it is expressed the elements present, their atomic numbers weight fractions, the material density, ρ, and the corresponding mean excitation energy, I.

Material	Weight fraction	Z	ρ (g cm^{-3})	I (eV)
Air			0.001	85.7
N	0.745	7		
O	0.229	8		
Ar	0.026	18		
Brass			8.489	333
Cu	0.615	29		.
Zn	0.352	30		
Pb	0.033	82		
Polyethylene			0.98	57.4
H	0.144	1		
C	0.856	6		
Copper		29	8.96	322
Kapton			1.42	79.6
H	0.026	1		
C	0.691	6		
O	0.209	8		
N	0.073	7		

In terms of scoring methods, it is important to have a clear idea of what the MLFC is. If a proton stops in a conductor plate, its contribution to the current is directly detected, in particular it attracts an electron from the ground, which then flows through the current integrator. In the case of an insulator, a stopping proton attracts electrons to adjacent conducting plates, which then flow through the integrator [82]. Thus, in a simplified way, the

MLFC measures the charge deposited in a pair of conducting and insulating plates. For this reason, in these simulations we will define a grid whose size corresponds to that of a pair of conductor-insulator plates.

For PENH the deposited charge has been extracted from the `penhmain-res.dat` file. This file, generated by PENH, calculates the net charge deposited on each part of the geometry. Therefore, by reading this file correctly, the charge deposited on all pairs of conducting and insulating plates in the geometry can be obtained. To do this, the net charge deposited on each pair of insulator and conductor plates is added up to give the net charge of each collector. In the case of FLUKA, the USRBIN scorer was used to obtain the charge distribution deposited on the MLFC. This scorer allows the definition of a point grid to determine the net charge deposited in a given region. Finally, to obtain the charge distribution of the MLFC in TOPAS, a scorer was used to measure the deposited charge in a given region. To do this, a parallelepiped was defined in the whole MLFC, used to mesh this part of the geometry, and within this region the different layers of insulators and conductors that make up the MLFC were defined.

Regarding the units used to represent the data, pC/10^9 protons has been used. Both PENH and TOPAS express their results in terms of fundamental units of charge per primary particle. In order to express the results of these two simulation codes in the correct units, the following conversion factor has been used

$$1\,\mathrm{e/proton} = 1.602 \cdot 10^2\ \mathrm{pC}/10^9\ \mathrm{protons}\,. \tag{3.12}$$

FLUKA uses fundamental units of charge per primary particle and per volume of the voxel used in the scoring process. Then, to express the results in pC/10^9 protons, the above conversion factor (eq. (3.12)) must be multiplied by the volume of the voxel used in the measurement.

The tracking parameters used in these simulations, for the case of PENH, are listed in Table 3.12. Moreover, following the recommendation for thin geometries, the DSMAX parameter has been set to one tenth of the smaller length for each body. For the simulations performed with TOPAS, due to the small size of the MLFC plates, interaction ranges of the particles have been modified in order to obtain results consistent with the physical situation under study. If the default values of the interaction ranges are used, it can produce that the particles do not interact properly with the MLFC plates due to their thinness. To avoid this problem, we will set the interaction range parameters to 0.0001 mm for heavy particles and

0.001 mm for electrons, positrons and photons. These values were taken from [137]. Apart from these modifications in the interaction range, the default parameters have been used. Finally, for the simulations carried out with FLUKA, the `DEFAULTS` card, which activates the `PRECISIOn` mode was used. This mode establishes absorption energies of 100 keV for photons, electron, positrons, protons, and other particles except for neutrons, for which $1 \cdot 10^{-5}$ eV has been used. The maximum fraction of kinetic energy lost in a step was set to 0.05 and the threshold for delta ray production was 100 keV.

Table 3.12 Tracking parameters used in PENH to implement the MLFC simulations.

	γ	$e^{\mp}$	p	n
E_{abs} (keV)	10	10	1000	100
C_1		0.1	0.01	0.0
C_2		0.1	0.01	0.0
W_{cc} (keV)		10	10	
W_{cr} (keV)		5		
`FNABS`				0.8

3.2.3 Results

In Figure 3.5, the results obtained by MC simulation are compared to the experimental ones of Gottschalk *et al.* [81]. As noted above, the Bragg peak was used to calibrate the source definition. However, the good agreement in the initial part of the charge distribution is due to the right implementation of the nuclear reaction models considered in the different MC codes used.

Despite the good agreement between MC and experimental data for this case, it is important to highlight some discrepancies. The FLUKA results show an overestimation of the signal at the beginning of the MLFC. This is due to the secondary particles produced by the proton interaction with air. These particles have a small range and are stopped at the first plates of the detector. An overestimation in the production of this type of particle can explain why there is an overestimation of the signal at the beginning of the MLFC for FLUKA. For TOPAS it is important to note an underestimation of charge deposition around 0.70 cm, which cannot be easily well explained. A similar data is also found for FLUKA around 1.60 cm.

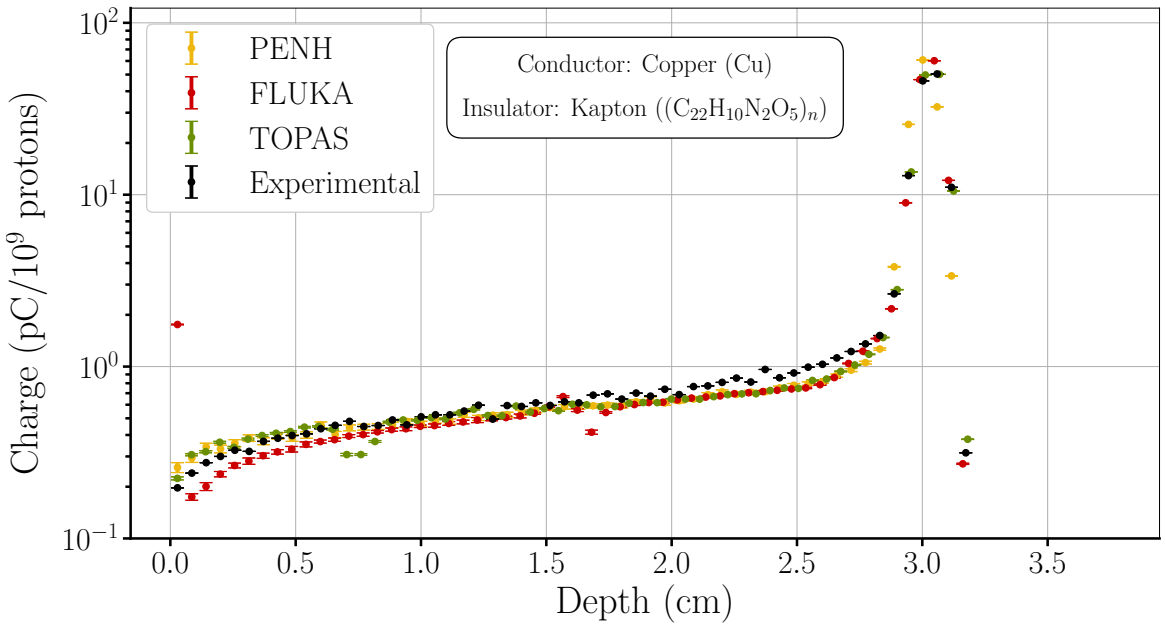

Fig. 3.5 Comparison between experimental and the MC data for the case of Gottschalk *et al.* [81]. Yellow, red and green represent the results obtained with PENH, FLUKA and TOPAS respectively. Experimental data is sketched in black. All the uncertainties shown have a coverage factor $k = 3$. In the plot, it is specified the material composition of the MLFC.

On the other hand, some discrepancies have been found between the MC and the experimental data for the dataset measured by Paganetti *et al.* [82]. Figure 3.6 shows these discrepancies. The only code that reproduces the experimental data is TOPAS. This is in agreement with the previous results published by Testa *et al.* [137], where a systematic revision of algorithms of proton transport in TOPAS is made. As part of this analysis, the experimental data given by Paganetti *et al.* are used. However, neither FLUKA nor PENH can reproduce the experimental data, being PENH the code that have large discrepancies with experimental data. These discrepancies have been previously observed for FLUKA by Rinaldi *et al.* [138] as well.

To explain the discrepancies between the FLUKA results and the experiment, Rinaldi *et al.* [138] concluded that it was necessary to take into account the background signal of the MLFC. In its work, Rinaldi *et al.* estimated that this background current has a constant value of 0.3 pC/10^9 protons. If the experimental signal of MLFC is corrected taking into account this problem, an improvement of the MC results is found. Figure 3.7 shows a comparison between the MC and experimental data when the background current of MLFC is eliminated. As can be seen in that figure, a better agreement for all the MC codes is found. With this correction of the experimental data, the TOPAS results are compatible with the

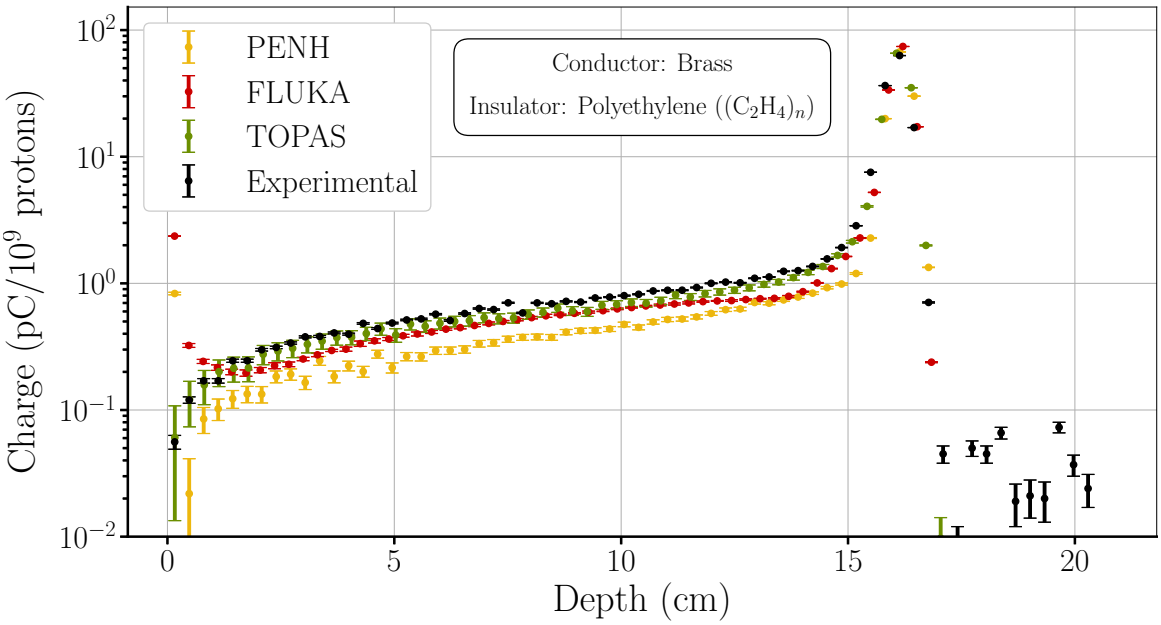

Fig. 3.6 Comparison between experimental and the MC data for the case of Paganetti *et al.* [82]. Yellow, red and green represent the results obtained with PENH, FLUKA and TOPAS respectively. Experimental data is sketched in black. In the plot, it is specified the material composition of the MLFC.

experimental measurement and the FLUKA results are close to it. However, the PENH results underestimate the charge deposition associated with proton nuclear reactions.

To explain the underestimation found in the PENH results, it is interesting to analyse the transport of the light products produced in proton nuclear reactions. Emitted light products other than protons (deuterons, tritons, ^{3}He, and alphas) are tracked as "weighted equivalent" protons as follows. A light product with kinetic energy E_b is replaced by a proton with initial kinetic energy (E) such that the proton travels the same average distance as the product. To ensure that the initial kinetic energy of a product with original weight w_b is effectively transferred to the material, the "weighted equivalent" proton is assigned the weight $w = w_b(E_b/E)$ [29].

The method used by PENH to transport the light products could cause problems with charge deposition due to a poor description of the charge deposition associated with this kind of particles. The charge deposition associated with the light products is modulated by the "weighted equivalent" proton, rather than taking the charge corresponding to the light product being simulated. This mechanism can explain why PENH can reproduce the experimental data of Gottschalk *et al.* [81] but not the data of Paganetti *et al.* [82]. Table 3.13 shows the

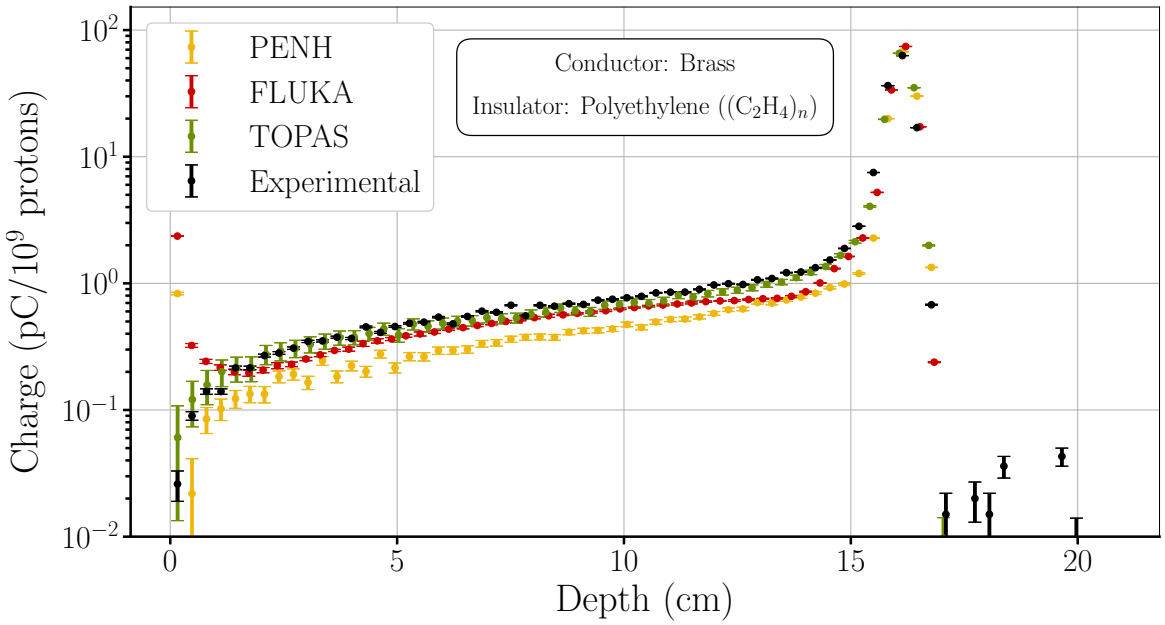

Fig. 3.7 Comparison between corrected experimental and the MC data for the case of Paganetti *et al.* [82]. Yellow, red and green represent the results obtained with PENH, FLUKA and TOPAS respectively. Corrected experimental data is sketched in black. For the correction, a background current of 0.3 pC/10^9 protons has been considered, following the indication of Rinaldi *et al.* [138].

normalised number of secondary particles produced in the nuclear reaction of protons with the different materials of the MLFC used. It can easily be seen that the contribution of light products to the signal is more relevant in the data of Paganetti *et al.* [82] than in the data of Gottschalk *et al.* [81]. This is illustrated by the fact that the nuclei most produced in the proton nuclear reactions with the materials constituting the MLFC used in the Paganetti *et al.* experiment are ^{4}He and protons, whereas in the Gottschalk *et al.* experiment they are protons and neutrons. The larger production of ^{4}He nuclei and the problem associated with the tracking may lead to the differences found between the results obtained for the two cases.

3.3 Nuclear elastic interactions

Finally, the last mechanism of proton interactions with matter that has been studied is nuclear elastic scattering. Nuclear elastic scattering of protons plays an important role in several processes such as the assessment of radiation effects in electronics [139–141] or dose deposition in proton therapy applications. In fact, in the latter case, proton nuclear elastic scattering contributes to the angular spread protons in matter and therefore has a direct effect on depth dose maps, especially off-axis and thus for dose assessment to nearby healthy tissue

Table 3.13 Contributions of the different secondary particles generated in nuclear reactions per primary proton obtained with FLUKA. It can be observed the nuclei most produced in the proton nuclear reactions with the materials constituting the MLFC used in the Paganetti *et al.* experiment are ^{4}He and protons, whereas in the Gottschalk *et al.* experiment they are protons and neutrons. Information extracted from [138].

	Paganetti (number/primary)	Gottschalk (number/primary)
Proton	0.231	0.261
Deuteron	0.044	0.033
Tritium	0.008	0.004
Helium-4	0.217	0.062
Helium-3	0.018	0.002
Neutron	0.102	0.384

[74].

The analysis in this section takes as reference the experimental dataset from Verbeek *et al.* [74]. This experimental dataset consists of a 2D dose map. Due to the nature of the dataset, different features of the proton transport can be studied, although in this section the implementation of the nuclear elastic scattering models used in the different MC codes considered will be analysed.

3.3.1 Experimental data

As mentioned at the beginning of this section, the dataset in Verbeek *et al.* [74] is used as a benchmark. These measurements were taken in the clinical proton accelerator of the West German Proton Therapy Centre in Essen (Germany). 2D dose maps in a water phantom were measured for proton energies of 100, 160 and 225 MeV. According to the results shown in the appendix C, only the data measured for an energy of 225 MeV are considered in the present analysis, due to the problems related to the source definition given by the Fermi-Eyges theory.

The experimental dataset presented in Verbeek *et al.* [74] consists of dose profiles for different radial distances, where the central axis is considered to be the point where the proton beam impinges on the water phantom. The dimensions of the water phantom used for the measurements are $40 \times 40 \times 40$ cm^3. This phantom is positioned so that its front surface coincides with the isocentre, which is 50 cm from the exit nozzle of the proton accelerator. These experimental measurements were made with a MatriXX PT 2D detector. This detector consists of a two-dimensional array of 1020 ionization chambers. The diameter of these ionization chambers is 0.42 cm. These detectors are placed on a square grid and their centres

are separated by 0.7619 cm.

Regarding the experimental procedure, the measurements were performed in such a way that the centre of the proton beam coincided with the centre of one of the ionization chambers of the detector array. To obtain the profiles, the detector was moved in the direction of the incident beam between 3 and 33 cm depth in the water phantom (Figure 3.8). Furthermore, the experimental results were normalized to their respective value of the dose at a depth of 3 cm at the central profile. Normalization was carried out at this depth to ensure that gradient effects are avoided, which could have led to biased results with a normalization conducted in the Bragg peak region.

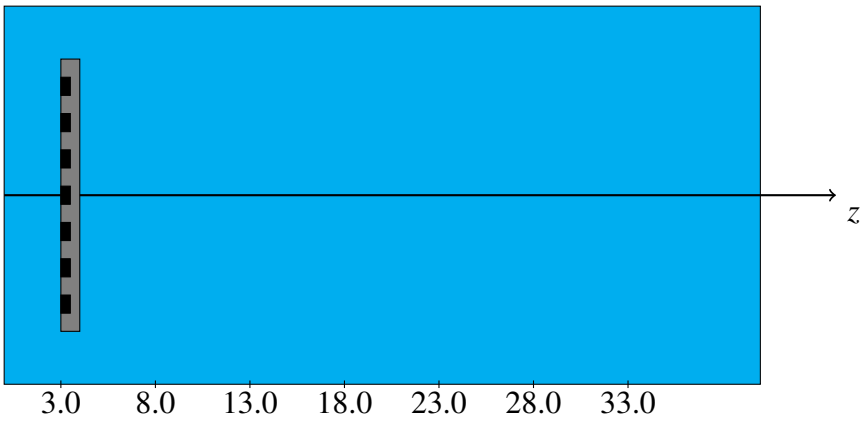

Fig. 3.8 Basic sketch of the experimental setup used by Verbeek *et al.* [74]. The water phantom is represented in blue and the MatriXX PT 2D detector in grey. The different points where a measurement has been taken are pointed out in the figure.

3.3.2 Monte Carlo simulation

10^8 protons have been considered in all the simulations. To reproduce the source used in this experiment at the entrance of the water phantom, z_0, the Fermi-Eyges theory was employed (a brief explanation is given in the section 1.2.2). To sum up, the source is described by the following probability density function:

$$\Phi(z_0;\vec{r},\vec{\Omega}) = F(z_0;x,\theta_x)F(z_0;y,\theta_y)\ . \tag{3.13}$$

where the analytical expression for $F(z_0;\xi,\theta_\xi)$ is:

Table 3.14 Values of $A_0(z_0)$, $A_1(z_0)$ and $A_2(z_0)$ employed in the simulation used to reproduce the results of Verbeek *et al.* [74]. This values for the source parametrization have been taken from the article cited before.

Energy [MeV]	$A_0(z_0)$ [mrad^2]	$A_1(z_0)$ [mrad·mm]	$A_2(z_0)$ [mm^2]
225	7.605	0.3865	0.0512

$$F(z_0;\xi,\theta_\xi) = \frac{1}{4\pi\sqrt{B(z_0)}} \exp\left(-\frac{A_0(z_0)\xi^2 - 2A_1(z_0)\xi\theta_\xi + A_2(z_0)\theta_\xi^2}{4B(z_0)}\right) , \tag{3.14}$$

with $B(z_0) = A_0(z_0)A_2(z_0) - A_1(z_0)^2$ being the emittance of the proton beam. ξ represents represents the spatial variable of the distribution (x or y), θ_ξ is the projected angle in the ξ axis, $2A_2(z_0)$ is the variance of the spatial distribution in z_0, $2A_0(z_0)$ is the variance of the angular distribution in z_0 and $2A_1(z_0)$ is the covariance. The values taken for $A_0(z_0)$, $A_1(z_0)$ and $A_2(z_0)$ are collected in the Table 3.14.

To sample the Fermi-Eyges probability density function, the Cholesky decomposition method [142] has been used. Using this method, the following equations are obtained to sample the position and direction of emission of the protons:

$$\begin{aligned} \xi &= \mu_\xi + \sqrt{2A_2(z_0)}\eta_1 , \\ \theta_\xi &= \mu_{\theta_\xi} + \sqrt{\frac{2A_1^2(z_0)}{A_2(z_0)}}\eta_1 + \sqrt{\frac{2B(z_0)}{A_2(z_0)}}\eta_2 , \end{aligned} \tag{3.15}$$

where η_1 and η_2 are two random numbers sampled from a Gaussian distribution and μ_ξ and μ_{θ_ξ} are the mean values of the spacial and angular distribution, respectively. In this case, both magnitudes will be considered as zero in the sampling process. The direction cosines from the projected angles are then obtained from

$$\begin{aligned} u &= \cos\left(\frac{\pi}{2} - \theta_\mathrm{x}\right) , \\ v &= \cos\left(\frac{\pi}{2} - \theta_\mathrm{y}\right) , \\ w &= \sqrt{1-u^2-v^2} . \end{aligned} \tag{3.16}$$

Table 3.15 Radial position of the ionization chamber used to calculate the dose profile in [74] for $E_0 = 225$ MeV.

	Radius [cm]
1^{st}	0.0
2^{nd}	1.52
3^{rd}	2.29
4^{th}	7.62
5^{th}	9.90
6^{th}	10.67

The energy distribution used to model the experimental source was a gaussian distribution:

$$f(E) = \frac{1}{\sqrt{2\pi\sigma_{\mathrm{E}}^2}} \exp\left[-\left(\frac{E-\mu_{\mathrm{E}}}{2\sigma_{\mathrm{E}}}\right)^2\right], \tag{3.17}$$

with $\mu_{\mathrm{E}} = 225.142$ MeV and $\sigma_{\mathrm{E}} = 0.513$ MeV.

Regarding the geometry, the water phantom has been modeled using a cylinder whose radius and length are 15 and 40 cm, respectively. To score the dose, a radial grid with $\Delta r = 0.42$ cm is considered, reproducing the size of the ionization chamber used to take the measurement. The radial distances have been chosen to reproduce the measurement condition described in Verbeek *et al.* [74] (see Table 3.15). As in the experimental case, results from all codes were normalized to their respective value of the dose at a depth of 3 cm at the central dose profile.

The tracking parameters used in these simulations, for the case of PENH, are listed in Table 3.16. From those given by Verbeek *et al.* [74], the laxest set of parameters was chosen for the PENH simulations. For the simulations performed with TOPAS, the default parameters are chosen. However, a smaller range cut was set for all particle (5 μm) to reduce the artifacts related to the abortion of particles. Finally, for the simulations carried out with FLUKA, the `DEFAULTS` card, which activates the `PRECISIOn` mode was used. This mode establishes absorption energies of 100 keV for photons, electron, positrons, protons, and other particles except for neutrons, for which $1 \cdot 10^{-5}$ eV has been used. The maximum fraction of kinetic energy lost in a step was set to 0.05 and the threshold for delta ray production was 100 keV.

Table 3.16 Tracking parameters used in PENH to implement the out-of-axis dose simulations

	γ	$e^{\mp}$	p	n
E_{abs} (keV)	10	100	1000	100
C_1		0.05	0.05	0.01
C_2		0.05	0.05	0.01
W_{cc} (keV)		100	100	
W_{cr} (keV)		10		
FNABS				0.8

3.3.3 Interpretation of the dose maps

Before analysing the data obtained with the MC simulation for the different codes considered, a brief review of how the proton interaction mechanisms shape the 2D dose maps is given. According to Gottschalk *et al.* [41], three zones can be distinguished in the 2D dose map related to a proton pencil beam: core, halo and aura (see Figure 3.9). These regions can be defined in the following way:

- *Core*: region of the dose map associated with the protons that only interact with the material via *soft* collisions (both elastic and inelastic collisions). This region corresponds to the space close to the depth axis with origin at the point where the proton beam impinges. This is due to the fact that *soft* collisions only produce small deflection in protons. In the Figure 3.9 this region can be easily identified in the positive direction of the z-axis. As already discussed, the dose contribution in this region is due to the *soft* collisions of primary protons with the medium.

- *Halo*: region of the dose map related to the dose deposited by the charged secondaries generated from *hard* scattering processes. Between these *hard* scattering processes can be found the *hard* electromagnetic interactions, the nuclear elastic, inelastic and nonelastic interactions. This can be clearly seen in the Figure 3.9. In particular, particles that deposit their energy in *halo* region are secondary protons produced in the nuclear interactions mentioned above.

- *Aura*: region of the dose map connected to the dose deposited by the uncharged secondary particles generated from nuclear reactions and all the particles they set in motion. As can be seen in the Figure 3.9, the only particle that reaches this zone is a neutron. This shows that the only particles with a sufficiently large range are the uncharged secondary particles produced by nuclear reactions.

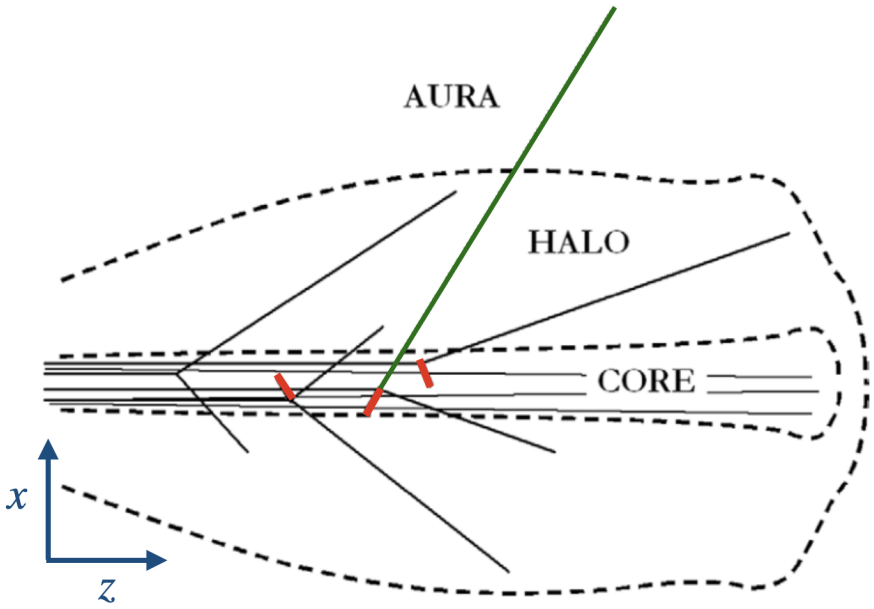

Fig. 3.9 Classification, given by Gottschalk *et al.* [41], of the regions that can be distinguished in a 2D dose maps of a proton pencil beam. In the figure, it has been assumed that protons moves through the positive direction of the z axis. The dashed lines are 10% and 0.01% isodoses drawn to scale. Due to the nuclear reaction, neutrons (sketched in green) and recoil nuclei (in red) have been produced. It is important to note that recoil nuclei ranges are exaggerated for their representation.

In order to determine at which radial depth the contribution of the nuclear elastic interactions to the dose deposition is more significant, a simulation was performed with FLUKA to identify the characteristics mentioned above. In this simulation, dose is filtered according to the interactions associated with the particles that deposit their energy in the medium. We have chosen FLUKA because it allows to implement the filtering process using the subroutine `stuprf.f`, that permits to label the particles according to their interaction with the medium. Furthermore, FLUKA has decoupled elastic nuclear interactions from elastic electromagnetic ones. This fact makes it easy to see when this type of interaction is being produced.

Figure 3.10 shows the contribution to the dose from the different proton interaction mechanisms. In this figure, four types of contributions can be distinguished: the total dose deposited in the water phantom (black) and further resolved into the contributions from particle histories where protons have only undergone ionization losses (EM, green), nuclear reactions (NR, red) and nuclear elastic scattering (NES, blue). As can be seen in the Figure 3.10, panels (a) and (b) refer to the *core* regions, since the main contribution to dose deposition

is related to ionization losses produced by *soft* collisions. Panels (c) and (d) can be related to the *halo* region. This is due to the fact that a strong contribution of nuclear interactions (nuclear reactions and elastic scattering) can be observed in these profiles. Finally, panels (e) and (f) belong to the *aura* region. This is because there is only a significant contribution from nuclear reactions. This indicates that only sub-products of the nuclear reactions reach this spatial region. The only particles with such a large range are the uncharged secondary particles produced in nuclear reactions.

As we are interested in validate the physics models that implement the nuclear elastic interaction in the MC codes under study, it is essential to determine which are the profile that allow to study easily the contribution to dose of this kind of interaction. So, for that reason, a dose profile of the *halo* region must be chosen, due to the importance that have nuclear elastic interactions to deposited dose in this region. Following this criterium, the radial distances where the contribution of the nuclear elastic interactions is more relevant are $r = 2.29$ and $r = 7.62$ cm (3^{th} and 4^{th} radii in Table 3.15). However, for $r = 2.29$ cm, there is an appreciable contribution of electromagnetic interactions to the Bragg peak area. For this reason, the following analysis will be focused in the dose profile whose radial distance is 7.62 cm.

In order to understand better the results for $r = 7.62$ cm, we have to take into account that there are two types of atoms in the water molecule: hydrogen and oxygen. The nuclei of these two atoms interact differently with the protons due to their different masses. This fact makes it possible to spatially separate the contribution to the dose due to nuclear elastic interactions on oxygen and hydrogen. Figure 3.11 illustrates this idea. On the one hand, when a proton undergoes an elastic interaction on hydrogen (panel (a) of the Figure 3.11), an isotropic dose deposition is found. This is due to the fact that the proton and hydrogen have the same mass, so that large deflections are more likely than for other processes. This allows the dose deposition due to the elastic nuclear interaction on hydrogen to be assigned to the middle depth of the dose profile with $r = 7.62$ cm. On the other hand, elastic nuclear interactions on oxygen are associated with an arrow-shaped dose profile (panel (b) of the Figure 3.11). This characteristic dose deposition is due to the fact that the projectile and the target nucleus have different masses. This fact leads to an anisotropic emission (forward direction) of the protons. This allows the deposited dose in the Bragg peak region of the considered dose profile to be related to the nuclear elastic interaction on oxygen.

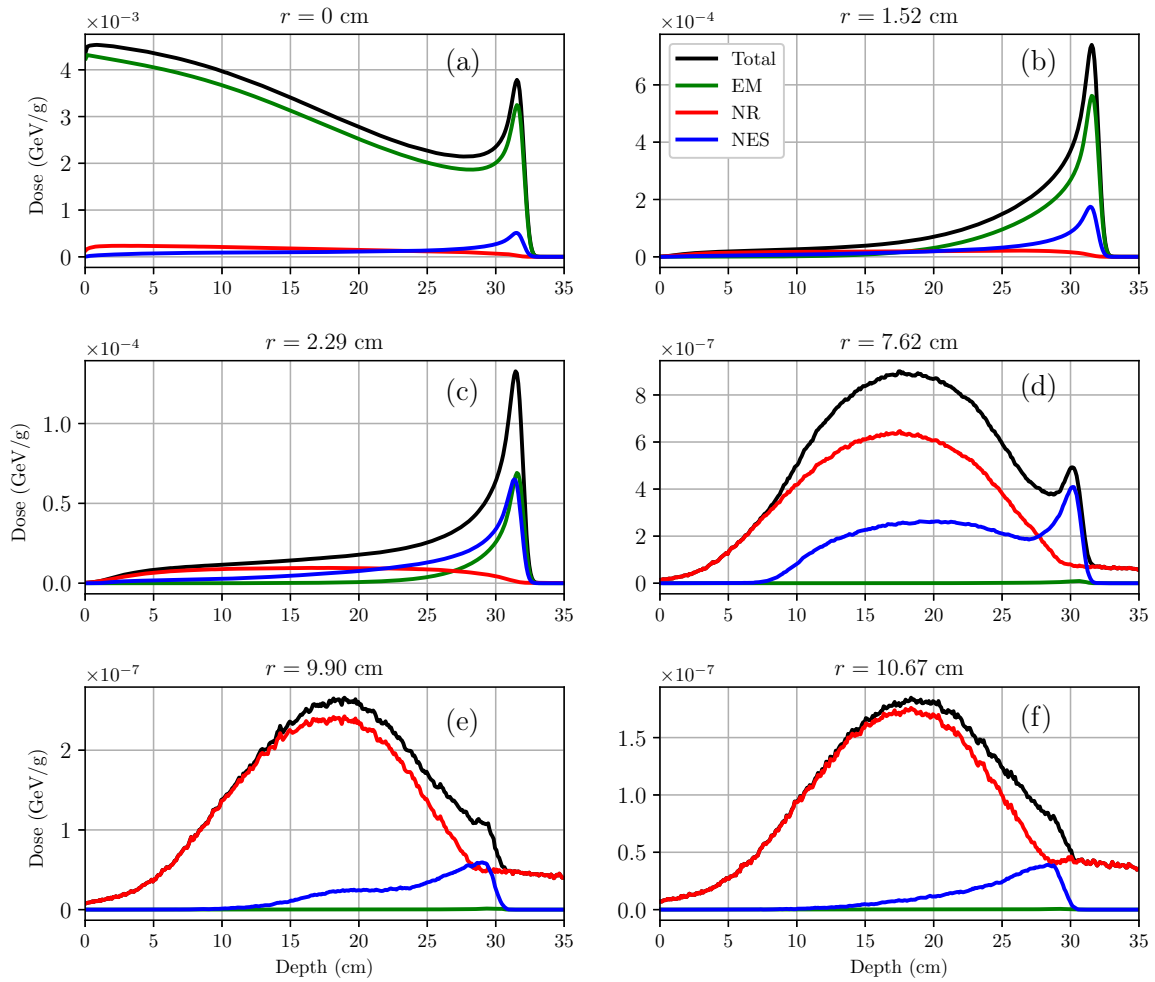

Fig. 3.10 Contribution to the dose of the different proton interaction mechanism. In this figure, the dose obtained with FLUKA (black) and further resolved into the contributions from particle histories where protons have undergone only ionization losses (green), nuclear reactions (red) and nuclear elastic scattering (blue) are shown.

3.3.4 Comparison with the experimental results

Significant differences between the experimental and MC data are obtained for the simulations performed by PENH and FLUKA (see Figure 3.12). In the case of PENH, a good description of the dose deposited in the Bragg peak region is found. The process governing this dose deposition is nuclear elastic scattering of protons on oxygen. This fact indicates that the nuclear elastic scattering differential cross section used in PENH is correctly implemented. However, serious problems are noted in the dose deposition for the central bump region in the dose profile at $r = 7.62$ cm. This feature of the dose profile is related to the nuclear reactions and the nuclear elastic interaction of protons on hydrogen. It is not appropriate to associate

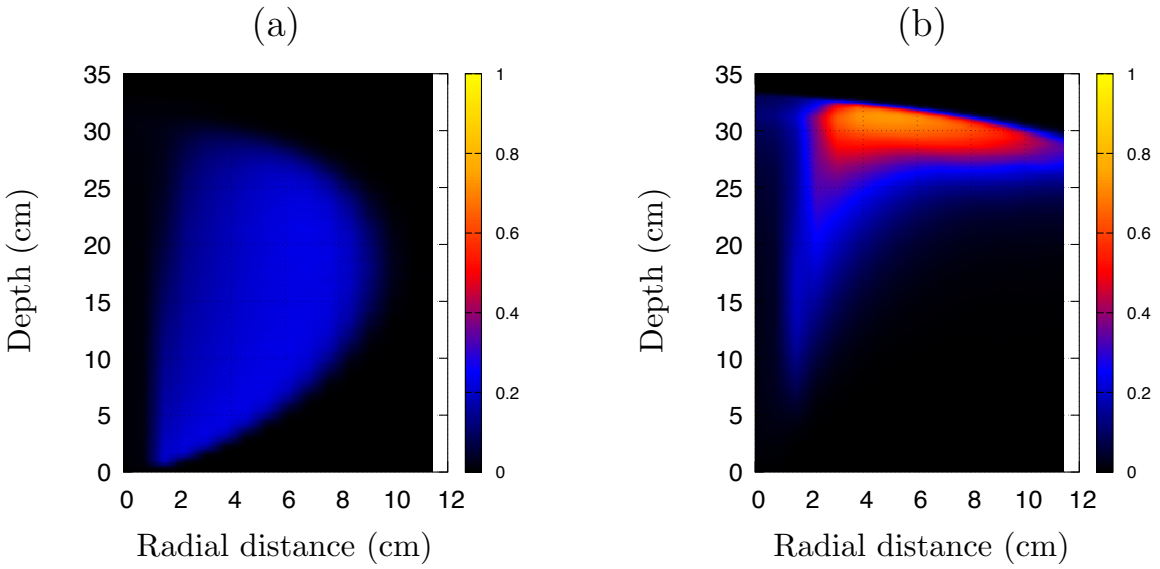

Fig. 3.11 Contribution to the dose of the nuclear elastic interaction on hydrogen (a) and oxygen (b). The data is normalised using the total dose map.

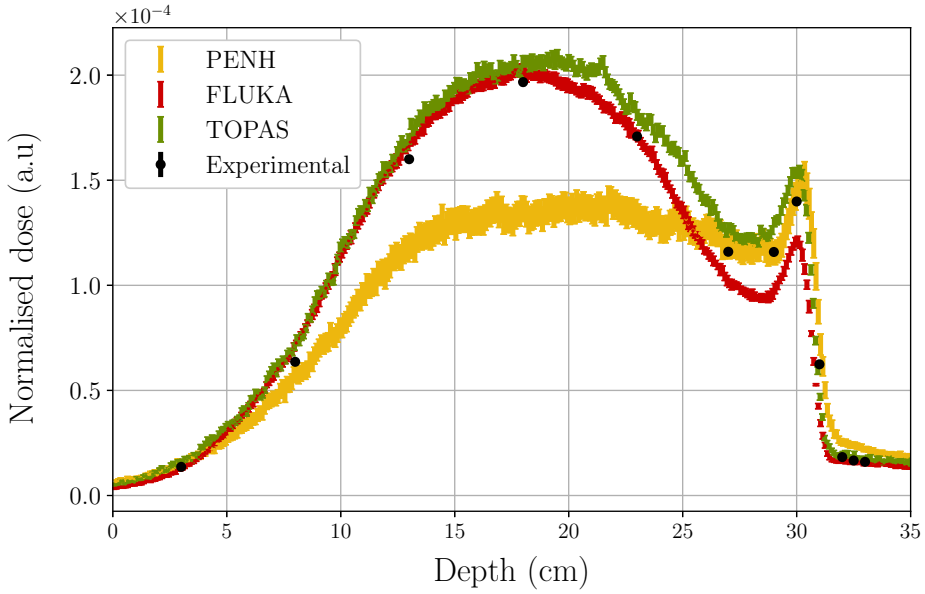

Fig. 3.12 Comparison between experimental obtained by Verbeek *et al.* [74] and MC data to study the nuclear elastic interactions models implemented in the MC codes considered. It has been considered the dose profile at $r = 7.62$ cm. Yellow, red and green represent the results obtained with PENH, FLUKA and TOPAS respectively. Experimental data is sketched in black. All the uncertainties shown have a coverage factor $k = 3$.

the discrepancies found between experimental and MC data to the effect of nuclear reactions, since previous results obtained for MLFC showed us that the implementation of nuclear

reaction is adequate in PENH. As it has been shown in section 3.2, the nuclear reaction models implemented in PENH are good enough to reproduce dose deposition for this kind of calculations. Thus, the discrepancies between the results obtained with PENH and the experimental data may be due to a misimplementation of the nuclear elastic interactions of protons on hydrogen.

Regarding the results obtained with FLUKA, in Figure 3.12, we can appreciate that there are only discrepancies in the dose deposition near the Bragg peak region. There is an underestimation in this region for the dose profile at $r = 7.62$ cm. This may indicate that there could be an underestimation in the nuclear elastic scattering of protons on oxygen, since the dose deposition in this region is due to this type of interaction. However, the nuclear elastic interaction of protons on hydrogen seems to be correctly implemented in FLUKA. This MC code reproduces the available experimental data of the dose deposition in the region where this type of interaction is more important.

Finally, it is important to note that the TOPAS results shown in Figure 3.12 can reproduce the experimental data used as reference. Similar results were obtained by Verbeek *et al.* [74], although they found an underestimation in their results. These small differences may be related to the version of the code used to calculate the results.

3.3.5 Nuclear elastic scattering on PENH

In this section the current model of nuclear elastic scattering implemented in PENH is reviewed. The possible inaccuracy related to the implementation of nuclear elastic scattering of protons on hydrogen is highlighted and a possible solution is offered to solve this problem.

The differential cross section that describes the interaction of protons with a nucleus is obtained solving the following Schrödinger equation [29]:

$$\left(-\frac{\hbar^2}{2\mu_\mathrm{r}}\nabla^2 + V_\mathrm{nuc}(r)\right)\psi(\vec{r}) = \frac{p_0^2}{2\mu_\mathrm{r}}\psi(\vec{r})\ , \tag{3.18}$$

where $\hbar$ is the reduced Plank constant, μ_r is the reduced mass of the system, ∇^2 is the Laplacian operator, $V_\mathrm{nuc}(r)$ is the optical potential that describes the interaction between the nucleus and the proton, p_0 is the initial momentum of the proton and $\psi(\vec{r})$ is the proton wave function in coordinate representation. As the optical potential has a spin-orbit term, the wave function is a two-component spinor. Assuming that before the interaction the projectile

moves in the positive direction of the z axis and using the distorted plane wave approximation, the wave function, for large values of r, can be written as

$$\psi(\vec{r}) \sim (2\pi)^{-3/2} \exp(ikr\cos\theta')\chi + (2\pi)^{-3/2} \frac{\exp(ikr)}{r} \mathfrak{F}(\theta',\phi')\chi \,, \tag{3.19}$$

where χ is a spinor, which defines the spin state of the incident nucleon, k is the projectile's wave number, and θ' and ϕ' are the polar and azimuthal scattering angles. The factor $\mathfrak{F}(\theta',\phi')$ is a 2×2 matrix defined by:

$$\mathfrak{F}(\theta',\phi') = \begin{pmatrix} f(\theta') & -\exp(-i\phi')g(\theta') \\ \exp(-i\phi')g(\theta') & f(\theta') \end{pmatrix} . \tag{3.20}$$

The functions $f(\theta')$ and $g(\theta')$ are called the "direct" and "splin-flip" scattering amplitudes, respectively. The reduced radial functions, $P_{\ell j}$, for large r values, are normalized so that:

$$P_{\ell j} \sim \sin\left(kr - \ell\frac{\pi}{2} + \delta_{\ell j}\right) \,, \tag{3.21}$$

where ℓ and j denote orbital and total angular momenta and $\delta_{\ell j}$ s the complex phase shift. Scattering observables are determined by the direct and spin-flip scattering amplitudes, which are obtained in terms of the phase shifts $\delta_{\ell j}$ of spherical waves with orbital and total angular momenta ℓ and j, respectively [29]. Calculations are performed by using the Fortran subroutine package `RADIAL` [111]. For spin-unpolarized projectiles, the elastic differential cross section per unit solid angle in the center-mass frame is given by:

$$\frac{d\sigma_{\text{nuc}}}{d\Omega} = |f(\theta)|^2 + |g(\theta)|^2 \,, \tag{3.22}$$

where

$$f(\theta) = f_{\text{Coul}}(\theta) + \frac{1}{2ik}\sum_{\ell} \exp(2i\Delta_\ell)\left[(\ell+1)(S_{\ell+}-1) + \ell(S_{\ell-}-1)\right] P_\ell(\cos\theta) \tag{3.23}$$

and

$$g(\theta) = \frac{1}{2ik}\sum_{\ell} \exp(2i\Delta_\ell)(S_{\ell-} - S_{\ell+}) P_\ell^1(\cos\theta) \,, \tag{3.24}$$

are the direct and spin-flip scattering amplitudes, respectively. In these partial-wave expansions, ℓ is the total angular momentum, k is the module of the incident wavevector, $P_\ell(\cos\theta)$ and $P_\ell^1(\cos\theta)$ are Legendre polynomials and associated Legendre functions of the first kind [143], respectively,

$$\Delta_\ell = \arg(\ell + 1 + i\eta) \,, \tag{3.25}$$

with

$$\eta = \frac{Ze^2\mu_r}{\hbar^2 k} , \tag{3.26}$$

is the Sommerfeld parameter,

$$S_{\ell a} = \exp(2i\delta_{\ell a}) , \tag{3.27}$$

are the nuclear parts of the S-matrix elements, with $a = \text{sign}(j-\ell)$, and

$$f_{\text{Coul}}(\theta) = -\eta \frac{\exp[2i\Delta_0 - i\eta \log(\sin^2(\theta/2))]}{2k\sin^2(\theta/2)} , \tag{3.28}$$

is the Coulomb scattering amplitude.

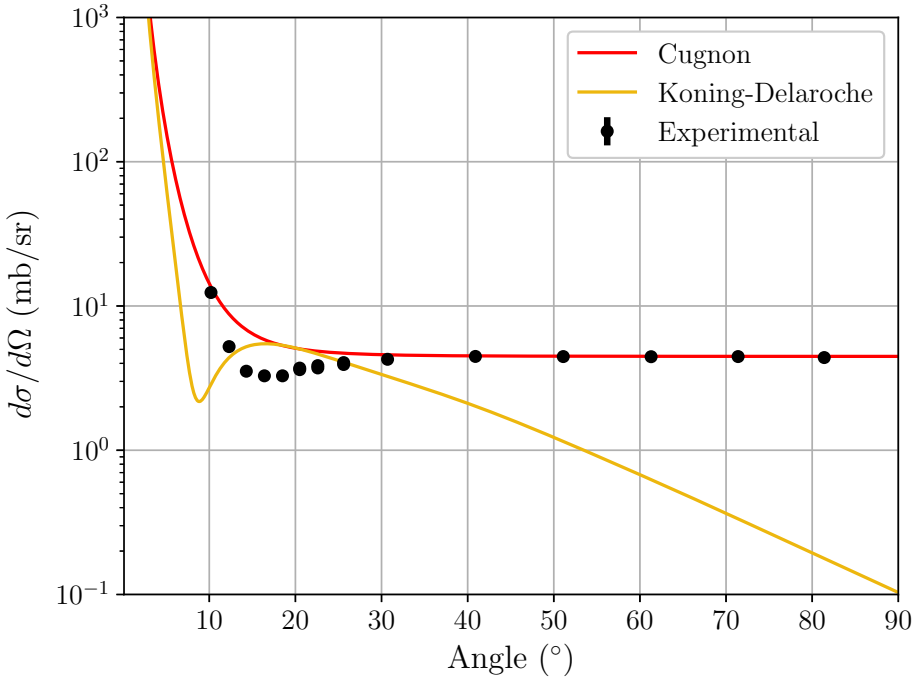

Fig. 3.13 Comparison between experimental and theoretical parametrization of the nuclear elastic differential cross section of proton on hydrogen. Nuclear elastic differential cross section on hydrogen implemented in PENH is plotted in yellow (Koning-Delaroche parametrization [112]). Nuclear elastic differential cross section on hydrogen given by the Cugnon's parametrization [144] is sketched in red. Experimental data extracted from EXFOR [145] is represented in black.

To calculate the nuclear elastic differential cross section, PENH use the optical potential given by the parametrization of Koning and Delaroche (2003) [112]. The potential parameters vary smoothly with the atomic number and the mass number and then, can be used for the calculation of the differential cross section due to the global description that offers. Moreover,

this adopted global model potential is considered to be valid only for energies up to 200 MeV [112], but it is found to give a reasonable description of the collisions also for much higher energies [29]. With respect to the atomic number, it is found that this parametrization give bad results for light elements ($Z < 5$). This fact can be understood taking into account that the global fit of this potential has been made for targets with $Z > 12$.

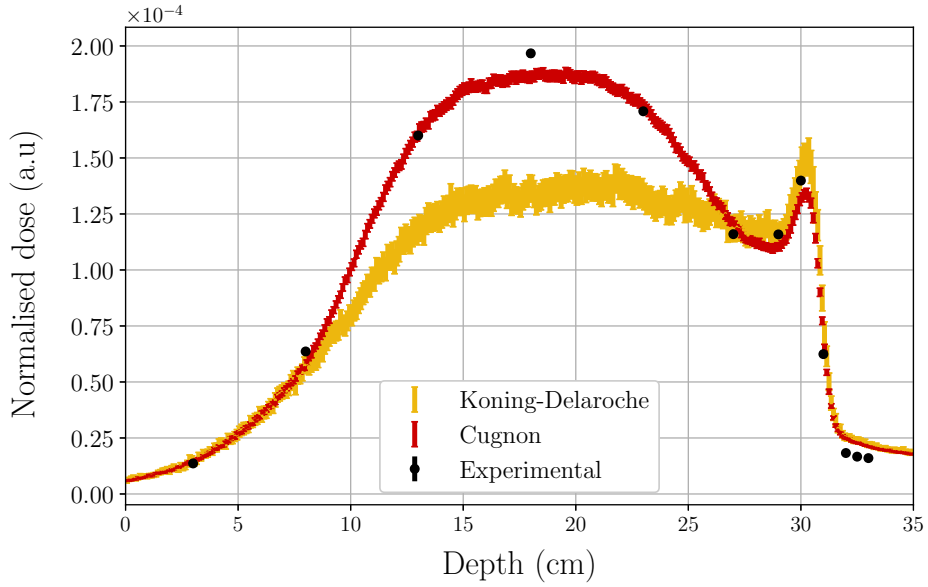

Fig. 3.14 Comparison between experimental obtained by Verbeek *et al.* (2021a) [74] and the different nuclear elastic models implemented in PENH during this analysis. The model based on the nuclear elastic differential cross section on hydrogen given by Koning-Delaroche parametrization [112]) is plotted in yellow. The model based on the nuclear elastic differential cross section on hydrogen given by the Cugnon's parametrization [144] is sketched in red. The experimental data of Verbeek *et al.* (2021a) [74] is represented in black.

Due to the lack of information for describing light elements, an alternative parametrization of the optical potential can be considered. Focusing on the measurements to be obtained with the MC simulations, the only problem that can arise due to a bad description of the optical potential is a wrong description for the elastic proton-proton interaction (case with $Z = 1$). In the scientific literature a wide range of fits to the cross section of elastic proton-proton interaction can be found. In this thesis, the Cugnon's parametrization [144] has been implemented to determine this cross section due to its simplicity. Figure 3.13 shows the comparison between experimental and theoretical (Koning-Delaroche and Cugnon parametrizations) cross sections for proton-proton elastic interaction. The experimental data of the proton-proton cross section were obtained from the EXFOR database [145]. As can be seen in Figure 3.13, the Koning-Delaroche's parametrization fails when it tries to reproduce the experimental

results extracted for large angles. However, the parametrization given by Cugnon *et al.* [144] can reproduce, in a global way, the experimental data used as reference.

To quantify the effect of the nuclear elastic differential cross section of protons on hydrogen on the dose deposition, the Cugnon's parametrization was implemented in PENH. Figure 3.14 shows the differences introduced by the use of the Cugnon's parametrization. As can be seen in that figure, a significant improvement can be found when the Cugnon's parametrization is used. This points out that the problem found for the dose profile at $r = 7.62$ cm was related to a bad implementation of the nuclear elastic interaction of protons on hydrogen. On top of that, it is also important to highlight that the description of the dose deposition in the Bragg peak area is very similar despite of the change in the elastic nuclear scattering cross section because, as we commented above, the dose deposition in this area is associated with the elastic nuclear scattering of protons on oxygen.

3.3.6 Nuclear elastic scattering on FLUKA

In this section the different models of nuclear elastic scattering implemented in FLUKA (v4-3.4 and v4-4.0) are reviewed. After this review, the implication of using one or other model to calculate the dose out-of-axis will be commented.

The total elastic scattering differential cross section is given by equation (3.22). If the following quantity is defined [139]

$$f_{\mathrm{N}}(\theta) = \frac{1}{2ik}\sum_{\ell}\exp(2i\Delta_{\ell})\left[(\ell+1)(S_{\ell+}-1)+\ell(S_{\ell-}-1)\right]P_{\ell}(\cos\theta)\,, \tag{3.29}$$

the equation (3.22) can be written as

$$\frac{d\sigma}{d\Omega} = |g(\theta)|^2 + |f_{\mathrm{C}}(\theta)|^2 + |f_{\mathrm{N}}(\theta)|^2 + 2\mathrm{Re}\left[f_{\mathrm{C}}^{*}(\theta)f_{\mathrm{N}}(\theta)\right]\,. \tag{3.30}$$

This expression allows to separate the contribution of the electromagnetic and nuclear interaction at the total elastic scattering differential cross section. This is necessary in FLUKA since the electromagnetic contribution is modelled in a common way for all charged particles and is given by the Molière MCS explained in section 1.2.1 and revised for protons in section 3.1. However, the nuclear interaction is treated independently for each type of particle. This way to express the total elastic scattering differential cross section introduces a problem due to the possibility that the term $2\mathrm{Re}\left[f_{\mathrm{C}}^{*}(\theta)f_{\mathrm{N}}(\theta)\right]$ (interference term) could become negative. This formally precludes treating nuclear and Coulomb elastic scattering as

additive interaction mechanisms, especially at energies near Coulomb barrier, as it have been reported by Şerban *et al.* [139]. Despite of this inconvenient, FLUKA parametrises the total elastic scattering differential cross section using the expression (3.30).

In the FLUKA version v4-3.4, the nuclear elastic differential cross section is given by the following parametrization (Ranft's fit) [146, 147]:

$$\frac{d\sigma_{nuc}}{d\Omega} \approx A^{1.33}\exp\left(60\cdot A^{0.33}t\right) + 0.4A^{0.40}\exp\left(10t\right) , \tag{3.31}$$

where A is the atomic mass of the element whose cross section is being calculated and t is the Mandelstam variable [115]. This model works well for high energies but it offers a description too simplistic for the 10-200 MeV range. On top of that, in the version v4-3.4 there is a lack of nuclear elastic scattering below 10 MeV. This lack in the model is due to the problems found to describe the contribution related to the interference term from equation (3.30) in this energy range.

In the FLUKA version v4-4.0, the nuclear elastic differential cross section is given by the Ranft's fit for energies larger that 250 MeV. For low energies (below 250 MeV) [139], a fit is made to the results obtained when the Schrödinger's equation is solved using the optical potential parametrization given by Koning and Delaroche [112]. The used fit is

$$\frac{d\sigma_0}{d\Omega} = \alpha k^2 R^4 \left[\left(\frac{J_1(Rq\delta_1)}{Rq}\right)^2 e^{-\beta_1 Rq} + \gamma J_0^2(Rq\delta_0)e^{-\beta_0 Rq}\right] , \tag{3.32}$$

where J_0 and J_1 are Bessel functions of the 1$^{\text{st}}$ kind, $R = 1.2A^{1/3}$ is the nuclear radius in fm, q is the center of mass wavevector transfer, k is the wavevector of the incident proton and the quantities α, β_0, β_1, γ, δ_0 and δ_1 are dimensionless fit parameters.

The expression (3.32) has some problems reproducing the differential cross section for large angles [139]. Therefore, to solve this difficulty, a further term is added to equation (3.32), prefaced by an additional fit parameter,

$$\frac{d\sigma_{\text{nuc}}(\theta)}{d\Omega} = \frac{d\sigma_0(\theta)}{d\Omega} + \zeta\frac{d\sigma_0(\pi-\theta)}{d\Omega} , \tag{3.33}$$

which improves the fit for large-angle scattering features.To calculate the nuclear elastic scattering differential cross section of hydrogen, both code versions used the Ranft's fit.

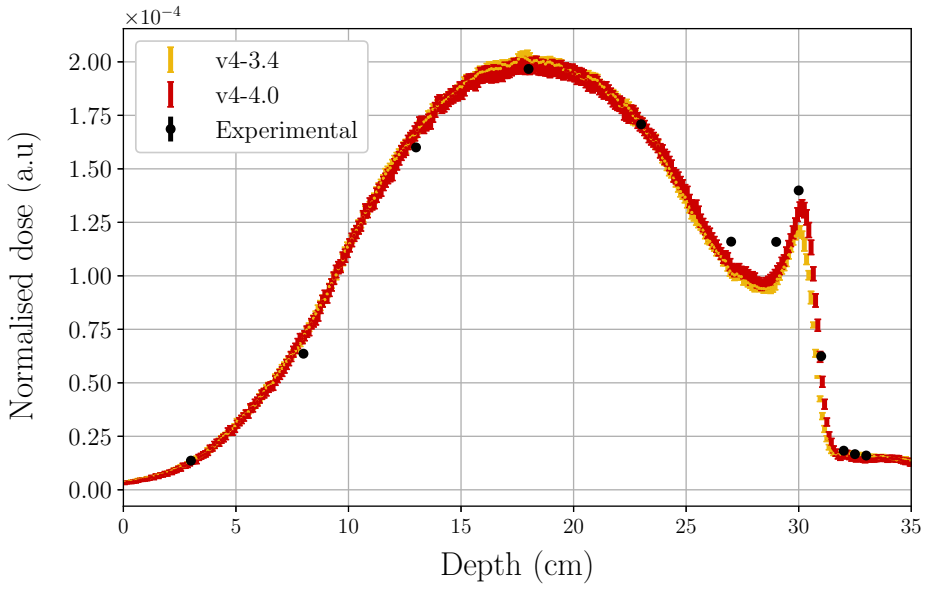

Fig. 3.15 Comparison between experimental obtained by Verbeek *et al.* [74] and the different nuclear elastic models implemented in FLUKA during this analysis. The model implemented in the version v4-3.4 is plotted in yellow. The model implemented in the version v4-4.0 is sketched in red. The experimental data of Verbeek *et al.* [74] is represented in black.

The dose deposition calculated with both models has been plotted in Figure 3.15. In general, there is good agreement between the experimental data and the MC data for the new version of FLUKA. The dose deposited in the Bragg peak zone has slightly increased, improving the agreement between MC and experimental data in this region. To sum up, the new model implemented in the version v4-4.0 improves the dose deposition associated with the nuclear elastic processes related to oxygen.

Chapter 4

Ionization chambers in proton therapy

> Measure what is measurable and make measurable what is not so
>
> *Galileo Galilei*

The control of the dose deposited in the patient by the clinical proton beam is one of the central issues in proton therapy and in radiotherapy in general. Correct dose measurement is essential to prevent accidents such as those in Zaragoza (Spain) and Białystok (Poland) [148]. In these accidents, high levels of radiation were delivered to patients due to a malfunction of the clinical accelerator. In these accidents, the dosimetric control of the facility was not a gold standard. In these cases, people would not have been exposed to a high level of radiation if correct dosimetric control had been used. These events highlight the importance of dosimetric control in clinical practice, as it allows the dose delivered to patients to be controlled.

A wide range of devices are used for dosimetric control of clinical equipment, such as radiochromic films, MOSFETs, TLDs and diodes. However, the most widely used devices for controlling the dose deposited in a patient are ionization chambers (ICs). ICs are gas-filled detectors like the proportional or Geiger-Muller counters. Gas-filled detectors are based on detecting the direct ionization produced in the gas by the radiation; ICs are, in principle, the simplest of them all. Their working principle is based on collecting of all ion-electron pairs created within the gas through the application of an electric field [149].

The output signal of these kind of detectors must be corrected [17] due to a wide range of factors such as temperature, atmospheric pressure or the type of particle used during irradiation. The correction factors k_{Q,Q_0} are used to correct the signal produced by the IC

used to measure the absorbed dose. Although these factors can be measured [18–20], it is difficult to calibrate these devices for each proton beam used in clinical practice due to the scarce time that proton accelerators are available [21, 22]. To avoid this problem, simulations can be used to determine the k_{Q,Q_0} factor. The gold standard for this type of calculation is the MC simulation [23–27].

In this chapter, the optimal parameters for particle tracking for protons in the MC simulation of the IC response are determined using the Fano test. On top of that, a brief summary of the formalism for calibration of the IC is reviewed. Finally, the k_{Q,Q_0} factor and the perturbation factors related to this quantity are calculated for the ionization chamber CRGR10/C5B/UG2 for a proton source. Part of the results presented in this chapter have been published in [150].

4.1 Fano test

As it has been reviewed in the chapter 3, the physical models implemented in the MC codes play an essential role to obtain robust results, but they are not the only factor to be considered. In addition to the physical models, other factors that need to be considered to obtain robust results are the tracking parameters. The tracking parameters allow to control the level of detail used in the MC simulation. In general, each MC code has its own tracking parameters, as they depend on the tracking algorithm used to simulate particle transport. The problem that must be faced when working with MC simulation is the following: if a very restrictive set of tracking parameters is chosen, the simulation time required to obtain the results will be too long. So the aim is to find a set of tracking parameters that are detailed enough to produce robust results, but within reasonable simulation time.

To find this set of parameters, the following theoretical result can be used: *"In a medium of a given composition exposed to a uniform flux of primary radiation (such as X-rays or neutrons), the flux of secondary radiation is also uniform and independent of the density of the medium as well as of density variations from point to point"* [151–153]. This result is known as the Fano theorem and is the main idea behind the Fano test. Thus, the Fano test can be defined as a validation proof used to verify the good performance of the MC simulation for a given set of tracking parameters. In this test, the independence of the dose deposition with density in the MC simulation is checked under the hypothesis of the Fano theorem (see section 4.1.1). Under the Fano test hypothesis, the dose deposition can be calculated by theoretically solving the Boltzmann transport equation. This theoretical value is a good

reference to check the performance of the MC codes for a given set of tracking parameters.

Currently, there is a wide range of works where the Fano test has been applied to FLUKA [24], TOPAS/Geant4 [23, 154] and an old version of PENH (v.2014) [154], obtaining that these MC codes verify this test within 0.1%-0.2% depending on the source type considered and propose optimal tracking parameters. In this section, a reproduction of these results for FLUKA and TOPAS is shown and the optimal tracking parameters for the used version of PENH is determined.

4.1.1 Fano test implementation

The Fano test has been implemented in a similar way to that used in previous works [23, 155]. It is based on the reciprocity theorem, according to which the absorbed dose in the detector can be calculated either by considering a small detector irradiated with a broad beam or a large detector irradiated by a small beam. In some cases, such as the one we are dealing with in this work, this theorem can be used as a kind of variance reduction technique that allows speeding up the calculations [155].

In the simulations carried out in the present work for verifying the Fano test, instead of a certain material phantom irradiated with an external wide beam, a source inside the phantom is considered. The whole setup must verify three conditions for the test implementation to be correct: (i) the radiation transport medium must be uniform with respect to its atomic composition and interaction properties; (ii) the spectral and angular distributions of the emitted particles must be the same at any emission point of the source, and (iii) the number of emitted particles per unit mass must be constant. These three conditions assure that Charged Particle Equilibrium (CPE) is reached. CPE exists for a defined volume if, in terms of expectation values, the expected number of charged particles of a given type and energy leaving that volume is equal to the expected number of identical particles of the same energy entering [156].

The simulation geometry is that sketched in Figure 4.1. Its consists of three stacked cylinders with radius r. The upper and lower ones (walls) have a height h_{w}, while that of the central cylinder (cavity) is h_{c}. As the Fano test was applied in the cavity, charged particles equilibrium must be fulfilled in it. To ensure this, the three conditions commented before must be achieved. To fulfil the first condition, a linear source, depicted in blue in the Figure 4.1, emits protons of a given initial energy, E_0, in the direction of the positive z-axis, as indicated by the arrows. Proton beams with energies of 50, 100, 150, 200 and 250 MeV have

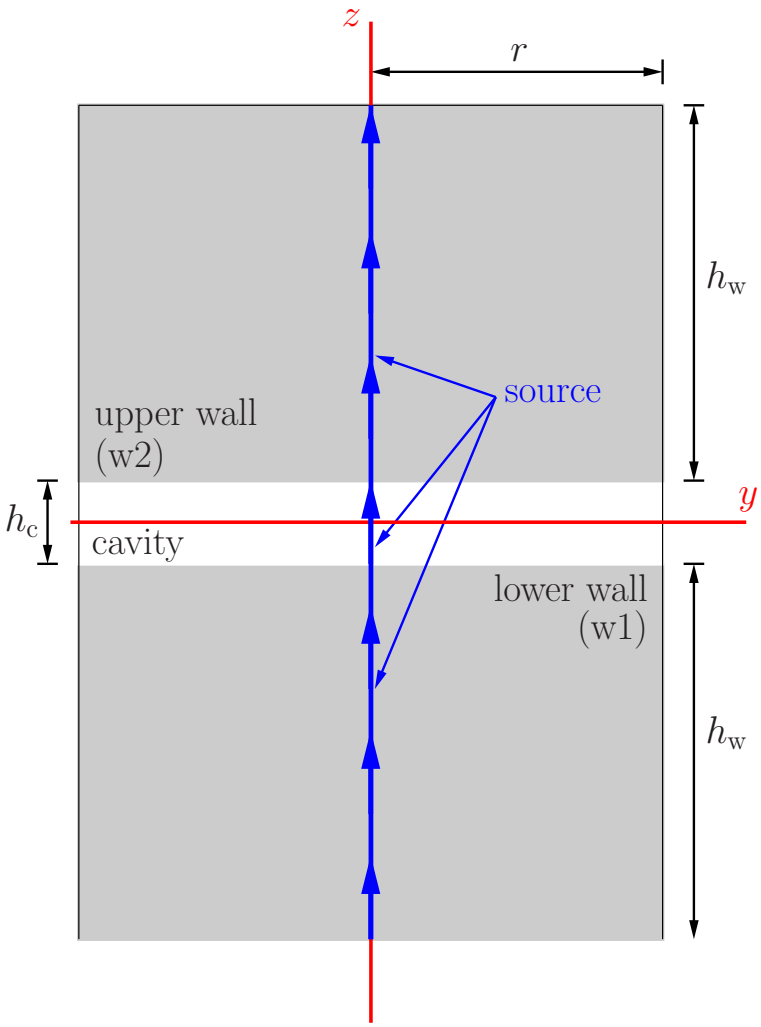

Fig. 4.1 Geometry considered to implement the Fano test in the present work. Two cylinders of radius r and height h_w have a third cylinder, of the same radius and height $h_c = 0.2\,\text{cm}$, in between. A linear source (in blue) emits protons of given initial energy, E_0, in the direction of the positive z-axis (as indicated by the arrows).

been considered in this work. Additionally, a second source type has been also considered in order to compare with previous results found in the scientific literature [23]. In this case the simulation setup is the same as described above but the source emits isotropically in all directions instead of only in the positive z-direction as before.

The material used to find the optimal tracking parameter in PENH is Al. The features of this material are listed in Table 4.2. The choice of this material is due to the fact that its characteristic parameters are well established. The geometrical parameters were chosen as follows. On the one hand, for the walls, $h_w = f\,R_w(E_0)$, where $R_w(E_0)$ are the CSDA ranges

Table 4.1 Values of the height h_w, as given by equation $h_w = f R_w(E_0)$, of the walls of the phantom used for the various energies analysed. N_w indicates the number of initial protons emitted from each of the two walls in the various simulations for the two sources, linear and isotropic, considered.

energy	h_w (cm)			N_w	
(MeV)	Al	water	C	linear	isotropic
50	1.52	3.12	1.75	$1.3 \cdot 10^8$	$3.0 \cdot 10^8$
100	5.19	10.81	6.07	$3.0 \cdot 10^8$	$4.5 \cdot 10^8$
150	10.54	22.08	12.41	$5.0 \cdot 10^8$	$6.5 \cdot 10^8$
200	17.28	36.34	20.42	$7.0 \cdot 10^8$	$8.0 \cdot 10^8$
250	25.18	53.12	28.89	$1.0 \cdot 10^9$	$1.0 \cdot 10^9$

of protons with an initial energy E_0 in Al and $f = 1.4$ (see Table 4.1). Here f is a safe value for all proton energies considered. The corresponding proton ranges are $R_w(E_0) = \tilde{R}_{Al}(E_0)/\rho_w$, where the mass ranges $\tilde{R}_{Al}(E_0)$ were obtained from the NIST database [58]. On the other hand, the cavity was filled with a fictitious material with the same composition as Al and a density $\rho_c = 0.001\,\mathrm{g\,cm^{-3}}$. In terms of the geometric parameter, the cavity has a height $h_c = 0.2$ cm. Finally, the whole geometry has a radius $r = 10 h_w$. This design allows the second condition to be met.

Table 4.2 Values of the material parameters (density and ionization energy) adopted in the simulations carried out with the different materials considered in this study.

material	I (eV)	ρ_w (g cm^{-3})	ρ_c (g cm^{-3})
C	81.0	2.0	0.001
Al	166.0	2.7	0.001
water	78.0	1.0	0.001

To compare with previous results, and to check the optimal parameters obtained for TOPAS and FLUKA, additional simulations have been conducted, wherein Al has been replaced by C and water. In these calculations, the values of the parameters defining the simulation geometry have been chosen by following the same prescriptions as in the case of Al (see Tables 4.1 and 4.2).

The third condition requires to obtain the probability of a proton being emitted as a function of the emission point, satisfying the constancy of the number of particles emitted

per unit mass. Let N_w and N_c the number of protons emitted from each of the two walls and from the cavity, respectively. The condition to be fulfilled imposes that

$$\frac{N_w}{m_w} = \frac{N_c}{m_c}\,, \tag{4.1}$$

where m_w is the mass of each wall and m_c is that of the cavity. Taking into account the densities of the wall, ρ_w, and cavity, ρ_c, materials, one has

$$N_c = \frac{\rho_c\, h_c}{\rho_w\, h_w} N_w\,, \tag{4.2}$$

and the total number of protons emitted is

$$N_{tot} = 2N_w + N_c = \left(2 + \frac{\rho_c\, h_c}{\rho_w\, h_w}\right) N_w\,. \tag{4.3}$$

The proton emission probabilities in the three elements composing the geometry are easily obtained from equations (4.2) and (4.3) and are given by

$$P_w \equiv \frac{N_w}{N_{tot}} = \frac{\rho_w\, h_w}{2\,\rho_w\, h_w + \rho_c\, h_c}\,, \tag{4.4}$$

and

$$P_c \equiv \frac{N_c}{N_{tot}} = \frac{\rho_c\, h_c}{2\,\rho_w\, h_w + \rho_c\, h_c}\,. \tag{4.5}$$

4.1.2 Fano test verification

To verify the compliance with the Fano test, secondary particles are considered to be locally absorbed in the simulations performed to study the tracking parameters. This implies a strong reduction in the computation time and avoids the uncertainties in choosing the transport parameters for these particles. On top of that, nuclear reactions have been switched off.

The z-dependence of the absorbed dose per proton emitted was studied by using a scoring grid composed of cylindrical voxels, with radius r as the phantom and height of 0.1 cm. As protons were emitted in the positive z-axis direction (for the case of the linear source), it is expected that the absorbed dose shows an increase with z up to a maximum value, labelled D_{Fano}, that indicates that charged particle equilibrium has been reached. For larger z values, the absorbed dose should remain constant, equal to this maximum value. The cavity should be within the region where this plateau appears to fulfil the condition concerning the charged

particle equilibrium above discussed.

In the conditions described above, the absorbed dose in the cavity per proton emitted should be:

$$D_{\text{Fano}} = \frac{E_0}{m_{\text{tot}}}, \tag{4.6}$$

where $m_{\text{tot}} = 2\,m_{\text{w}} + m_{\text{c}}$ is the total mass of the phantom. The verification of the Fano test was done by considering the ratio

$$Q = \frac{D_{\text{c}}}{D_{\text{Fano}}}, \tag{4.7}$$

with D_{c} the absorbed dose in the cavity, per proton emitted, obtained in the MC simulation. The further Q deviates from 1, the lower the degree of compliance with the Fano test. Q can be also written as follows:

$$Q = \frac{(\Delta E)_{\text{c}}}{m_{\text{c}}} \frac{2\,m_{\text{w}} + m_{\text{c}}}{E_0} = \frac{(\Delta E)_{\text{c}}}{E_0} \left(1 + \frac{2\,\rho_w\,h_w}{\rho_c\,h_c}\right), \tag{4.8}$$

where $(\Delta E)_{\text{c}}$ is the energy deposited in the cavity, per proton emitted, found in the simulation. It is easy to check that eq. (4.8) can be expressed as

$$Q = \frac{(\Delta E)_{\text{c}}}{E_0 \cdot P_{\text{cav}}}. \tag{4.9}$$

From the this equation, it is easy to remark that CPE is reached. This due to the fact that the mean deposited energy is equal to the mean energy of the emitted particle in the cavity.

4.1.3 Radiation yield and nuclear reactions

So far radiation yield has not been considered in the previous deduction of Q. Radiation yield represents the fraction of the total energy of a particle that is emitted in the form of radiation as it slows down while moving in a material medium. For light charged particles, *bremsstrahlung* is the main process contributing to radiation yield. However, the *bremsstrahlung* produced by protons with the energies considered in this thesis is not significant. Nevertheless, other non-negligible contributions to radiation yield must be taken into account for the case of proton's transport: those linked to nuclear reactions, in which neutrons and photons can be produced. The situation described in the previous section, in which $Q \sim 1$ provided the Fano test is satisfied, corresponds to simulations performed by switching off nuclear reactions and absorbing locally all secondary particles.

Let assume now that nuclear reactions are considered and secondary particles are transported and let D_c^{nr} be the absorbed dose in the cavity, per proton emitted, obtained in the simulation in these circumstances. It is obvious that the absorbed dose under these circumstances will be smaller than in the previous case due to the radiation yield effect. Therefore, the following expression describes this relation:

$$D_c^{nr} = D_c \left[1 - Y(E_0)\right] . \tag{4.10}$$

This equation defines $Y(E_0)$, the total radiation yield, produced in the conditions of the simulation, by protons with energy E_0. Then, the radiation yield is given by:

$$Y(E_0) = 1 - \frac{D_c^{nr}}{D_c} = 1 - \frac{Q_{nr}}{Q} , \tag{4.11}$$

where it has been defined

$$Q_{nr} = \frac{D_c^{nr}}{D_{Fano}} . \tag{4.12}$$

This magnitude makes possible to estimate the radiation yield for different proton energies, using the MC estimation of Q_{nr} and results obtained with each simulation code can be compared to estimate the contribution related with the nuclear reactions and the radiation produced by secondary light particles.

4.1.4 Details of the simulation

In what follows some specific details of the simulations done with the MC codes considered in the present work are summarized.

The simulations performed can be gathered in two groups. First, those aiming at verifying the compliance with the Fano test. As said above, in these simulations nuclear reactions are switched off and secondary particles have not been followed. Within this group, we have first the simulations in which the optimal conditions for PENH to verify the Fano test are established. Specifically, the aim is to determine the proton tracking parameters required for this purpose.

A second set of simulations in the first group has involved the other two codes considered. In what refers to FLUKA, simulations using the optimal parameters recommended by Lourenço *et al.* [24] have been conducted. These authors used a different procedure, with a different geometry, to check the verification of the Fano test in this code. In addition,

different simulations have been performed with TOPAS to study the role of proton tracking parameters in the accomplishment of the Fano test, as well as to carry out a comparison with the results quoted in the work by Wulff *et al.* [23].

In the second group of simulations, the nuclear reactions have been activated and all secondary particles have been transported, thus permitting a complete analysis of the role played by *bremsstrahlung* production and nuclear reactions in the Fano test verification. Different simulations with the three codes have been conducted to study the contribution associated with every kind of interaction that affect the radiation yield.

As indicated in equation (4.8), the quantity to be estimated in the Monte Carlo simulations is E_c, the energy deposited in the cavity per proton emitted from the source. In these simulations, the contribution of the protons emitted from each of the three cylinders conforming the simulation phantom have been separately calculated , assuming that, within each cylinder, the source points are situated in the axis, uniformly distributed along its height. In this case, the quantity of interest is given by:

$$E_c = P_{w1} \cdot E_c^{w1} + P_{cav} \cdot E_c^{cav} + P_{w2} \cdot E_c^{w2} , \tag{4.13}$$

where E_c^{w1} and E_c^{w2} indicate the contributions to E_c of the protons emitted from the lower and the upper walls and E_c^{cav} that of the protons emitted from the cavity itself (see Figure 4.1). The total number of initial protons considered for each simulation performed to implement the Fano test in each of the three codes analysed is listed in the Table 4.1. The values of the total number of initial protons simulated were chosen to give the same relative uncertainty for all energies considered in the analysis.

Regarding the direction of the emitted particle, the following parametrization has been used:

$$\vec{d} = \sin(\theta)\cos(\phi)\,\hat{i} + \sin(\theta)\sin(\phi)\,\hat{j} + \cos(\theta)\,\hat{k} , \tag{4.14}$$

where $\hat{i}$, $\hat{j}$ and $\hat{k}$ are the Cartesian unitary vectors. To implement the linear source, $\theta = 0$ and $\phi = \pi/2$ have been fixed. For the case of the isotropic source, the following expression has been used to sample the angles:

$$\theta = \arccos(1 - 2\xi_1) , \tag{4.15}$$

$$\phi = 2\pi\xi_2 , \tag{4.16}$$

where ξ_1 and ξ_2 are two pseudo-random numbers sampled using a uniform distribution between 0 and 1.

Table 4.3 Values of the simulation parameters adopted in PENH for the tracking of electrons, positrons, photons, protons, and neutrons. Note that, in the case of the simulations performed to analyse the verification of the Fano test, only the protons are transported and the secondary particles are assumed to be absorbed at the point where they are produced. It is important to point out that the values of the parameters in case of protons are obtained as optimal after the first group of simulations.

	γ	$e^{\mp}$	p	n
E_{abs} (keV)	50	50	1	100
C_1		0.1	0.05	0.0
C_2		0.1	0.05	0.0
W_{cc} (keV)		50	10	
W_{cr} (keV)		50		
FNABS				0.8

In order to fulfil the three necessary conditions to correctly implement the Fano test in PENH, the material of the cavity has been generated by duplicating the corresponding material file used for the walls (Al, water or C) and changing the density value by hand. The parameter s_{max} was set to 1 cm in the walls and 0.01 cm in the cavity. In the simulations conducted to determine the proton tracking parameters for which the Fano test is verified, the parameter NISOT was set to 0 to switch off the nuclear reactions and the absorption energies of photons, electrons, positrons and neutrons were set to 1 GeV in all materials.

In the simulations performed to study the role of the nuclear reactions and the radiation production, the values of the parameters used for the various particles were those quoted in Table 4.3. It is worth mentioning that the values indicated for the proton parameters are those that resulted from the previous study and that guarantee the verification of the Fano test. Also NISOT was set to the number of isotopes involved in the simulation to switch on the nuclear reactions in this second group of simulations.

For the case of FLUKA, the cavity material was generated by means of the MATERIAL card, by modifying the density to the appropriate value and leaving the remaining parameters that characterize Al, water or C at their original values. In the simulations done for the verification of the Fano test, the maximum step size for the proton transport has been set to 0.01 cm and the corresponding absorption energy to 10 keV. The absorption energies of the

other particles have been set to 1 GeV and nuclear reactions were switched off by setting an energy value of 1 GeV in the card THRESHOLd. In the simulations carried out to analyse the role of the radiation production and the nuclear reactions, the DEFAULT card has been used in the mode PRECISIOn.

Finally, for the simulations carried out with TOPAS, the material in the phantom walls and in the cavity has been generated with the same parameters, changing only the density value. In the simulations conducted to check the verification of the Fano test, only protons have been transported by setting CutForAllParticles = 1000 m and CutForProton = 0.05 mm and not including the modules describing nuclear reactions in the physics list of the calculations. The electromagnetic physics list g4e-standard_opt4 has been used.

Regarding the proton transport, the key parameters are dRoverRange, finalRange and MaxStepSize. The first one limits the step of the transported particle: the ratio between the step and the range of the particle must remain smaller than dRoverRange. The parameter finalRange is related to the absorption energy used in other MC codes: it establishes an upper limit to the range of the particle above which its transport ends. Finally, MaxStepSize imposes an overall limit to the step of the transported particle, independently of its range.

Two sets of values for the key parameters have been chosen. On the one hand, the default values of g4e-standard_opt4 have been considered (default case): dRoverRange = 0.1 and finalRange = 50 μm. On the other hand, the values suggested as optimal by Wulff *et al.* [23] and Baumann *et al.* [122] have been assumed (optimised case): dRoverRange = 0.05 and finalRange = 0.1 μm. In these simulations we have used MaxStepSize = 0.01 cm in the cavity and 1 cm in the walls, the same values as in the PENH calculations.

A second set of simulations has been conducted to study the role of the radiation production and the nuclear reactions. In these simulations, the parameter CutForAllParticles has been set to its default value, 0.05 mm, MaxStepSize has been used with the same values as in the previous simulations for all the particles transported, the values of dRoverRange and finalRange for protons have been the same as in the previous simulations and those for electrons and positrons have been 0.003 and 1 nm, respectively. Nuclear reactions are activated by using the corresponding modules in the physics list; in our case g4h-phy QGSP_BIC_HP and g4h-phy_QGSP_BERT_HP have been used. Neutron tracking parameters have been left at their default values. The values of MaxStepSize for neutrons and photons,

which establish their absorption energies, were the same as those indicated above for protons.

4.1.5 Results

Checking of the correct implementation of the simulation

It is worth checking that charged particle equilibrium is accomplished in the cavity. Figure 4.2 shows the results obtained in the PENH (black points), TOPAS using the default parameters set (red points) and FLUKA (green points) simulations carried out for the 250 MeV proton beam in Al. Note that FLUKA and TOPAS values have been shifted down to avoid the overlapping with PENH results. In the three cases, the buildup region is clearly seen and the maximum dose is reached at $z \sim -7$ cm, far enough from the cavity (see white strip at $z \sim 0$ cm). For lower energies, similar results to those shown in Figure 4.2 were obtained for the three MC codes analysed.

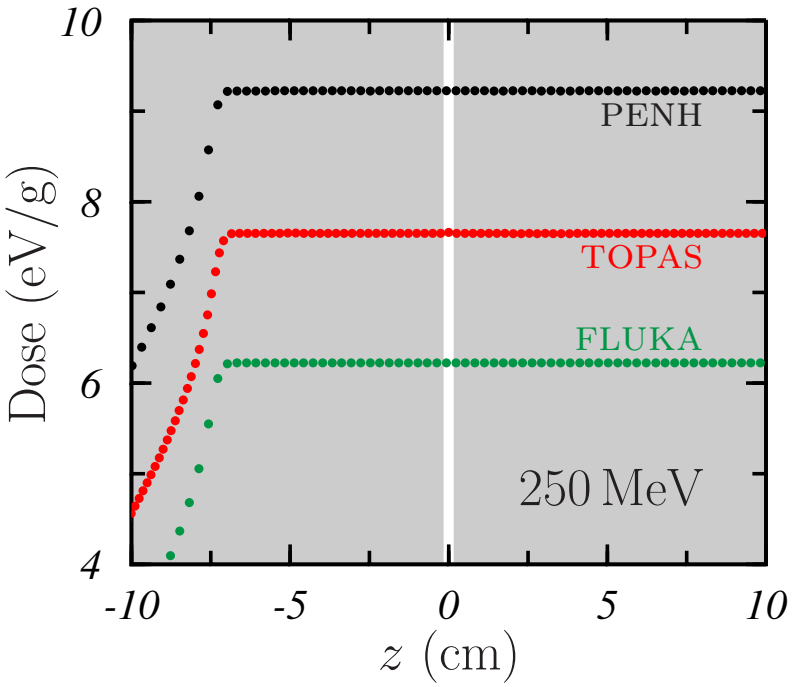

Fig. 4.2 Dose absorbed in the phantom as a function of z for the 250 MeV beam. The results obtained in the simulations carried out with PENH (black points), TOPAS (red points), and FLUKA (green points) are shown. The white strip represents the cavity, while the gray correspond to part of the walls. The uncertainties are smaller than the symbols used. TOPAS and FLUKA results have been shifted -1.5 eV/g and -3.0 eV/g, respectively, to avoid overlapping with PENH data.

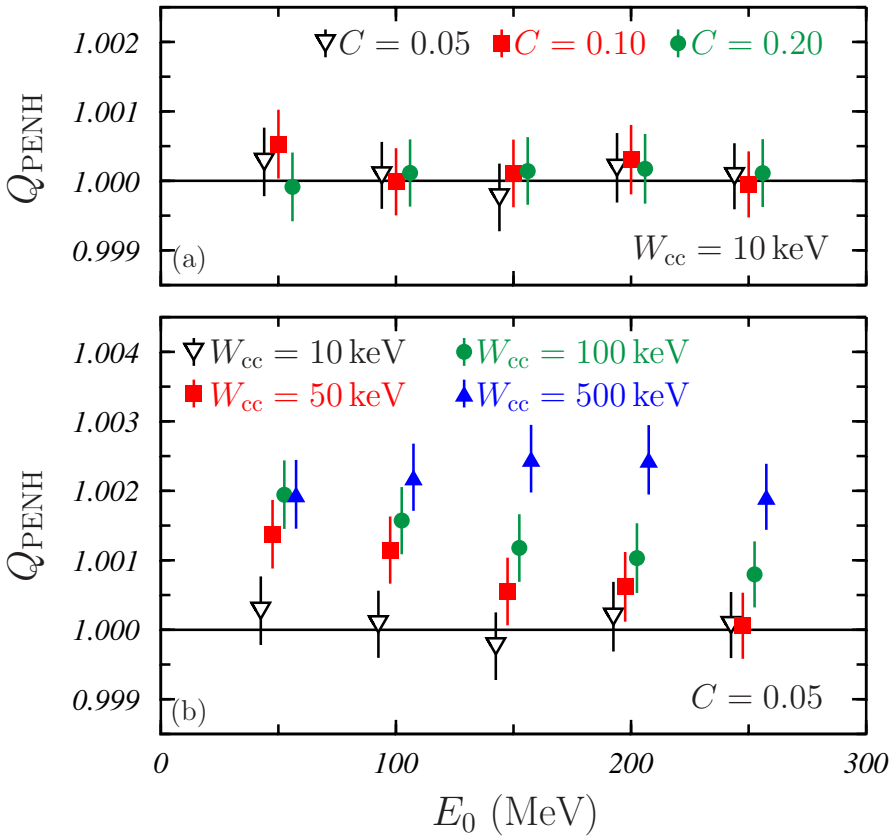

Fig. 4.3 The ratio Q, as defined in equation (4.7), as a function of the initial proton energy E_0, obtained with PENH in Al. In panel (a) the results obtained for $C_1 = C_2 = C = 0.05$, 0.1 and 0.2, maintaining $W_{cc} = 10\,keV$ are shown. The values in panel (b) have been found by keeping $C_1 = C_2 = C = 0.05$ and varying W_{cc} between 10 keV and 500 keV. Uncertainties are given with a coverage factor $k = 3$.

Optimal tracking parameters for PENH

First of all, we have established the optimal PENH tracking parameters to fulfil the Fano test. Several simulations have been conducted by varying the three parameters affecting proton transport. We have considered $C_1 = C_2 = C$ and we have calculated the ratio Q as indicated in eq. (4.8).

In Figure 4.3 it is shown the results obtained by maintaining $W_{cc} = 10$ keV and varying C, whose range in PENH is between 0 and 0.2. The Q values corresponding to $C = 0.05$ (black open triangles) are compared to those for $C = 0.1$ (red solid squares) and $C = 0.2$ (green solid circles). It is important to highlight that it can be observed that all calculations verify the Fano test within the uncertainty, independently of the value of C, for all the protons

energies considered.

While Q seems to be not significantly affected by the tracking parameters C_1 and C_2, it shows up to be strongly dependent on W_{cc}. In Figure 4.3, the ratio Q obtained for $W_{cc} = 10$ keV (black open triangles), 50 keV (red solid squares), 100 keV (green solid circles) and 500 keV (blue solid triangles), are shown for the various initial proton energies considered. These calculations have been done by maintaining $C_1 = C_2 = C = 0.05$. As can be seen, the Fano test is accomplished, within the uncertainties, for all energies analysed only for $W_{cc} = 10$ keV. For the other values of W_{cc}, Q approaches 1 as the energy E_0 increases, but, with the exception of the case $W_{cc} = 50$ keV for $E_0 = 250$ MeV, the values of Q are significantly different from 1 (take into account that the uncertainties shown correspond to a coverage factor $k = 3$).

Similar results were found by Sterpin *et al.* [154], who analysed the problem with a different geometry to that we have used here. For a proton beam of 100 MeV, they obtained a Q value almost independent of C_1 and C_2 for $W_{cc} = 10$ keV, while using $C = 0.05$, Q increases with W_{cc}, reaching values above 1.005, which did not verify the Fano test even if the uncertainties of their results were much larger than obtained in this study.

In the following simulations with PENH, the values $C_1 = C_2 = C = 0.05$ and $W_{cc} = 10$ keV have been used for protons (see Table 4.3).

Verification of the Fano test

The next step has been to compare how the three simulation codes considered verify the Fano test for the linear source (setup I). Figure 4.4 shows the Q values obtained for Al, panels (a) and (d), water, panels (b) and (e), and C, panels (c) and (f). As shown in Figures 4.4a-4.4c, both PENH (black open triangles) and FLUKA (green solid circles) satisfy the Fano test across all considered energies and materials. The optimal PENH tracking parameters selected for Al also perform well for water and C. Meanwhile, it is important to note that FLUKA simulations were conducted using the optimal parameters recommended by Lourenço *et al.* [24], who confirmed the test's validity for a significantly different simulation geometry than the one used in these calculations.

TOPAS results exhibit a different behavior. For Al (see Figure 4.4d), the Fano test fails when using the default parameters (red open squares) for some energies. While the test is satisfied at $E_0 = 100\,\text{MeV}$ and $150\,\text{MeV}$, a value of $Q^{\text{default}}_{\text{TOPAS}} = 1.0006(5)$ is obtained at

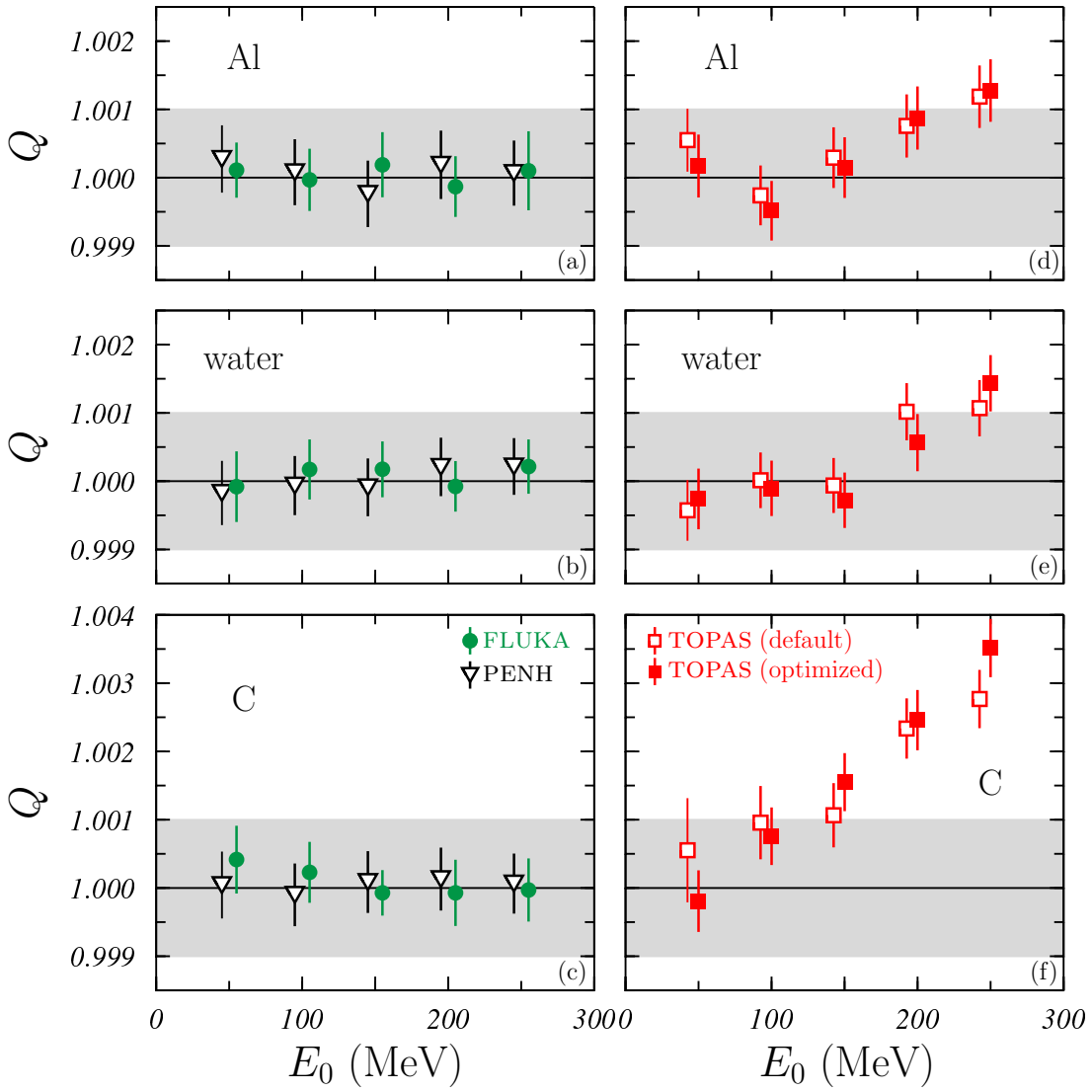

Fig. 4.4 The ratio Q, as defined in equation (4.7), as a function of the initial proton energy E_0, for the linear source (setup I). Left panels show the PENH (black open triangles) and FLUKA (green solid circles) results, while those obtained TOPAS (red squares) are shown in right panels. Red open squares correspond to the default tracking parameters with the physics list module `g4e-standard_opt4`, while red solid squares have been obtained with the optimized parameters. Upper, medium and lower panels show the Q values found for Al, water and C, respectively. The gray band indicates a $\pm 0.1\%$ maximum difference with respect to the expected value $Q = 1$.

$E_0 = 50\,\text{MeV}$. Above 150 MeV, $Q^{\text{default}}_{\text{TOPAS}}$ increases with E_0, reaching 1.0012(5) for a 250 MeV proton beam. A similar trend is observed for $Q^{\text{optimized}}_{\text{TOPAS}}$ (red solid squares) and for both parameter sets in the case of water (see Figure 4.4e). However, the results worsen for C

(see Figure 4.4f), with values of $Q_{\mathrm{TOPAS}}^{\mathrm{default}} = 1.0027(4)$ and $Q_{\mathrm{TOPAS}}^{\mathrm{optimized}} = 1.0035(4)$ at 250 MeV.

Wulff *et al.* [23] conducted an analysis closely resembling to the shown here, using TOPAS (version 3.1) with Geant4.10.03.p01 and the same physics list module. They assumed default tracking parameters (`dRoverRange` $= 0.1$, `finalRange` $= 20\,\mu$m) and employed a similar geometry, considering water and C as materials. For a linear source, Wulff *et al.* found that Q values deviated from 1 by at most 0.1% for all energies between $E_0 = 30$ MeV and 250 MeV.

The Q_{TOPAS} calculated in this work for Al and water (Figures 4.4d and 4.4e) align with those of Wulff *et al.* [23], remaining within 0.1% of $Q = 1$, except at $E_0 = 250$ MeV. However, for C, our TOPAS simulations (using both default and optimized parameters) yielded values for Q exceeding 1.001 for $E_0 \geq 150$ MeV. No significant differences were observed when using `finalRange` $= 20\,\mu$m (as in [23]) instead of `finalRange` $= 50\,\mu$m, the default in our TOPAS simulations. Furthermore, as the uncertainties shown in our results are approximately three times smaller than those reported by Wulff *et al.* [23], it is found that TOPAS fails the Fano test for proton energies $E_0 \geq 200$ MeV in Al and water, and $E_0 \geq 100$ MeV in C.

Lastly, the relative contributions of the different simulations to eq. (4.13) were analysed. Regardless of material, at $E_0 = 50$ MeV, the ratio $P_{\mathrm{w1}} \cdot E_{\mathrm{c}}^{\mathrm{w1}}/E_{\mathrm{c}}$ is 99.997% in PENH, 99.995% in FLUKA and 99.998% in TOPAS. For $E_0 \geq 100$ MeV, this ratio exceeds 99.999% in all codes and increases with E_0. The cavity contribution, $P_{\mathrm{cav}} \cdot E_{\mathrm{c}}^{\mathrm{cav}}/E_{\mathrm{c}}$, is consistent across codes at $E_0 = 50$ MeV: 0.0019% for Al, 0.0025% for water and 0.0022% for C. In TOPAS simulations, the upper wall contribution, $P_{\mathrm{w2}} \cdot E_{\mathrm{c}}^{\mathrm{w2}}/E_{\mathrm{c}}$, is always zero (for both default and optimized parameters). This suggests that, in this setup, the Fano test can be validated by considering only proton emission from the lower wall of the phantom.

For the isotropic source (setup II), the results are less clear. Using the default tracking parameters, Wulff *et al.* [23] obtained the Q values in water shown in Figure 4.5 (blue open circles). As it is shown in that figure, $Q_{\mathrm{Wulff}}^{\mathrm{default}}$ increases from 1.005 at $E_0 = 30$ MeV to 1.014 at $E_0 = 250$ MeV. A similar trend was observed in C, where $Q_{\mathrm{Wulff}}^{\mathrm{default}}$ ranged from 1.003 to 1.012 over the same energy range. The uncertainties in these calculations varied from 0.04% at low energies to 0.12% at high energies, clearly indicating a violation of the Fano test at all proton energies.

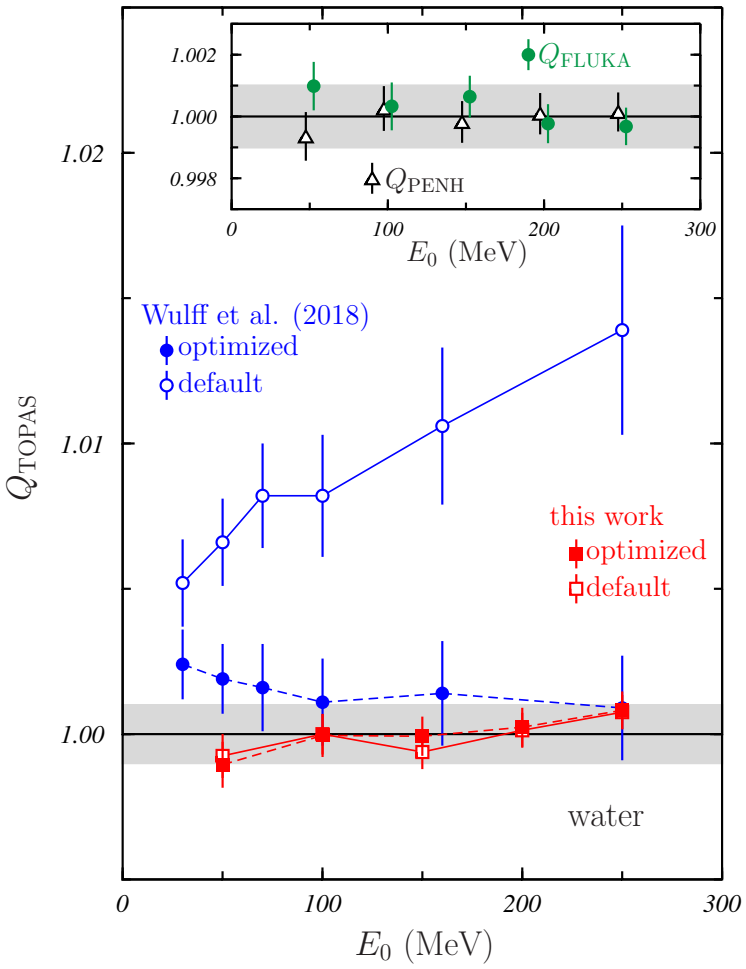

Fig. 4.5 The ratio Q, as defined in equation (4.7), as a function of the initial proton energy E_0 obtained with TOPAS in water for the isotropic source (setup II). Blue circles show the results quoted by [23], while red squares correspond to those found in the present work. The Q values obtained with the default (optimized) tracking parameters are shown with solid (open) symbols. The gray band indicates a $\pm 0.1\%$ maximum difference with respect to the expected value $Q = 1$. The lines are just joining the results corresponding to the same calculation type. In the inset, the Q values obtained for the same source with FLUKA and PENH are shown with green solid circles and black open triangles, respectively.

To solve this issue, Wulff *et al.* suggested using `dRoverRange` $= 0.05$ and `finalRange` $= 0.1\,\mu$m, the optimal tracking parameters identified above. The resulting values for Q were similar in C and water, with the latter shown in Figure 4.5 as blue solid circles. As it is seen there, $Q^{\mathrm{optimized}}_{\mathrm{Wulff}}$ decreases from approximately 1.002 at $E_0 = 30\,$MeV to around 1.001 at $E_0 = 250\,$MeV. Wulff *et al.* concluded that using these optimized parameters allowed the Fano test to be satisfied at the 0.2% level.

However, Figure 3 of [23] shows that, based on their reported uncertainties (corresponding to a coverage factor of $k = 1$), the Fano test was not statistically verified at any energy for either water or C; in other words, their simulation results were not statistically compatible with $Q = 1$. If instead a coverage factor of $k = 3$ is assumed, as in our analysis and as applied to the data of Wulff *et al.* in Figure 4.5 (see blue circles), $Q_{\text{Wulff}}^{\text{optimized}}$ passes the Fano test for $E_0 \geq 100\,\text{MeV}$ in water, but fails at lower energies. Under the same conditions in C, the results obtained by Wulff *et al.* meet the criteria of the Fano test only at $E_0 = 250\,\text{MeV}$.

We simulated the isotropic source in water using TOPAS, and the results for the default and optimized tracking parameters are shown in Figure 4.5 as red open and solid squares, respectively. The observed behaviour differs significantly from that reported by Wulff *et al.* [23]. In both cases, the Q values are quite similar, consistent with the trend observed for the linear source, and deviate from 1 by at most 0.1%. The Fano test is satisfied for all proton energies, except for the optimized parameters at $E_0 = 50\,\text{MeV}$, where $Q_{\text{TOPAS}}^{\text{optimised}} = 0.9989(8)$, and at $E_0 = 250\,\text{MeV}$, where $Q_{\text{TOPAS}}^{\text{default}} = 1.0008(6)$ for both parameter sets.

The inset of Figure 4.5 presents the results for the isotropic source obtained with PENH (black open triangles) and FLUKA (green solid circles). As it can be seen in the figure, these results closely resemble those for the linear source, with both codes verifying the Fano test for all energies, except for FLUKA at $E_0 = 50\,\text{MeV}$.

Role of the tracking parameters in TOPAS

To conclude our analysis, a detailed study on the impact of tracking parameters in TOPAS simulations is carried out. To this end, a series of simulations with various parameter combinations is performed. The effect of the following parameters have been studied: `finalRange`, `MaxStepSize` and `dRoverRange`. The key finding is that the only parameter that significantly influences the Q values is `dRoverRange`.

Figure 4.6 presents the Q values obtained for Al using TOPAS. Open symbols correspond to simulations with `dRoverRange` $= 0.1$ (identical to those in Figure 4.4d), while solid symbols represent results using `dRoverRange` $= 0.01$. Contrary to expectations for a more restrictive transport parameter, reducing `dRoverRange` to 0.01 leads to $Q_{\text{TOPAS}} \sim 1.003$ across all proton energies, failing to satisfy the Fano test. Similar results are observed for `dRoverRange` $= 0.05$. These findings suggest that below a certain threshold, the tracking algorithm becomes unstable. This instability has also been reported in Geant4 simulations for electron beams by Elles *et al.* [127].

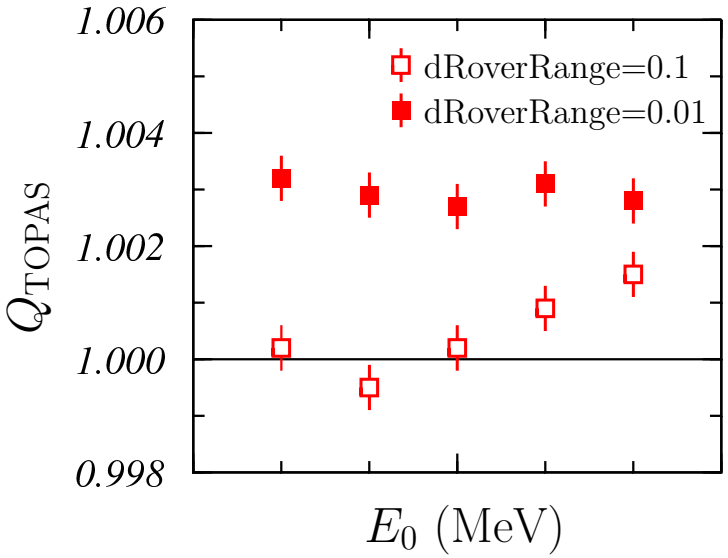

Fig. 4.6 The ratio Q, defined in equation (4.7), as a function of the initial proton energy E_0, for the linear source (setup I). The results obtained with TOPAS for Al are shown. Simulations have been performed using `finalRange`$= 0.1\,\mu$m and `MaxStepSize`$= 0.1$ mm. Open and solid symbols show the results found with `dRoverRange` $= 0.1$ and 0.01, respectively.

Fano test and the role of nuclear reactions

With the values of the tracking parameters indicated in section 4.7, complete simulations have been carried out to study the role of radiation yield and nuclear reactions. The results obtained for the yield Y, defined in eq. (4.11), as a function of the initial proton energy, are shown in Figure 4.7. Therein the Y values found for PENH and FLUKA are shown with black open triangles and green solid circles, respectively. In the case of TOPAS, two physics modules describing the nuclear reactions have been considered: BIC and Bertini. The corresponding results have been shown with red open and solid squares, respectively.

As can be seen, the Y values are below 0.1, but are not negligible. As expected, nuclear reactions and radiation production make the theoretical value $Q = 1$ to be underestimated in actual calculations. The overall trend observed is that Y grows with E_0 showing a quadratic behaviour, as indicated by the fitted second degree polynomials also plotted in Figure 4.7.

The Y values obtained with PENH and TOPAS/Bertini are practically overlapping for all the proton energies studied. The yields found with TOPAS/BIC are rather close to those corresponding to FLUKA. The differences between the two calculations carried out with TOPAS range between 8%, for $E_0 = 50$ MeV, and 22%, for $E_0 = 250$ MeV. The biggest

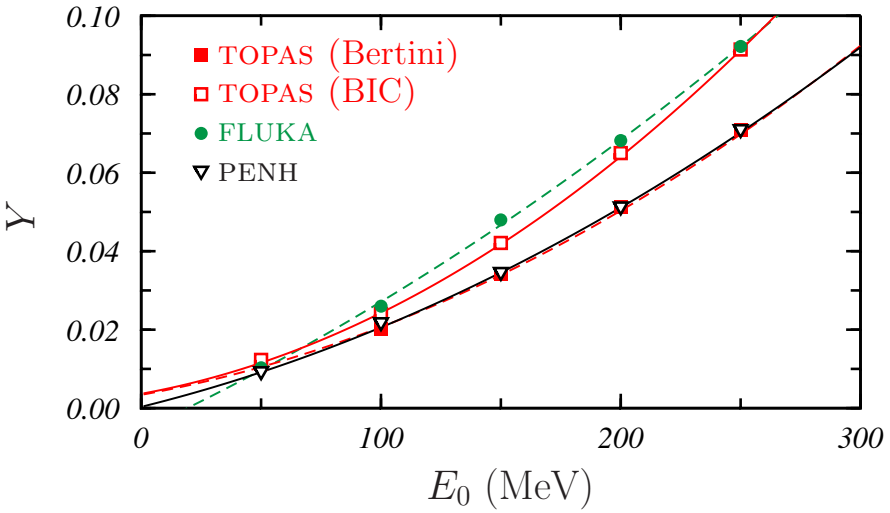

Fig. 4.7 Yield Y, defined in equation (4.11), as a function of the initial proton energy E_0, obtained in simulations performed in Al with PENH (black open triangles), FLUKA (green solid circles) and TOPAS using the physics modules BIC (red open squares) and Bertini (red solid squares). Uncertainties are given with a coverage factor $k = 3$ and are smaller than the size of the symbols used.

values (except for 50 MeV) are those of the FLUKA simulations.

To understand the source of these yields, simulations have been carried out in which nuclear reactions are switched off but all secondary particles generated by protons in any other processes are followed. The absence of nuclear reactions produced a strong reduction of Y: above 90% for PENH, above 95% in the case of FLUKA and between 58% and 88% for TOPAS/BIC and between 50% and 84% in case of TOPAS/Bertini. The general trend is that the reduction is larger as the initial energy of the protons increases, except for FLUKA. This indicates that the radiation yield is mainly due to nuclear reactions and the particles they generate.

4.2 Method of calibration of ionization chambers

This section briefly describes how to calculate the dose associated with the charge generated in the ICs. In this description, an introduction to a general formalism is presented. This theoretical framework is independent of the type of particle considered. On top of that, the general standard used in clinical practice to classify proton beams will be reviewed.

As mentioned in this thesis, dose calculation is one of the most important topics in the field of radiotherapy. One of the most widely used devices to control the deposited dose in radiotherapy are the ICs. ICs are gas-filled detectors like the proportional counters or Geiger-Muller detectors. The gas-filled detectors are based on detecting the direct ionization produced in the gas by the radiation. ICs are, in principle, the simplest of all gas-filled detectors. Their principle of operation is based on collecting all the ion-electron pairs created in the gas by the application of an electric field. Taking this into account, it is necessary to relate the charge generated by the radiation to its deposited dose in a given medium (usually water).

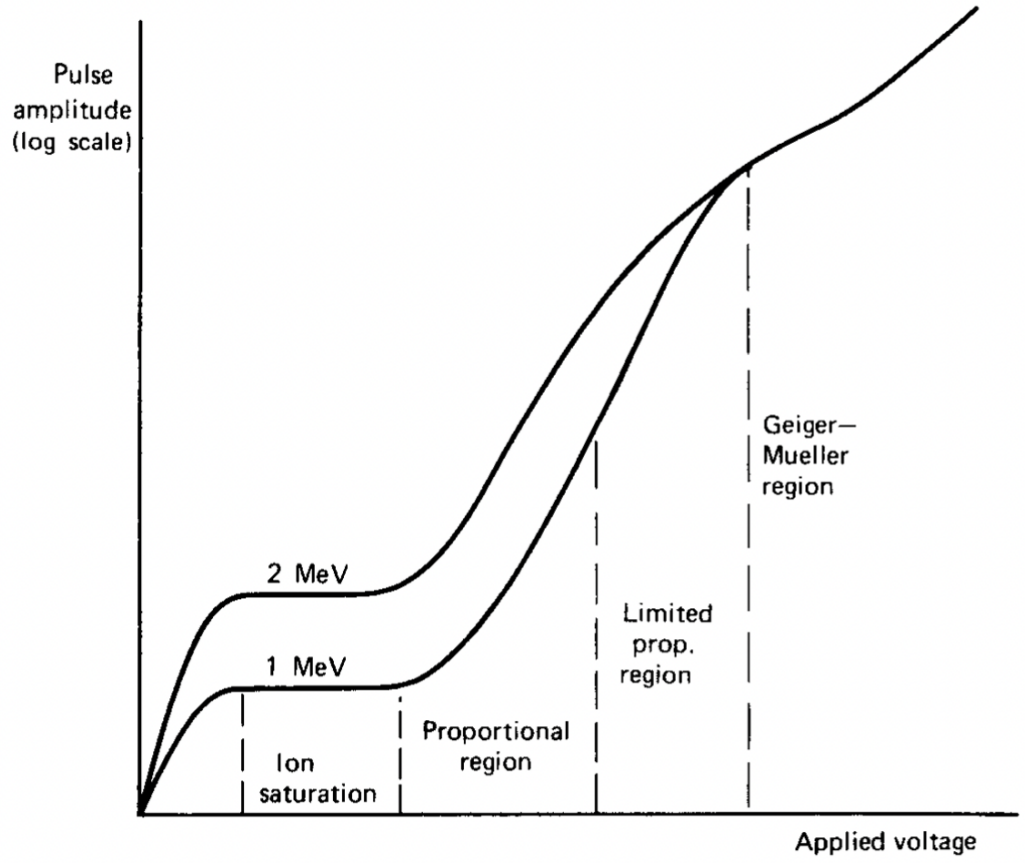

Fig. 4.8 Pulse amplitude and applied voltage diagram associated with the gas-filled detectors. Picture extracted from [149]

To calculate the dose associated with the charge generated in the ICs, it is assumed that the device under consideration operates in the ion saturation region of the pulse amplitude and applied voltage diagram associated with the gas-filled detectors (Figure 4.8). Under this

hypothesis, the following relation can be used[1]:

$$D_{\mathrm{w,Q_0}} = M_{\mathrm{w,Q_0}}\, N_{\mathrm{D,w,Q_0}}\ , \tag{4.17}$$

where $D_{\mathrm{w,Q_0}}$ is the absorbed dose deposited in water by a beam whose quality factor is Q_0, $M_{\mathrm{w,Q_0}}$ is the charge generated in the IC when measurements are made in water using a beam whose quality factor is Q_0, and $N_{\mathrm{D,w,Q_0}}$ is the calibration coefficient used to convert charge to absorbed dose in water for a particle beam whose quality factor is Q_0. This calibration factor is usually calculated using a ^{60}Co source. If another radiation source is used, whose quality factor is Q, we have:

$$D_{\mathrm{w,Q}} = M_{\mathrm{w,Q}}\, N_{\mathrm{D,w,Q_0}}\, k_{\mathrm{Q,Q_0}}\ , \tag{4.18}$$

where $k_{\mathrm{Q,Q_0}}$ is a correction factor that accounts for the fact that a source other than the one used to calibrate the detector, Q_0, has been used. The mathematical expression of this correction factor is:

$$k_{\mathrm{Q,Q_0}} = \frac{N_{\mathrm{D,w,Q}}}{N_{\mathrm{D,w,Q_0}}}\ , \tag{4.19}$$

where $N_{\mathrm{D,w,Q}}$ is the calibration coefficient used to convert charge to absorbed dose in water for a particle beam whose quality factor is Q. Expanding equation (4.19), the correction factor can be written as:

$$k_{\mathrm{Q,Q_0}} = \frac{W_{\mathrm{gas,\,Q}}}{W_{\mathrm{gas,\,Q_0}}}\, \frac{D_{\mathrm{w,Q}}}{D_{\mathrm{IC,Q}}}\, \frac{D_{\mathrm{IC,Q_0}}}{D_{\mathrm{w,Q_0}}}\ , \tag{4.20}$$

where $W_{\mathrm{gas,\,Q}}$ ($W_{\mathrm{gas,\,Q_0}}$) is the mean energy required, on average, to produce an ion-electron pair in a gas for a beam quality Q (Q_0), $D_{w,Q}$ (D_{w,Q_0}) is the dose deposited by a particle beam with quality factor Q (Q_0) in water at the position where the measurement is done and $D_{IC,Q}$ (D_{IC,Q_0}) is the dose deposited by a particle beam with quality factor Q (Q_0) in the IC at the position where the measurement is taken. Equation (4.20) is very useful because it allows to calculate the correction factor using magnitudes that can easily be obtained with MC simulations. Moreover, the correction factor can also be written as:

$$k_{\mathrm{Q,Q_0}} = \frac{W_{\mathrm{gas,\,Q}}}{W_{\mathrm{gas,\,Q_0}}}\, \frac{D_{\mathrm{IC,Q_0}}}{D_{\mathrm{w,Q_0}}}\, p_{\mathrm{wall}}\, p_{\mathrm{fl}}\, p_{\mathrm{cel}}\ , \tag{4.21}$$

where p_{wall}, p_{fl} and p_{cel} are perturbation factors [43]. These perturbation factors take into account how the different elements of the IC affect to its final signal. p_{wall} is the wall

[1]The notation followed in this text was been taken from [43]. In the following, calibration coefficients are denoted by $N_{\mathrm{a,b,c}}$, where a is the calibration quantity (in this case absorbed dose), b is the medium in which the quantity is measured (usually water) and c is the reference beam quality.

perturbation factor and it corrects for the non-medium equivalence of the chamber walls with water. p_{fl} is the fluence perturbation factor and it corrects for the lack of out-scattering of electron from the chamber cavity, compared to the out-scattering that occurs in the medium in the absence of the gas cavity. Finally, the p_{cel} factor is the electrode correction and it corrects for the effect on the dose deposition in the gas cavity produced by the central electrode. This correction factors can be obtained using the dose deposition calculated with a MC simulation of a simplified geometry. The definition of these factors, using dose quantities, is:

$$p_{\mathrm{fl}} = \frac{D_{\mathrm{w,Q}}}{D_{\mathrm{gas,Q}}} \,, \tag{4.22}$$

$$p_{\mathrm{wall}} = \frac{D_{\mathrm{gas,Q}}}{D_{\mathrm{wall,Q}}} \,, \tag{4.23}$$

$$p_{\mathrm{cel}} = \frac{D_{\mathrm{wall,Q}}}{D_{\mathrm{IC,Q}}} \,, \tag{4.24}$$

where $D_{gas,Q}$ is the dose deposited by a particle beam with quality factor Q in a small gas cavity situated at the position where the measurement is done (panel (b) in Figure 4.9) and $D_{\mathrm{wall,Q}}$ is the dose deposited by a particle beam with quality factor Q in a small gas cavity in a geometry where the external covering of the IC is considered (panel (c) in Figure 4.9).

On top the formalism previously explained, it is necessary to classify the proton beams through the quality factor. The IAEA (International Atomic Energy Agency) published an international criterion in the TRS398 Code of Practice (CoP) [17]. For monoenergetic beams, the residual range is chosen as quality factor. The residual range is defined as:

$$R_{\mathrm{res}} = R - z_{\mathrm{m}} \,, \tag{4.25}$$

where R is the range of the monoenergetic beam and z_{m} is the position where the measurement is made. For proton beams with a range greater than or equal to 5 g/cm^2, z_{m} is fixed at a depth of 2 g/cm^2 and, for the remaining ranges, z_{m} is considered at a depth of 1 g/cm^2. When a SOBP is used as a proton source, the same definition of the quality factor is used as for the monoenergetic proton beams. In the case of a SOBP, z_{m} is considered at the centre of the plateau region of the SOBP.

Last but not least, a simple relation between the dose calculated with a MC simulation ($D_{\mathrm{IC,Q}}$) and the induced current in the IC (I_{IC}) can be established:

$$I_{\mathrm{IC}} = e\,\frac{D_{\mathrm{IC,Q}}\,S\,\dot{\phi}}{W_{\mathrm{gas,Q}}}\,m_{\mathrm{gas}}\,f_R\,, \tag{4.26}$$

where e is the charge of electron, m_{gas} is the gas mass within the active volume of the IC, S is the effective surface of the ionization chamber, $\dot{\phi}$ is the clinical fluence rate and f_R is the recombination factor. For the calculation presented in this thesis, the recombination factor will be taken as 1, because it is supposed that the ICs analysed in this work will be irradiated in the ion saturation region (Figure 4.8).

4.3 Monte Carlo characterization of the ionization chamber

After introducing the formalism used to correct the IC signal, the correction coefficients (p_{wall}, p_{fl}, p_{cel} and $k_{\mathrm{Q,Q_0}}$) are calculated for the ionization chamber CRGR10/C5B/UG2. This IC was chosen because it was recently ordered by our research group. This could allow the experimental characterisation of the IC and the comparison of these results with the MC data presented in this work in the near future. Regarding the correction coefficients calculated in the simulation, which will be described in the following section, a wide range of proton beam energies has been considered for the calculation. In this way, a global view of the behaviour of these parameters will be obtained.

4.3.1 Monte Carlo simulation

In the study of the correction factors for the ionization chamber CRGR10/C5B/UG2, a monoenergetic proton beam is used with an irradiation field of 10×10 cm^2. The energy of this proton beam has been varied in order to analyse the dependence of the correction factors on this magnitude. The following energies were used in the study: 100, 150, 200 and 250 MeV. Moreover, to obtain the $k_{\mathrm{Q,Q_0}}$ factor, a ^{60}Co source is considered as a reference. In the simulation, the ^{60}Co source was modelled as a monoenergetic photon beam of 1.25 MeV. This parametrization of the cobalt source was used by Baumann *et al.* [122]. As in the case of protons, a field of 10×10 cm^2 was used in the simulation. The simulation geometry corresponded to the measurement conditions for a standard IC. A water phantom of $20 \times 20 \times 10$ cm^3 [122] was placed at a source-to-surface distance of 100 cm. The element considered between the source and the phantom was a layer of air. The reference point was

at a depth of $2\,\mathrm{g/cm^2}$, following the recommendation of the TRS398 CoP [17]. The centre of the implemented IC was at the reference depth. In each simulation, $1 \cdot 10^9$ primary particles were used.

Table 4.4 Composition of different materials considered in the simulations of the IC. For each material it is expressed the elements present, their atomic numbers and weight fractions, the material density, ρ, and the corresponding mean excitation energy, I.

material	Z	weight fraction	ρ ($\mathrm{g\,cm^{-3}}$)	I (eV)
Al	13	1.000	2.70	166
Ar	18	1.000	$8.803 \cdot 10^{-3}$	188
Stainless steel			8.00	283
Cr	24	0.225		
Fe	26	0.746		
Ni	28	0.029		
Air			$1.205 \cdot 10^{-3}$	85.7
C	6	0.001		
N	7	0.755		
O	8	0.231		
Ar	18	0.013		
Water			1.00	78.0
H	1	0.111		
O	8	0.889		

Regarding the IC, the dimensions of this detector were obtained from [157]. This technical report gives a wide range of information about the dimensions of this model of IC (see panel (d) of Figure 4.9). Furthermore, the gas cavity is filled with argon at a pressure of 5 bar. The pressure of the gas has been taken into account by modifying its density value (see Table 4.4). Due to the lack of information on the composition of the IC, the following materials were chosen for the implementation of this device: argon (gas cavity), aluminium (central anode) and stainless steel (walls). Table 4.4 collects all the information about the materials used in the simulation. As far as the scoring method used in this simulation is concerned, the dose deposited in the gas cavity has been calculated for the proton and ^{60}Co source. To calculate the $k_{\mathrm{Q,Q_0}}$ factor, the expression (4.20) has been used. To apply this expression, it is necessary to calculate the dose deposited in the water at the point of interest, at a depth of $2\,\mathrm{g/cm^2}$ on the water phantom (see panel (a) of Figure 4.9). To calculate this quantity, the same geometry explained above was taken into account but the IC was removed. The chosen volume used to obtain the deposited energy is a cylinder whose dimensions are 0.25 mm of height and 0.5 cm of radius [122]. To calculate the number of electron-ion pairs produced by the ra-

diation, $W_{\text{gas,Q}}$ was taken to be 26.4 eV. This value corresponds to the argon value [149, 158].

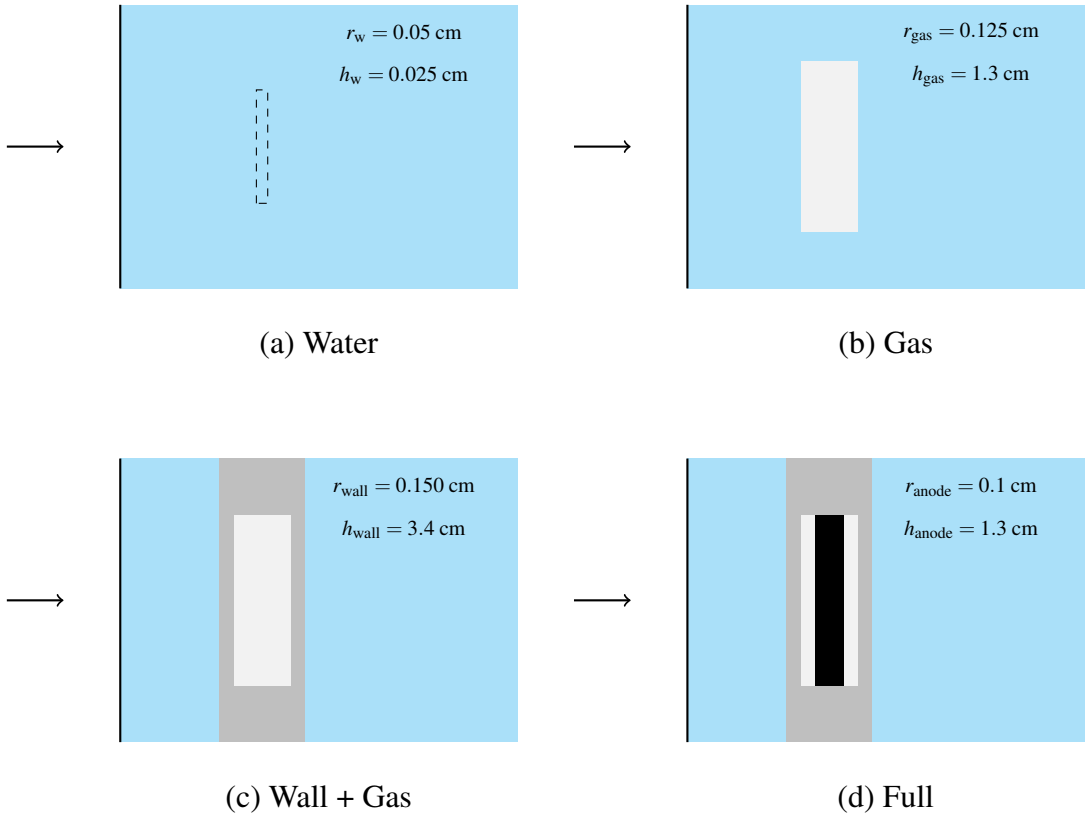

(a) Water (b) Gas

(c) Wall + Gas (d) Full

Fig. 4.9 Basic sketch of the simplified geometries of the ionization chamber used to calculate the correction factors p_{fl}, p_{wall} and p_{cel}. The materials used in this set of simulations are: water (blue), argon (white), stainless steel (grey) and aluminium (black). The sizes of the cylinders used to model the different elements of the IC are sketched in each panel. Using these geometries, the following quantities have been calculated: (a) $D_{\text{w,Q}}$, (b) $D_{\text{gas,Q}}$, (c) $D_{\text{wall,Q}}$ and (d) $D_{\text{IC,Q}}$. The arrows indicate the incident direction of the proton beam used in the simulation.

On top of that, in order to quantify the effect of the different elements that compose the IC, a series of simplified simulations were performed to calculate the correction factors p_{fl}, p_{wall} and p_{cel}, using the definitions given by eq. (4.22), (4.23), and (4.24). Figure 4.9 shows the different simulations used. The "water" geometry was used to know the amount of dose deposited by the different monoenergetic beams. The active volume used to calculate the dose deposited at $2\,\text{g/cm}^2$ was a cylinder with a height of 0.25 mm and a radius of 0.5 cm [122]. The "gas" geometry was used to determine the effect in the signal IC of using a gas cavity (p_{fl}), the "gas + wall" geometry was used to study the effect of the wall (p_{wall}) and the "full" geometry was used to determine the effect introduced by the anode (p_{cel}). In these simulations, the active volume used to calculate the dose was the gas cavity. The gas cavity

was modelled as a cylinder with a height of 1.3 cm and a radius of 0.125 cm. When the anode is included in the simulation, the active volume is reduced by introducing an aluminium cylinder with a height of 1.3 cm and a radius of 0.1 cm inside the gas cavity.

4.3.2 Results

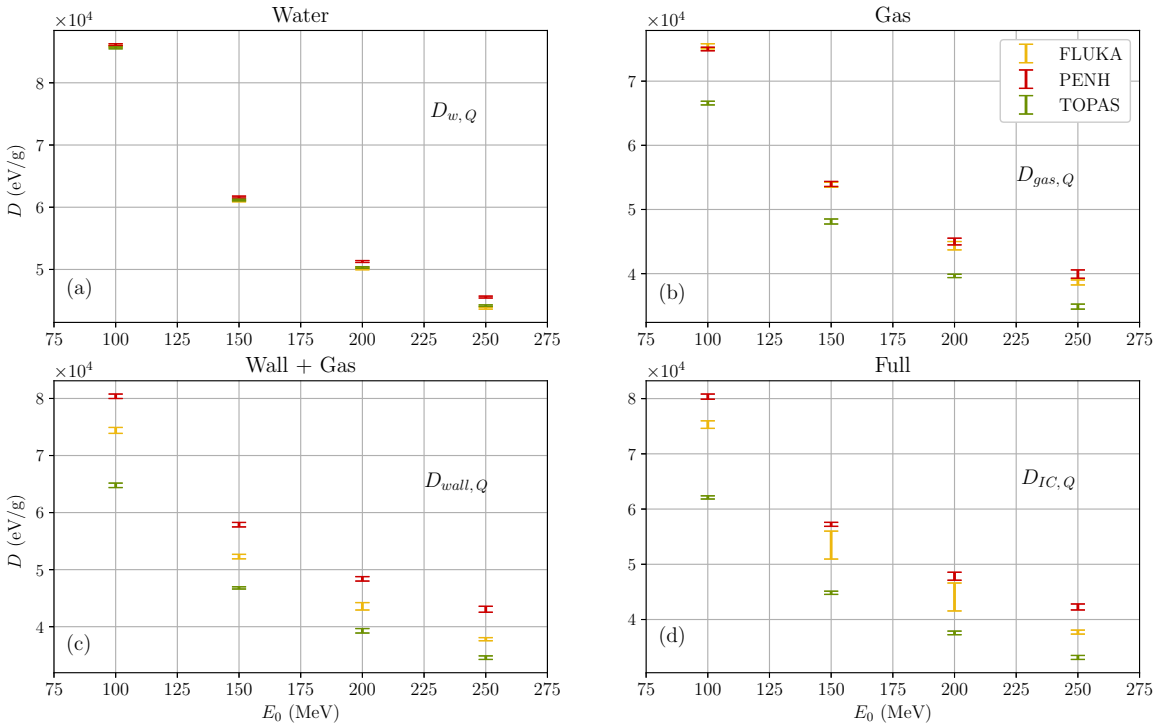

Fig. 4.10 Dose deposition in the gas cavity of the ionization chamber for the different geometries under consideration.

As a first step, the correction factors of the ionization chamber have been calculated (p_{wall}, p_{fl} and p_{cel}). To better understand the results obtained for these correction factors, the dose depositions used to calculate them are analysed. In general term, Figure 4.10 shows an inverse proportional relation between the initial beam energy and the dose deposition for any of the geometries considered in this work. This fact can be explained by considering the mass stopping power of argon in the clinical energy range. In this energy range, the mass stopping power of this element is monotonically decreasing (Figure 4.11). This leads to the relation found between the initial beam energy and the dose deposition.

On top of that, it is clear that there are significant differences between the results obtained with MC simulations. To shed some light on this issue, the dose deposited in the gas cavity

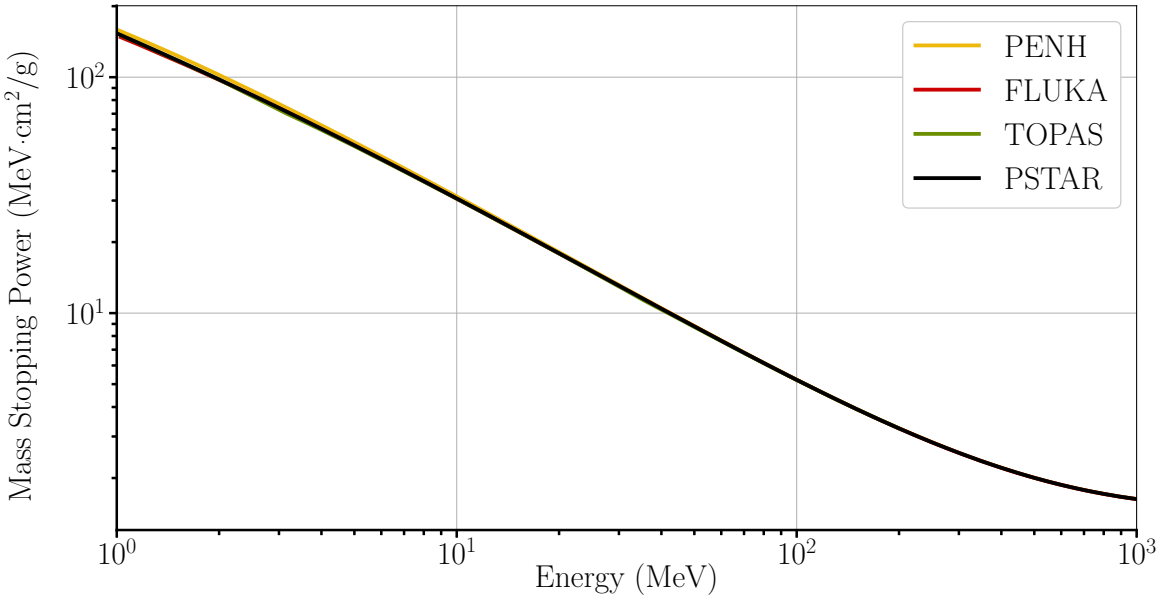

Fig. 4.11 Representation of the mass stopping power of Argon for protons used in the MC codes. Additionally, the mass stopping power extracted from the PSTAR database [58] is plotted.

is plotted as a function of the geometry considered (Figure 4.10). With the exception of the panel (a), there are non negligible differences in the dose deposition obtained with the different MC simulation codes. This seems to condition the results obtained for the ionization chamber correction factors. A clear trend can be inferred from these differences. In general, PENH gives the highest dose deposition in the gas cavity, followed by FLUKA and TOPAS (panels (b)-(d) of Figure 4.10).

Figure 4.12 shows the corrections factors obtained by the MC simulations. It could be seen in that figure that there are large discrepancies among the results obtained with the different MC simulation used in this thesis. These differences derived from the discrepancies found for the dose deposition profiles commented above. For the values of p_{fl} (panel a), a systematic difference around to -11% have found for the TOPAS results if they are compared with the data obtained with the other codes. Conversely, if the values of p_{wall} are analysed (panel b), a systematic difference around to 10% have been found for the PENH results compared to the FLUKA and TOPAS ones. However, for the values of p_{cel} (panel c), compatible results have been found for the three codes. Even so, there are discrepancies for 50 and 100 MeV between the TOPAS results and those obtained with FLUKA and PENH.

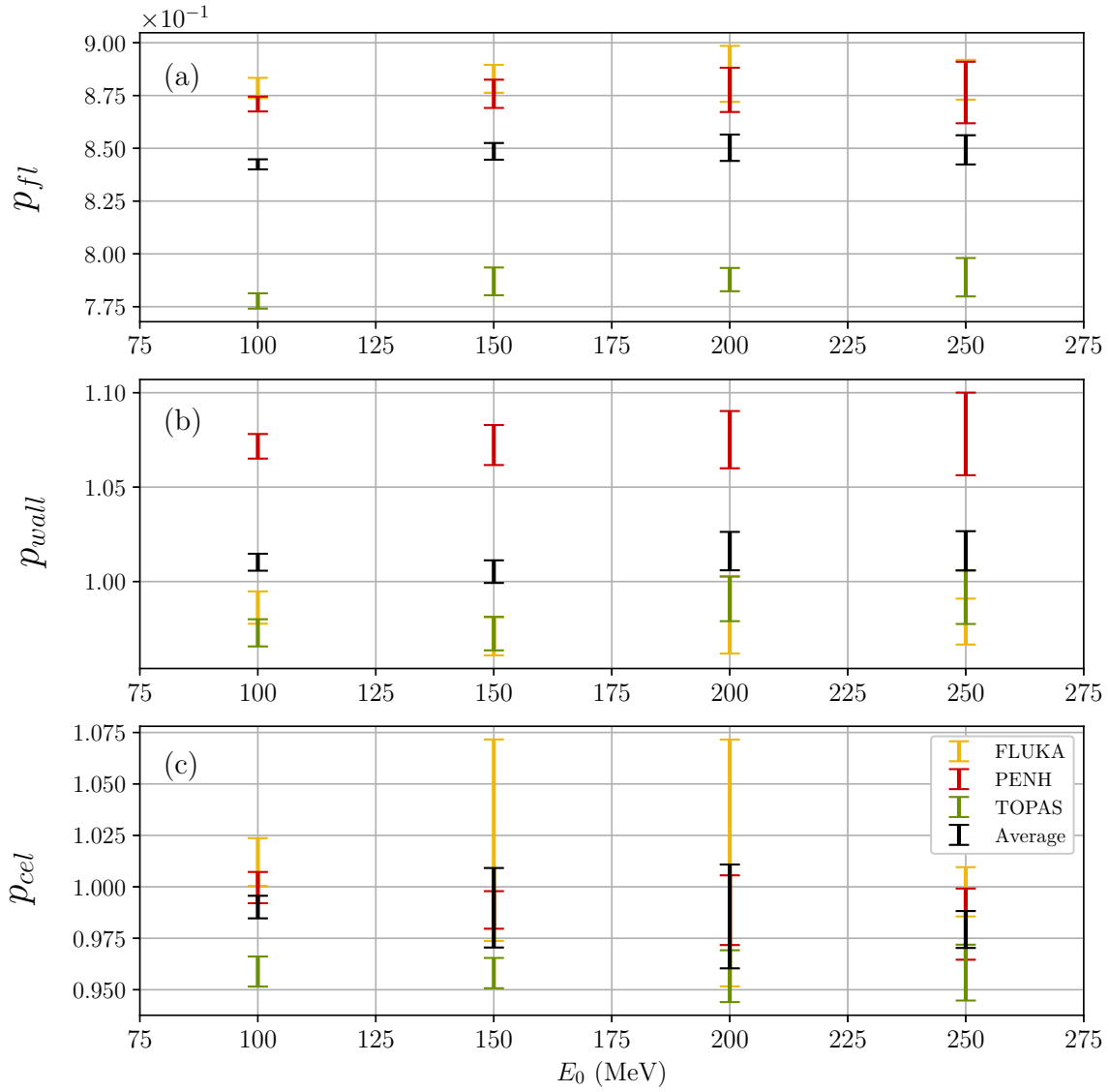

Fig. 4.12 Panel (a): effect produced for considering a gas cavity instead of a water volume (p_{fl}). Panel (b): effect related to the walls of the ionization chamber (p_{wall}). Panel (c): effect associated with the central anode of the ionization chamber (p_{cel}).

In order to obtain a trend from the results obtained with the MC simulations, the average value of the data obtained with the three MC codes used was calculated (black dots in Figure 4.12). From these averages it can be concluded that the main change in the signal is due to the effect of the gas cavity. This is reflected in the fact that the correction factor p_{fl} is significantly different from unity for all energies considered in this study. Furthermore, the effect of the gas cavity can also be observed in Figure 4.10. For all MC codes, a reduction is found when the active volume changes from water (panel (a)) to argon (panel

(b)). For this reason the value of p_{fl} is less than unity. Regarding the results obtained for p_{wall} and p_{cel}, values close to unity were found. This means that the effect of the wall and anode in the IC signal has a small impact if it is compare with the impact of the gas cavity.

Table 4.5 $k_{\mathrm{Q,Q_0}}$ factor for the ionization chamber CRGR10/C5B/UG2.

E_0 (MeV)	PENH	FLUKA	TOPAS
100	1.18 (6)	1.23 (4)	1.22 (4)
150	1.18 (6)	1.23 (6)	1.21 (4)
200	1.18 (6)	1.22 (8)	1.19 (4)
250	1.18 (6)	1.25 (4)	1.18 (4)

Regarding the $k_{\mathrm{Q,Q_0}}$ factor, compatible results have been obtained with the three codes used (Table 4.5). A similar value, around 1.2, is obtained. No dependence on the energy is found in the regime considered. At the level of precision obtained with these calculations, these results are consistent with the data available in the TRS398 CoP for all ionization chamber models studied there. In this CoP, a maximum variation of 0.20% with respect to the signal at 100 MeV has been found along the energy regime considered. Due to the uncertainties (relative uncertainties $\sim 3\%$) obtained in the MC simulations carried out, the small changes observed in the signal due to the energy described in [17] cannot be observed in the results obtained with MC simulations. It is important to note that there are larger uncertainties associated with this set of data when compared with those obtained for the previous results (relative uncertainties $\sim 1\%$). This increase in uncertainties may be related to the ^{60}Co simulations.

Table 4.6 Induced current in the ionization chamber CRGR10/C5B/UG2 by a proton beam.

	I(pA)		
E_0 (MeV)	PENH	FLUKA	TOPAS
100	45.5 (3)	42.7 (4)	35.1 (3)
150	32.4 (3)	30.3 (4)	25.4 (3)
200	27.1 (3)	25.0 (4)	21.3 (3)
250	24.0 (3)	21.4 (4)	18.8 (3)

Finally, the current induced by a proton beam under the irradiation conditions described above was determined. For this purpose, eq. (4.26) was used. For the calculation, it was assumed that the clinical fluence rate of the radiation field used is 10^{10} protons$/\mathrm{s}\cdot\mathrm{cm}^2$. Figure 4.6 shows the induced current as a function of the initial energy used for the proton

beam. As with the correction factors, there are significant differences in the results. This quantity is derived from the dose deposition, so it is normal to find these differences.

Table 4.6 shows an inverse proportional relationship between the initial beam energy and the induced current in the ionization chamber. This can be explained by considering that the induced current is a quantity derived from the dose deposition, and the dose deposition has this dependence on the initial energy of the proton beam, as discussed above.

Chapter 5

Simulation of *in vivo* dosimeters

As to diseases, make a habit of two
things: to help, or at least to do no harm

Hippocrates of Kos

As have been discussed in previous chapters, dose measurements in clinical practice are usually performed using ionization chambers as a gold standard. However, these devices have some limitations compared to other systems, such as those based on semiconductors: large size, high voltage required for biasing or high price. In addition, semiconductor-based dosimeters can perform measurements in certain situations where ionization chambers could not be used. A clear example of this is *in vivo* dosimetry, that consists in estimating the deposited dose in a patient during a treatment session. In this way, deviations in the dose delivered to the patient respect to the prescribed one due to any reason can be taken into account rescheduling the planning treatment [34, 159].

There are currently two types of *in vivo* dosimeters. The first type is known as point detectors. This type of *in vivo* dosimeters consists of a small device that is placed on the patient's skin and allows to know the dose deposited in that point. Diodes or MOSFETs are placed between the point detectors. These detectors are employed when only a few fields are used during treatment. The other type of *in vivo* dosimeter is the Electronic Portal Imaging Device (EPID). EPIDs allow to measure a map dose of the beam used to irradiate the patient. EPIDs are usually used with new and complex photon techniques such as Intensity Modulated Radiation Therapy (IMRT) or Volumetric Modulated Arc Therapy (VMAT).

However, in this thesis only point detector will be analysed because, in principle, only a few radiation fields are used during a proton therapy treatment. This fact makes point

detectors the perfect candidate for using in this area of radiotherapy. In this chapter, a MC model is introduced to calculate the angular dependence of a commercial photodiode and an extension of it based on a 3D structure. Experimental data acquired using a photon beam are used to validate the MC models. Then, the viability of this type of dosimeters in proton therapy will be analysed to quantify the possible changes introduced in the depth dose deposition. Finally, the MC models will be used to characterise this kind of photodiode for use in proton therapy.

5.1 Characterization of *in vivo* dosimeters for a photon clinical beam

As a first step in the implementation of a method based on MC simulation to characterize the response of the *in vivo* dosimeter, the response of the BPW34S photodiode (Vishay, Malvern, Pennsylvania, USA) and a 3D detector for a photon clinical beam is analysed. The 3D detector, proposed by Ruiz-García [160], consists of a cube with a BPW34S photodiode in each face, connected in parallel, allowing the induced charge to accumulate throughout the device. Theoretically, this configuration should reduce the angular dependence due to its symmetry. These devices have been chosen because there are preliminary experimental data [160] that allow to check and validate the MC scheme used to characterize these types of *in vivo* detectors. In this analysis, the angular dependence of the detectors mentioned above will be studied when the device is irradiated with a 6 MV photon source. On top of that, the available experimental data will be employed to validate the MC scheme used. Furthermore, a practical solution to reduce the angular dependence of the 3D device will be given. Finally, changes in the depth dose profiles due to the positioning of the 3D detector are investigated to ensure that the dose delivered to the patient is not significantly altered by its presence.

5.1.1 Details of the MC simulation

The MC model described in this subsection aims to reproduce the results obtained by Ruiz-García [160]. Regarding the experimental study of angular dependence of the BPW34S photodiode and the 3D detector, the irradiation setup used in the simulation corresponds to the schematic representation in Figure 5.1. An *in vivo* detector is positioned above a water phantom measuring $20 \times 20 \times 5\,\mathrm{cm}^3$. The source is assumed to be in air at a distance of 97.5 cm from the detector's centre. The incidence angle varies as $\alpha = 0^\circ$, 15°, 30°, 45°, 60° and 75°. Photon beams with a field size of $10 \times 10\,\mathrm{cm}^2$ have been considered, corresponding to a

Varian Clinac C-series operating at 6 MV [161].

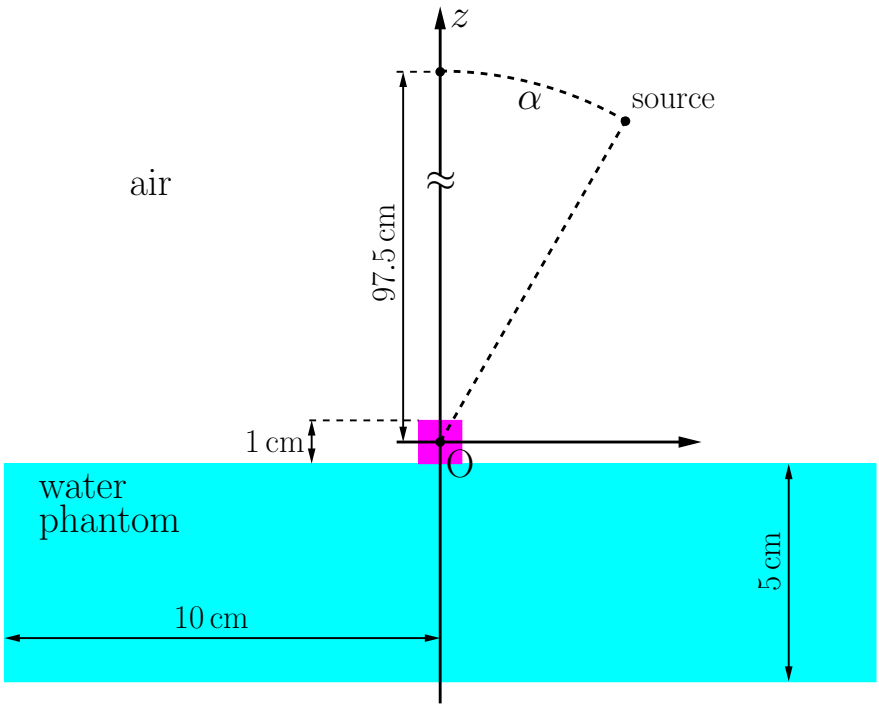

Fig. 5.1 Scheme of the irradiation setup (plane xOz) considered in the simulations. The 3D detector is situated above a water phantom and irradiated with the source at 97.5 cm and a variable incidence of angle α (rotated around the y axis). An irradiation field of 10×10 cm^2 is considered. The origin of coordinates, O, is situated in the centre of the cube and the vertical axis is considered the Oz axis.

The 3D detector is a cube with a side length of 1 cm, composed of polylactic acid (PLA), a common plastic polymer used in 3D printing. A photodiode is embedded at the centre of each face of the PLA cube, defining the planes $a = \pm 0.5$ cm, where $a = x$, y, or z (see Figure 5.2a). These photodiodes are labelled as $\mathrm{d}_{a\pm}$, respectively. Regarding the photodiode, the BPW34S model, manufactured by Vishay Semiconductors, has been modeled based on the available technical specifications [162]. Figure 5.2b illustrates the scheme considered in the simulation geometry. The device consists of a silicon (Si) die measuring $0.3 \times 0.3 \times 0.028$ cm^3 (depicted in green in the figure), with an active region of 0.07 cm^2 in surface area and the same thickness. The Si die is encapsulated in an epoxy cover measuring $0.44 \times 0.39 \times 0.12$ cm^3 (shown in blue in the figure). The materials used in the simulation are listed in Table 5.1. The number of primaries used in each simulation was $1 \cdot 10^{11}$.

The angular dependence of the response of the detector has been analysed using the ratio:

$$\eta(\alpha) = \frac{D(\alpha)}{D(\alpha = 0)}, \tag{5.1}$$

where $D(\alpha)$ is the absorbed dose in the active volume of the photodiode (single or 3D), per photon emitted, for a beam incidence angle α.

Simulations have also been conducted to analyse the angular dependence of the response of a single photodiode. These simulations use the same setup as in Figure 5.1, but with a single photodiode replacing the 3D detector. The photodiode is positioned to coincide with d_{z-}, the one embedded in the bottom face of the cube, in direct contact with the entrance surface of the water phantom. For clarity in referencing the different geometric setups, we designate the configuration including the 3D cube detector (Figure 5.1) as "3Dcube" and the alternative setup using only a single photodiode as "SPhoto".

5.1.2 Validation of the MC model

In Figure 5.3 the simulated results obtained from the study of the angular dependence for the SPhoto and 3Dcube setups are shown, together with the available experimental data. It is clear that a reduction in the angular dependence is obtained with the 3D device. Analysing the data, an angular dependence at 75° of $\sim 35\%$ with respect to normal incidence is obtained for the single photodiode, but only a $\sim 5\%$ is found for the 3D detector. Therefore, the use of the 3D sensor brings a significant improvement in that sense.

On the one hand, the results obtained by the MC simulation reproduce well the tendencies shown by the experimental data. This is important, because in this way MC model can help to predict the angular dependence of this *in vivo* device for other irradiation conditions. Regarding the results obtained with the different MC codes, it is worth to comment that they are statistically compatible.

On the other hand, in Figure 5.3, there is a systematic overestimation of the response calculated with MC simulations. This discrepancy could be due to several factors, the most important of which is probably the geometric simplification used in the simulations. In fact, the simulation setup does not take into account the electrical connections of the dosimeters, whose effect could be relevant through, for example, the induced current in the irradiated wires [163], which is difficult to quantify in MC simulations.

Table 5.1 Composition of different materials considered in the present simulations. For each material it is expressed the elements present, their atomic numbers and weight fractions, the material density, ρ, and the corresponding mean excitation energy, I.

material	Z	weight fraction	ρ (g cm^{-3})	I (eV)
Si	14	1.000	2.33	173
Epoxi			1.180	68.9
H	1	0.071		
C	6	0.741		
O	8	0.188		
Air			$1.205 \cdot 10^{-3}$	85.7
C	6	0.001		
N	7	0.755		
O	8	0.231		
Ar	18	0.013		
PLA			1.320	74.4
H	1	0.056		
C	6	0.500		
O	8	0.444		
ABS			1.040	65.4
H	1	0.081		
C	6	0.853		
N	7	0.066		
Water			1.00	78.0
H	1	0.111		
O	8	0.889		

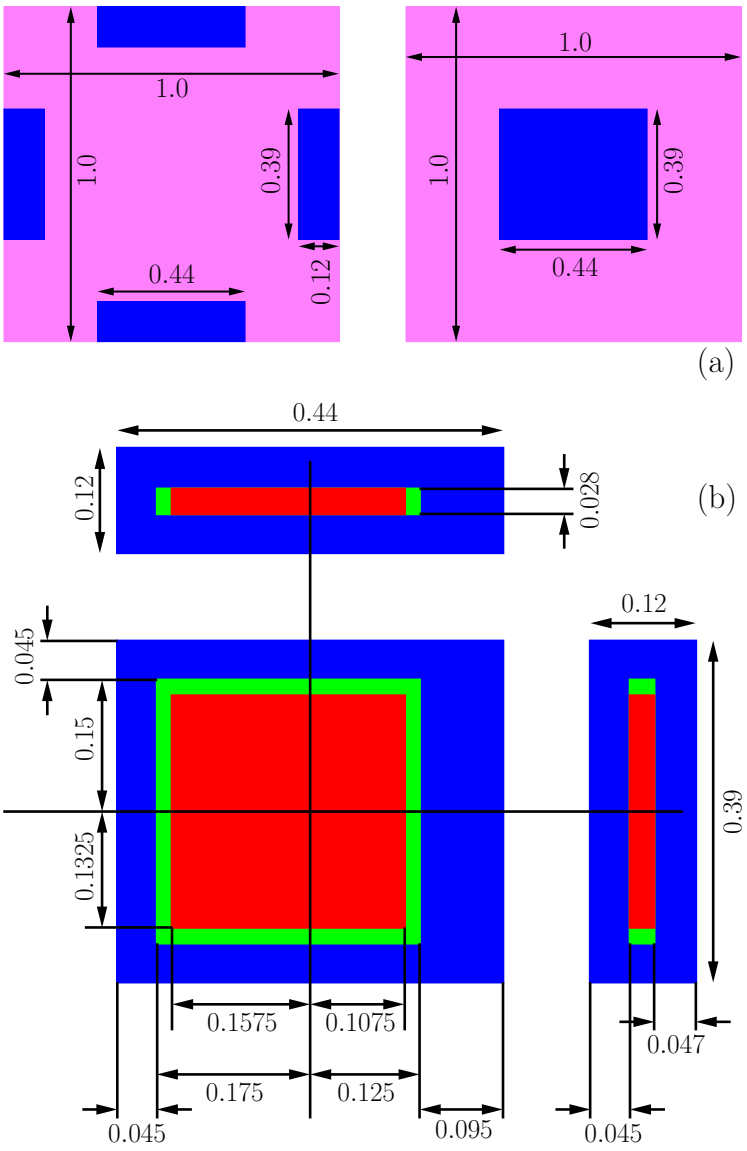

Fig. 5.2 (a) Plane $z = 0$ (left panel) and cube face (right panel) of the 3D cube detector considered in this work. The photodiodes (in blue) are embedded in each of the six faces of a cube made of PLA (in violet). (b) Scheme of the photodiode. It consists of a Si die of $0.3 \times 0.3 \times 0.028\,\mathrm{cm}^3$ (in green), with an active volume of $0.265 \times 0.265 \times 0.028\,\mathrm{cm}^3$ (in red), embedded in an epoxy encapsulation (in blue). Dimensions are given in cm.

If Figure 5.3 is carefully examined, there are larger discrepancies between MC and experimental data for the photodiode ($\sim 10\%$) than for the 3D sensor ($\sim 5\%$) results. This dependence on the studied device could be explained by small uncertainties in the geometry, due to the fact that there is no electronic equilibrium in the position where the *in vivo* dosimeter is placed. In the zone where electronic equilibrium is not reached for photons,

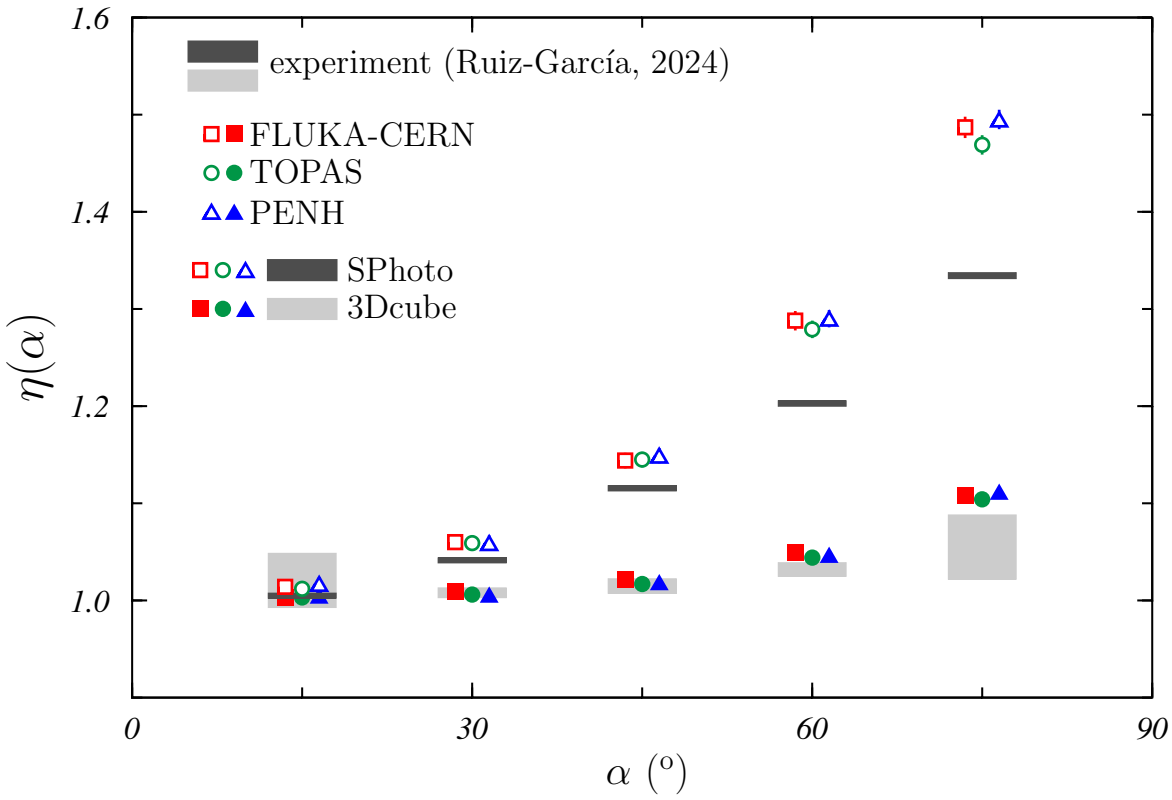

Fig. 5.3 Angular dependence of the response of the single photodiode in the SPhoto setup (open symbols) and of the 3D detector in the 3Dcube setup (solid symbols), in case of the 6 MV beam. The quantity η, as defined in equation (5.1), is shown for the various incidence angles α considered. Squares correspond to the simulations done with the FLUKA, while circles and triangles are those obtained with TOPAS and PENH, respectively. Black and gray bands indicate the uncertainty of the preliminary experimental results of [160] carried out with a single photodiode and the 3D cube, respectively. Uncertainties correspond to a coverage factor $k = 1$.

there is a large change in the dose curve related to these particles (Figure 5.4). For this reason, a small uncertainty in the dimensions of the simulated device can have a large effect on the deposited dose in the active volume of the detector. This effect is less significant for the 3D sensor because the dose accumulation takes place in six different areas instead of just one, as in the case of the photodiode. This effect can explained the differences between the results obtained with MC simulation for the photodiode and the 3D detector.

5.1.3 Reduction of the angular dependence

In the previous section, the limitations of the MC model presented for the characterisation of *in vivo* dosimeters were pointed out. In addition to giving some reasons for the shortcomings of the model, an overestimation in the prediction of the signal of the devices

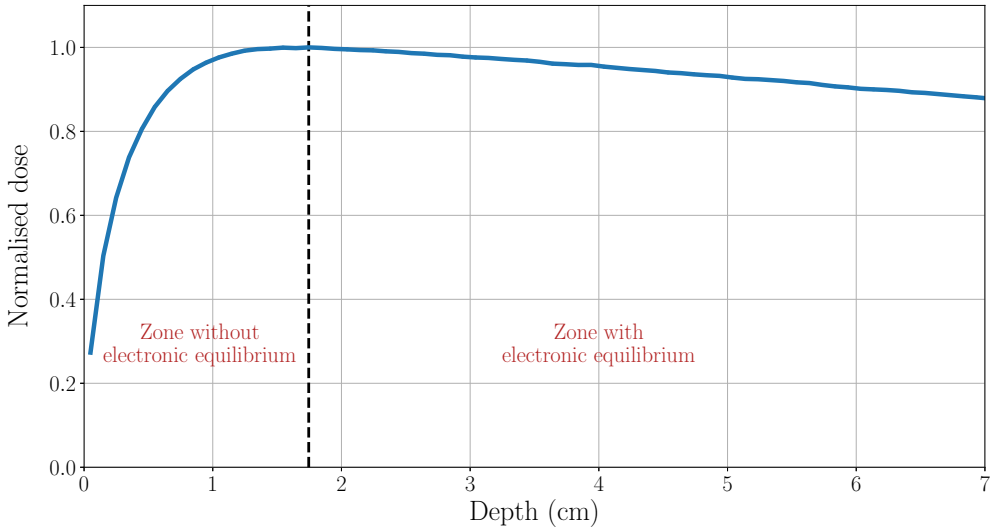

Fig. 5.4 Depth dose deposited in a water phantom by a photon pencil beam with a 6 MV energy spectrum. The vertical dashed line separates the zones with and without electronic equilibrium. The simulation has been done with PENH using 10^8 primary particles.

is noted. In spite of that, it can help to make a reliable prediction if it is taken into account that the model is able to describe the global tendency observed in the experimental data and offers a maximum value for the signal of the devices.

Considering all the things mentioned above, an analysis is carried out to reduce the angular dependence of the 3D dosimeter. On the one hand, in the case where the experimental measurements were made, the 3D dosimeter was in the zone without electronic equilibrium (Figure 5.4). On the other hand, there is a clear relation between the angle of incidence and the distance travelled within the active volume of the dosimeter under consideration. The combination of these two factors produces the angular dependence observed in the detector. In the non-electronic equilibrium zone, there is a high gradient in the deposited dose, so an increase in the distance travelled within the active volume due to a change in the angle of incidence can cause a significant increase in the deposited dose in the dosimeter. This effect can be reduced by encapsulating the detector to allow it to reach the electronic equilibrium zone [164].

In the case under consideration, a cubic encapsulation made of ABS (Acrylonitrile Butadiene Styrene) will be used in the simulation (see composition in Table 5.1). This material have been chosen for the encapsulation because it is a common printer material. It allows to make

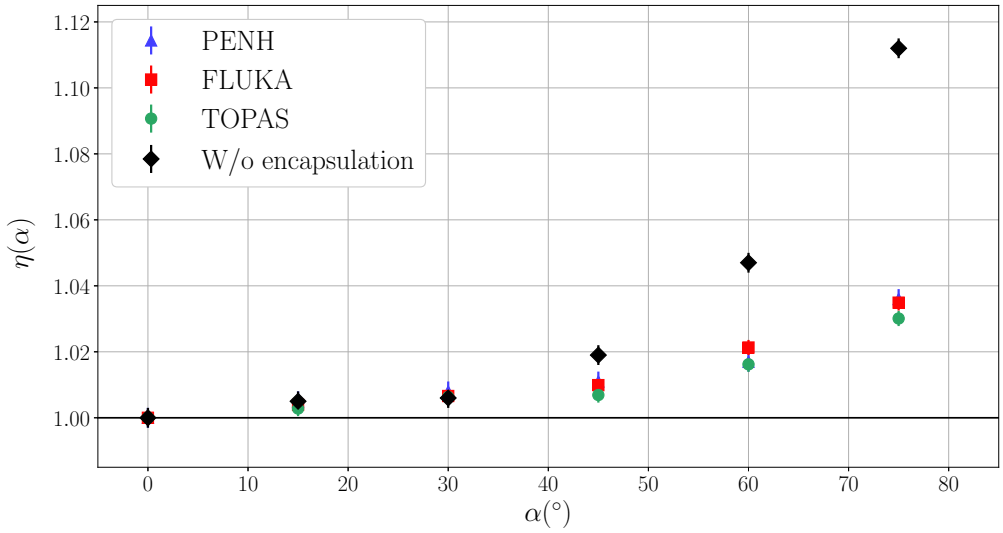

Fig. 5.5 Results obtained with MC model for the angular response of 3D dosimeter when an encapsulation is used. Blue triangles, red squares and green circles represent the results obtained with PENH, FLUKA and TOPAS respectively. The results obtained without encapsulation are sketched using black diamond and they have been calculated with PENH. The unity is highlighted using a black line.

an encapsulation in a easy way to measure its effect in the reduction of angular dependence. The thickness of this encapsulation depends on the energy of the photon spectrum [149, 164], since the non-electronic equilibrium zone is determined by this magnitude. In the simulation performed in this thesis, a value has been taken for the thickness equal to 0.8 cm. This thickness has been chosen because it assures that the electronic equilibrium is reached in the 3D dosimeter. If a spectrum with more energetic photons is employed, alternatives to ABS can be used to reduce the amount of material used in the encapsulation, or the thickness of the ABS can be increased. A contrasted alternative could be brass. Brass was successfully used in the encapsulation of a MOSFET in [164].

Figure 5.5 shows the results obtained when this encapsulation is used to cover the 3D detector. The MC model indicates that there is an important reduction in angular dependence, being less than 4%.

5.1.4 Viability of the 3D dosimeter for a photon clinical beam

To complete the analysis of the 3D cube detector's capabilities, its potential impact on the absorbed dose in the phantom has been examined. This is crucial because, when used as

an *in vivo* device for verifying dosimetry during actual treatment sessions, the detector could alter the prescribed doses.

To assess this impact, the results obtained with the 3Dcube setup at $\alpha = 0$ were compared to those from irradiating the water phantom without the 3D detector. The absorbed dose in the phantom was measured using a voxel grid of $1 \times 1 \times 0.1\,\mathrm{cm}^3$, centered on the beam axis. The same radiation field as in the previous simulations was applied.

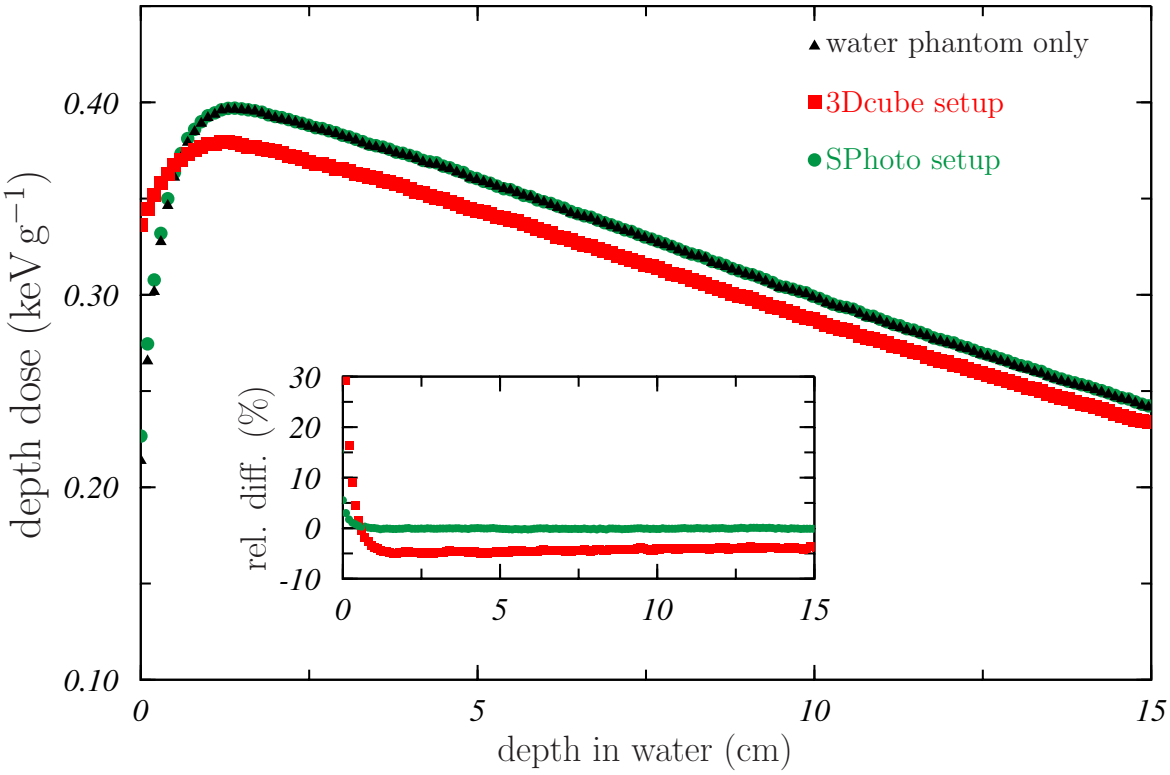

Fig. 5.6 Depth doses in the water phantom obtained using the 6 MV photon beam with PENH. Red solid squares correspond to the simulation performed with the 3Dcube setup. Blue solid triangles have been obtained by including only the water phantom in the simulation geometry. The inset shows the relative differences between both results.

Figure 5.6 shows the comparison for the 6 MV beam. In this case, the simulations have been performed using PENH, although the results obtained with the other two codes are very similar. It can be observed that the presence of the 3D cube detector (red solid squares) modifies the depth dose curve compared to the scenario where the phantom is irradiated directly, without the dosimeter (black solid triangles). This modification is particularly significant in the build-up region, up to a depth of approximately 2 cm. In this region, the presence of the 3D detector increases the dose at the phantom surface by a factor of 3 compared to direct

irradiation. Additionally, a slight reduction in dose is observed beyond this point. This effect would lead to an increase in the absorbed dose in the patient's skin.This must be taken into account when assessing the absorbed dose in the patient skin when this 3D detector is used as an *in vivo* dosimeter.

For depths greater than that at which the maximum dose is reached, i.e. once charged particle equilibrium is reached, the impact of the 3D cube stabilizes. This results in a reduction of the absorbed dose by approximately 5%, a percentage that gradually decreases with increasing depth in water.

If, instead of the 3D cube detector, a single photodiode is used (green solid circles in Figure 5.6), the modification in the absorbed dose is significantly smaller. The absorbed dose at the phantom entrance increases slightly (by less than 4%) compared to the phantom-alone case. Beyond the dose maximum, both depth dose curves overlap.

5.2 Viability of *in vivo* dosimeters in proton therapy

The importance of *in vivo* dosimetry in improving the quality of treatments in traditional radiotherapy is clear. This type of detector helps to verify the dose received by a patient during a session of radiotherapy. However, there is an important lack of information concerning to the possible secondary effects of the *in vivo* detectors in proton therapy. Protons are highly sensitive to irradiation geometries. Consequently, the introduction of any new element can significantly alter how protons deposit their energy in the patient. As a result, the use of *in vivo* devices may substantially impact dose distribution. Therefore, it is crucial to investigate their potential effects on treatments delivered by a proton therapy machine.

In this section, following on from what was done for photons at the end of the previous section, we will carry out an analogous study for protons. MC simulations will be used to determine the effect of *in vivo* dosimeters on the depth-dose curve as a function of energy. The results of these simulations will be used to study possible changes in the dose deposited in the patient.

5.2.1 Details of the Monte Carlo simulation

In order to quantify the changes induced by the use of the *in vivo* dosimeter, two sets of geometries are considered. In the first set of geometries, only a water phantom is considered.

Within this phantom, a scoring grid is defined with a transversal size of 1×1 cm^2. This transverse size corresponds to the detector size (Figure 5.7). In the second set of geometries, in addition to considering the water phantom, a device is included in the geometry (3Dcube or SPhoto setup). This detector is on the phantom surface. In the simulation, the 3D detector is modelled as a $1 \times 1 \times 1$ cm^3 PLA cube, while the single photodiode is represented as a $0.39 \times 0.44 \times 0.12$ cm^3 epoxy parallelepiped. For more details on the materials used, refer to Table 5.1.

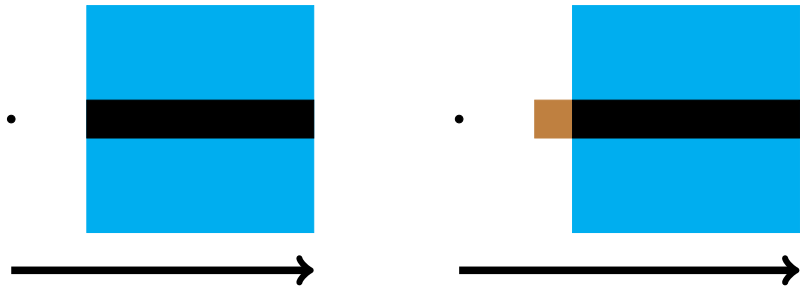

(a) phantom (b) phantom + detector

Fig. 5.7 Basic scheme of the geometry used to calculate the dose deposition in the water phantom for the analysis considered. Figure (a) represents the case where no *in vivo* detector is used, while Figure (b) represents the opposite case. The black point indicates the position of the proton source, the arrow indicates the direction of emission, the black area represents the position of the grid used to evaluate the dose and the brown square illustrates the position of the *in vivo* detector.

The proton source used in this simulation is located 2 cm above the water phantom and the material used between these elements of the geometry is vacuum. Thus, if we find some discrepancies between the dose profiles calculated in the two scenarios, they must be related to the presence of the detector. In these simulations, a wide source with a square field (10×10 cm^2) is considered. From this source, monoenergetic protons will be fired into the phantom with a direction perpendicular to the surface of this target. To study the energy dependence, 60, 100, 150 and 200 MeV are considered as initial energies. On top of that, two SOBPs are included in this analysis. Their characteristics are a full range (d_b) of 10 and 15 cm and a width of 5 cm in both cases.

Regarding the scoring results, since the main objective is to quantify the change in the dose profile, all the curves obtained with the MC simulation are normalised to their maximum value. To obtain these results, 10^6 protons were simulated at each case considered.

5.2.2 Results

First at all, it is important to note that, in general, the results obtained for the SPhoto setup indicates that there is no significant changes in the dose deposition when the single photodiode is used in an *in vivo* application (see Figures 5.8 and 5.9). Only a slight modification in the dose deposition is appreciable for the case of 60 MeV (panel (a) of Figure 5.8).

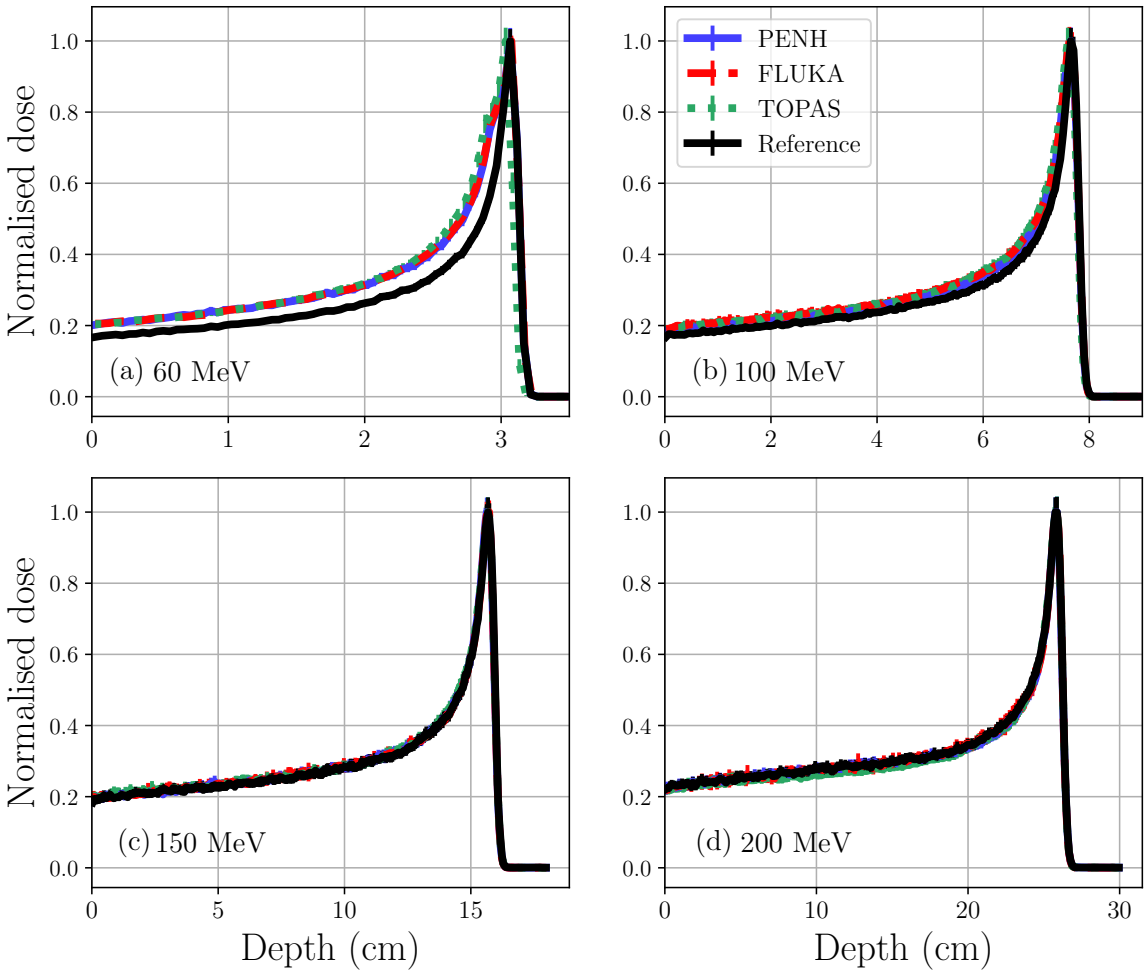

Fig. 5.8 Results obtained from the study of the viability of *in vivo* dosimeters in proton therapy when a proton pencil beam is used as source for the SPhoto setup. Blue, red and green represent the results obtained with PENH, FLUKA and TOPAS respectively when the presence of the dosimeter is taken into account in the simulation. The reference dose curve (without the dosimeter) obtained with PENH is shown in black.

Figures 5.10 and 5.11 show the results obtained with the proposed geometry for the 3DCube setup. For the cases where a proton pencil beam is considered (Figure 5.10), it is important to note the double Bragg peak structure found in the calculated dose profile. The

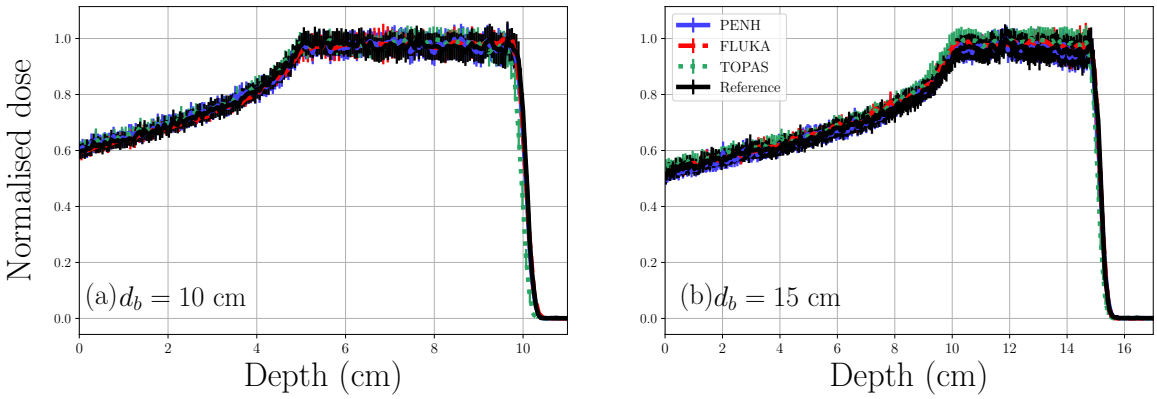

Fig. 5.9 Results obtained from the study of the viability of *in vivo* dosimeters in proton therapy when a SOBP is used as proton source for the SPhoto setup. Blue, red and green represent the results obtained with PENH, FLUKA and TOPAS respectively when the presence of the dosimeter is taken into account in the simulation. The reference dose curve obtained with PENH is shown in black.

first distinguishable Bragg peak (less deep peak) is produced by the interaction between the protons and the detector. As can be seen in Table 5.2, the interaction between the detector and protons produces a reduction in their range. The second Bragg peak shown in Figure 5.10 is due to the use of a wide beam. Due to scattering interactions, protons that do not interact with the *in vivo* device are deflected by scattering interaction in the water and enter the shadow of the detector. These deflected protons do not lose as much energy as the protons that have interacted with the detector. This means that the deflected protons produce a Bragg peak with a larger range than that associated with protons that have interacted with the detector.

In the cases where a SOBP has been considered as a proton energy spectrum source (Figure 5.11), the same effect is found as for proton pencil beams. In Figure 5.11 is shown a displacement in the full range of the SOBP due to the interaction with the *in vivo* detector. Additionally, a small step can be seen at the end of the dose curve. This small step is a consequence of the use of a wide beam related to the dose deposition of protons that do not interact with the *in vivo* device; they are scatter in water and enter in the shadow of the detector.

As have been previously commented, the results have shown that the use of the 3D dosimeter produces a significant change in dose deposition after the devices. On top of that, an energy dependence can be found in these changes. For low energies (Figures 5.10.a and 5.11.a) there is a stronger dependence than for high energies (Figure 5.10.d and 5.11.b). This can be easily explained by the shape of the proton stopping power curve. At high energies, the protons do not interact much with the medium through which they are moving. This

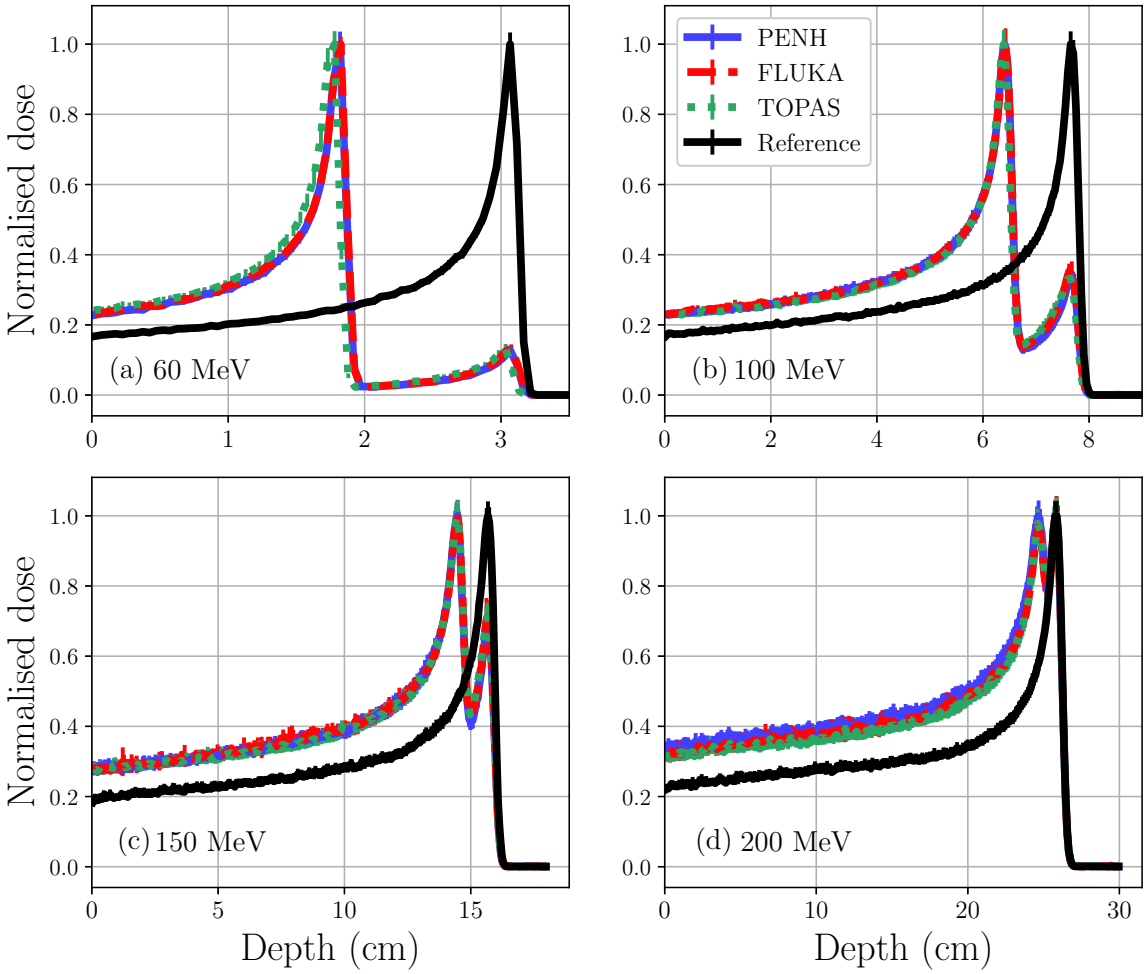

Fig. 5.10 Results obtained from the study of the viability of *in vivo* dosimeters in proton therapy when a proton pencil beam is used as source for the 3DCube setup. Blue, red and green represent the results obtained with PENH, FLUKA and TOPAS respectively when the presence of the dosimeter is taken into account in the simulation. The reference dose curve (without the dosimeter) obtained with PENH is shown in black.

causes a small loss of energy when they interact with the detector, resulting in a small shift in the Bragg peak region. For low energies, on the other hand, the effect is the opposite of that described above.

To summarize, the single photodiode demonstrates superior performance compared to the 3D detector, as it causes a smaller variation in the dose curve. For this reason, the energy and angular studies in the following sections will be conducted for the single photodiode.

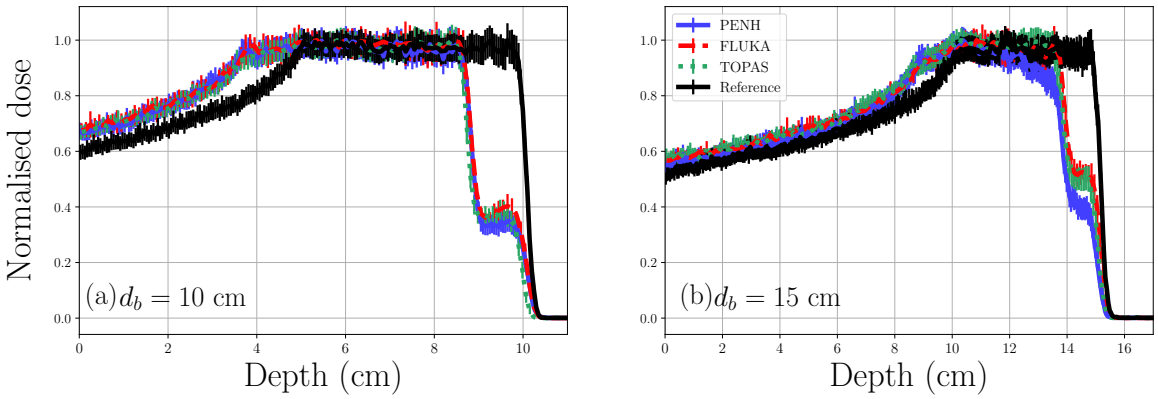

Fig. 5.11 Results obtained from the study of the viability of *in vivo* dosimeters in proton therapy when a SOBP is used as proton source for the 3DCube setup. Blue, red and green represent the results obtained with PENH, FLUKA and TOPAS respectively when the presence of the dosimeter is taken into account in the simulation. The reference dose curve obtained with PENH is shown in black.

Table 5.2 Ranges obtained when considering the shift effect on the dose profile due to the 3D dosimeter. These ranges have been calculated from the depth-dose curve using the eq. (1.12). For this calculation only the first Bragg peak is taken into account. Mean projected range for water (without considering the effect of the 3D dosimeter) have been extracted from [58].

Energy (MeV)	R_{mp} [cm]	R_{PENH} [cm]	R_{FLUKA} [cm]	R_{TOPAS} [cm]
60	3.089	1.840(8)	1.844(5)	1.694(7)
100	7.707	6.506(20)	6.504(20)	6.470(20)
150	15.76	14.63(4)	14.66(4)	14.66(4)
200	25.93	24.7(6)	24.7(6)	24.7(6)

5.2.3 Correction of the dose profiles

As seen in the previous section, the use of 3D detector can introduce changes in the position of the Bragg peak. This can be disastrous for clinical treatment, as any change in the position of the Bragg peak can drastically alter the dose deposited in the patient's tumour region. It is therefore essential to correct for this detector-induced range shift. In spite of the problems found for the 3DCube set up, this type of dosimeters could be used in proton therapy, provided that the dose shift due to interaction with the detector is taken into account, using the method that is explained in this subsection.

Modern proton beam lines allow the energy of the outgoing protons to be modified [3]. Using this type of machine, the initial energy of the clinical beam can be adjusted to interact with the *in vivo* detector. By increasing the initial energy of the protons interacting with the detector, assuming that the technical specifications of the treatment allow it, the range shift

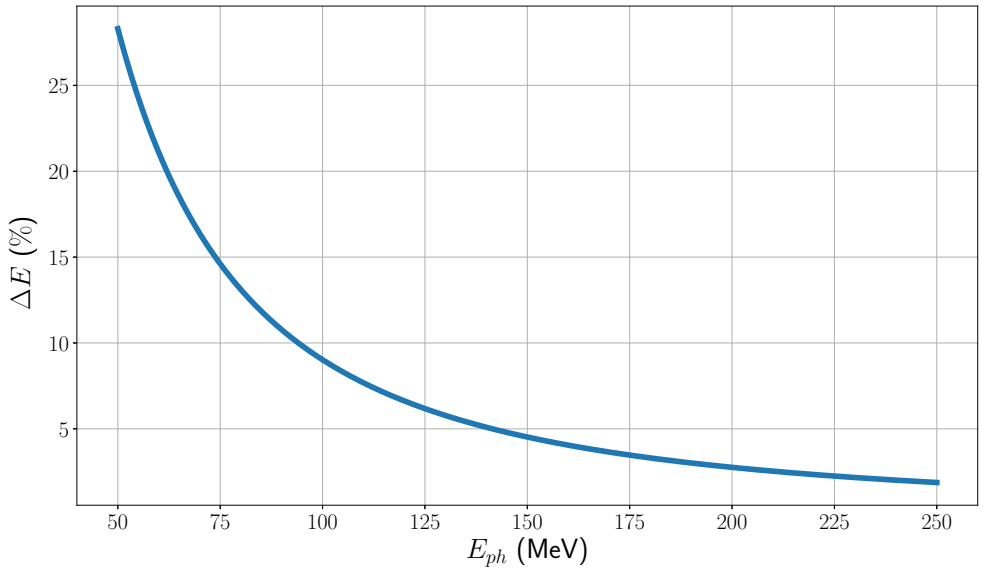

Fig. 5.12 Energy shift due to the interaction between protons and the *in vivo* dosimeter, calculated using the Bragg-Kleeman relation (equation (5.2)).

can be minimised.

To estimate the energy shift required to correct this problem, the interaction between the protons and the detectors can be modelled using the Bragg-Kleeman relation [4, 59] (see section 1.1.4). From this relation, it is obtained that:

$$E_0 = \left(\frac{\alpha E_{\text{ph}}^p + d}{\alpha_{\text{BK}}} \right)^{1/p}, \tag{5.2}$$

where E_0 is the new initial energy of the proton that are going to interact with the detector, E_{ph} is the energy that the proton must have at the entrance of the phantom (60, 100, 150 and 200 MeV), d is the length of the detector and α_{BK} and p are fit parameters of the Bragg-Kleeman relation. For PLA, $\alpha_{\text{BK}} = 2.01 \cdot 10^{-3}$ cm/MeV^p and $p = 1.743$. Due to the lack of information about this material, these parameters have been calculated from a fit to the stopping power data generated by PENH.

Applying the change in energy proposed by equation (5.2), the curve presented in Figure 5.12 is obtained. In addition, the range shift could be corrected if the initial proton energy is changed (Figures 5.13 and 5.14). To check this, the same simulation as before was carried out, but the energy of the protons that interact with the detector was changed using equation

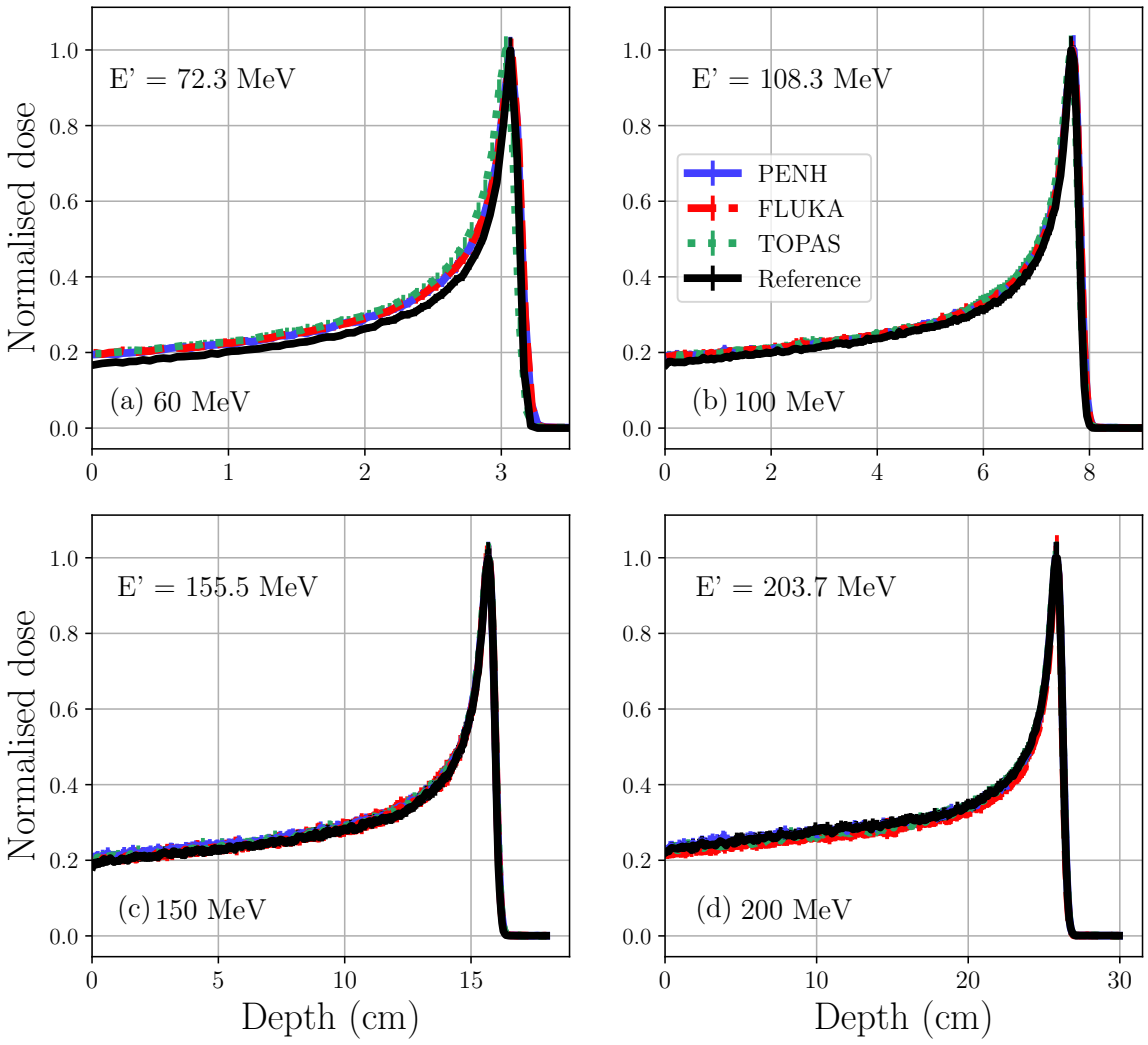

Fig. 5.13 Results obtained from the study of the method used to correct the effect of the *in vivo* dosimeter on the dose deposition when a proton pencil beam is used as source for the 3DCube setup. Blue, red and green represent the results obtained with PENH, FLUKA and TOPAS respectively when the presence of the dosimeter is taken into account in the simulation. The reference dose curve obtained with PENH is shown in black. The energy used to compensate the energy shift due to the 3D detector is denoted as E' in the figure.

(5.2). Taking into account this correction could be possible to use this 3D device as an *in vivo* detector to be used in clinical practice.

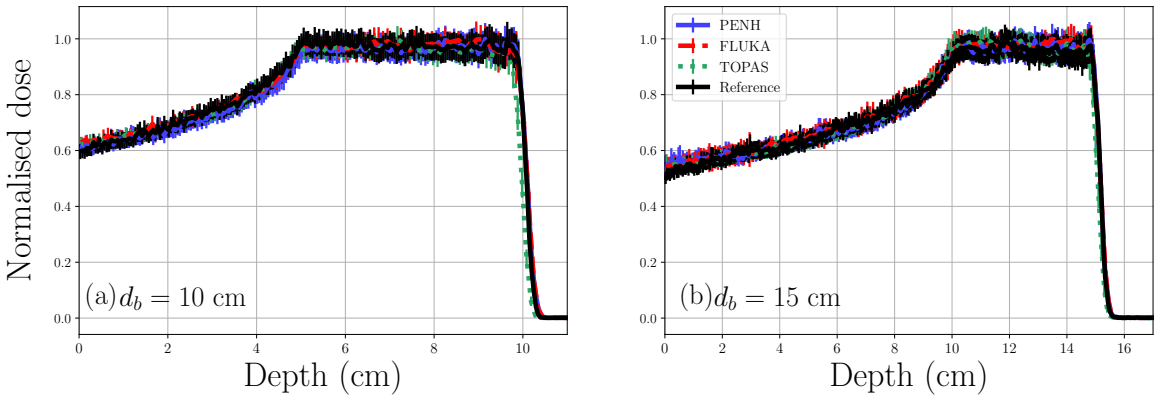

Fig. 5.14 Results obtained from the study of the method used to correct the effect of the *in vivo* dosimeter on the dose deposition when a SOBP is used as proton source for the 3DCube setup. Blue, red and green represent the results obtained with PENH, FLUKA and TOPAS respectively when the presence of the dosimeter is taken into account in the simulation. The reference dose curve obtained with PENH is shown in black.

5.3 Characterization of *in vivo* dosimeters for proton clinical beams

Having studied the model used to characterise the *in vivo* dosimeters in a realistic case and its viability when they are used in proton therapy, it is time to study their angular response. Due to the results obtained in the previous section, we are going to analyse only the case of the single photodiode, because it is not necessary to take into account the energy correction to ensure the correct delivery of the treatment.

As it is known, the dose deposition associated with protons depends on their kinetic energy (see section 1.1). Due to this fact, it is clear that there must be a relation between the energy of the impinging proton and the charge generated in the active volume of the sensor. Moreover, taking into account the geometry of the active volume, it is clear too that there must be a relation between the angle of incidence of the proton and the charge generated in the *in vivo* sensor. This is due to the fact that there is a relation between the angle of incidence and the distance travelled within the active volume of the dosimeter under consideration. Because of the way in which protons interact with matter, a greater distance travelled inside the active volume of the sensor will generate a greater number of charges on the device under study.

After all this, there could be a relation between the response of the *in vivo* dosimeter considered in this work and the two quantities commented above. For this reason, in this

section we will focus on determining how the response of the photodiode varies with the angle of incidence and the initial energy of the impinging proton. To carry out this study, the MC model presented in section 5.1 will be used.

5.3.1 Energy study

To begin the analysis of the response of *in vivo* dosimeters to a proton field, the energy dependence of these devices is studied. To carry out this task, the SPhoto setup was implemented. This choice, as we commented above, is made because the single photodiode demonstrates superior performance compared to the 3D detector, causing a smaller variation in the proton dose curve (see section 5.2). The geometry used in this study consists of a water phantom whose dimensions are $10 \times 10 \times 5$ cm^3. The *in vivo* dosimeter is placed on the proximal face of this water phantom, simulating a real case where the dosimeter is placed on the patient's skin. All these elements are integrated inside an air sphere to take account the scattering effects produced by this material. This simulation geometry corresponds to the case of normal incident ($\alpha = 0°$) sketched in Figure 5.1.

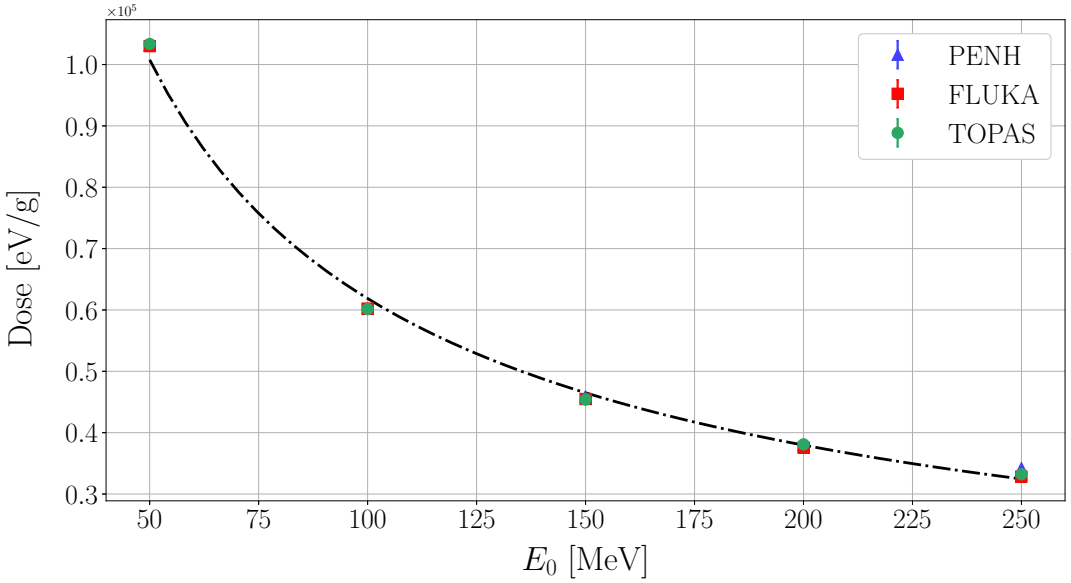

Fig. 5.15 MC data of the energetic dependence of single photodiode for a proton field. Blue, red and green represent the results obtained with PENH, FLUKA and TOPAS respectively. The deposited dose in the active volume of the detector has been considered as reference magnitude to quantify the energetic dependence of the photodiode. A fit to the MC data is sketched in black, showing a good description of the data tendency.

As regards the source used, a wide beam with a square field (10×10 cm^2) is considered. Monoenergetic protons with energies of 50, 100, 150, 200 and 250 MeV have been used to study the energy dependence of the device. Protons impinge with normal incidence with respect to the water phantom surface. The distance between the isocentre and the position of the source used is 97.5 cm. The number of protons produced in each simulation was $1 \cdot 10^9$.

In Figure 5.15, the results obtained from this simple simulation are shown. As can be seen in this plot, a relation of inverse proportionality between the initial energy of the incident proton and the deposited dose in the active volume of the detector is found. Taken the mean value of the MC data obtained from the simulation and fitting to these data a function of the form:

$$D(E_0) = aE_0^b, \tag{5.3}$$

with D the deposited dose in the sensor, E_0 the initial energy of the proton , we can obtained thi fit parameters a and b, that have the values $a = 1582822$ eV/g and $b = -0.704$. The tendency shown in the Figure 5.15 is described properly ($r^2 = 0.9975$).

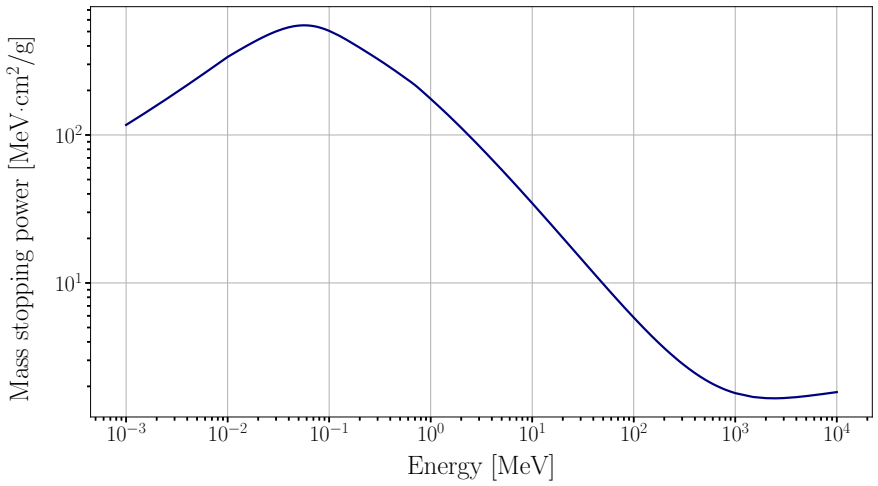

Fig. 5.16 Proton mass stopping power for silicon obtained from the NIST's database PSTAR [58].

This result can be qualitatively explained by using the stopping power. Figure 5.16 shows the total stopping power of silicon. For small energies ($E \sim 50$ MeV), it is clear that the mass stopping power values are larger than for higher energies. Therefore, a proton of low energy will deposit a larger amount of dose than a proton of high energy. This leads to the results shown in Figure 5.15, where is found a greater amount of deposited dose for low energies than for the high energy cases. With this fact in mind, it is not unreasonable to think that the main contribution to the photodiode signal is due to the electromagnetic interaction of

Table 5.3 Dimensions used in the theoretical model for the energetic dependence of the BPW34S photodiode for a proton field [162].

d_1	99.5 cm
d_2	0.082 cm
d_3	0.028 cm

protons with silicon. Under this consideration and imposing that the secondary particles generated by proton are locally absorbed, a simple theoretical model can be proposed.

This theoretical model is sustained in the Bragg-Kleeman's rule [4, 59]:

$$E(z) = \left(\frac{R-z}{\alpha_{\mathrm{BK}}}\right)^{1/p}, \tag{5.4}$$

where E is the energy of the proton for a depth z, R is the range of the proton with an initial energy E_0 and β and p are the parameters of the Bragg-Kleeman's rule. The Bragg-Kleeman's rule allows to calculate the energy the proton has after travelling a distance z.

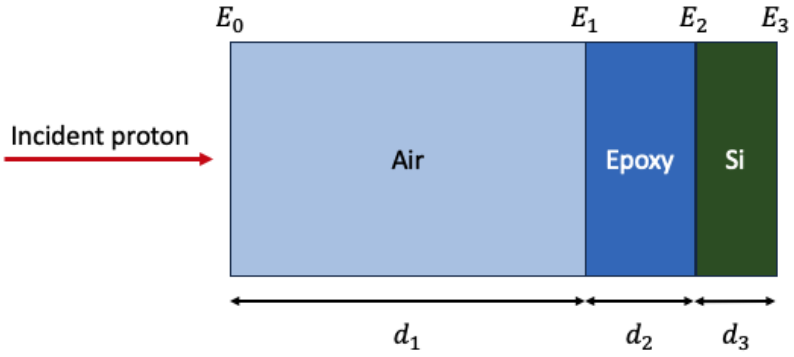

Fig. 5.17 Geometry implemented in the theoretical model used to describe the energy dependence of the single photodiode. The dimension considered in this geometry are specified in Table 5.3.

If a planar geometry is considered (Figure 5.17), the energies of the proton at the entrance (E_2) and exit (E_3) of the silicon die can be calculated using equation (5.4). With this information, the theoretical dose deposited in the silicon die is:

$$D_{\mathrm{th}} = \frac{E_2 - E_3}{m_{\mathrm{AV}}}, \tag{5.5}$$

where m_{AV} is the active volume mass of the silicon die. To obtain a reasonable value for the deposited dose, it is necessary to take into account that only a reduced fraction of the protons in the square field reach the sensor. To normalize the values of dose, the following equation is used:

$$D_{AV} = \frac{S_{AV}}{S_{SF}} D_{th}, \tag{5.6}$$

where D_{AV} is the dose deposited in the active volume of the photodiode, S_{AV} is the transversal surface of the active volume of the single photodiode and S_{SF} is the transverse surface of the square field used as source.

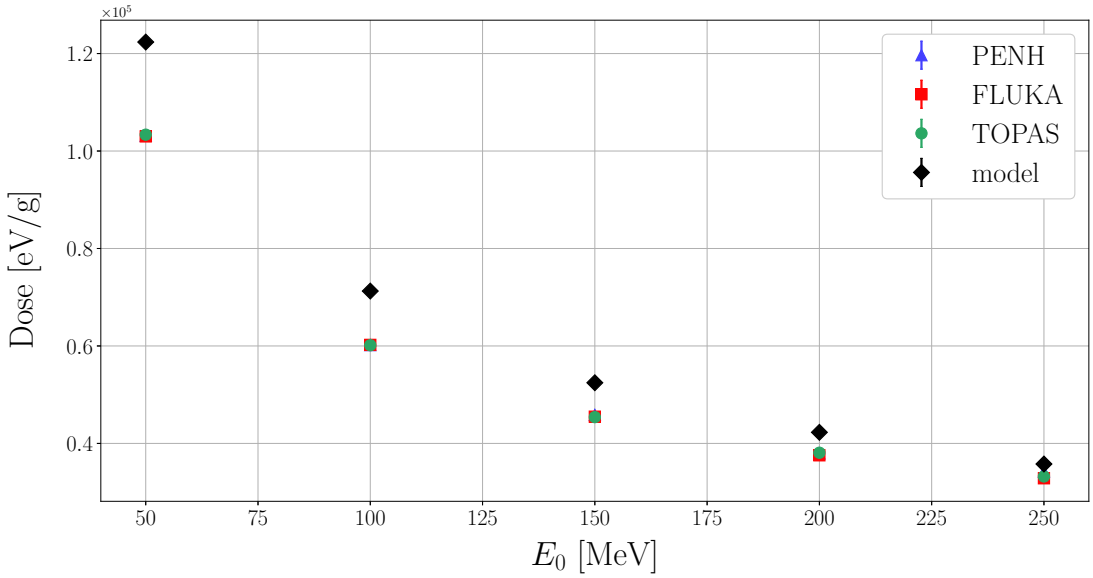

Fig. 5.18 Comparison between the results of the theoretical model and MC data of the energetic dependence of the single photodiode for a proton field. Blue, red and green represent the results obtained with PENH, FLUKA and TOPAS respectively. The deposited dose in the active volume of the detector has been considered as reference magnitude to quantify the energetic dependence of the photodiode. The results of the theoretical model are sketched in black.

In Figure 5.18 we can see that the theoretical model gives close values when it is compared with the MC data. This shows that, as a first approximation, the energetic dependence can be described by taking into account only the electromagnetic interactions of the incident protons and the secondary particles produced by protons are locally absorbed. For high energies the agreement between theoretical and MC data is good. However, at low energies there are significant discrepancies between the results obtained by these two methods. These discrepancies can be explained by using the approximation of local absorption of the

secondary particles. At low energies, a larger number of secondary particles are produced than at high energies, and for both energy regimes the energetic spectrum of these secondary particles is similar. For this reason, it is more likely that secondary particles will escape from the silicon die in the case of low energy protons, as more particles are produced in this case. Therefore, the local absorption approximation at low energies is a poor approximation to reproduce the MC results for the above-mentioned reasons.

5.3.2 Angular study

Finally, an angular dependence study analogous to the one performed for photons will be carried out for protons. In order to analyse the angular dependence, the response of the single photodiode is studied for $\alpha = 0^\circ$, 15°, 30°, 45°, 60° and 75°.

Following the simulation scheme explained in the section 5.1.1, the following geometry has been used in the implemented simulations used to study the angular dependence. It consists of a water phantom whose dimensions are $10 \times 10 \times 5$ cm^3. The single photodiode is placed on this water phantom. The single photodiode has been model as an epoxy encapsulation covering a silicon die. This silicon die has an active surface of 7 mm^2. The dimensions used in the simulations are given in the Figure 5.2b and have been extracted from its datasheet [162]. All these elements are integrated inside an air sphere to take account of the scattering effects of air. The distance between the isocentre and the position of the source used is 97.5 cm, as in the experimental case (Figure 5.1).

Regarding the source, a wide beam with a square field (10×10 cm^2) is considered. In this study the following monoenergetic proton beams has been used: 50, 100, 150, 200 and 250 MeV. The number of protons used in each simulation was $1 \cdot 10^9$.

Finally, to analyse the angular dependence the following magnitude is defined:

$$\eta(\alpha) = \frac{D(\alpha)}{D(\alpha = 0)} \, , \tag{5.7}$$

where $\eta(\alpha)$ is the normalised response of the *in vivo* device under study for an incident angle α obtained with the MC model, $D(\alpha)$ is the deposited dose in the active volume of the silicon die for an incident angle α.

With respect to the results obtained from these simulations, a similar angular dependence has been found in function of the energy. Table 5.4 shows the maximum value of the angular

Table 5.4 Maximum value of the angular dependence, for each energy, averaged for the three MC codes.

Energy (MeV)	$[\eta(\alpha)]_{\max}$
50	1.048 (10)
100	1.029 (9)
150	1.028 (14)
200	1.046 (13)
250	1.051 (13)

dependence for each value of the beam energy considered, averaged for the three MC codes. As can be seen there, there is no a big dependence of this value with the initial energy of the beam. The maximum value found can be bounded by a 5% variation from the normal incidence response. This behaviour is very different to that obtained for a photon beam (see Figure 5.3). This is due to the fact that protons reach the electronic equilibrium in a very small distance, if it is compared to photons. For example, Carvajal *et al.* [164] observed that the build-up region in case of photons is energy dependent.

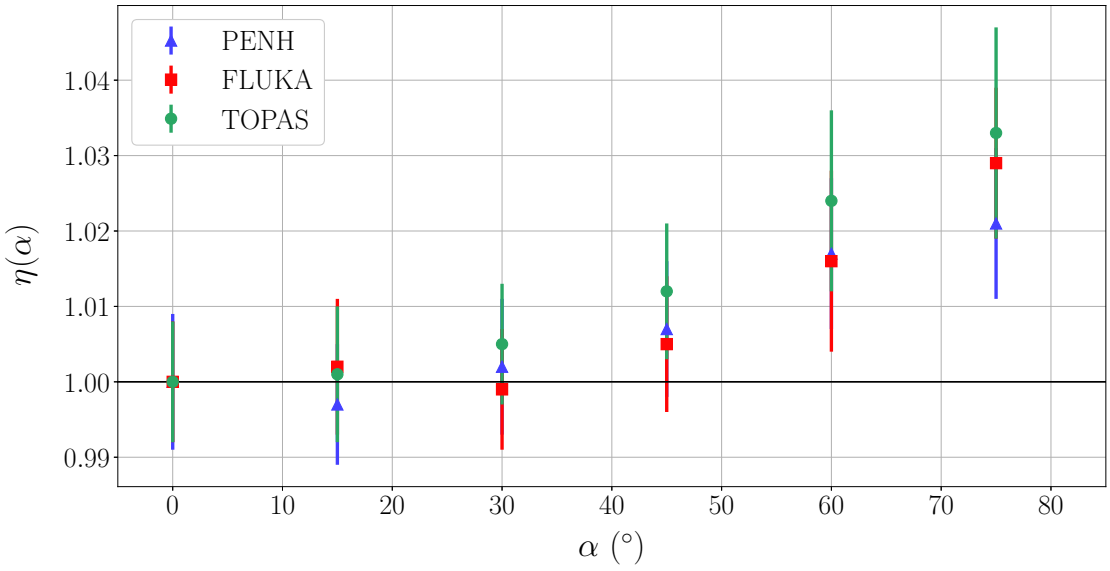

Fig. 5.19 Angular response of the single photodiode for a 150 MeV proton beam. Blue, red and green represent the results obtained with PENH, FLUKA and TOPAS respectively. The unity is highlighted using a black line.

As there are no dependence in the angular response with the initial energy of the proton beam used, the 150 MeV case will be taken as reference to analyse the angular dependence.

Figure 5.19 shows the angular response of the single photodiode for the reference case. As can been see in this figure, the maximum value of the angular dependence is around 1.03 (as it is indicates in Table 5.4). In addition, the response of the photodiode, in general, is compatible with the normal response until a angular value of 30°. For the results obtained with FLUKA, this compatibility is found up to the case of 45°.

Chapter 6

Conclusions and future prospect

Particle therapy, and proton therapy in particular, is opening up a revolutionary new way of treating cancer. The use of proton therapy helps to reduce the dose absorbed by healthy tissue without changing the dose deposited in the tumour. This would be of great benefit to young patients as there would be less chance of secondary tumour development as a result of treatment. Furthermore, this technique makes it possible to treat regions close to radiosensitive organs, such as the case of the prostate. This improvement in sparing healthy tissue is changing the current paradigm in this area of medicine.

Due to the increasing importance of proton therapy, it is necessary to provide a correct description of the deposited dose associated with this type of radiation. For this purpose, it is necessary to have the correct knowledge and tools to predict how the dose will change depending on the situation under consideration. The gold standard used in clinical practice to describe the interaction of protons with matter is the Monte Carlo simulation. This mathematical tool makes it possible to determine several different quantities, such as the dose deposition in a patient, the calibration factor of the dosimetric devices (ionization chambers, photodiode, photoresistance, ...) or its angular dependence. For this reason, the Monte Carlo simulation, properly calibrated, is one of the most powerful tools available to describe the effects and improvements of proton therapy.

In this work, some of the physical models related to proton transport in matter implemented in the general purpose Monte Carlo codes PENH, FLUKA and TOPAS have been validated. For this purpose, a brief review of the theoretical framework used to describe the interactions of the proton with matter is carried out. This is followed by a detailed comparison with the available experimental data. In this validation, on the one hand, the multiple Coulomb scattering algorithms have been checked against the experimental data of

Gottschalk *et al.* [130] and Verbeek *et al.* [131]. On the other hand, a revision of the nuclear reactions (using as experimental reference the data of Gottschalk *et al.* [81] and Paganetti *et al.* [82]) and nuclear elastic scattering (using the dose maps measured by Verbeek *et al.* [74]).

After this validation, the optimal proton tracking parameters for PENH have been determined and those proposed in the scientific bibliography for FLUKA and TOPAS have been revised. In order to find the optimal set of parameters, the Fano test has been implemented, following the indications of Sempau *et al.* [155]. In addition, a novel way of estimating the effect of nuclear reactions using the Fano test has been applied to the Monte Carlo codes considered in this work. Once the optimal tracking parameters for the Monte Carlo codes used have been established, the calibration factor k_{Q,Q_0} and the perturbation factors p_Q have been determined for the CRGR10/C5B/UG2 ionization chamber. This model was chosen due to the availability of this device in our research group for future experimental measurements.

Finally, a Monte Carlo model has been implemented to estimate the response of a *in vivo* dosimeter for proton therapy. The BPW34S photodiode was chosen because of its good response to photon radiation [35]. Furthermore, this Monte Carlo model was tested considering the experimental data for a clinical photon source [160]. After checking the goodness of this Monte Carlo model, the viability of *in vivo* dosimeters for proton therapy has been studied and the characterization of the BPW34S photodiode for energy and angular dependence is carried out.

The main conclusions of this work related to the Monte Carlo codes validation can be summarized as follow:

- The three codes provide a reasonably accurate description of the proton multiple scattering distributions through material slabs. Among them, PENH reproduces most accurately the experimental characteristic angles measured by Gottschalk *et al.* [130] and Verbeek *et al.* [131]. TOPAS gives slightly less accurate results than PENH, while FLUKA shows considerably larger discrepancies. The relative differences observed in these calculations are consistent with those from similar simulations using other code versions. In particular, in TOPAS, the Wentzel multiple scattering model is in better agreement with measurements than the Urban model. Finally, brass stands out as the material least accurately modelled by all three codes. This could probably be due to a lack of information on the characteristic of the alloy considered in the experimental measurements.

- The three codes have a reasonably good implementation of nuclear reactions, as it is shown by comparing experimental data regarding MLFC with simulation results. However, there are small discrepancies between the results obtained with PENH and experimental data. These discrepancies could be related to the transporting of the light product produced in these events.

- A good description of the nuclear elastic scattering interaction has been found for TOPAS, replicating the results obtained by Verbeek *et al.* [74]. However some discrepancies between the experimental and MC data have been obtained for PENH and FLUKA. As far as PENH is concerned, a deficiency has been found in the optical potentials used for the calculation of the effective cross section controlling nuclear elastic scattering on hydrogen. A parametrization for the optical potential given in Cugnon et al. [87] has been used in this thesis to overcome the problem encountered in the validation tests. Using this cross section, a better agreement between experimental and MC results is obtained. Thanks to the results of this work, the problem of nuclear elastic scattering on hydrogen has been solved in the latest version of the code (PENH). In the case of FLUKA, the origin of the discrepancies can be associated with a bad description of the nuclear elastic interaction of protons with oxygen. In the version 4-4.0 of this code, a new model to describe the nuclear elastic interaction in the low energy regime ($E < 250$ MeV) is introduced. Performing the validation test with this new version of FLUKA, a better agreement between experimental and MC results is obtained.

In relation to the characterization of the ionization chambers:

- The Fano test have been implemented in the different Monte Carlo codes used to determine the optimal tracking parameters employed to perform detailed simulation for proton beams with energies up to 250 MeV. First, the optimal tracking parameters for fulfilling the Fano test in the case of PENH have been obtained. It has been found that, while C_1 and C_2 do not play a relevant role, W_{cc} results to be the key parameter: the verification of the Fano test requires a value $W_{cc} = 10$ keV at most. Regarding to TOPAS, it has been found that this code fails to accomplish the test for energies above 100 MeV. These findings deserve a deeper investigation concerning the optimal values of the tracking parameters to be used in these two codes. On the other hand, FLUKA verify the test in all the considered cases.

- The radiation yield was calculated using the Fano test. It is mainly produced by nuclear reactions and account for, at most, a 10% reduction of the absorbed dose in the cavity. This yield increases quadratically with the initial energy of the proton beam.

- The correction factors related to the different elements of the ionization chamber (gas cavity, wall and anode) have been obtained. By analysing their contributions, it has been concluded that the gas cavity is the element that modifies the ionization chamber signal the most.

- The k_{Q,Q_0} factor has been calculated for different energy values used in clinical practice for proton therapy. A similar trend to that of the results shown in the TRS398 CoP [17] for other ionization chamber models has been obtained.

Finally, regarding to the *in vivo* dosimetry in proton therapy, the main results have been the following:

- Monte Carlo simulations performed with TOPAS, FLUKA and PENH are able to reproduce the tendencies found in the experimental data in case of a single photodiode and a 3D device proposed by Ruiz-García [160]. Furthermore, the results obtained with the three codes used for the simulation are statically compatible.

- The change in the dose profile associated with the use of these *in vivo* devices has been analysed by Monte Carlo simulation. Firstly, this study showed that the use of the single photodiode has no relevant effect on the dose deposited in the patient. However, the 3D detector, used as *in vivo* device, has significant effects on the dose deposition behind the detector. This problem could be overcome by using an algorithm to calculate and correct for the energy degradation in the detector by increasing the initial energy of the protons interacting with the device.

- The dependence with the proton energy of the single photodiode response has been studied. On top of that, a theoretical relation has been established between the energy dependence and the stopping power of proton in silicon.

- Finally, a study of the angular dependence of the single photodiode response has been done for 50, 100, 150, 200 and 250 MeV. The maximum variation respect to the normal incident is $\sim 5\%$ ($\theta = 75^\circ$ and $E = 250$ MeV). In addition, the response of the photodiode for a specific incident angle is compatible with the normal response until 30°. This small angular dependence makes the BPW34S photodiode a suitable candidate to be used in proton therapy.

To conclude this section, we would like to highlight the possible lines of investigation that can be followed to continue the work presented here. First at all, it could be interesting to characterize a wide range of ionization chambers used in proton therapy. This could have a significant impact on clinical practice, as these kinds of detectors are the gold standard for

verifying the correct operation of clinical accelerators used in proton therapy.

On top of that, it would be interesting to continue analysing the performance of the BPW34S photodiode, to carry out its experimental characterization and to start the characterization of other dosimetric devices, such as MOSFETs or LDRs, to be used in proton therapy. These actions could help introduce *in vivo* detectors in the field of proton therapy. Apart from that, it is clear that the Monte Carlo codes used and validated in this thesis in the energy range of the proton therapy could be a perfect tool to analyse other problems of interest in this type of technique. For example, they can be used to study neutron contamination in a proton therapy room or material activation in the bunker.

Another interesting research line could be analyzing the performance of the physics models used in PENHAN, the currently available version of PENH, which is an extension of PENELOPE and allows the transport of light hadrons such as protons, neutrons, and alpha particles. In this thesis, we have been able to see the importance of verifying the physics models implemented in Monte Carlo codes to ensure the robustness of the results obtained with these codes. For this reason, it would be important to check the performance of the transport algorithms implemented in PENHAN. On top of that, this code could be used to improve the calculation of the off-axis dose, due to the new modifications introduced in its latest version related to the nuclear elastic collisions, allowing to have a major control in this quantity and how can affect to the radiation-induced second primary tumours.

Following the steps of this thesis, it would be essential to study the optimal tracking parameters in the transport of light hadrons in general-purpose Monte Carlo codes, to ensure their optimal performance. Due to the increasing interest in particle therapy, determining the tracking parameters related to the transport of the particles used in this type of radiotherapy can play a crucial role in order to have reliable results by using the Monte Carlo codes, going further in the development of this type of techniques to be used in the Medical Physics field.

Resumen extenso en español

La terapia de partículas es una de las técnicas más consolidadas en el campo de la radioterapia [1]. Este tipo de terapia utiliza haces de iones para tratar a pacientes con cáncer. Si se utilizan protones como fuente de partículas, este tipo de terapia se conoce como protonterapia. La protonterapia es el método más desarrollado dentro del amplio abanico de técnicas que componen la terapia de partículas.

La idea de utilizar protones como fuente de partículas en radioterapia fue propuesta por Robert R. Wilson en 1946 en el Harvard Cyclotron Laboratory (HCL) [2]. En el artículo en el que Wilson sugirió esta idea, introdujo el concepto de terapia de partículas para el tratamiento de tumores profundos. Señaló el importante papel de los protones debido a su bajo rango de energía para la práctica clínica. En aquella época, los aceleradores compactos eran sólo un sueño y los iones más factibles de conseguir eran los protones.

Por un lado, en dicho artículo, se discuten las ventajas de utilizar protones en lugar de fotones. Se señalan estas ventajas, claramente evidentes en la curva de dosis, y que son consecuencia de la forma en que los protones interactúan con la materia y que dan lugar a que estos tengan un alcance finito dentro de los medios materiales. Estas ventajas, características de dosis, ayudan a reducir la dosis absorbida en el tejido sano sin modificar la dosis depositada en el tumor. Además, la dosis absorbida es practicamente nula más allá de la región donde se deposita la dosis máxima. Esta particularidad se conoce como pico de Bragg. Esto permite al físico médico modelar muy bien la zona irradiada, evitando órganos críticos como, por ejemplo, los pulmones, el nervio óptico o el recto, dependiendo de la zona del cuerpo irradiada.

Por otro lado, Wilson señaló dos problemas relacionados con este tipo de terapia: el *straggling* energético y la gran dispersión de los protones, que producen un ensanchamiento significativo del haz. Sin embargo, estas dos características pueden ser útiles para la práctica clínica. Por un lado, el *straggling* energético puede ayudar con la implementación de un

pico de Bragg extendido (SOBP). Un SOBP es una superposición de haces de protones monoenergéticos [3, 4], pesados correctamente para administrar una dosis constante a lo largo del volumen tumoral del paciente. Por otra parte, el ensanchamiento del haz de protones debido a la dispersión permite irradiar una región tumoral sin utilizar técnicas complejas. Una prueba de ello es el uso de los métodos de dispersión pasiva durante la irradiación con protones [3].

Después de que Wilson propusiera la terapia de protones, el primer experimento que utilizó esta técnica se llevó a cabo con un sincrociclotrón en el Laboratorio Lawrence Berkeley (LBL) a principios de la década de 1950 [5]. En aquel experimento se estudiaron los posibles efectos biológicos que los protones podían producir en ratones. En la actualidad, se ha demostrado que los efectos biológicos de los protones de alta energía son similares a los efectos de los fotones. Sin embargo, se ha encontrado un gran impacto biológico para los protones de baja energía [3, 6]. Esto aumentaría la eficacia de la terapia de protones en comparación con las técnicas tradicionales. No obstante, es importante señalar que la precisión en la terapia de protones es vital si se quiere evitar que una gran cantidad de dosis se deposite en el tejido sano próximo a la zona cancerosa. Debido al elevado gradiente de deposición de dosis en el pico de Bragg, se puede producir un daño importante en el tejido sano, si no se delimita adecuadamente la zona tumoral. La búsqueda de una solución a este problema ha motivado el desarrollo de diferentes técnicas (gamma cámaras [7], PET *in vivo* [8] o resonancia magnética nuclear [9]) para seguir el haz de protones durante la irradiación del paciente y asegurar que la deposición de dosis del tratamiento se hace de la forma más óptima posible.

A pesar de que la terapia de protones es una técnica bien establecida, debe hacer frente a algunos retos, como la verificación del alcance *in vivo* [7, 8, 12] o la reducción de las incertidumbres de las dosis absorbidas en los pacientes [13, 14]. En la terapia con protones, así como en otras formas de radioterapia (por ejemplo, con fotones o electrones), el objetivo principal es administrar la dosis prescrita en la región tumoral. Para lograr este objetivo, la incertidumbre máxima permitida por el Comité Internacional de Unidades Radiológicas (ICRU) es del 5% [15].

Los sistemas de planificación del tratamiento (TPS) se utilizan para diseñar el tratamiento de los pacientes en la práctica clínica. Para ello, los TPS utilizan una amplia gama de algoritmos para simular la interacción entre los protones y la materia. El objetivo principal del TPS es obtener un 3% para las incertidumbres relativas obtenidas en el cálculo de la dosis.

Para conseguir este objetivo, estos algoritmos se calibran con perfiles de dosis medidos en agua y aire para diferentes tipos de haces [16].

Para medir estos perfiles de dosis, los dispositivos más utilizados son las cámaras de ionización. Sin embargo, la señal que producen estos detectores debe corregirse utilizando los factores de corrección k_{Q,Q_0} [17]. Aunque estos factores pueden ser medidos [18–20], es difícil caracterizar estos dispositivos para cada haz de protones empleado en la práctica clínica debido, entre otros problemas, al escaso tiempo que el acelerador de protones está disponible [21, 22]. Por todas las razones mencionadas anteriormente, las simulaciones Monte Carlo pueden ser utilizadas para determinar el factor k_{Q,Q_0}, siendo el el método de referencia para este tipo de cálculos [23–27] para los que se utilizan normalmente algunos códigos Monte Carlo como PENELOPE/PENH [28, 29], TOPAS [30, 31] y FLUKA-CERN [32, 33]. Otra forma de aplicar simulaciones Monte Carlo para mejorar la práctica clínica es la caracterización de detectores para dosimetría *in vivo*. La dosimetría *in vivo* consiste en la estimación directa de la dosis administrada al paciente durante el tratamiento. Su implementación podría ser clave para detectar cualquier problema durante una sesión de irradiación [34]. Existe una amplia gama de detectores utilizados en este campo, por ejemplo, detectores de termoluminiscencia (TLD), transistores de efecto de campo de óxido metálico (MOSFET), diodos, fotodiodos, resistencias dependientes de la luz (LDR) o películas radiocrómicas [34–37].

El desarrollo de las técnicas de Monte Carlo ha hecho posible realizar experimentos *in silico* que habrían requerido un gran esfuerzo para llevarlos a cabo experimentalmente. Además, este tipo de técnicas ha permitido ahorrar una gran cantidad de tiempo de haz. Por todas estas razones, las simulaciones Monte Carlo son una herramienta muy valiosa para la práctica clínica.

A pesar del uso generalizado de la simulación Monte Carlo, es importante señalar que los resultados obtenidos con este tipo de técnicas pueden no ser siempre compatibles con los datos experimentales. Esto es debido a que los resultados Monte Carlo están fuertemente condicionados por los modelos físicos implementados en este tipo de códigos y por cómo se implementan estos modelos en los algoritmos de transporte utilizados para describir como interaccionan las partículas de interés con la materia. Por esta razón, se pueden encontrar algunas discrepancias entre los datos experimentales y los obtenidos con Monte Carlo. Teniendo esto en cuenta, es importante comprobar la validez de los modelos físicos utilizados en los códigos Monte Carlo de propósito general para describir la interacción entre los protones

y la materia. Para lograr este objetivo, se pueden utilizar datos experimentales para validar los resultados obtenidos con las simulaciones Monte Carlo. Esta información podría ayudar a identificar los límites del uso de estas técnicas. Además, el conocimiento de las limitaciones de los códigos Monte Carlo proporciona una gran robustez a los resultados obtenidos con este tipo de simulaciones.

Teniendo en cuenta todo lo dicho previamente, el objetivo principal de esta tesis es utilizar los códigos Monte Carlo PENH, TOPAS y FLUKA-CERN (vía FLAIR [40]) para caracterizar algunos dispositivos dosimétricos pensados para ser utilizados en la terapia de protones. Para lograr este objetivo es esencial comprobar la validez de los modelos físicos implementados en estos códigos Monte Carlo, con el fin de describir correctamente los mecanismos de interacción de los protones con la materia. Para esto se utilizarán algunos datos experimentales encontrados en la literatura científica. A esto le seguirá un análisis de los parámetros de *tracking* que se van a emplear en nuestras simulaciones Monte Carlo. Con todas estas validaciones, podemos garantizar que obtendremos resultados robustos en los análisis posteriores que llevaremos a cabo.

En los dos primeros capítulos se revisan los fundamentos teóricos de la interacción de los protones con la materia, describiendo los tipos de procesos de interacción que estos sufren con la materia. Se describen también de forma detallada los formalismos teóricos que nos permiten cuantificar los mecanismos de pérdida de energía y dispersión de los protones a su paso por un medio material dado. Además, se hace una breve descripción de los conceptos básicos asociados a los códigos de simulación Monte Carlo. Se explican los tipos de códigos que existen en función de los algoritmos de *tracking*. También se hace una descripción de la implementación de los modelos físicos que se utilizan en los diferentes códigos que se han considerado en esta tesis.

En el tercer capítulo, se ofrece un análisis de los algoritmos de *scattering* múltiple de Coulomb, usando los datos experimentales obtenidos por Gottschalk *et al.* [130] y Verbeek *et al.* [131], comparando el resultado para los distintos códigos Monte Carlo considerados. Estos tipos de algoritmos tienen un papel importante para simular adecuadamente la deposición de energía en la simulación Monte Carlo. Además, se comprueban los modelos físicos utilizados para describir las interacciones nucleares elásticas (usando los mapas de dosis obtenidos por Verbeek *et al.* [74]) y las reacciones nucleares (analizando los resultados obtenidos con las Multilayer Faraday Cups (MLFC) por Gottschalk *et al.* [81] y Paganetti *et al.* [82]). Estas interacciones son fundamentales para calcular la dosis fuera del eje en

un tratamiento de protonterapia y es esencial comprobar su funcionamiento para validar los resultados de los códigos Monte Carlo cuando se realiza un análisis de la dosis depositada en tejido sano.

De la validación de los modelos de física implementados en los distintos códigos Monte Carlo contemplados, se ha llegado a la conclusión de que los modelos de *scattering* múltiple de Coulomb y los mecanismos que describen las reacciones nucleares están correctamente descritos en los tres códigos de simulación estudiados. En lo que respecta al *scattering* múltiple de Coulomb, PENH es el código que reproduce con mayor precisión los ángulos característicos experimentales medidos por Gottschalk *et al.* y Verbeek *et al.*. TOPAS ofrece resultados ligeramente menos precisos que PENH, mientras que FLUKA muestra discrepancias considerablemente mayores. En lo referente a las reacciones nucleares, los tres códigos logran reproducir bien la señal de la MLFC que se relaciona con este tipo de interacciones medida por Gottschalk *et al.*. En cambio, para la señal de la MLFC dada por Paganetti *et al.*, existen discrepancias entre los resultados obtenidos con PENH y el experimento. Estas diferencias pueden estar vinculadas a la forma que este código hace el transporte de los iones pesados producidos en las reacciones nucleares. Para FLUKA y TOPAS, la señal de esta segunda MLFC se reproduce sin problemas.

Por otra parte, se han encontrado algunos problemas en la descripción del *scattering* elástico nuclear en los modelos implementados en PENH y FLUKA. En lo que respecta a PENH, se ha encontrado una deficiencia en los potenciales ópticos usados para el cálculo de la sección eficaz que controla el *scattering* elástico nuclear en el hidrógeno. En esta tesis se ha usado una parametrización de dicha sección eficaz dada en Cugnon *et al.* [87] que subsana el problema encontrado en la validación con los datos experiemntales. En el caso de FLUKA, el origen de las discrepancias puede estar asociado a una mala descripción de la interacción elástica nuclear de los protones con el oxígeno. En la versión 4-4.0 de este código, se introduce un nuevo modelo para describir la interacción elástica nuclear en el régimen de baja energía ($E < 250$ MeV). Realizando la prueba de validación con esta nueva versión de FLUKA, se obtiene una mejor concordancia entre los resultados experimentales y los obtenidos en las simulaciones Monte Carlo.

En el cuarto capítulo, se lleva a cabo la caracterización de las cámaras de ionización mediante simulación Monte Carlo. Para ello, se realiza un estudio de los parámetros de *tracking*. Para optimizar los parámetros de transporte utilizados en las simulaciones, se ha empleado el test de Fano con el fin de analizar el desempeño de los códigos Monte Carlo

considerados. En lo referente a los resultados obtenidos con este test, en primer lugar, se han obtenido los parámetros de *tracking* óptimos para el caso del PENH. Se ha encontrado que, mientras que C_1 y C_2 no juegan un papel relevante, W_{cc} resulta ser el parámetro clave: la verificación del test de Fano requiere un valor $W_{cc} = 10$ keV como máximo. En cuanto a TOPAS, se ha visto que este código no logra pasar el test para energías superiores a 100 MeV. Estos resultados merecen una investigación más profunda sobre los valores óptimos de los parámetros de seguimiento a utilizar en este código. Además, no se encontraron diferencias significativas entre los parámetros de *tracking* propuestos por Wulff *et al.* [23] y los que usa el código por defecto. Por otro lado, FLUKA pasa el test en todos los casos considerados. Además, se ha calculado también el *radiation yield* usando el test de Fano. Se produce principalmente por reacciones nucleares y representa como máximo, una reducción del 10% de la dosis absorbida en la cavidad. Este valor aumenta cuadráticamente con la energía inicial del haz de protones.

Tras la determinación del set de parámetros óptimos en cada código, se revisa el formalismo de calibración y se aplica a un modelo simplificado. Los resultados obtenidos con este modelo simplificado nos ayudarán a comprender cómo afectan las distintas partes de la cámara de ionización al factor de corrección. De este estudio se determina que el elemento que más influye en la señal de la cámara de ionización es el volumen de gas. Por último, se caracteriza una cámara de ionización mediante Monte Carlo para protonterapia, obteniendo resultados en la línea de los publicados en el código de prácticas TRS398 [17] para otros modelos de cámaras de ionización.

En el quinto capítulo, se hace una breve introducción a la dosimetría *in vivo*, centrándose en el estudio de los fotodiodos. Se implementa la geometría de un tipo particular de fotodiodo (en versiones 1D y 3D) y se analiza su respuesta a un haz de fotones, como prueba de concepto para la caracterización de este tipo de dispositivos. Esto es debido a que, en la bibliografía científica, existen datos experimentales que pueden ser comparados con los resultados obtenidos en las simulaciones Monte Carlo realizadas en esta tesis. De esta comparación se ha obtenido que TOPAS, FLUKA y PENH son capaces de reproducir las tendencias encontradas en los datos experimentales medidos por Ruiz-García [160]. Además, los resultados obtenidos con los tres códigos utilizados para la simulación son estadísticamente compatibles entre sí.

Posteriormente, se realiza un estudio de la viabilidad de este tipo de detectores para dosimetria *in vivo* en protonterapia. Se encontraron cambios significativos en la deposición

de dosis en el maniquí de agua usado para dosimetría debido al uso del detector *in vivo*, en particular, para la versión 3D del dispositivo. Debido a los pequeños cambios en las deposición que produce el dispositivo 1D, este detector se convierte en un sólido candidato para su uso en la dosimetría *in vivo* aplicada a protonterapia. Aparte, se propone una solución a este problema utilizando un algoritmo para calcular y corregir la degradación de la energía del haz que produce el detector *in vivo*. En definitiva, para corregir el efecto del detector basta con aumentar la energía inicial de los protones que interactúan con el detector.

Además, se ha caracterizado la dependencia energética y angular para el caso del fotodiodo sencillo, en su versión 1D, que es el mejor candidato a dosimetría *in vivo* por las razones explicadas anteriormente. Para el caso de la dependencia energética, se ha establecido una relación entre el *stopping power* del Si y la energía depositada en el volumen sensible del sensor. En lo que concierne a la dependencia angular, se ha determinado que la variación máxima respecto a la incidencia normal es $\sim 5\%$ ($\theta = 75^\circ$ y $E = 250\,\mathrm{MeV}$). Por último, cabe destacar que la respuesta del fotodiodo es compatible con la respuesta para incidencia normal hasta un valor para el ángulo de incidencia de alrededor de 30°. La pequeña dependencia angular encontrada hace del fotodiodo analizado un candidato adecuado para implementar su uso como dosímetro *in vivo* en protonterapia.

References

[1] C. Grau, M. Durante, D. Georg, J. A. Langendijk, and D. C. Weber. Particle therapy in Europe. *Mol. Oncol.*, 14(7):1492, 2020.

[2] R. R. Wilson. Radiological use of fast proton. *Radiology*, 47(5):487, 1946.

[3] H. Paganetti. *Proton therapy physics*. CRC-Press, 2011.

[4] T. Bortfeld and W. Schlegel. An analytical approximation of depth-dose distributions for therapeutic proton beams. *Phys. Med. Biol.*, 41(8):1331, 1996.

[5] C. A. Tobias, H. O. Anger, and J. H. Lawrence. Radiological use of high energy deuterons and alpha particles. *Am. J. Roentgenol. Radium. Ther. Nucl. Med.*, 67:1, 1952.

[6] J. A. Schuff, L. Policastro, H. Durán, A. J. Kreiner, A. Mazal, B. L. Molinari, A. Burlón, M. E. Debray, J. M. Kesque, H. Somakal, and *et al.* Relative biological effectiveness measurements of low energy proton and lithium beams on tumor cells. *Nucl. Instrum. Meth. in Phys. Res. B*, 187(3):345, 2002.

[7] F. Hueso-González, M. Rabe, T. A. Ruggieri, T. Bortfeld, and J. M. Verburg. A full-scale clinical prototype for proton range verification using prompt gamma-ray spectroscopy. *Phys. Med. Biol.*, 63(18):185019, 2018.

[8] M. Moteabbed, S. España, and H. Paganetti. Monte Carlo patient study on the comparison of prompt gamma and PET imaging for range verification in proton therapy. *Phys. Med. Biol.*, 56(4):1063, 2011.

[9] J. J. W. Lagendijk, B. W. Raaymakers, C. A. T. Van der Berg, M. A. Moerland, M. E. Philippens, and M. van Vulpen. MR guidance in radiotherapy. *Phys. Med. Biol.*, 59(21):R349, 2014.

[10] J. H. Lawrence. Proton irradiation of the pituitary. *Cancer*, 10(4):795, 1957.

[11] Particle Therapy Co-Operative Group (PTCOG) website, January 2025. [online] http://www.ptcog.site.

[12] J. M. Verburg and J. Seco. Proton range verification through prompt gamma-ray spectroscopy. *Phys. Med. Biol.*, 59(23):7089, 2014.

[13] J. Schuemann, S. Dowdell, C. Grassberger, C. H. Min, and H. Paganetti. Site-specific range uncertainties caused by dose calculation algorithms for proton therapy. *Phys. Med. Biol.*, 59(15):4007, 2014.

[14] C. D. Vestergaard, L. P. Muren, U. V. Elstrøm, J. G. Johansen, and V. T. Taasti. Tissue-specific range uncertainty estimation in proton therapy. *Phys. Imaging Radiat. Oncol.*, 26:100441, 2023.

[15] A. Wambersie. ICRU Report 62, "Prescribing, recording and reporting photon beam therapy (supplement to ICRU Report 50)". *ICRU News*, 1999.

[16] C. Bäumer, B. Koska, J. Lambert, B. Timmermann, T. Mertens, and P. T. Talla. Evaluation of detector for acquisition of pristine depth-dose curves in pencil beam scanning. *J. Appl. Clin. Med. Phys.*, 16(6):151, 2015.

[17] P. Andreo, D. T. Burns, K. Hohlfeld, M. Huq, T. Kanai, F. Laitano, V. Smyth, and S. Vynckier. *Absorbed Dose Determination in External Beam Radiotherapy*. Number 398 in Technical Reports Series. INTERNATIONAL ATOMIC ENERGY AGENCY, Vienna, 2001.

[18] J. Medin, C. K. Ross, N. V. Klassen, H. Palmans, E. Grusell, and J. Grindborg. Experimental determination of beam quality factor, k_Q, for two types of Farmer chamber in a 10 MV photon and a 175 MeV proton beam. *Phys. Med. Biol.*, 51(6):1503, 2006.

[19] J. Medin. Implementation of water calorimetry in a 180 MeV scanned pulse proton beam including an experimental determination of k_Q for a Farmer chamber. *Phys. Med. Biol.*, 55(12):3287, 2010.

[20] S. M. Vatnitsky, J. V. Siebers, and D. W. Miller. k_Q factor for ionization chamber dosimetry in clinical proton beams. *Med. Phys.*, 23(1):25, 1996.

[21] C. Gòma, B. Hofstetter-Boillat, S. Safai, and S. Vörös. Experimental validation of beam quality correction factors for proton beams. *Phys. Med. Biol.*, 60(8):3207, 2015.

[22] S. Gagnebin, D. Twerenbold, E. Pedroni, D. Meer, S. Zenklusen, and C. Bula. Experimental determination of the absorbed dose to water in scanned proton beam using a water calorimeter and a ionization chamber. *Nucl. Instrum. Meth. in Phys. Res. B*, 268(5):524, 2010.

[23] J. Wulff, K. S. Baumann, N. Verbeek, C. Bäumer, B. Timmermann, and K. Zink. TOPAS/Geant4 configuration for ionization chamber calculations in proton beams. *Phys. Med. Biol.*, 63(11):115013, 2018.

[24] A. Lourenço, H. Bouchard, S. Galer, G. Royle, and H. Palmans. The influence of nuclear interaction of ionization chamber perturbation factors in proton beams: FLUKA simulations supported by a Fano test. *Med. Phys.*, 46(2):885, 2019.

[25] C. Gòma and E. Sterpin. Monte Carlo calculation of beam quality correction factors in proton beam using PENH. *Phys. Med. Biol.*, 64(18):185009, 2019.

[26] K. S. Baumann, S. Kaupa, C. Bach, R. Engenhart-Cabillic, and K. Zink. Monte Carlo calculation of beam quality correction factor in proton beams using TOPAS/GEANT4. *Phys. Med. Biol.*, 65(5):055015, 2020.

[27] J. Kretschmer, A. Dulkys, L. Brodbek, T.S. Stelljes, H.K. Looe, and B. Poppe. Monte Carlo simulated beam quality and perturbation correction factors for ionization chambers in monoenergetic proton beams. *Med. Phys.*, 47(11):5890, 2020.

[28] F Salvat, J Fernández-Varea, and J Sempau. PENELOPE 2018: A code system for Monte Carlo simulation of electron and photon transport. Barcelona, Spain, 2019. Nuclear Energy Agency.

[29] F. Salvat and J.M. Quesada. Collisions of Nucleons with Atoms: Calculated Cross Sections and Monte Carlo Simulation. *Frontiers in Physics*, 9:733949, 2021.

[30] J. Perl, J. Shin, J. Schümann, B. Faddegon, and H. Paganetti. TOPAS: an innovative proton Monte Carlo platform for research and clinical application. *Med. Phys*, 39(11):6818, 2012.

[31] B. Faddegon, J. Ramos-Méndez, J. Schümann, A. McNamara, J Shin, J. Perl, and H. Paganetti. The TOPAS tool for particle simulation, a Monte Carlo simulation tool for physics, biology and clinical research. *Physica Medica*, 72:114, 2020.

[32] G. Battistoni, T. Boehlen, F. Cerutti, P. W. Chin, L. S. Esposito, A. Fassò, A. Ferrari, A. Lechner, A. Empl, A. Mairani, and *et al.* Overview of the FLUKA code. *Annals of Nuclear Energy*, 82:10, 2015.

[33] C. Ahdida, D. Bozzato, D. Calzolari, F. Cerutti, N. Charitonidis, A. Cimmino, A. Coronetti, G. L. D'Alessandro, A. Donadon-Servelle, L.S. Esposito, and *et al.* New Capabilities of the FLUKA Multi-Purpose Code. *Frontiers in Physics*, 9:788253, 2022.

[34] B. Mijnheer. State of the art of *in vivo* dosimetry. *Radiat. Prot. Dosimetry.*, 131(1):117, 2008.

[35] I. Ruiz-García, J. Román-Raya, J. Banqueri, A. J. Palma, D. Guirado, and M. A. Carvajal. Commercial photodiodes and phototransistor as dosimeters of photon beams for radiotherpy. *Med. Phys*, 48(9):5440, 2021.

[36] J. Román-Raya, I. Ruiz-García, P. Escobedo, A. J. Palma, D. Guirado, and M. A. Carvajal. Ligth-Dependent Resistors as Dosimetric Sensors in Radiotherapy. *Sensors*, 20(6):1568, 2020.

[37] P. Casolaro, L. Campajola, G. Breglio, S. Buontempo, M. Consales, A. Cusano, A. Cutolo, F. Di Capua, and F. Fienga. Real-time dosimetry with radiochromic films. *Sci. Rep.*, 9(1):5307, 2019.

[38] M. Vilches, S. García-Parja, R. Guerrero, M. Anguiano, and A. M. Lallena. Monte Carlo simulation of the electron transport through thin slabs: A comparative study of PENELOPE, GEANT3, GEANT4, EGSNCR and MCNPX. *Nucl. Instrum. Meth. in Phys. Res. B*, 254(2):219, 2007.

[39] L. A. Kulchitsky and G. D. Latyshev. The Multiple Scattering of Fast Electrons. *Phys. Rev.*, 61:254, 1942.

[40] V. Vlachoudis. FLAIR: A Powerful But User Friendly Graphical Interface For FLUKA. In *Proc. Int. on Mathematics, Computational Methods & Reactors Physics*, Saratoga Springs, New York, 2009.

[41] B. Gottschalk, E. W. Cascio, J. Daartz, and M. S. Wagner. On the nuclear halo of a proton pencil beam stopping in water. *Phys. Med. Biol.*, 60(14):5627, 2015.

[42] D. Schardt. Five Years Tumor Therapy with Heavy Ions at GSI Darmstadt. In A. Méndez-Vilas, editor, *Recent Advances in Multidisciplinary Applied Physics*, page 253. Elsevier Science Ltd, Oxford, 2005.

[43] P. Andreo, D. T. Burns, A. E. Nahum, J. Seuntjens, and F. H. Attix. *Fundamentals of Ionizing Radiation Dosimetry*. Wiley-VCH, 2017.

[44] H. A. Bethe. Zur Theorie des Durchgangs schneller Korpuskularstrahlen durch Materie. *Ann. Phys.*, 397(3):325, 1930.

[45] W. D. Newhauser and R. Zhang. The physics of proton therapy. *Phys. Med. Biol.*, 60:R155, 2015.

[46] H. Nikjoo, S. Uehara, and D. Emfietzogl. *Interaction of radiation with matter*. CRC Press, 2012.

[47] F. Salvat. Bethe stopping-power formula and its corrections. *Phys. Rev. A*, 106:032809, 2022.

[48] L. H. Andersen, P. Hvelplund, H. Knudsen, S. P. Møller, J. O. P. Pedersen, Uggerhøj, K. Elsener, and E. Morenzoni. Measurement of the Z_1^3 Contribution to the Stopping Power Using MeV Protons and Antiprotons: The Barkas Effect. *Phys. Rev. Lett.*, 62(15):1731, 1989.

[49] M. J. Berger, M. Inokuti, H. H. Anderson, H. Bischsel, J. A. Denis, D. Powers, S. M. Seltzer, and J. E. Turner. ICRU Report 37, "Stopping Powers for Electron and Positrons". *Reports of the International Commission on Radiation Units and Measurements*, 1984.

[50] M. J. Berger, M. Inokuti, H. H. Andersen, H. Bichsel, D. Powers, S. M. Seltzer, D. Thwaites, and D. E. Watt. ICRU Report 49, Stopping Powers for Protons and Alpha Particles. *Reports of the International Commission on Radiation Units and Measurements*, 1993.

[51] U. Fano. Penetration of protons, alpha particles and mesons. *Annu. Rev. Nucl. Part. Sci.*, 13:1, 1963.

[52] S. M. Seltzer and M. J. Berger. Evaluation of the collision stopping power of elements and compounds for electrons and positrons. *Int. J. Appl. Radiat. Isot.*, 33(11):1189, 1982.

[53] W. H. Barkas, J. N. Dyer, and H. H. Heckman. Resolution of the Σ^--mass anomaly. *Phys. Rev. Lett.*, 11:26, 1963.

[54] F. Salvat and C. Heredia. Electromagnetic interaction models for Monte Carlo simulation of protons and alpha particles. *Nucl. Instrum. Meth. in Phys. Res. B*, 546:165157, 2023.

[55] A. Wambersie, P. M. DeLuca, and S. M. Seltzer. ICRU Report 73, Stopping of Ions Heavier Than Helium. *Reports of the International Commission on Radiation Units and Measurements*, 2005.

[56] E. B. Podgoršak, editor. *Radiation Physics for Medical Physicist*. MCGill University, Montreal, 3th printing edition, 2016.

[57] B. Gottschalk. Radiotherapy Proton Interaction in Matter, March 2018. [online] https://arxiv.org/abs/1804.00022.

[58] Stopping-Power & Range Tables for Electrons, Protons and Helium Ions. NIST Standard Reference Database 124. [online] https://www.nist.gov/pml/stopping-power-range-tables-electrons-protons-and-helium-ions.

[59] T. Bortfeld. An analytical approximation of the Bragg curve for therapeutic proton beams. *Med. Phys.*, 24(12):2024, 1997.

[60] E. J. Williams. The straggling of β-particles. *Proc. R. soc. London Ser. A-Contain.*, 125(798):420, 1929.

[61] N. Bohr. On the theory of the decrease of velocity of moving electrified particles on passing through matter. *Philos. Mag.*, 25(145):10, 1913.

[62] N. Bohr. On the decrease of velocity of swiftly moving electrified particles in passing through matter. *Philos. Mag.*, 30(178):581, 1915.

[63] L. D. Landau. On the energy loss of fast particles by ionization. *J. Phys. USSR*, 8(4):201, 1944.

[64] W. Börsch-Supan. On the Evaluation of the Function $\varphi(\lambda) = \frac{1}{2\pi i}\int_{\sigma-i\infty}^{\sigma+i\infty} e^{u\,ln\,u+\lambda u}du$ for Real Values of λ. *J. Res. Natl. Bur. Standards*, 65B(4):245, 1961.

[65] P.V. Vavilov. Ionization Losses of High-Energy Heavy Particles. *Sov. Phys. JETP*, 5:749, 1957.

[66] M. Abramowitz and I. A. Stegun, editors. *Handbook of Mathematical Functions with Formulas, Graphs, and Mathematical Tables*. Dover, New York, 9th printing edition, 1972.

[67] S. M. Seltzer and M. J. Berger. *Studies in Penetration of Charged Particles in Matter*. The National Academies Press, Washington, DC, 1964.

[68] A. Crispin and G. N. Fowler. Density Effect in the Ionization Energy Loss of Fast Charged Particles in Matter. *Rev. Mod. Phys.*, 42:290, 1970.

[69] G. Molière. Theorie der streuung schneller geladener Teilchen I. Einzelstreuung am abgeschirmten Coulomb-feld. *Z. Naturforsch*, 2A:133, 1953.

[70] H. A. Bethe. Molière's Theory of Multiple Scattering. *Phys. Rev.*, 89:1256, 1953.

[71] R. Piessen. *The transforms and applications handbook: second edition*. CRC Press LLC, 2000.

[72] B. Rossi and K. Greisen. Cosmic-Ray Theory. *Rev. Mod. Phys.*, 13:240, 1941.

[73] L. Eyges. Multiple Scattering with Energy Loss. *Phys. Rev.*, 74:1534, 1948.

[74] N. Verbeek, J. Wulff, C. Bäumer, S. Smyczek, B. Timmermann, and L. Brualla. Single pencil beam benchmark of a module for Monte Carlo simulation of proton transport in the PENELOPE code. *Med. Phys.*, 48(1):456, 2021.

[75] C. Behrends, C. Bäumer, N. Verbeek, J. Ehlert, R. Prasad, J. Wulff, A. Lühr, and B. Timmermann. Technical note: Providing proton fields down to the few-MeV level at clinical pencil beam scanning facilities for radiobiological experiments. *Med. Phys.*, 49(1):666, 2022.

[76] W. Matysiak, D. Yeung, R. Slopsema, and Z. Li. Evaluation of the range shifter model for proton pencil-beam scanning for the Eclipse v.11 treatment planning system. *J. Appl. Clin. Med. Phys.*, 17(2):391, 2016.

[77] E. Almhagen, D. J. Boersma, H. Nyström, and A. Ahnesjö. A beam model for focused proton pencil beams. *Physica Medica*, 52:27, 2018.

[78] M. De Saint-Hubert, N. Verbeek, C. Bäumer, J. Esser, J. Wulff, R. Nabha, O. Van Hoey, J. Dabin, F. Stuckmann, F. Vasi, and *et al.* Validation of a Monte Carlo Framework for Out-of-Field Dose Calculations in Proton Therapy. *Frontiers in Oncology*, 12:882489, 2022.

[79] B. Gottschalk. Techniques of proton radiotherapy: Transport theory. https://arxiv.org/abs/1204.4470, 2012.

[80] H. H. Barschall, M. B. Chadwick, D. T. L. Jones, J. P. Meulders, H. Schuhmacher, and P. G. Young. ICRU Report 63, Nuclear Data for Neutron and Proton Radiotherapy and for Radiation Protection. *Reports of the International Commission on Radiation Units and Measurements*, 2000.

[81] B. Gottschalk, R. Platais, and H. Paganetti. Nuclear interactions of 160 MeV protons stopping in copper: a test of Monte Carlo nuclear models. *Med.Phys.*, 26(12):2597, 1999.

[82] H. Paganetti and B. Gottschalk. Test of GEANT3 and GEANT4 nuclear models for 160 MeV protons stopping in CH_2. *Med.Phys.*, 30(7):1926, 2003.

[83] M. Lee, A. E. Nahum, and S. Webb. An empirical method to build up a model of proton dose distribution for a radiotherapy treatment-planning package. *Phys. Med. Biol.*, 38:989, 1993.

[84] J. F. Janni. Proton range-energy tables 1 keV-10 GeV. *At. Data Nucl. Data Tables*, 27:147, 1982.

[85] W. Newhauser and M. Durante. Assessing the risk of second malignancies after modern radiotherapy. *Nat. Rev. Cancer*, 11(6):438, 2011.

[86] K.S. Krane. *Introductory nuclear physics*. Wyley, 1987.

[87] J. Cugnon. Intranuclear cascade model. A review. *Nucl. Phys. A*, 387(1):191, 1982.

[88] Physics Reference Manual. Geant4's webpage. [online] https://geant4-userdoc.web.cern.ch/UsersGuides/PhysicsReferenceManual/html/index.html.

[89] K. K. Gudima, S. G. Mashnik, and V. D. Toneev. Cascade-exciton model of nuclear reactions. *Nucl. Phys. A*, 401(2):329, 1983.

[90] M. Blann. Preequilibrium Decay. *Ann. Rev. Nucl. Part. Sci.*, 25:123, 1975.

[91] M. Mascagni. Monte Carlo Methods: Early History and The Basics. https://www.cs.fsu.edu/~mascagni/MC_Basics.pdf, 2025. Accessed: February 25, 2025.

[92] S. Ulam and J. von Neumann. On combination of stochastic and deterministic processes. *Bull. Amer. Math Soc.*, 53:1120, 1947.

[93] N. Metropolis. THE BEGINNING of the MONTE CARLO METHOD. *Los Alamos Science Special Issue*, 15:125, 1987.

[94] M. L. Goldberger. The Interaction of High Energy Neutrons and Heavy Nuclei. *Phys. Rev.*, 74:1269, 1948.

[95] M. J. Berger. Monte Carlo calculation of the penetration and diffusion of fast charged particles. *Methods in Computational Physics*, 1:135, 1963.

[96] S. M. Seltzer. Electron-photon Monte Carlo calculations: The ETRAN code. *Int. J. Rad. Appl. Instr. A*, 42(10):917, 1991.

[97] A. F. Bielajew, H. Hirayama, W. R. Nelson, and D. W. O. Rogers. History, overview and recent improvements of EGS4 Technial Report PIRS-0436. Ottawa, Canada, 1994. National Research Council of Canada.

[98] I. Kawrakow, D. W. O. Rogers, E. Mainegra-Hing, F. Tessier, R. W. Townson, and B. R. B. Walters. EGSnrc toolkit for Monte Carlo simulation of ionizing radiation transport. doi:10.4224/40001303 [release v2023], 2000.

[99] T. Sato, Y. Iwamoto, S. Hashimoto, T. Ogawa, T. Furuta, S. Abe, T. Kai, Y. Matsuya, N. Matsuda, Y. Hirata, and *et al.* Recent improvements of the particle and heavy ion transport code system – PHITS version 3.33. *J. Nucl. Sci. Technol.*, 61(1):127, 2024.

[100] J. A. Kulesza, T. R. Adams, J. C. Armstrong, S. R. Bolding, F. B. Brown, J. S. Bull, T. P. Burke, A. R. Clark, R. A. Forster, III, J. F. Giron, and *et al.* MCNP® Code Version 6.3.0 Theory & User Manual. Technical Report LA-UR-22-30006, Rev. 1, Los Alamos National Laboratory, Los Alamos, NM, USA, September 2022.

[101] J. Allison, K. Amako, J. Apostolakis, P. Arce, M. Asai, T. Aso, E. Bagli, A. Bagulya, S. Banerjee, G. Barrand, and *et al.* Recent developments in Geant4. *Nucl. Instrum. Meth. Phys. Res. A*, 835(1):186, 2016.

[102] J. Allison, K. Amako, J. Apostolakis, H. Araujo, P. Arce, M. Asai, G. Barrand, R. Capra, S. Chauvie, R. Chytracek, and *et al.* Geant4 developments and applications. *IEEE Trans. Nucl. Sci.*, 53(1):270, 2006.

[103] S. Agostinelli, J. Allison, K. Amako, J. Apostolakis, H. Araujo, P. Arce, M. Asai, D. Axen, S. Banerjee, G. Barrand, and *et al.* Geant4—a simulation toolkit. *Nucl. Instrum. Meth. Phys. Res. A*, 506(3):250, 2003.

[104] P. A. Mayorga-Sierra. *Optimización de la radioterapia externa dek retinoblastoma por medio de simulación Monte Carlo con el código PENELOPE*. PhD thesis, Universidad de Granada, Departamento de Física Atómica, Molecular y Nuclear, 2015.

[105] S. García-Pareja. *Optimización basada en algoritmos de colonias de hormigas de la simulación Monte Carlo del transporte de radiación*. PhD thesis, Universidad de Granada, Departamento de Física Atómica, Molecular y Nuclear, 2012.

[106] W. González-Infantes. *Modelo de fuentes virtuales para cálculos Monte Carlo en radioterapia externa con haces de fotones*. PhD thesis, Universidad de Granada, Departamento de Física Atómica, Molecular y Nuclear, 2015.

[107] M. A. Carvajal. *Diseño de un sistema dosimétrico portátil*. PhD thesis, Universidad de Granada, Departamento de Electrónica y Tecnología de Computadores, 2008.

[108] M. J. Berger. *Methods in Computational Physics: Advances in Research and Applications, Vol. 1. Statistical Physics*. Academic Press, 1964.

[109] P. Andreo and A. Brahme. Restricted Energy-Loss Straggling and Multiple Scattering of Electrons in Mixed Monte Carlo Procedures. *Radiat. Res.*, 100(1):16, 1984.

[110] J. M. Fernández-Varea, R. Mayol, J. Baró, and F. Salvat. On the theory and simulation of multiple elastic scattering of electrons. *Nucl. Instrum. Meth. in Phys. Res. B*, 73(4):447, 1993.

[111] F. Salvat and J. M. Fernández-Varea. `RADIAL`: a Fortran subroutine package for the solution of the radial Schrödinger and Dirac wave equations. *Comput. Phys. Commun.*, 240:165, 2019.

[112] A. Koning and J. Delaroche. Local and global nucleon optical models from 1 keV to 200 MeV. *Nucl. Phys. A*, 713(3):231, 2003.

[113] X. W. Su and Y. L. Han. Global optical model potential for alpha projectile. *Int. J. Mod. Phys. E*, 24(12):1550092, 2015.

[114] B. A. Watson, P. P. Sing, and R. E. Segel. Optical-model analysis of nucleon scattering from 1p-shell nuclei between 10 and 50 MeV. *Phys. Rev.*, 182:977, 1969.

[115] A. A. Galyuzov and M. V. Kosov. Approximation of differential cross sections for elastic proton-nucleus scattering. *Phys. Atom. Nucl.*, 84:615, 2021.

[116] A. Ferrari, P. R. Sala, R. Guaraldi, and F. Padoani. An improved multiple scattering model for charged particle transport. *Nucl. Instrum. Meth. in Phys. Res. B*, 71(4):412, 1992.

[117] A. Fassò, A. Ferrari, J. Ranft, and P. R. Sala. New developments in FLUKA modeling of hadronic and EM interactions. In *KEK Proceedings 3rd. Workshop on Simulating Accelerator Radiation Environments*, Tsukuba, 1997.

[118] K. Parodi and S. Squarcia. Improvement of low-energy stopping power algorithms in the FLUKA simulation program. *Nucl. Instrum. Meth. in Phys. Res. A*, 456(3):352, 2001.

[119] Manual of FLUKA-CERN. Website of FLUKA-CERN collaboration. [online] https://flukafiles.web.cern.ch/manual/index.html.

[120] A. Ferrari and P. R. Sala. The Physics of High Energy Reactions. In *Proceedings Workshop on Nuclear Reaction Data and Nuclear Reactor Physics, Design and Safety*, 1998.

[121] A. M. Plaza. Dose distribution and Multiple Coulomb Scattering for protons by PENELOPE, TOPAS and FLUKA. Master's thesis, Universidad de Granada, Granada, Spain, 2020. unpublished.

[122] K. S. Baumann, F. Horst, K. Zink, and C. Gomà. Comparison of PENH, FLUKA and Geant4/TOPAS for absorbed dose calculations in air cavities representing ionization chambers in high-energy photon and proton beams. *Med. Phys.*, 46(10):4639, 2019.

[123] Guide for Physics List. Geant4's webpage. [online] https://geant4-userdoc.web.cern.ch/UsersGuides/PhysicsListGuide/html/index.html.

[124] ENDF/B-VII validation of G4 low energy neutron-nuclear elastic XS. CERN. [online] https://indico.cern.ch/event/84659/contributions/1262480/attachments/1075480/1533859/CHIPS_LE_nA.pdf.

[125] G4SEE Documentation. CERN. [online] https://g4see-docs.web.cern.ch/v0.5/physics_list.html.

[126] G4StoppingPhysics header. CERN. [online] https://github.com/hyperk/Geant4/blob/main/source/4.10.01.p02/source/physics_lists/constructors/stopping/include/G4StoppingPhysics.hh.

[127] S. Elles, V. N. Ivanchenko, M. Maire, and L. Urban. Geant4 and Fano cavity test: where are we? *J. Phys. Conf. Ser.*, 102:012009, 2008.

[128] TOPAS Collaboration. *TOPAS Documentation*, 2025. Accessed: 2025-02-25.

[129] J. A. de la Torre, A. M. Plaza, A. M. Lallena, F. Salvat, and M. Anguiano. Multiple scattering calculations for proton beams: Comparison of results from the general-purpose Monte Carlo codes PENH, FLUKA and TOPAS. *Rad. Phys. Chem.*, 213:111225, 2023.

[130] B. Gottschalk, A. M. Koehler, R. J. Schneider, J. M. Sisterson, and M. S. Wagner. Multiple Coulomb scattering of 160 MeV protons. *Nucl. Instrum. Meth. in Phys. Res. B*, 74(4):467, 1993.

[131] N. Verbeek, J. Wulff, M. Janson, C. Bäumer, S. Zahid, B. Timmermann, and L. Brualla. Experiments and Monte Carlo simulations on multiple Coulomb scattering of protons. *Med. Phys.*, 48(6):3186, 2021.

[132] A. Makarova, B. Gottschalk, and W. Sauerwein. Comparison of Geant4 multiple Coulomb scattering models with theory for radiotherapy protons. *Phys. Med. Biol.*, 62(15):5959, 2017.

[133] W. H. Press, S. A. Teukolsky, W. T. Vetterling, and B. P. Flannery. *Numerical recipes in Fortran77: The art of scientific computing*. Cambridge University Press, Cambridge, 1992.

[134] H. Fuchs, S. Vatnitsky, M. Stock, D. Georg, and L. Grevillot. Evaluation of GATE/Geant4 multiple Coulomb scattering algorithms for a 160 MeV proton beam. *Nucl. Instrum. Meth. in Phys. Res. B*, 410:122, 2017.

[135] E. G. Androulakaki, M. Kokkoris, M. Mayer, E. Mitsi, N. Patronis, and E. Vagena. A comparative study of multiple scattering calculations implemented in general–purpose Monte Carlo and selected ion beam analysis codes. *Nucl. Instrum. Meth. in Phys. Res. B*, 496:71, 2021.

[136] D. C. Hall, A. Makarova, H. Paganetti, and B. Gottschalk. Validation of nuclear models in Geant4 using the dose distribution of a 177 MeV proton pencil beam. *Phys. Med. Biol.*, 61(1):N1, 2016.

[137] M. Testa, J. Schümann, H. M. Lu, J. Shin, B. Faddegon, J. Perl, and H. Paganetti. Experimental validation of the TOPAS Monte Carlo system for passive scattering proton therapy. *Med. Phys.*, 40(12):121719, 2013.

[138] I. Rinaldi, A. Ferrari, A. Mariani, H. Paganetti, K. Parodi, and P. Sala. An integral test of FLUKA nuclear models with 160 MeV proton beams in multi-layer Faraday cups. *Phys. Med. Biol.*, 56(13):4001, 2011.

[139] A. G. Şerban, A. Coronetti, R. García-Alía, and F Salvat-Pujol. Nuclear elastic scattering of protons below 250 MeV in FLUKA v4-4.0 and its role in single-event-upset production in electronics. *Comput. Phys. Commun.*, 303:109276, 2024.

[140] A. Akkerman, J. Barak, and N. M. Yitzhak. Role of Elastic Scattering of Protons, Muons, and Electrons in Inducing Single-Event Upsets. *IEEE Trans. Nucl. Sci.*, 64(10):2648, 2017.

[141] P. Caron, C. Inguimbert, L. Artola, R. Ecoffet, and F. Bezerra. Physical Mechanisms of Proton-Induced Single-Event Upset in Integrated Memory Devices. *IEEE Trans. Nucl. Sci.*, 66(7):1404, 2019.

[142] A. Genz. Numerical Computation of Multivariate Normal Probabilities. *J. Comput. Graph. Stat.*, 1(2):141, 1992.

[143] F. Olver, D. Lozier, R. Boisvert, and C. Clark. *NIST Handbook of Mathematical Functions*. Cambridge University Press, 2010.

[144] J. Cugnon, D. L'Hôte, and J. Vandermeulen. Simple parametrization of cross-sections for nuclear transport studies up to GeV range. *Nucl. Instrum. Meth. in Phys. Res. B*, 111(3):215, 1996.

[145] N. Otuka, E. Dupont, V. Semkova, B. Pritychenko, A. I. Blokhin, M. Aikawa, S. Babykina, M. Bossant, G. Chen, S. Dunaeva, and *et al.* Towards a More Complete and Accurate Experimental Nuclear Reaction Data Library (EXFOR): International Collaboration Between Nuclear Reaction Data Centres (NRDC). *Nuclear Data Sheets*, 120:272, 2014.

[146] J. Ranft. Estimation of radiation problems around high-energy accelerators using calculations of the hadronic cascade in matter. *Particle Accelerators*, 3:129, 1972.

[147] A.G. Şerban and F. Salvat-Pujol. Recent FLUKA developments for an improved description of SEU production in electronics, June 2023. [online] http://nvd.nist.gov/nvd.cfm?cvename=CVE-2008-1368.

[148] Accident prevention in case of radiotherapy equipment malfunction. IAEA's website, June 2024. [online] https://www.iaea.org/resources/rpop/health-professionals/radiotherapy/accident-prevention/equipment-malfunction.

[149] G.F. Knoll. *Radiation Detection and Measurement*. John Wiley & Sons, 2000.

[150] J. A. de la Torre, A. M. Lallena, and M. Anguiano. Fano test, clinical proton beams and nuclear reactions. *Rad. Phys. Chem.*, 230:112538, 2025.

[151] L. V. Spencer. Some comments on Fano's theorem. *Radiat. Res.*, 63(1):191, 1975.

[152] U. Fano. Inelastic Collisions and the Molière Theory of Multiple Scattering. *Phys. Rev.*, 93:117, 1964.

[153] U. Fano. Note on the Bragg-Gray cavity principle for measuring energy dissipation. *Rad. Res.*, 1(3):237, 1954.

[154] E. Sterpin, K. Souris, S. Vynckier, and H. Bouchard. A Fano cavity test for Monte Carlo proton transport algorithms. *Med. Phys.*, 41(1):011706, 2014.

[155] J. Sempau and P. Andreo. Configuration of the electron transport algorithm of PENELOPE to simulate ion chambers. *Phys. Med. Biol.*, 51(14):3533, 2006.

[156] F. H. Attix, editor. *Introduction to radiological physics and radiation dosimetry*. WILEY-VCH Verlag GmbH & Co. KGaA, Weinheim, 2004.

[157] D. Rapisarda and L. Vermeeren. private communication, Feb. 2010.

[158] H. Bichsel, D. H. Peirson, J. W. Boring, A. Green, M. Inokuti, and Hurst G. ICRU Report 31, "Average, Energy Required to Produce An Ion Pair". *Reports of the International Commission on Radiation Units and Measurements*, 1979.

[159] I. Olaciregui-Ruiz, S. Beddar, P. Greer, N. Jornet, B. McCurdy, G. Paiva-Fonseca, B. Mijnheer, and F. Verhaegen. In vivo dosimetry in external beam photon radiotherapy: Requirements and future directions for research, development, and clinical practice. *Phys. Imaging Radiat. Oncol.*, 15:108, 2020.

[160] I. Ruiz-García. *Desarrollo de instrumentación portátil microcontrolada en el ámbito de la salud y el deporte*. PhD thesis, Universidad de Granada, 2024.

[161] L. Brualla, M. Rodriguez, J. Sempau, and P. Andreo. PENELOPE/PRIMO-calculated photon and electron spectra from clinical accelerators. *Radiat. Oncol.*, 14:1, 2019.

[162] VISHAY. Datasheet of the BPW34S photodiode, 2024. Accessed on November 17, 2024. [online] https://www.vishay.com/en/product/81128/.

[163] L. Vermeeren and R. Van Nieuwenhove. Theoretical study of radiation induced electromotive force effects on mineral insulated cables. *Rev. Sci. Instrum.*, 74:4667, 2003.

[164] M. A. Carvajal, S. García-Pareja, D. Guirado, M. Vilches, M. Anguiano, A. J. Palma, and A. M. Lallena. Monte Carlo simulation using PENELOPE code with an ant colony algorithm to study MOSFET detectors. *Phys. Med. Biol.*, 54(20):6263, 2009.

[165] A. Allisy, W. A. Jennings, A. M. Kellerer, J. W. Müller, H. H. Rossi, and S. M. Seltzer. ICRU Report 60, "Fundamental Quantities and Units for Ionizing Radiation". *Reports of the International Commission on Radiation Units and Measurements*, 1998.

[166] H. P. Wieser, E. Cisternas, N. Wahl, S. Ulrich, A. Stadler, H. Mescher, L. R. Müller, T. Klinge, H. Gabrys, L. Burigo, and *et al.* Development of the open-source dose calculation and optimization toolkit matRad. *Med. Phys.*, 44(6):2556, 2017.

[167] Scipy(https://docs.scipy.org/doc/scipy-1.13.1/reference/generated/scipy.optimize.minimize.html). Scipy.optimize.minimize, 2024. Accessed on June 18, 2024.

[168] J. A. Nelder and R. Mead. A Simplex Method for Function Minimization. *Comput. J.*, 7(4):308, 1965.

[169] F. Gao and L. Han. Implementing the Nelder-Mead simplex algorithm with adaptive parameters. *Comput. Optim. Appl.*, 51:259, 2012.

[170] J. F. Almansa, R. Guerrero, F. M. O. Al-Dweri, M. Anguiano, and A. M. Lallena. Dose distribution in water for monoenergetic photon point source in the energy range of interest in brachytherapy: Monte Carlo simulations with PENELOPE and GEANT4. *Rad. Phys. Chem.*, 76(5):766, 2007.

[171] A. G. Frodesen, O. Skjeggestad, and H. Tofte. *Probability and Statistics in Particle Physics*. Universitetsforlaget, Bergen, 1979.

[172] G. O. Sawakuchi, X. R. Zhu, F. Poenisch, G. Ciangaru, U. Titt, A. Anand, R. Mohan, M. T. Gillin, and N. Sahoo. Experimental characterization of the low-dose envelope of spot scanning proton beams. *Phys. Med. Biol.*, 55(12):3467, 2010.

Appendix A

Dosimetric magnitudes

In this appendix, a compilation of basic magnitudes used in proton therapy is reviewed in order to facilitate the description of the results obtained in the thesis. The concepts reviewed include basic dosimetric definitions extracted from [165].

A.1 Fluence, Φ

Fluence, Φ, is defined by the following expression:

$$\Phi = \frac{dN}{da}, \tag{A.1}$$

where dN is the number of particles incident on a sphere of cross-sectional area da. The use of a sphere of cross-sectional area da as the volume considered to define this quantity reflects the fact that this definition is looking for the simplest way to have a uniform area regardless of the direction of particle impact. The unit, in the S.I., used for this magnitude is m^{-2}.

Another important dosimetric magnitude is the energy fluence. This magnitude is defined by the following expression:

$$\Phi_E = \frac{d\Phi}{dE} = \frac{dN}{dEda}, \tag{A.2}$$

where $d\Phi$ is the fluence of particles of energy between E and $E + dE$. The energy fluence is usually used to calculate the average of a physical magnitude when a polyenergetic beam is

considered in the calculation. For that, the following definition is used:

$$\bar{q} = \frac{\int_E q(E) \cdot \Phi_E(E)\, dE}{\int_E \Phi_E(E)\, dE}, \tag{A.3}$$

where $q(E)$ is the physical quantity to be averaged and $\bar{q}$ is the averaged value.

A.2 Dose, D

A basic magnitude used in proton therapy treatments is dose. Dose is define as:

$$D = \frac{d\bar{\varepsilon}}{dm}, \tag{A.4}$$

where $d\bar{\varepsilon}$ is the net energy deposition in a small volume (dV) with a mass dm. $d\bar{\varepsilon}$ can be calculated as:

$$d\bar{\varepsilon} = \varepsilon_{\text{in}} - \varepsilon_{\text{out}} + Q, \tag{A.5}$$

with ε_{in} and ε_{out} the energy of the incident and leaving ionizing particles, respectively. Additionally, Q is the change in the rest energies of the nucleus and all particles involved in the interaction produced in the studied volume.

Dose is the main quantity used in radiotherapy treatments. This makes dose a cornerstone magnitude in medical physics. The unit of dose in the International System of Units is $\text{J} \cdot \text{kg}^{-1}$. This unit is also called Gray (Gy) in honour of Louis Harold Gray.

A.3 Lineal energy transfer, L_Δ

The Linear Energy Transfer (LET), L_Δ, of a material for a given charged particle is defined as:

$$L_\Delta = \frac{dE_\Delta}{dl}, \tag{A.6}$$

where dE_Δ is the energy loss by a charged particle due to electronic collisions in traversing a distance dl minus the sum of the kinetic energies of all the electrons released with kinetic energies in excess of Δ. Expand the previous expression using the definition for E_Δ, the LET can be express as:

$$L_\Delta = S_{\text{el}} - \frac{dE_{\text{ke},\Delta}}{dl}, \tag{A.7}$$

where S_{el} is the electronic stopping power and $dE_{\text{ke},\Delta}$ is the sum of the kinetic energies of all the electrons released with a bigger kinetic energies than Δ. As can be seen in the expression (A.7), if Δ is set as ∞ (no restriction condition) the LET is equal to the electronic stopping power. In this case L_∞ is termed as unrestricted linear energy transfer.

The unit used to express this magnitude is keV $\cdot$ μm^{-1}.

Appendix B

Monte Carlo description of a SOBP

In this appendix, a brief description of a SOBP is given. In addition, the current techniques used to implement this type of source in MC codes are review.

B.1 Definition of a SOBP

As commented in section 1, proton dose deposition has a flat plateau at the beginning and a characteristic peak at the end of the dose curve [42]. This characteristic peak is too sharp to treat extended tumour volumes. To overcome this problem, the spread-out Bragg peak (SOBP) is used in clinical practice. A SOBP is a superposition of elementary Bragg peak depth-dose curves [3, 4], correctly weighted to deliver a constant dose along the extended tumour volume of the patient. Thanks to this technique, all the benefits of the proton therapy can be put it into practice, avoiding the problem of non-uniformity in the tumour area associated with the Bragg curve. An example of the dose distribution associated with this type of proton source is shown in Figure B.1. This figure shows the depth dose curve used to treat a cancer with an extension of 5 cm located at a depth of 20 cm.

B.2 Analytical model to build a SOBP

This section describes a method for implementing SOBPs in MC simulation. In the scientific bibliography there is an analytical method proposed by T. Bortfeld and W. Schlegel [4] that allows to reproduce the source that generates SOBPs in a simple way. To implement this method, these authors used an analytical description of the Bragg curve given by:

$$D(R,z) = \frac{K}{(R-z)^{1-1/p}} \tag{B.1}$$

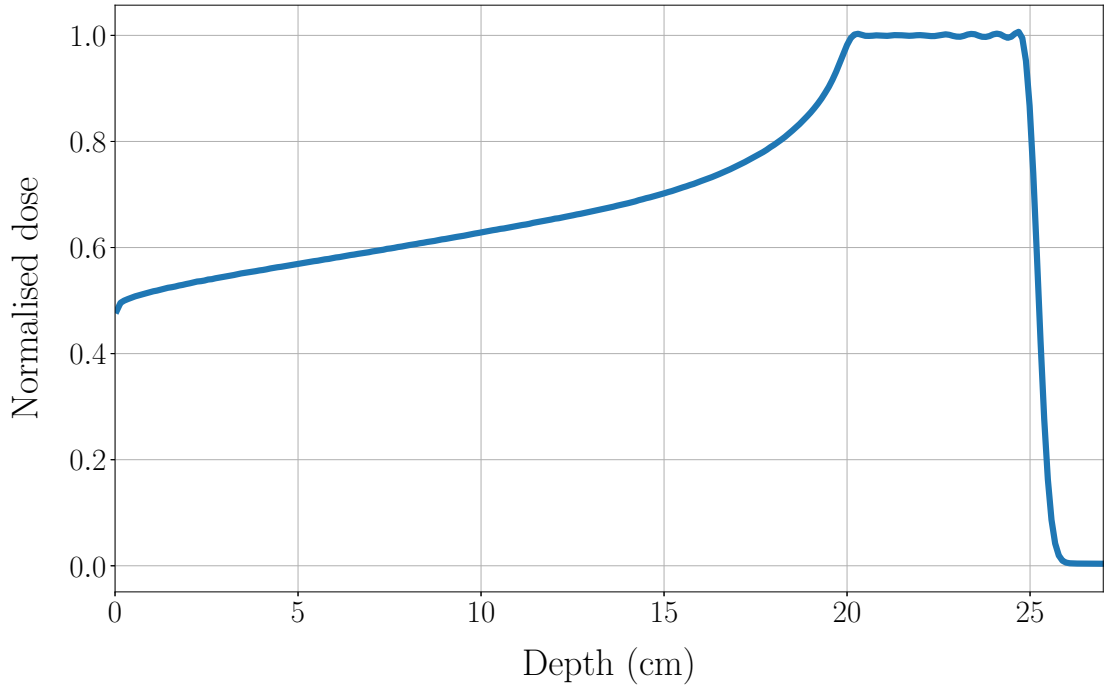

Fig. B.1 Example of a SOBP depth dose curve used to treat a 5 cm long tumour located at 20 cm.

where R is the range of the monoenergetic beam to be described, K is a material dependent constant and p is a fit parameter that is obtained from the Bragg-Kleeman relation (see section 1.1.4).

From equation (B.1), a weight function $W(R)$ is sought which, when it is convolved with the dose curve specified above, reproduces the dose deposition of a SOBP. The expression of the function $W(R)$ which satisfies this condition is:

$$W(R) = \begin{cases} \dfrac{\eta}{(d_\mathrm{b} - R)^{1/p}} & \text{if} \quad d_\mathrm{a} < R < d_\mathrm{b}\,, \\ \\ 0 & \text{else}\,, \end{cases} \tag{B.2}$$

where η is a scaling factor, d_a and d_b are the minimum and maximum depths of the dose uniform region in the SOPB on the z axis.

B.2.1 Sample method and its implementation

The expression (B.2) provides a first approach to building a SOBP curve, but to get the most out of it, it is essential to be able to implement it easily in the MC codes. To do

this, a sampling method is reviewed in this section. This method allows the calculation of the weighted factors needed to implement the superposition of elementary Bragg peak depth-dose curves, following the weighting distribution given by $W(R)$.

To implement this sampling method, the probability of emission p of a proton beam with a range r smaller than a given distance d can be defined as:

$$p(r<d) = \frac{\int_{d_\mathrm{a}}^{d} W(R)dR}{\int_{d_\mathrm{a}}^{d_\mathrm{b}} W(R)dR}. \tag{B.3}$$

If (B.2) is replaced in (B.3) and the expression is expanded, it is obtained that:

$$p(r<d) = \frac{\chi^x - (d_\mathrm{b}-d)^x}{\chi^x}, \tag{B.4}$$

where χ is the length of SOBP ($\chi = d_\mathrm{b} - d_\mathrm{a}$) and $x = \dfrac{p-1}{p}$.

Once the probability of emitting a beam with a smaller range at a given distance has been defined, it is possible to sample this probability distribution using the inverse transform method [28]. For the application of this method, it is considered that

$$p(r<d) = \frac{\chi^x - (d_\mathrm{b}-d)^x}{\chi^x} = \xi, \tag{B.5}$$

where ξ is a random number distributed according to the uniform distribution between 0 and 1 ($U(0,1)$). Solving the latter expression for d gives:

$$d = d_\mathrm{b} - \xi^{1/x}\chi, \tag{B.6}$$

where the latter is the expression that will be used to select the initial energy of the protons that will be used in the MC simulation. As it can be seen, the expression (B.6) provides a sampling of the range space. A way to transform the distances given by (B.6) into initial energies is needed to implement this method in the MC codes. The Bragg-Kleeman relation is used to perform this variable transformation.

B.2.2 Deficits of the Bortfeld's model

The Bortfeld model provides a simple way of constructing a source that produces a SOBP. However, if the sampling method described in the previous section is implemented, it will be found that the dose deposition in the tumour region is not homogeneous (Figure B.2). Figure B.2 shows the results obtained with PENH when the sampling method given by eq. (B.6) is implemented in the MC simulation. It is clear that the SOBP obtained with the Borfeld's method is not accurate enough to be used in the clinical practice, due to its high inhomogeneity. The problem of non-homogeneity is related to the function used to describe the dose deposited by protons, eq. (B.1). The analytical expression of the Bragg curve given by Bortfeld and Schlegel [4], eq. (B.1), has three main problems:

1. *Energy straggling*: it is clear that the energy straggling is a fundamental process in the proton dose deposition. Energy straggling broadens the area of the Bragg peak. In the analytical approximation given by Bortfeld and Schlegel this process is neglected when they derived their expression using the Bragg-Kleeman relation. The dose expression derived from the Bragg-Kleeman relation is too narrow because it does not consider energy straggling. This leads to discrepancies between the experimental curves and those given by this theoretical model.

2. *Secondary particles produced in nuclear reactions*: uncharged particles produced in a nuclear reaction deposit a non-negligible amount of dose beyond the Bragg peak. The curve derived by Bortfeld and Schlegel does not take into account this contribution.

3. *Change in fluence profile*: when a proton undergoes a nuclear reaction, a reduction in the proton fluence is produced. This type of event has a significant effect on the dose deposition related to protons. This process is not taken into account by the expression derived by Bortfeld and Schlegel.

B.2.3 Applying the Bortfeld's formalism in simulation without nuclear reactions

The main problems with Bortfeld's formalism have been commented on above. In summary, the lack of description of the nuclear interaction (points 2 and 3 of the section B.2.2) causes this theoretical framework to fail. For low energies, such as those used to treat eye cancers, the effect of nuclear reactions can be neglected. In such cases, the Bortfeld's formalism can be a good approach to simulate a SOBP.

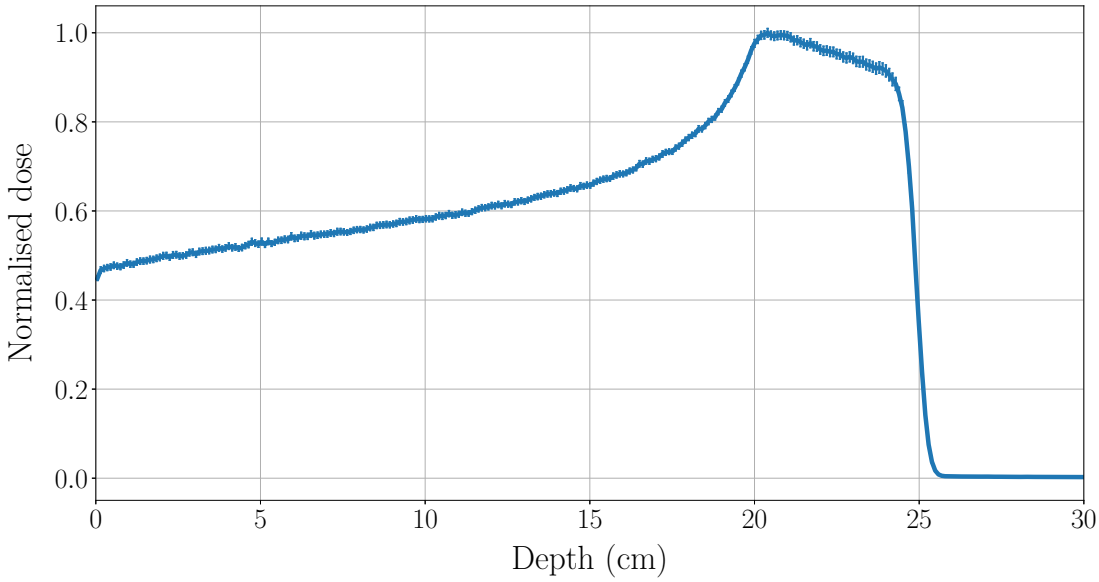

Fig. B.2 SOBP curve calculated with the Bortfeld method. This depth dose curve was obtained by using PENH, considering monoenergetic proton beams according to the sampling method of Bortfeld (eq. (B.6)), with $d_a = 20$ cm and $d_b = 25$ cm.

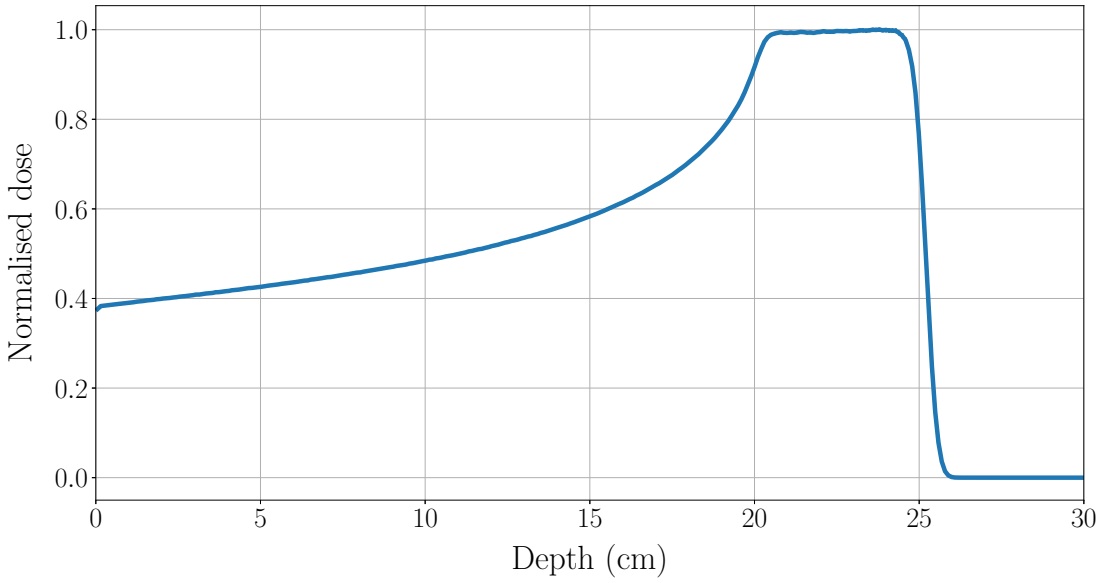

Fig. B.3 SOBP dose curve calculated with the Bortfeld's formalism without taking into account nuclear reactions in the MC calculation. The code PENH has been used to calculate the dose profile.

Figure B.3 shows an SOBP obtained using Bortfeld's formalism. In the simulation used to obtain it, the nuclear reactions were switched off. As can be seen in this figure, the dose deposition problem observed in Figure B.2 has disappeared. A small effect of energy

Table B.1 Dimension used in the Cartesian grid employed to calculate the dose for the Bragg peak database.

Axis	$\chi_{\min}$ (cm)	$\chi_{\max}$ (cm)	N. of bins
x	-10	10	1
y	-10	10	1
z	0	40	400

straggling can be appreciated in the homogeneity of the SOBP, but in general the results calculated under these circumstances are better than those obtained in the general case.

B.3 An alternative model to describe SOBPs

Although all problems that have been commented were corrected by Bortfeld [59], the expression that he obtains is too complex to use the method described in Bortfeld and Schlegel (1996) [4] to derive $W(R)$. In order to define a source that produces a SOBP curve, the following alternative method can be used.

First at all, a Bragg curve database is calculated using PENH in water. This database collects information on the dose deposited by pencil proton beams with ranges between 0 and 40 cm. The chosen step to build this database is 0.1 cm in the range space. This choice makes that the step took in the energy space is not constant. This means that the energies used in the source sampling are not equispaced. To collect all this information about dose curves, a Cartesian grid, whose dimensions are specified in the Table B.1, was used in the simulations. Furthermore, $1 \cdot 10^6$ protons have been used in each performed simulation.

All the information collected in this database can be described by a matrix $D_{i,j}$ where the index j refers to the energy of the pencil beam and the index i to the spatial information of where the dose is deposited. The dose deposited at a given position i can be calculated as [166]:

$$d_i(\vec{\omega}) = \sum_j \omega_j \, D_{i,j}, \tag{B.7}$$

where ω_j is the weight factor that corresponding to the pencil beam with initial energy j. These weight factors are the unknown variables in this problem. These unknown variables must be positive, because they are the probabilities of emitting a proton. To find their values,

an additional constrain condition must be set. This constrain condition will be to minimise the following function:

$$f(\vec{\omega}) = \sum_{i \in T} (d_i(\vec{\omega}) - d_{\mathrm{SOBP}})^2, \tag{B.8}$$

where T is the set of spatial positions where the SOBP is flat and d_{SOBP} is the dose of the SOBP in this flat region

A Python script was used to calculate the values of the weight factors. In this script, the database calculated with PENH is used to implement the method mentioned above. To minimise equation (B.8), the function `optimize.minimize` [167] from scipy is used. This function minimises the value of the objective function using the Nelder-Mead algorithm [168, 169].

Figure B.4 shows a comparison between the results obtained by the numerical method and the Bortfeld method. A SOBP with $d_a = 20$ cm and $d_b = 25$ cm has been calculated with PENH. As can be seen in the Figure B.4, the numerical method described in this section (orange points) improves the description of the SOBP given by Bortfeld method (blue points). Using the numerical method, the dose reduction in the SOBP flat area can be eliminated, thus improving the homogeneity of the dose deposition in the tumour zone. In addition, the numerical method provides a general recipe for constructing a SOBP that can be used to describe SOBPs with other heavy ions such as helium, carbon or oxygen.

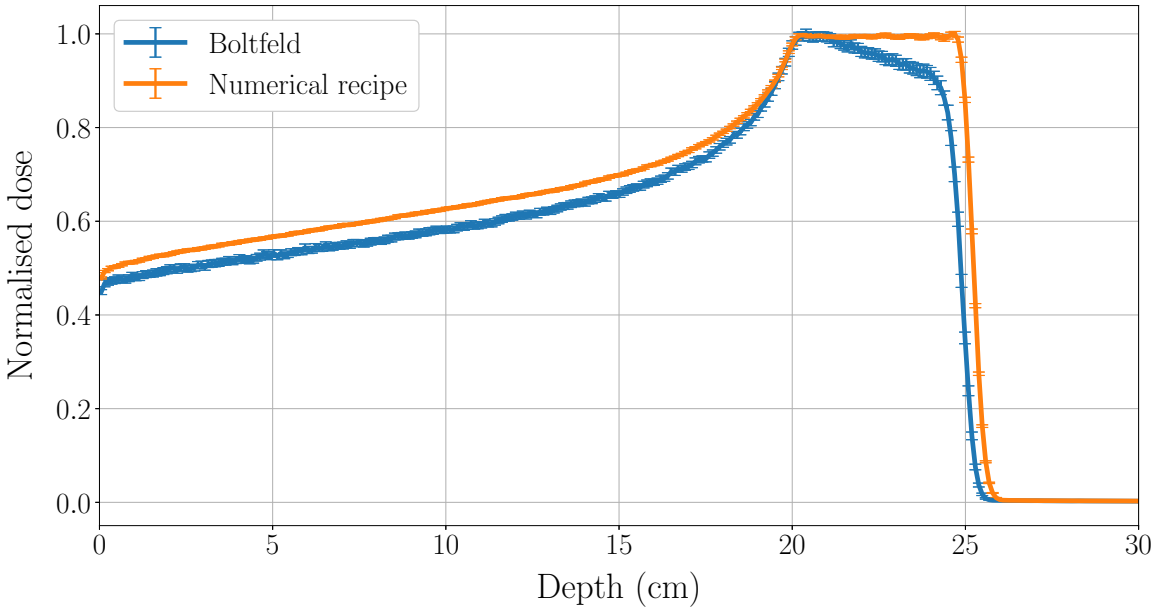

Fig. B.4 The results obtained with the two different methods presented in this appendix are shown. The SOBP curve calculated with the Bortfeld method is shown in blue and the SOBP calculated with a numerical optimisation is shown in orange. For the determination of these SOBPs, the different methods have been implemented in PENH.

Appendix C

Validity of the Fermi-Eyges theory to characterise a clinical proton source

In order to implement a realistic problem in a MC simulation, it is necessary to have three very clear ingredients in the simulation being carried out: what is the radiation source used in the case under study, what is the geometry of the irradiated object and where and how is the detector used to measure the magnitude to be determined. These three factors are essential to calculate results that are compatible with the data obtained from the experiment that is aimed to reproduce. With this in mind, this appendix shows a study of the validity of Fermi-Eyges theory for characterising a clinical proton source.

C.1 Description of the problem

The theoretical framework provided by the Fermi-Eyges theory (briefly described in section 1.2.2) is widely used in the field of proton therapy. An example of its use can be found in the work of Verbeek *et al.* [74] or De Saint-Hubert *et al.* [78]. On top of that, this formalism is used to model the spatial and angular distribution of the pencil beams used in TPS. Despite its widespread use, the results obtained from this theory have not been validated. For this reason, a method will be introduced to study the goodness of this theoretical framework.

To check the validity of the Fermi-Eyges theory, a simple simulation scheme will be followed. On the one hand, a detailed simulation is carried out. This detailed simulation will reproduce the interaction of a monoenergetic proton pencil beam with an air layer of

thickness 50 cm. After that, the dose deposition in a water phantom is calculated. To study the influence of the secondary particles and the protons that have undergone a hard scattering event, a particle phase space is obtained at the end of the air layer. This phase space makes it possible to eliminate from the simulation the contributions of the particles commented on above by filtering it. On the other hand, a characterization of the proton beam is calculated at the entrance of the water phantom. To do this characterization, the Fermi-Eyges theory is used, following the indications given by Verbeek *et al.* [74]. Once the proton beam is characterised, the dose deposition in the water phantom is calculated for this case too (Figure C.1).

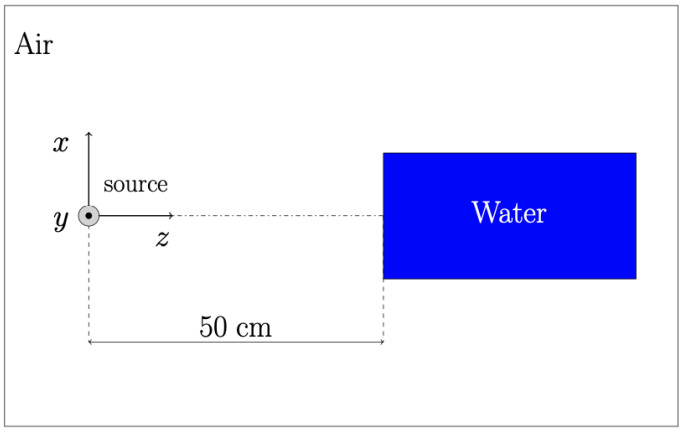

(a) Detailed simulation

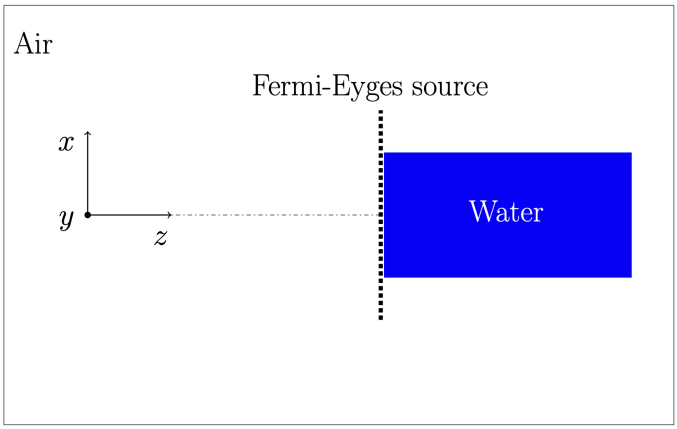

(b) Fermi-Eyges simulation

Fig. C.1 Simulation scheme used to study the validity of the Fermi-Eyges theory

Table C.1 Radial distance used to obtain the dose profiles analysed in the study of validity of the Fermi-Eyges formalism.

Energy (MeV)	100	160	225
1^{st} radius (cm)	0.0	0.0	0.0
2^{nd} radius (cm)	0.76	1.52	1.52
3^{rd} radius (cm)	2.29	3.05	2.29
4^{th} radius (cm)	3.05	4.57	7.62
5^{th} radius (cm)	4.57	6.10	9.90
6^{th} radius (cm)	6.10	7.62	10.67

For this analysis, the following proton energies have been considered: 100, 160 and 225 MeV. This set of energies are used by Verbeek *et al.* [74] too. To score the dose, a radial grid with $\Delta r = 0.42$ cm is considered. Due to the strong dependence of the lateral scattering on the energy, different radial profiles have been obtained as a function of this magnitude (Table C.1). The radial distance has been chosen to reproduce the measurement condition described in Verbeek *et al.* [74]. In all the simulations performed in this study, 10^7 histories have been used.

To compare the results obtained from the different simulation, a χ^2-type statistic is employed. The definition of this statistic is:

$$\chi^2_{\mathrm{D}_1,\mathrm{D}_2} = \sum_{j=1}^{M} \frac{(D_1^j - D_2^j)^2}{(\sigma_1^j)^2 + (\sigma_2^j)^2}, \tag{C.1}$$

where M is the number of bins in the dose profiles (see Table C.2), D_1^j and D_2^j label the j-th bin of the first and second dose profile, respectively, and σ_1^j and σ_2^j are the corresponding uncertainties [170]. One can state that the two dose profiles are similar, if $\chi^2_{\mathrm{D}_1,\mathrm{D}_2}/M \sim 1$. On the one hand, if a value of $\chi^2_{\mathrm{D}_1,\mathrm{D}_2}/M$ below to 1 is obtained, this points out the presence of correlation between the dose profiles. On the other hand, a value of $\chi^2_{\mathrm{D}_1,\mathrm{D}_2}/M$ above to 1 indicates that there is a discrepancy between the dose profiles [133, 171]. The uncertainty of this statistic is given by $\sqrt{2\chi^2_{\mathrm{D}_1,\mathrm{D}_2}}$ [171].

C.1.1 Fermi-Eyges parameters

In the Fermi-Eyges formalism, the probability of finding a proton with $(\vec{r},\vec{\Omega})$ is given by the following probability distribution:

$$\Phi(z;\vec{r},\vec{\Omega}) = F(z;x,\theta_x)F(z;y,\theta_y), \tag{C.2}$$

Table C.2 Number of bins used in the dose profiles calculated for the study of validity of the Fermi-Eyges formalism. The numbers of bins have been chosen in order to reproduce the experimental case described in Verbeek *et al.* [74].

Energy (MeV)	# of bins
100	120
160	230
220	400

where z is the distance travelled by the proton, x and y are the lateral displacements in the x and y axes respectively, θ_x and θ_y are the projected angles with the the x and y axes respectively and $F(z;\xi,\theta_\xi)$ is the following probability distribution:

$$F(z;\xi,\theta_\xi) = \frac{1}{4\pi\sqrt{B(z)}} \exp\left(-\frac{A_0(z)\xi^2 - 2A_1(z)\xi\theta_\xi + A_2(z)\theta_\xi^2}{4B(z)}\right), \tag{C.3}$$

with $B(z) = A_0(z)A_2(z) - A_1^2(z)$ being the emittance of the proton beam. $2A_2(z)$ is the variance of the spatial distribution in z, $2A_0(z)$ is the variance of the angular distribution in z and $2A_1(z)$ is the covariance.

As can be seen in eqs. (C.2) and (C.3), six parameters are needed to describe the probability of finding a proton with $(\vec{r},\vec{\Omega})$ in a given depth z. This number is reduced to three due to the symmetry between the x and y axes, because it is supposed that the parameters that define $F(z;x,\theta_x)$ and $F(z;y,\theta_y)$ are identical, due to the scattering symmetry. To find these three parameters for each case that is going to be analysed in this work, the procedure described by Verbeek *et al.* [74] will be followed. To apply this method, the spatial distribution of the proton beam is needed for three distances. To calculate them, a phase space file is calculated for $z = 30,\ 50$ and 70 cm, using a MC simulation of a monoenergetic proton pencil beam travelling through an air layer. Using these phase space files, the fluence distribution can be calculated in these three positions (Figure C.2). Once these profiles have been obtained, using the following equation, the parameters can be determined:

$$\frac{\sigma_\xi^2(z)}{2} = A_2(z_0) + A_1(z_0)(z-z_0) + A_0(z_0)(z-z_0)^2, \tag{C.4}$$

where $\sigma_\xi^2(z)$ is the variance of the spatial distribution of the proton beam in any of the three position considered, z could be any of the three position considered and z_0 is the position where the air layer ends in the geometry ($z_0 = 50$ cm). With the data obtained in the three

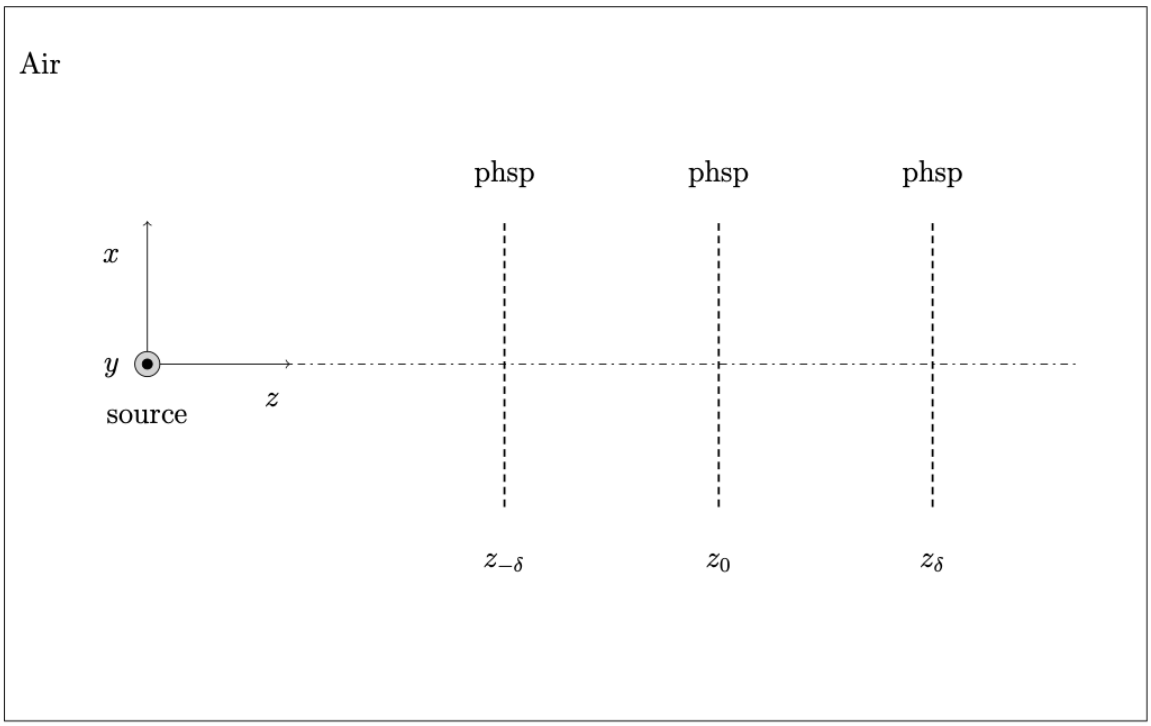

Fig. C.2 Simulation scheme used to obtain the parameters of the Fermi-Eyges probability distribution. In the simulation carried out, $z_0 = 50$ cm and δ was considered 20 cm.

Table C.3 Fermi-Eyges parameters used in the validation of the Fermi-Eyges formalism.

Energy(MeV)	$A_0(z_0)$ (mrad^2)	$A_1(z_0)$ (mrad·mm)	$A_2(z_0)$ (mm^2)
100	2.714	0.699	0.217
160	1.095	0.284	0.089
225	0.581	0.152	0.048

positions, a equation system can be proposed, allowing to fix the parameters at $z_0 = 50$ cm.

To calculate the Fermi-Eyges parameters, it is fundamental to know the variance of the spatial distribution of the proton beam in all the positions considered. As it has been commented above, the fluence distribution can be calculated through the phase space file (Figure C.3). The variance of the spatial distribution is calculated fitting the fluence profile to the following expression:

$$f(\xi) = a \exp\left(-\frac{\xi^2}{2\sigma_\xi}\right), \tag{C.5}$$

where ξ is the spatial variable used in the fit and with $a \equiv f(\xi = 0)$. These fits were performed by means of the Levenberg-Marquardt method [133]. Blending the spatial variance obtaining

with these fits and the equation (C.4), the values shown in Table C.3 has been determined. These values will be use in the simulation scheme where the proton source has been modeled as a Fermi-Eyges probability distribution.

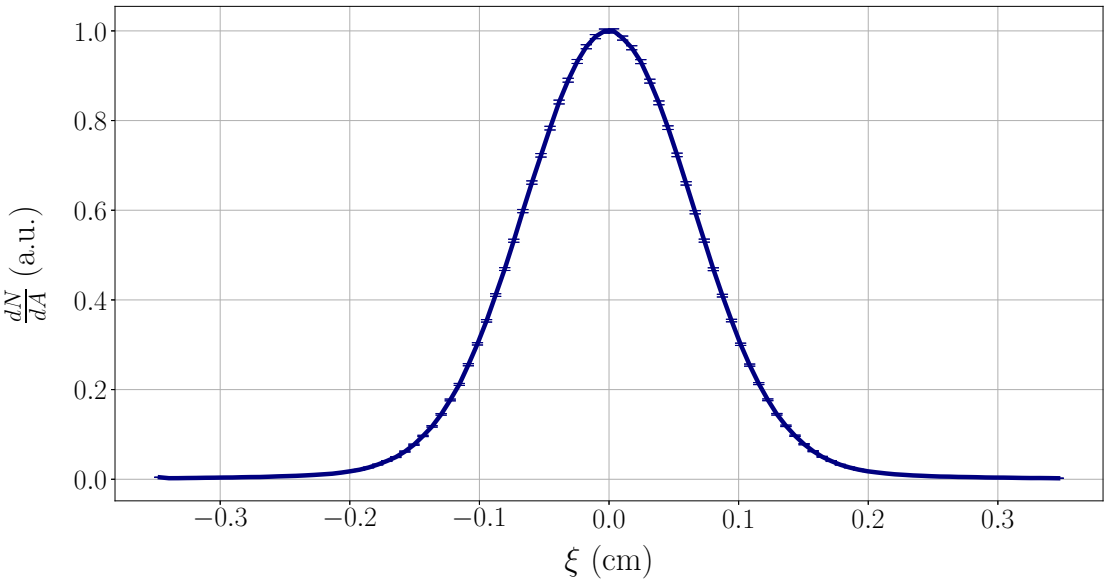

Fig. C.3 Fluence profile of a proton beam after travelling an air layer of 50 cm. The energy used in this simulation was 100 MeV.

C.2 Results

To check the validity of the Fermi-Eyges theory as a function of energy, a comparison is made between the detailed and the Fermi-Eyges simulations. Using the $\chi^2_{D_1,D_2}$ statistic, the results shown in Figure C.4 are obtained. It is important to note that Fermi-Eyges fit fails significantly for $E = 100$ MeV. This fact can be deduced by revising the $\chi^2_{D_1,D_2}/M$ values. For all radial profiles the condition $\chi^2_{D_1,D_2}/M > 1$ is verified. This shows that the Fermi-Eyges formalism fails when trying to describe a proton beam for low clinical energies. It is also important to note that for all energies considered, the Fermi-Eyges formalism cannot describe the central dose profile. This is because the Fermi-Eyges formalism underestimates the number of protons in the non-gaussian tails of the probability distribution (see Figure C.5). This underestimation of the non-gaussian tails (outer region of the water phantom) leads to an overestimation of the central dose profile. As the non-gaussian tails depend on the scattering of the protons, their importance decreases as the initial energy of the protons increases. This effect is caused by the reduction in scattering events as the energy of the

proton increases. For the remaining dose profiles, this theoretical framework provides a decent description of the proton beam.

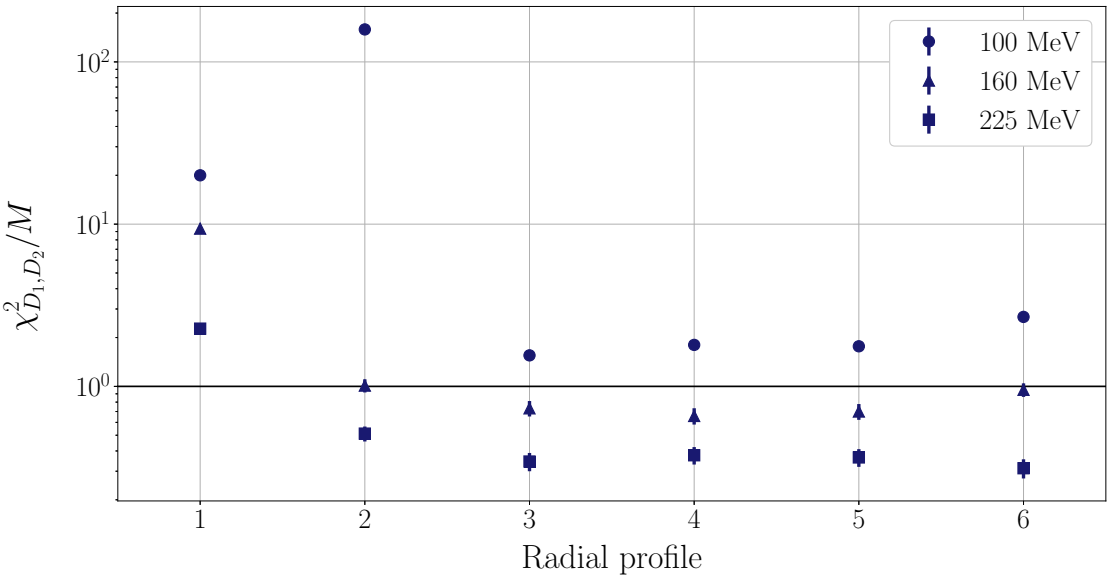

Fig. C.4 $\chi^2_{D_1,D_2}/M$ values calculated for the comparison between the detailed and Fermi-Eyges simulation. The data calculated for 100 MeV appears as a circle, for 160 MeV, as a triangle and for 225 MeV, as a square. The unity is highlighted using a black line.

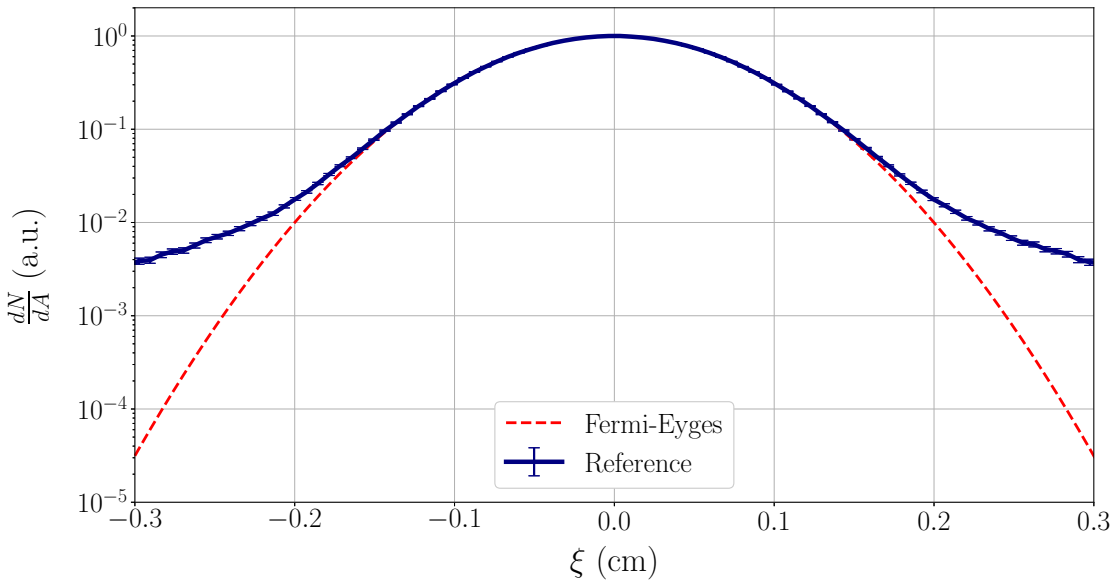

Fig. C.5 Comparison between the fluence profile given by the detailed and the Fermi-Eyges simulation at the entrance of the water phantom. The energy used to obtain this profile was 100 MeV.

To find the cause of the discrepancies between the detailed and Fermi-Eyges simulation, it necessary to locate where are the differences in the dose deposition. For that, the 100 MeV case will be take as example. In Figures C.6 and C.7 , the central and the most distal radial profile are shown. For the central profile, it is found a systematic overestimation of the dose deposition with the Fermi-Eyges. This could be caused by the underestimation of the number of protons experiencing large deflection angles due to the approximation introduced by the Fermi-Eyges formalism. Due to the Gaussian nature of the Fermi-Eyges formalism, there is an underestimation of protons with large deflection angles due to hard elastic events (HEE) in air. For the external dose profile, on top to the problem with HEE, a high dose deposition appears at the beginning of the phantom. This is produced by the secondary particles produced by protons in air.

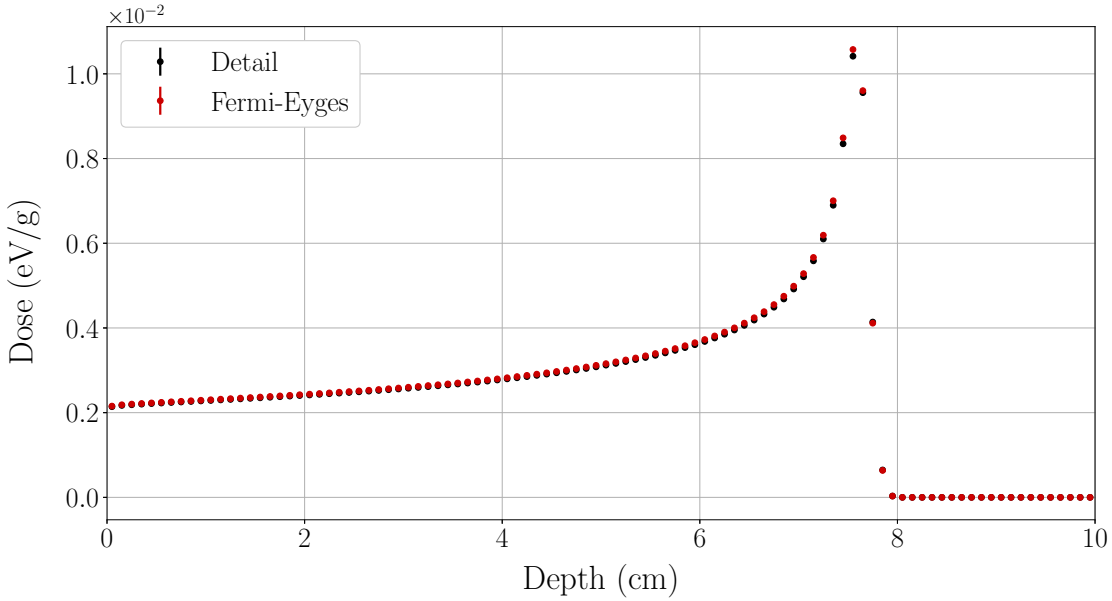

Fig. C.6 Comparison of the central dose profile for 100 MeV case. The data obtained for the detailed simulation appears in black and for the Fermi-Eyges approach, in red.

To quantify the effect of the secondary particles and the protons that undergoes a HEE, a simulation filtering this particles was made. In Figure C.8 are shown the results obtained from this simulation for 100 MeV. When the effect of secondary particles are removed, a better agreement between both simulation schemes is found. This shows that the dose deposition due to secondary particles is not reproduced by the Fermi-Eyges formalism and this is a discrepancy source between the detailed simulation and the theoretical approach.

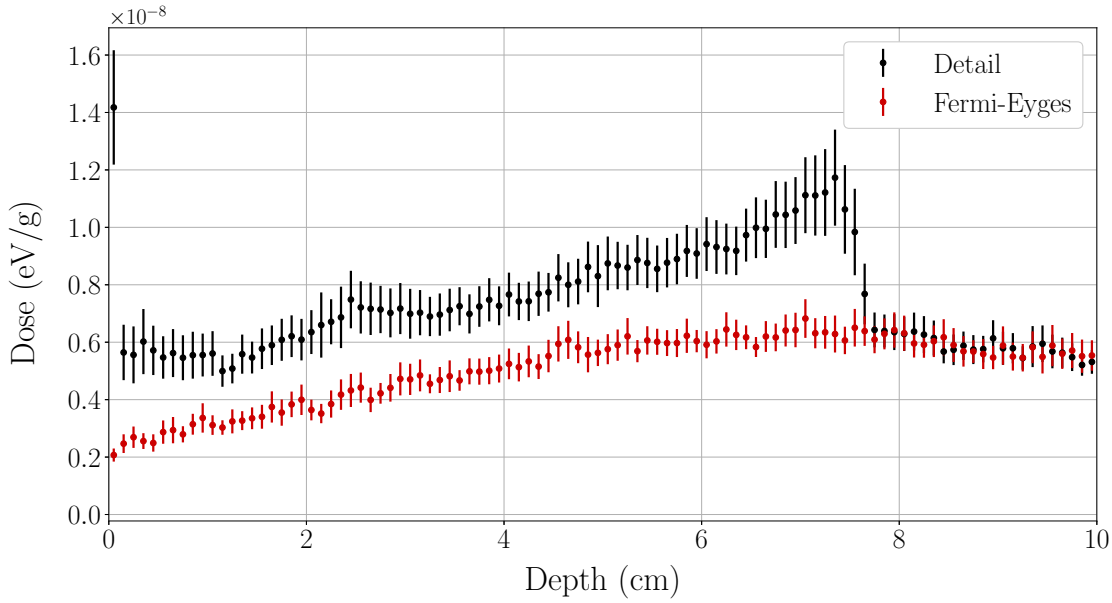

Fig. C.7 Comparison of the external dose profile (6^{th} radius) for 100 MeV case. The data obtained for the detailed simulation appears in black and for the Fermi-Eyges approach, in red.

When, additionally, the protons that undergo a HEE are removed from the phase space used as the simulation source, a best agreement between both simulations is found. For the external profiles, the improvement is significant, because removing this kind of protons makes that a correlation between the two simulation schemes appears.

Due to the large influence of the HEE in the 100 MeV case, a similar analysis was carried out for the 160 MeV case. Figure C.9 shows the results obtained by filtering the secondary particles and the protons with a large scattering angle for this energy. As can be seen, the effect of the secondary particles is negligible, since the values of the statistics hardly change when this type of particle is filtered. However, by filtering the contribution related to the protons that undergo an HEE, the value of the statistic is significantly improved. The underestimation in the number of protons with a large scattering angle implies that the number of protons in the central axis is increased, leading to an overestimation of the dose deposition in the central profile, creating a discrepancy between the detailed and Fermi-Eyges simulation. This proves that the effect of these protons is important in order to correctly reproduce the central dose profile.

Despite the fact that the problem with the central profile appears for all the energies considered in the simulation (see Figure C.4), problems with the outer radii appear only for the 100 MeV case. Figures C.10 and C.11 show a comparison between the detailed and

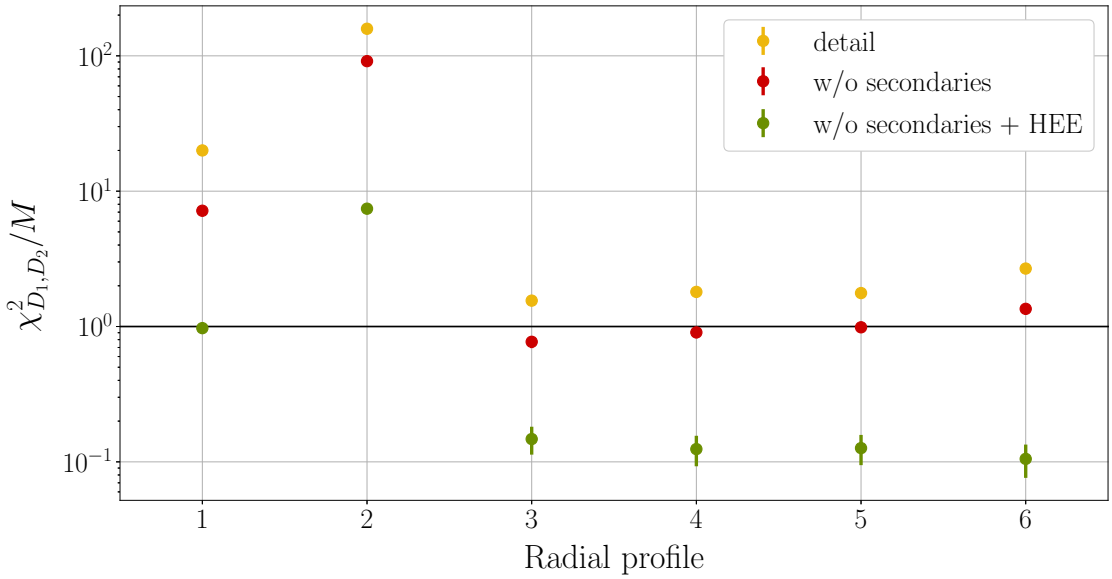

Fig. C.8 $\chi^2_{D_1,D_2}/M$ values calculated for the comparison between the filtered and Fermi-Eyges simulation for $E = 100$ MeV. The data calculated for detailed simulation appears in yellow, for the simulation without secondary particles, in red and for the simulation without secondary particles and HEE, in green. The unity is highlighted using a black line.

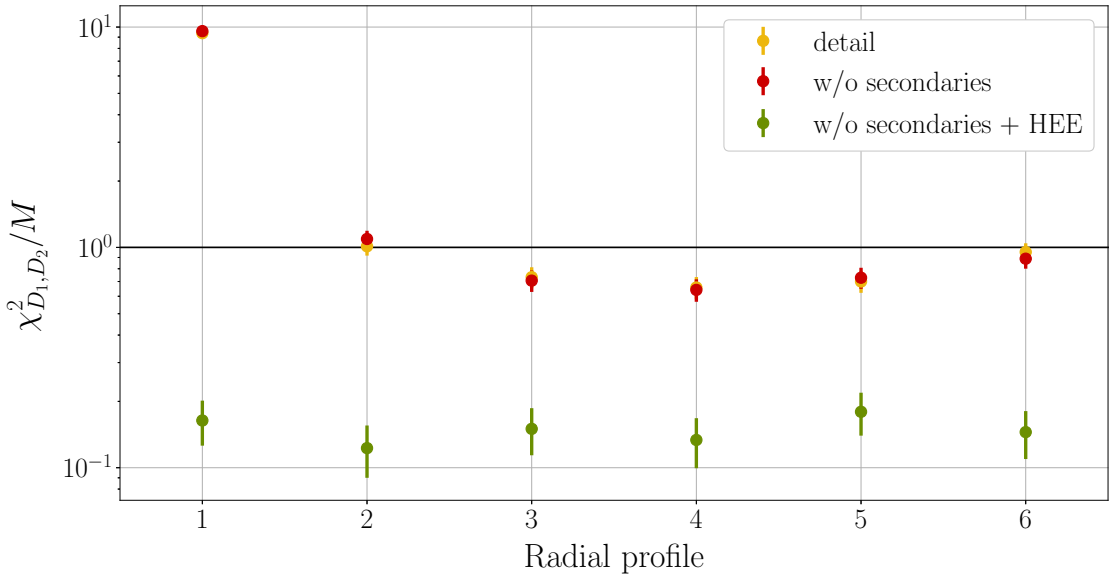

Fig. C.9 $\chi^2_{D_1,D_2}/M$ values calculated for the comparison between the filtered and Fermi-Eyges simulation for $E = 160$ MeV. The data calculated for detailed simulation appears in yellow, for the simulation without secondary particles, in red and for the simulation without secondary particles and HEE, in green. The unity is highlighted using a black line.

Table C.4 Normalised radial distance used to obtain the dose profiles analysed in the study of validity of the Fermi-Eyges formalism.

Energy (MeV)	100	160	225
1^{st} radius	0.0	0.0	0.0
2^{nd} radius	0.10	0.09	0.05
3^{rd} radius	0.30	0.17	0.07
4^{th} radius	0.40	0.26	0.24
5^{th} radius	0.60	0.34	0.30
6^{th} radius	0.79	0.43	0.33

Fermi-Eyges simulation for the central and the most external profiles for the 160 MeV case. For the central profile, a slight dose overestimation for the Fermi-Eyges simulation can be observed. This fact is also indicated by the statistic used (Figure C.4). Although there are some discrepancies in the central dose profile, these differences are smaller than for the 100 MeV case, as it can be seen in Figure C.4. For the external profile, small differences in the dose deposition between both simulations can be highlighted at the beginning and the end of the water phantom. The discrepancies at the beginning are associated with the secondary particles produced in air. Instead, the differences at the phantom end are relate to HEE. It is important to note that these differences are not significant because they do not have a appreciable impact in the statistic defined above (Figure C.4).

However, if the scoring positions are normalised using the range of the particle at the specific energy used, it is found that there are significant differences between the radial profiles used (Table C.4), that could explained why there is no differences in the dose profile for large radii at high energy. For low energy, a better mapping of the out-of-axis region is made than for high energies. For the 160 and 225 MeV cases, only radial distances of less than 50% of the range of the used protons have been analysed. Therefore, these differences at the scorer position could help to improve the results for high energies. This improvement is due to a worse mapping for the outer region at high energy. Using the Fermi-Eyges formalism, the central region is well described due to the consideration of what this theoretical framework is based on. Add to this the fact that the scattering contributions decrease as the energy used increases, the combination of these facts can explain why better results are obtained at high energies.

In order to compare the results obtained with the three energies considered in a similar situation, the radial distances have been chosen to correspond to 30% of the range of the protons used. The Table C.5 shows the values of the $\chi_{D_1,D_2}/M$ statistics for all the energies

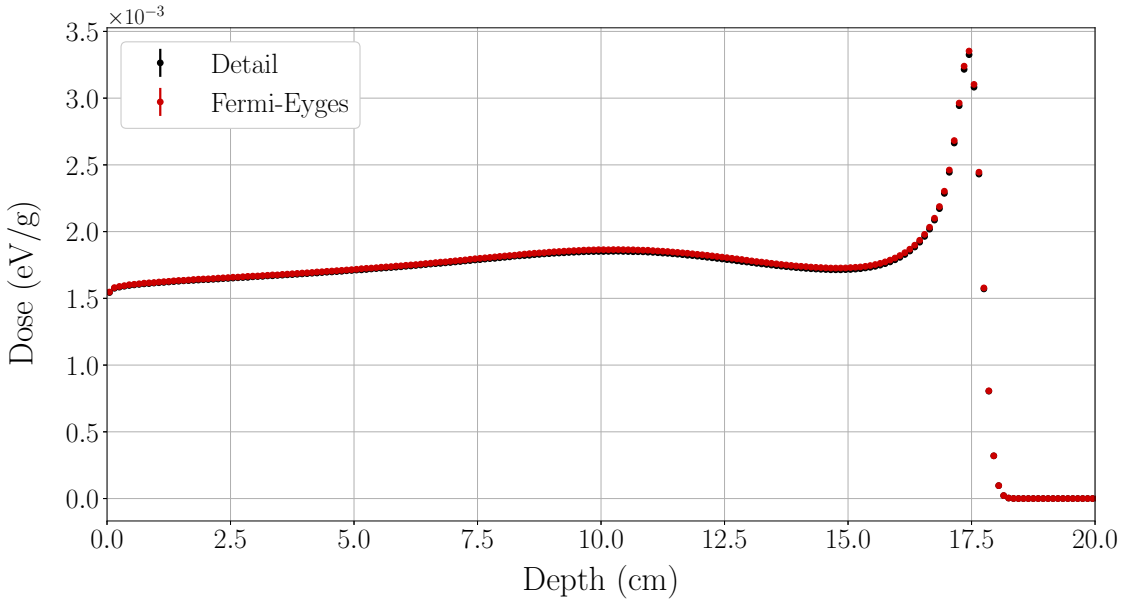

Fig. C.10 Comparison of the central dose profile for 160 MeV case. The data obtained for the detailed simulation appears in black and for the Fermi-Eyges approach, in red.

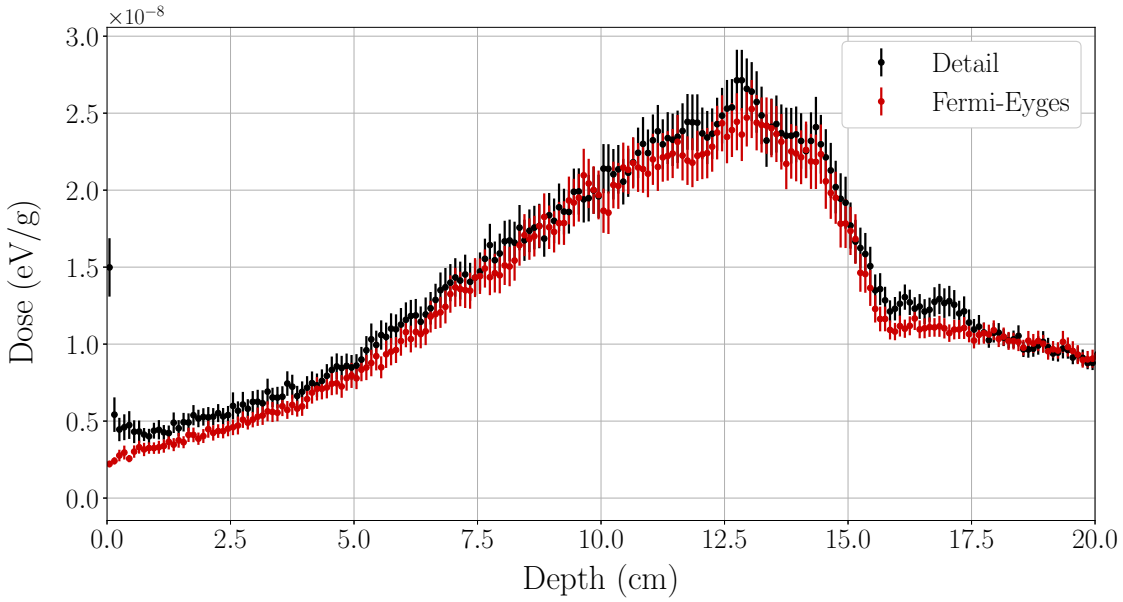

Fig. C.11 Comparison of the external dose profile (6^{th} radius) for 160 MeV case. The data obtained for the detailed simulation appears in black and for the Fermi-Eyges approach, in red.

considered under similar measurement conditions. As can be seen, the results obtained are quite similar, although the results improve as the energy used increases. As commented above, this is due to the scattering dependence with energy.

Table C.5 Comparison of the $\chi_{D_1,D_2}/M$ statistics between the different energies considered under similar measurement conditions.

Energy (MeV)	Radial profile	Normalised distance	$\chi_{D_1,D_2}/M$
100	3	0.30	1.55 (11)
160	5	0.34	0.70 (8)
225	5	0.30	0.36 (5)

Due to the effect described above, the underestimated count of protons with a large scattering angle suggests an increased number of protons along the central axis, resulting in overestimation of the dose deposited in the central axis. This problem appears for the 225 MeV case too (see Figure C.4). It can be solved for by filtering the protons undergoing a HEE, although this does not introduce significant changes for other radial distances, as in the case of 160 MeV.

C.3 Conclusion

In short, it is clear that the Fermi-Eyges formalism fails when it tries to describe the beam angular and spacial profile for low energies. The main cause of this failure is the neglecting of the contribution of protons that undergo a HEE. This fact causes an underestimation of the dose for the external radial profile and an overestimation for the central profile for low energies. This effect was pointed out by Sawakuchi *et al.* [172]. In their analysis, this group found experimental evidence that a poor description of the protons that interact through a HEE could cause an underestimation of the dose out-of-axis for low energies.

Moreover, the Fermi-Eyges formalism also suffers from a bad description of the secondary particles produced in air. This produces a systematic underestimation of the absorbed dose at the entrance of the water phantom for any energy.

Appendix D

List of publications

D.1 Articles in peer reviewed international journals

- **J. A. de la Torre**, A. M. Lallena, M. Anguiano, 2025 "Fano Test, Clinical Proton Beams and Nuclear Reactions" *Rad. Phys. Chem.* **230** 112538.

- **J. A. de la Torre**, A. M. Plaza, A. M. Lallena, F. Salvat, M. Anguiano, 2023 "Multiple scattering calculations for proton beams: Comparison of results from the general-purpose Monte Carlo codes PENH, FLUKA and TOPAS" *Rad. Phys. Chem.* **213** 111225.

- J. A. Moreno-Pérez, A. Marchena, P. Araya, J. J. López-Peñalver, **J. A. de la Torre**, A. M. Lallena, S. Becerril, M. Anguiano, A. J. Palma, M. A. Carvajal, 2025 "Characterization of Different Types of Micro-Fission and Micro-Ionization Chambers Under X-Ray Beams" *Sensors* **25**(6) 1862.

- A. G. Şerban, **J. A. de la Torre**, M. Anguiano, A. M. Lallena, F. Salvat-Pujol "On the improved performances of FLUKA v4-4.0 in out-of-field proton dosimetry" [Manuscript submitted for publication].

- **J. A. de la Torre**, I. Ruiz-García, D. Guirado, A. J. Palma, M. A. Carvajal, A. M. Lallena, M. Anguiano "A Monte Carlo analysis of the feasibility of a 3D structure build up with silicon photodiodes for in vivo dosimetry in radiotherapy" [Manuscript submitted for publication]

D.2 Participation in scientific conferences

- **J. A. de la Torre**, I. Ruiz-López, M. A. Carvajal, M. Anguiano, A. M. Lallena. "Feasibility of a photodiode-based dosimeter use in proton therapy: study of the angular dependence using Monte Carlo simulation". Congress: Workshop on Technologies and Applied Research at the Future Valencian Proton-Therapy Facility. Valencia (Spain), February 2024. Oral presentation.

- **J. A. de la Torre**, I. Ruiz-López, D. Guirado, M. A. Carvajal, M. Anguiano, A. M. Lallena. "Study of the angular dependence of a photodiode-based dosimeter using Monte Carlo simulation". Congress: RAD-11. Herceg-Novi (Montenegro) June 2023. Oral presentation.

- **J. A. de la Torre**, M. Anguiano, A. M. Lallena. "Validación Monte Carlo de la teoría de Fermi-Eyges". Congress: 8º Congreso conjunto SEFM/SEPR. Oviedo (Spain) May 2023. Oral presentation.

- **J. A. de la Torre**, A. M. Lallena, M. Anguiano. "Ionization chamber for use in radiotherapy: simulation with Monte Carlo codes". Congress : Elicsir symposium. Nis (Serbia) January 2023. Oral presentation.

- **J. A. de la Torre**, M. Anguiano, A. M. Lallena. "Monte Carlo simulations for protons beams: A test of nuclear models". Congress: XIV jornadas CPAN (Centro Nacional de Física de Partículas, Astropartículas y Nuclear). Bilbao (Spain) November 2022. Oral presentation.

- **J. A. de la Torre**, M. Anguiano, A. M. Lallena. "Monte Carlo simulation for proton beams supported by a Fano test". Congress: XIII jornadas CPAN (Centro Nacional de Física de Partículas, Astropartículas y Nuclear). Huelva (Spain), March 2022. Oral presentation.